OPTICAL CHARACTERIZATION OF GROUP-IV SEMICONDUCTOR ALLOYS USING SPECTROSCOPIC ELLIPSOMETRY AND HIGH RESOLUTION X-RAY DIFFRACTION

BY

NALIN S. FERNANDO, B.S., M.S.

A dissertation submitted to the Graduate School

in partial fulfillment of the requirements

for the degree

Doctor of Philosophy

Major Subject: Physics

New Mexico State University

Las Cruces New Mexico

May 2017

"Optical characterization of group-IV semiconductor alloys using spectroscopic ellipsometry and high resolution X-ray diffraction", a dissertation prepared by Nalin S. Fernando in partial fulfillment of the requirements for the degree, Doctor of Philosophy of Science, has been approved and accepted by the following:

Loui Reyes
Dean of the Graduate School

Stefan Zollner
Chair of the Examining Committee

Date

Committee in charge:

Dr. Stefan Zollner, Chair

Dr. Heinrich Nakotte

Dr. Michael Engelhardt

Dr. David Voelz

DEDICATION

I dedicate this work to my beloved parents Gration and Ethal Fernando, my lovely wife Melisha for their unceasing encouragement and support.

ACKNOWLEDGMENTS

First and foremost, I would like to thank my advisor Dr. Stefan Zollner for his guidance and encouragement throughout this work. Without his guidance and persistent help this dissertation would not have been possible. I would also like to thank Dr. Heinrich Nakotte, Dr. Michael Engelhardt and Dr. David Voelz for taking time from their busy schedules to serve in my Ph.D. dissertation committee. I am grateful to our collaborators: Dr. Kolodzey, Ryan Hickey, John Hart, Ramsey Hazbun, and Dainan Zhang at University of Delaware, Dr. Kouvetakis, Dr. Menendez, and Dr. Chi Xu at Arizona State University, and Dr. Matt Kim at QuantTera for providing us samples, invaluable advice and support.

I would like to thank current and former members of Dr. Zollner's ellipsometry group. Special thanks to Nathan Nunley, Nuwanjula Sandamali, Farzin Abadizaman, Jaime Moya, Jacqueline Cooke, Lina Abdallah, Ayana Ghosh, Dennis Trujillo, and visiting researcher Dr. Sudeshna Chattopadhyay for their support. Many thanks to Rosa Christensen, our department fiscal assistant, for her dedicated work.

The FTIR ellipsometry measurements were performed at the J.A. Woollam Co., Inc., Lincoln, NE and at the Center for Integrated Nanotechnologies (CINT), an Office of Science User Facility operated for the U.S. Department of Energy (DOE) Office of Science by Los Alamos National Laboratory (Contract DE-AC52-06NA25396) and Sandia National Laboratories (Contract DE-AC04-94AL85000).

This work was supported by the Air Force Office of Scientific Research (FA9550-13-1-0022) and by the Army Research Office (W911NF-14-1-0072). Support during 2016 was provided by the National Science Foundation (DMR-1505172).

VITA

2005-2009	B.S. in Engineering Physics, University of Colombo, Colombo, Sri Lanka
2013	M.S. in Physics, New Mexico State University
2017	Ph.D. in Physics New Mexico State University

PUBLICATIONS

R. Hazbun, J. Hart, R. Hickey, A. Ghosh, **N. Fernando**, S. Zollner, T. Adam, and J. Kolodzey, J. Crystal Growth, **444**, 21 (2016).

J. Hart, R. Hazbun, D. Eldridge, R. Hickey, **N. Fernando**, T. Adam, S. Zollner, and J. Kolodzey, Thin Solid Films **604**, 23 (2016).

T.N. Nunley, **N.S. Fernando**, N. Samarasingha, J.M. Moya, C.M. Nelson, A.A. Medina, S. Zollner, J. Vac. Sci. Technol. B **34**, 061205 (2016).

N.S. Fernando, T.N. Nunley, A. Ghosh, C.M. Nelson, J. Cooke, A.A. Medina, C. Xu, J. Menendez, J. Kouvetakis, S. Zollner, Appl. Surf. Sci. **XX**, xxxx (2016) (in press).

N.S. Fernando, J. Hart, D. Zhang, R. Hickey, R. Hazbun, J. Kolodzey, and S. Zollner, IEEE Summer Topicals Conference on Emerging Technology for Integrated Photonics, July 2016, Newport Beach, CA.

T.N. Nunley, **N.S. Fernando**, N. Samarasingha, J.M. Moya, C.M. Nelson, A.A. Medina, S. Zollner, IEEE Summer Topicals Conference on Emerging Technology for Integrated Photonics, July 2016, Newport Beach, CA.

C. Xu, **N.S. Fernando**, S. Zollner, J. Kouvetakis, and J. Menndez, (Submitted November 2016).

R. Hickey, **N. Fernando**, S. Zollner, J. Hart, R. Hazbun, and J. Kolodzey, J. Vac. Sci. Technol. B **35**, 021205 (2017).

N.S. Fernando, R. Hickey, J. Hart, D. Zhang, R. Hazbun, J. Kolodzey, and S. Zollner, J. Vac. Sci. Technol. B (in preparation).

CONFERENCE PRESENTATIONS

N. Fernando, R. Hickey, J. Hart, R. Hazbun, D. Zhang, J. Kolodezy, and S. Zollner, *Optical Properties of Pseudomorphic* $Ge_{1-x-y}Si_xSn_y$ *on Ge*, 2017 International Conference on Frontiers of Characterization and Metrology for Nanoelectronics (FCMN), Monterey, CA, 21-23 March 2017.

N. Fernando, R. Hickey, J. Hart, R. Hazbun, D. Zhang, J. Kolodezy, and S. Zollner, *Effects of composition and strain on band gaps of pseudomorphic* $Ge_{1-x-y}Si_xSn_y$ *on Ge*, AVS 63rd International Symposium, Nashville, TN, 6-11 November 2016.

N. Fernando, S. Zollner, R. Hickey, J. Hart, D. Zhang, R. Hazbun, and J. Kolodzey, *Band gap engineering of pseudomorphic* $Ge_{1-x-y}Si_xSn_y$ *alloys on Ge for photonic applications*, APS Four Corners Section Meeting, Las Cruces, NM, 21-22 October 2016.

N.S. Fernando, J. Hart, D. Zhang, R. Hickey, R. Hazbun, J. Kolodzey, and S. Zollner, *Band structure and optical properties of pseudomorphic* $Ge_{1-x-y}Si_xSn_y$ *on Ge*, IEEE Summer Topicals Conference on Emerging Technology for Integrated Photonics, Newport Beach, CA, 11-13 July 2016.

N.S. Fernando, R. Hickey, J. Hart, R. Hazbun, D. Zhang, J. Kolodzey, and S. Zollner, *Band structure of pseudomorphic* $Ge_{1-x-y}Si_xSn_y$ *on Ge*, AVS 2016 New Mexico Symposium, Albuquerque, NM, 24 May 2016.

N. Fernando, J. Moya, S. Zollner, J. Hart, D. Zhang, R. Hickey, R. Hazbun, and J. Kolodzey, *Strain dependence of the band structure and critical points of pseudomorphic* $Ge_{1-y}Sn_y$ *alloys on Ge*, APS Four Corners Section Meeting, Tempe, AZ, 16 October 2015.

N. Fernando, T. Nunley, S. Zollner, D. Zhang, R. Hickey, J. Kolodzey, *Compositional and strain dependence of the band gaps of pseudomorphic* $Ge_{1-y}Sn_y$ *alloys on Ge*, AVS 2015 New Mexico Symposium, Albuquerque, NM, 19 May 2015.

N. Fernando, T.N. Nunley, S. Zollner, S. Xu, J. Menendez, and J. Kouvetakis, *Temperature dependent band gaps of GeSiSn alloys grown on Ge buffered Si substrates*, American Physical Society March meeting, San Antonio, TX, March 2-6, 2015.

Nalin Fernando, Ayana Ghosh, Cayla Nelson, Amber Medina, Seth Chi Xu, Jose Menendez, John Kouvetakis, Stefan Zollner, *Experimental and theoretical investigation of critical point energy shift of Ge films grown on Si (100) substrate due to strain*, American Physical Society Four Corners Section Meeting, Denver, CO, October 18-19 2013.

N. Fernando, A. Ghosh, C.M. Nelson, A.A. Medina, S.C. Xu, J. Menendez, J. Kouvetakis, and S. Zollner, *Dynamic strain measurements of Ge on Si using spectroscopic ellipsometry*, Rio Grande Symposium, Albuquerque, NM, 07 October 2013.

Nalin Fernando, Tyne Richele Johns, Yue Qi, Chang H. Kim, Abhaya Datye and Boris Kiefer, *Sintering of* Pd_n/Pt_n *(n=1, 9) monometallic clusters on* γ-Al_2O_3 *(100) Surfaces*, North American Catalysis Society (NAM) meeting, Louisville KY, 2-7 June 2013.

Nalin Fernando, Tyne Richele Johns, Yue Qi, Chang H. Kim, Abhaya Datye and Boris Kiefer, *A DFT study of the interaction of monometallic* Pd_n/Pt_n *(n=1, 9) clusters with* γ-Al_2O_3 *(100) surfaces*, American Physical Society March meeting, Baltimore, MD, 18-22 March, 2013.

Nalin Fernando, Tyne Richele Johns, Yue Qi, Chang H. Kim, Abhaya Datye and Boris Kiefer, *Exploration of bimetallic alloys for the design of efficient low temperature car exhaust catalysts*, Las Cruces Museum of Natural History, Mesilla Valley Mall, NM, June-2012.

N. Samarasingha, C. Rodriguez, J. Moya, S. Zollner, **N. Fernando**, S. Chattopadhyay, P. Ponath, and A.A. Demkov, *Structural and optical properties of* $SrTiO_3$ *thin films on semiconductors*, 43rd Conference on the Physics and Chemistry of Surfaces and Interfaces, Palm Springs, CA, 17-21 January 2016.

T.N. Nunley, **N. Fernando**, J. Moya, and S. Zollner, *Optical constants of Ge and*

GeO_2 from ellipsometry, 80. Jahrestagung der DPG und DPG-Fruhjahrstagung, Regensburg, Germany, 6-11 March 2016.

N. Samarasingha, C. Rodriguez, J. Moya, **N. Fernando**, S. Zollner, P. Ponath, K. Kormondy, A. Demkov, D. Pal, A. Mathur, A. Singh, S. Dutta, J. Singhal, and S. Chattopadhyay, *Excitons at interfaces in ellipsometric spectra*, AVS 63rd International Symposium and Exhibition, Nashville, TN, 6-11 November 2016.

ABSTRACT

OPTICAL CHARACTERIZATION OF GROUP-IV SEMICONDUCTOR ALLOYS USING SPECTROSCOPIC ELLIPSOMETRY AND HIGH RESOLUTION X-RAY DIFFRACTION

BY

NALIN S. FERNANDO, B.S., M.S.

Doctor of Philosophy

New Mexico State University

Las Cruces, New Mexico, 2017

Dr. Stefan Zollner, Chair

Germanium is a group IV semiconductor widely used in the semiconductor optoelectronic industry. It is an indirect band material with the conduction band minimum at the L point, which is 0.140 eV below the conduction band at the Γ point. However, the band structure of Ge is a strong function of temperature, strain, alloy composition and dopant concentration. It has been reported that, at about ∼ 2% tensile strain, Ge becomes a direct band gap material, indicating the possibility of wide spread applications of Ge-based photonic devices. Alloying Ge with Sn also makes it a direct band gap material, relaxed $Ge_{1-y}Sn_y$ alloys become direct at 6-10% Sn. In addition, $Ge_{1-x-y}Si_xSn_y$ ternary alloy with two compositional degrees of freedom allows decoupling of the lattice constant and electronic structures simultaneously. Band gap engineering of Ge by controlling

strain, alloying composition and dopant concentration has attracted the interest of researchers in materials science. Hence, the knowledge of the compositional, strain, and temperature dependence of the $Ge_{1-x-y}Si_xSn_y$ band structure is critical for the design of photonic devices with desired interband transition energy.This dissertation focuses on the optical characterization of the compositional, strain, and temperature dependence of the optical properties of Ge-Si-Sn alloys on Ge/Si substrates using spectroscopic ellipsometry. We use high resolution X-ray diffraction (HRXRD), X-ray reflectivity (XRR) and atomic force microscopy (AFM) to characterize the strain, composition, thickness, surface roughness of the Ge-Si-Sn epilayers on Ge/Si substrates.

The temperature dependent thermal expansion coefficient of Ge is larger than Si. Therefore a Ge film, which is relaxed at the growth temperature ($\sim$ 800 K) on Si substrate, likes to contract more rapidly compared to Si upon cooling down to lower temperatures, and will experience a temperature dependent biaxial tensile stress. We predict the strain dependence the E_1 and $E_1+\Delta_1$ critical points of Ge on Si from 80 - 780 K using deformation potential theory and employing a model for the thermal expansion coefficients of Si and Ge. The predictions are validated experimentally, using spectroscopic ellipsometry. A pseudomorphically grown $Ge_{1-x-y}Si_xSn_y$ layer on Ge also experiences a biaxial stress due to the lattice mismatch between the alloy layer and the Ge substrate. We use elasticity theory and deformation potential theory to predict the variation of the energy band structure of pseudomorphic $Ge_{1-x-y}Si_xSn_y$ on Ge at the Γ, L and X symmetry points in the Brillouin zone as a function of Si (x) and Sn (y) compositions. The critical Si (x) and Sn (y) compositions needed for an indirect to direct band gap transition are identified. The effects of the substrate on the band gaps and indirect-direct transition are investigated when the active $Ge_{1-x-y}Si_xSn_y$ is pseu-

domorphically grown on Ge buffered Si substrates and on GaAs. The theoretical predictions from deformation potential theory are experimentally validated using spectroscopic ellipsometry for pseudomorphic $Ge_{1-y}Sn_y$ on Ge.

The complex pseudodielectric functions of the samples were measured using spectroscopic ellipsometry in the 0.5-6.6 eV energy range. Temperature dependent measurements were taken in a UHV cryostat at temperatures from 80-780 K. A multilayer model consisting of a surface layer/epilayer/substrate was used for the treatment of the experimental data. The surface layer was modeled as a surface oxide layer- GeO_2, where the accurate optical constants were determined by multisample spectroscopic ellipsometry analysis of thermally grown GeO_2. Critical point energies and related parameters were obtained by the analyzing second-derivative spectrum $d^2\epsilon/d^2\omega$ of the dielectric function. Our experimental results are in excellent agreement with the theoretical predictions from deformation theory.

CONTENTS

LIST OF TABLES xv

LIST OF FIGURES xvii

1 Introduction 1

2 Semiconductor materials 5

2.1 Interband transitions and critical points 6

2.2 Temperature dependence of the critical points 14

2.3 Ge band gap engineering *via* strain and alloying 17

3 Sample preparation and characterization techniques 28

3.1 Chemical vapor deposition (CVD) 28

3.2 Molecular beam epitaxy (MBE) 29

3.3 Spectroscopic ellipsometry 29

3.3.1 Data acquisition 30

3.3.2 Modeling ellipsometry data 34

3.3.3 Second derivative analysis 36

3.3.4 Temperature dependent measurements inside the cryostat 37

3.4 High resolution X-ray diffraction 39

3.4.1 Diffraction from epilayers 41

3.4.2 Reciprocal space maps 43

3.5 X-ray reflectivity 47

3.6 Atomic force microscopy 51

4 Optical constants of germanium and thermally grown germanium dioxide from 0.5 to 6.6 eV via a multi-sample ellipsometry investigation **54**

4.1 Abstract 54

4.2 Introduction 55

4.3 Thermal oxidation of Ge 58

4.4 Ellipsometry measurements and data analysis 64

4.5 Results for GeO_2 on Ge with uniform layer fits 68

4.6 Results for GeO_2 on Ge with non-uniform layer fits 74

4.7 Discussion 75

4.8 Summary 78

5 Temperature dependence of the interband critical points of bulk Ge and strained Ge on Si **80**

5.1 Abstract 80

5.2 Introduction 81

5.3 Sample preparation and characterization 82

5.4 Thermal expansion mismatch 86

5.5 Ellipsometric measurements and data processing 88

5.6 Results and discussion for E_1 and $E_1 + \Delta_1$ 92

5.7 Higher-energy critical points E_0' and E_2 102

5.8 Conclusion 105

6 Band gap and strain engineering of pseudomorphic $Ge_{1-x-y}Si_xSn_y$ alloys on Ge and GaAs for photonic applications **109**

6.1 Abstract 109

6.2 Introduction 110

6.3 Continuum elasticity and deformation potential theory 113

6.4 Pseudomorphic $Ge_{1-y}Sn_y$ alloys on Ge: Sample preparation and characterization 126

6.5 Ellipsometry data analysis 129

6.6 Results and discussion 132

6.7 Conclusion 141

7 Properties of pseudomorphic and relaxed $\text{Germanium}_{1-x}\text{Tin}_x$ alloys (x < 0.185) grown by MBE 143

7.1 Abstract 143

7.2 Introduction 144

7.3 Preparation and Growth 145

7.4 Analysis 147

7.4.1 X-ray diffraction 147

7.4.2 Atomic force microscopy 151

7.4.3 Spectroscopic ellipsometry 154

7.5 Discussion 156

7.6 Conclusion 161

8 Conclusion 163

REFERENCES 166

LIST OF TABLES

1 Different types of critical points in one, two and three dimensions with the corresponding joint density of states D_j [18]. 11

2 List of GeO_2 oxides produced by thermal oxidation of Ge substrates at 2.7 atm oxygen pressure at 550°C. d is the oxide thickness from ellipsometry, t the oxidation time, Δd the relative thickness non-uniformity determined from the ellipsometry depolarization spectra, d_{XRR} the thickness determined by x-ray reflectance (XRR) (samples 4 and 5 were fit with a fixed thickness), and $<\rho>$ the electron density determined by XRR. Ellipsometry results are from two models (uniform and graded) as discussed in Sec. 4.5 (MSE=14) and 4.6 (MSE=6.9). Probable errors are given in parentheses. . . 62

3 Deal-Grove parameters A, B, and τ from Eq. (55) for thermal oxidation of Ge in pure O_2 at temperature T and pressure p. Probable errors are given in parentheses. 62

4 Values of the parameters a, b, and θ_B obtained by fitting the E_1 and $E_1+\Delta_1$ critical point energy vs temperature to Eq. (72) and the values of the parameters a', b$'$, and θ'_B which describe the temperature dependence of the E_1 and $E_1+\Delta_1$ taking into account the effects of the thermal expansion using Eq. (71). Parameters marked (f) were fixed during the fit. 99

5 Bose-Einstein parameters to describe the critical-point broadenings using Eq. (73). The phonon energy parameter θ_B was fixed to be the same as in Table 4. Parameters marked (f) were fixed during the fit. 101

6 Deformation potentials, band gaps, and bowing parameters for Ge, Si, and Sn and their alloys used in the model, in units of eV. Deformation potential parameters a, b, $\left[\Xi_d + \frac{1}{3}\Xi_u\right]^L$, Ξ_u^Δ, and $\left[\Xi_d + \frac{1}{3}\Xi_u\right]^\Delta$ were taken from Refs. [5, 49, 72, 202]. The band gaps E_0^Γ, E_i^L, E_i^Δ and related parameters were taken from Refs. [9, 68, 66, 67, 203, 204, 205]. The E_1, $E_1 + \Delta_1$ band gaps and related parameters were taken from Refs. [66, 69]. The asterisk indicates that the value of Ge was used for our calculations. Elastic constants C_{ij} are in units of GPa from Ref. [49, 55]. 117

7 Sn composition y and thickness t from (004) XRD; in-plane ($\epsilon_{\parallel}$) and out-of-plane strain ($\epsilon_{\perp}$) from ($\bar{2}\bar{2}4$) reciprocal space maps. Band gaps E_0^Γ, E_1, E_1+Δ_1, and thickness from spectroscopic ellipsometry (SE). Also growth temperature T_g. 139

8 List of materials parameters for the eight samples in this series. Sn concentration, relaxation, in and out of plane strain, thickness and FWHM of the (004) xrd peak were calculated from XRD as described in the text. The RMS roughness was determined via AFM scans over a 3×3 μm surface region. The spectroscopic ellipsometry (VASE) roughness is a calculated from a peak-to-valley surface layer model, which includes the thickness of a native oxide layer. 152

LIST OF FIGURES

1 Band structure of bulk Ge calculated by “full-zone k·p method. [18] The conduction band minimum is at the L point in the Brillouin zone with an experimentally determined indirect band gap (E_g^L) of 0.66 eV. The conduction band at the center of the Brillouin zone is 0.14 eV above the L point, the direct band gap at the Γ point (E_g^Γ) is measured to be 0.8 eV. 6

2 Schematic representation of the frequency dependence of the imaginary part of the dielectric function ϵ_2 near interband critical points in one, two and three dimensions [18]. 11

3 Real (ϵ_1, dashed) and imaginary (ϵ_2, solid) parts of the dielectric function of bulk Ge at room temperature obtained using spectroscopic ellipsometry (This work). 12

4 Real (ϵ_1, dashed) and imaginary (ϵ_2, solid) parts of the complex dielectric function of bulk Ge measured at temperatures between 80 K and 780 K (This work). 14

5 Temperature dependence of the E_0 critical point, obtained from second derivative analysis of the dielectric function (explained in the next chapter) of bulk Ge. The solid line shows the best fit of the data using Eq. (72) with parameters a=0.963 ±0.006 eV, b=0.090±0.006 eV and θ_B=347±27 K (This work). 15

6 Temperature dependence of the linear thermal expansion coefficients of Si (α_{Si}) and Ge (α_{Ge}) modeled by Eq. (62) taken from ref. [42]. Experimental data (symbols) were taken from Ref. [44, 45, 46, 47, 48]. 18

7 Compositional dependence of the lattice parameter of relaxed $Ge_{1-x-y}Si_xSn_y$ alloys, calculated using Eq. (76) (this work). 22

8 Compositional dependence of the in-plane strain $\epsilon_{\parallel}(x, y)$ on pseudomorphic $Ge_{1-x-y}Si_xSn_y$ on Ge, calculated using Eq. (77) (this work). 23

9 Schematic overview of the measurement principle of spectroscopic ellipsometry. [76] 31

10 Experimental data (solid) of ellipsometric angles Ψ and Δ for $Ge_{91}Si_3Sn_6$ on Ge buffered Si versus photon energy. The model data (dashed) obtained, assuming a multilayer system as illustrated in the inset is also shown (this work). 32

11 Pseudodielectric function $\langle\epsilon_1\rangle$ (solid) and $\langle\epsilon_2\rangle$ (dashed) for $Ge_{91}Si_3Sn_6$ on Ge buffered Si versus photon energy obtained from measured ellipsometric angles Ψ and Δ (this work). 33

12 Real (ϵ_1, short-dashed) and imaginary (ϵ_2, long-dashed) parts of the dielectric function of $Ge_{91}Si_3Sn_6$ obtained from a point-by-point fit. Solid lines represent the dielectric function of Ge (this work). . . . 33

13 Second derivatives of the real (ϵ_1) and imaginary (ϵ_2) part of the dielectric function of $Ge_{91}Si_3Sn_6$ with respect to photon energy near the E_1 and $E_1 + \Delta_1$ critical points. Symbols represent the experimental data and the solid line shows the best fit with a two dimensional critical point assuming parabolic bands and constant dipole matrix elements (this work). 36

14 A view of the ellipsometry cryostat mounted on the J.A. Woollam variable angle-of-incidence ellipsometer. 38

15 The sample holder with a sample held by two horizontal metal clamping strips. The thermocouple is clamped between the front sample surface and the upper clamping strip in order to measure the temperature of the sample surface accurately. 38

16 Schematic representation of $\omega - 2\theta$ symmetric scans. An initial plane wave with wave vector $\vec{k}$ is irradiated on the sample surface with an angle $\omega(=\theta)$ and the outgoing scattered waves $\vec{k}'$ are analyzed under the same angle [85]. 40

17 Logarithmic intensity versus diffraction angle for the symmetric (004) $\omega - 2\theta$ reflections of the pseudomorphic $Ge_{93.2}Sn_{6.8}$ on Ge. Symbols represent the experimental data and the solid line shows the model (this work). 40

18 Schematic representation of reciprocal space mapping, where several $\omega - 2\theta$ scans are performed with stepped ω to cover an area of the Bragg peaks for the epilayer and the substrate [85]. 43

19 Schematic representation of RSMs of a fully relaxed, pseudomorphic (fully strained), and partially relaxed epilayers on a substrate [85]. 44

20 Schematic representation of a tilted epilayer relative to the substrate. Tilting causes a rotation of the epilayer reflections about the origin in reciprocal space [85]. 45

21 Reciprocal space maps around $(\bar{2}\bar{2}4)$ reflections of (a) fully strained $Ge_{93.2}Sn_{6.8}$ and (b) partially (60%) relaxed $Ge_{87.5}Sn_{12.5}$ on Ge. Solid lines show the fully strained and fully relaxed conditions (this work). 45

22 X-ray reflectivity spectrum of a 33 nm thick GeO_2 layer on Ge (∘: experimental data, line: model). Electron density profile versus depth obtained from the model for the same sample is shown in the inset (this work). 50

23 Left: Schematic of an AFM detection system, showing the laser beam (light source), tip, cantilever, and photodiode detector. Right: The force between the tip of the oscillating cantilever and the surface as a function of the distance between them [93]. 51

24 Atomic force microscopy image of the $Ge_{89}Sn_{11}$ on Ge surface showing an RMS roughness of 0.8 nm (this work). 52

25 Thermal oxide thickness versus oxidation time at atmospheric pressure (Ref. [78]) and at 2.7 atm (this work). The solid line shows the best fit to Eq. (55), while the dashed lines assume a quadratic dependence of the thickness on oxidation time (A=0). 61

26 (a) Grazing-incidence x-ray reflectance spectrum (red: model; blue: data) and (b) electron density versus depth for sample 2 (33 nm thickness). 63

27 Ellipsometric angles ψ and Δ (symbols) at four angles of incidence (60°, 65°, 70°, 75°) for a Ge wafer with native oxide, after the standard clean described in Sec. 4.3. Two data sets from 0.5 to 3.0 eV and from 0.76 to 6.6 eV were merged. Lines: Data calculated from our model. 69

28 Same data as in Fig. 27 for four angles of incidence, but displayed as a complex pseudodielectric function with real part $<\epsilon_1>$ (green) and imaginary part $<\epsilon_2>$ (blue). Data from our model are shown in red. 70

29 Ellipsometric angles (ψ, Δ) and depolarization (symbols) for 34 nm GeO_2 on Ge. Our model with a uniform oxide (lines) is nearly indistiguishable from the experimental data. 71

30 As Fig. 29, but for a Ge wafer with 89 nm GeO_2. 72

31 As Fig. 29, but for a Ge wafer with 136 nm GeO_2. The uniform layer model (lines) matches the maxima of ψ, but not the minima. This is a clear indication for a gradient in the refractive index of the GeO_2 film. 72

32 Complex dielectric function for Ge from a fit to our ellipsometry results in comparison with literature data [83, 102, 111, 116, 130]. 76

33 Complex dielectric function for GeO_2 from the uniform layer fit to our ellipsometry results in comparison with literature data [78, 140]. 78

34 To estimate the accuracy of the optical constants for GeO_2, we plot the dielectric function obtained from various methods: From a Tauc-Lorentz fit to all data assuming uniform oxide density, from fits of single samples (89 nm and 136 nm thickness) with uniform density, and a two-oscillator fit (Tauc-Lorentz and Gaussian) to all data allowing a density gradient for the thicker oxides. 79

35 Pseudodielectric function of a Ge epitaxial layer on Si at 300 K (solid: data; dashed: model). Interference fringes between 0.8 and 1.2 eV allow the determination of the Ge epilayer thickness (1460 nm). The native oxide thickness obtained from the fit is 3.1 nm. . 83

36 Inset: Logarithmic intensity versus diffraction angle for the symmetric (004) ω-2θ x-ray reflections of Ge on Si, showing a strong peak from the Si substrate at ω=34.5° and a weaker peak from the Ge epilayer at 33°. Main graph: High-resolution x-ray diffraction ($\bar{2}\bar{2}4$) grazing exit reciprocal space map of Ge on Si. The relaxation line (solid) shows that the Ge epilayer is not fully relaxed relative to the Si substrate. The residual in-plane strain $\epsilon_{||}$ is 0.14±0.04% (tensile) and the out-of-plane strain $\epsilon_{\perp}$ is −0.11±0.03% (compressive) as a result of the difference in thermal expansion of Ge and Si. 84

37 Temperature dependence of the in-plane strain $\epsilon_{||}$ and the out-of-plane strain $\epsilon_{\perp}$ in the Ge epilayer caused by the thermal expansion mismatch between the Si substrate and the Ge layer as shown in the inset. Ge experiences a temperature dependent biaxial tensile stress which leads to a tensile in-plane strain calculated using Eq. (63) from the thermal expansion coefficients of Si and Ge assuming different growth temperatures T_g. The resulting out-of-plane strain is compressive (negative). ∘: Strain components derived from high resolution x-ray diffraction ($\bar{2}\bar{2}4$) grazing exit reciprocal space map at 300 K. 87

38 Real (ϵ_1, dashed) and imaginary (ϵ_2, solid) parts of the dielectric function of Ge on Si at temperatures between 80 K and 785 K. . . 90

39 Second derivatives of the real (ϵ_1) and imaginary (ϵ_2) parts of the dielectric function of Ge on Si (solid) and bulk Ge (dotted) with respect to photon energy near the E_1 and E_1+Δ_1 CPs at 80 K. Symbols (∘: Ge on Si, □: bulk Ge) represent the experimental data, the lines the best fit with a two dimensional minimum critical point using Eq. (68). 91

40 Temperature dependence of the E_1 (•, ∘) and E_1+Δ_1 (■, □) energies of bulk Ge (solid) and Ge on Si (open). The statistical errors of the CP energies determined from the second derivatives are on the order of 1 meV. Solid lines show the best fit of the data using Eq. (72) with parameters given in Table 4. The dash-dotted line shows the results from [30] for comparison. 94

41 Temperature dependence of the dimensionless amplitudes (A) of the E_1 (•, ∘) and E_1+Δ_1 (■, □) transitions of bulk Ge (solid) and Ge on Si (open). 94

42 Temperature dependence of the excitonic phase angle (ϕ) defined in Eq. (68) for the E_1 transitions of bulk Ge (•) and Ge on Si (□). We assumed that $E_1 + \Delta_1$ had the same phase angle as E_1. 95

43 Temperature dependence of the E_1 (•, ∘) and E_1+Δ_1 (■, □) broadening parameter Γ defined in Eq. (68) for bulk Ge (solid) and Ge on Si (open). The dash-dotted line shows the results for E_1 of bulk Ge from [30] for comparison. The solid and dashed lines show the best fit to Eq. (73) with parameters in Table 5. 95

44 Temperature dependence of the spin orbit splitting Δ_1 of the valence band for bulk Ge (■) and Ge on Si (∘). 96

45 Energy difference of the E_1 (○) and $E_1+\Delta_1$ (□) critical point energies between bulk Ge and Ge on Si. Lines show the predicted energy difference for three growth temperatures T_g using Eqs. (89) and (90). ● and ■ represent the calculated energy difference of the E_1 and $E_1+\Delta_1$ critical point energies using the measured XRD strain at 300 K. 97

46 Temperature dependence of the E_0' energies of bulk Ge (solid) and Ge on Si (open). Solid lines show the best fit of the data using Eq. (72) with parameters given in Table 4. 103

47 (Color online) Temperature dependence of the amplitudes (A) of the E_0' transitions of bulk Ge (solid) and Ge on Si (open). 103

48 Temperature dependence of the excitonic phase angle (ϕ) defined in Eq. (68) for the E_0' transitions of bulk Ge (solid) and Ge on Si (open). 104

49 Temperature dependence of the E_0' broadening parameter Γ defined in Eq. (68) for bulk Ge (solid) and Ge on Si (open). 104

50 Temperature dependence of the E_2 energies of bulk Ge (solid) and Ge on Si (open). Solid lines show the best fit of the data using Eq. (72) with parameters given in Table 4. 105

51 Temperature dependence of the amplitudes (A) of the E_2 transitions of bulk Ge (solid) and Ge on Si (open). 106

52 Temperature dependence of the excitonic phase angle (ϕ) defined in Eq. (68) for the E_2 transitions of bulk Ge (solid) and Ge on Si (open). 106

53 Temperature dependence of the E_2 broadening parameter Γ defined in Eq. (68) for bulk Ge (solid) and Ge on Si (open). The dash-dotted line shows the results of bulk Ge from [30] for comparison. 107

54 Band structure maps (energy in eV versus composition) of pseudomorphic $Ge_{1-x-y}Si_xSn_y$ alloys (i) on Ge for band gaps at the (a) Γ, (b) L, and (c) Δ CB minima, (ii) grown on a thick Ge buffer on a Si substrate, at the (a) Γ, (b) L, and (c) Δ CB minima. The Ge buffer is assumed to have been grown at 770 K. We assume full relaxation of the buffer at the growth temperature, but no additional relaxation when cooling down to room temperature, resulting in a tensile biaxial stress of the Ge buffer, and (iii) on GaAs substrate at the (a) Γ, (b) L, and (c) Δ CB minima. 120

55 Compositional dependence of the lowest band gap (either direct or indirect) of pseudomorphic $Ge_{1-x-y}Si_xSn_y$ alloys (a) on Ge, (b) on Ge buffered Si, and (c) on GaAs. 121

56 Energies of the three top valence bands at the Γ point (v_1, v_2, v_3), the conduction band minimum at the Γ point (E_c^Γ) and at the L point (E_c^L) in pseudomorphic $Ge_{1-y}Sn_y$ alloys grown on Ge as a function of Sn content calculated using Eqs. (82)-(88). The reference energy (0 eV) was chosen as the valence band maximum for any composition and shear strain. 125

57 Real (dashed) and imaginary (solid) parts of the complex dielectric function of pseudomorphic $Ge_{1-y}Sn_y$ on Ge versus photon energy determined from ellipsometry. 128

58 Experimental data (solid) and model (dashed) of the ellipsometric angles Ψ and Δ for pseudomorphic $Ge_{0.89}Sn_{0.11}$ on Ge versus photon energy in the infrared region obtained by merging data from two instruments. 128

59 (a) High-resolution X-ray diffraction ($\bar{2}\bar{2}4$) grazing exit reciprocal space map showing contours of equal intensity of a $Ge_{0.904}Sn_{0.096}$ layer on Ge. The Ge substrate and the $Ge_{1-y}Sn_y$ layer peaks have the same $Q_{\|}$ indicating that the epilayer is fully strained. Inset: Logarithmic intensity versus diffraction angle for the symmetric (004) ω-2θ X-ray reflections. (b) Atomic force microscopy image of the GeSn surface showing an RMS roughness of 1.6 nm. 131

60 Compositional dependence of the lattice parameter of relaxed $Ge_{1-y}Sn_y$ alloys calculated from Vegard's Law shown in Eq. (76) (solid) and out-of-plane lattice parameter $a_\perp$ of pseudomorphic $Ge_{1-y}Sn_y$ alloys on Ge (dashed) from Eqs. (76)-(78). The dotted line shows the Ge lattice constant. Symbols show the in-plane and out-of-plane lattice constants $a_\perp$ and $a_\|$ determined from ($\bar{2}\bar{2}4$) grazing exit reciprocal space maps and the relaxed lattice constant from Eqs. (95)-(96). 133

61 Lines show the compositional dependence of the in-plane $\epsilon_\|$, out-of-plane $\epsilon_\perp$, hydrostatic ϵ_H, and shear strain ϵ_S for pseudomorphic $Ge_{1-y}Sn_y$ alloys on Ge calculated using Eqs. (77)-(78) and (80)-(81). In-plane ($\circ$) and out-of-plane strain ($\square$) results derived from ($\bar{2}\bar{2}4$) XRD. 135

62 Compositional dependence of the direct (solid) and indirect (dashed) band gaps of pseudomorphic $Ge_{1-y}Sn_y$ alloys grown on bulk Ge at 300 K, calculated from Eqs. (83) and (86), derived from Fig. 56. The dotted line shows the direct gap for $Ge_{1-y}Sn_y$ grown on a Ge buffer on Si, see Fig. 54(b). □: Direct band gap of pseudomorphic $Ge_{1-y}Sn_y$ on Ge taken from Ref. [199]. +: Direct band gap of pseudomorphic $Ge_{1-y}Sn_y$ grown on relaxed Ge on Si from ellipsometry [200]. 136

63 Compositional dependence of the E_1 (○) and $E_1+\Delta_1$ (◇) critical point energies of pseudomorphic $Ge_{1-y}Sn_y$ alloys grown on Ge from ellipsometry (derivative analysis). The statistical errors of the CP energies are on the order of 1 meV. The solid lines are E_1 (black) and $E_1+\Delta_1$ (blue) for relaxed $Ge_{1-y}Sn_y$ alloys. The dashed lines are for E_1 (black) and $E_1+\Delta_1$ (blue) of pseudomorphically strained $Ge_{1-y}Sn_y$ alloys grown on Ge calculated using deformation potential theory. 137

64 Compositional dependence of amplitudes (A) for E_1 and $E_1 + \Delta_1$ in pseudomorphic $Ge_{1-y}Sn_y$ alloys. 140

65 Compositional dependence of the exitonic phase angle ϕ for E_1 in pseudomorphic $Ge_{1-y}Sn_y$ alloys. 140

66 Compositional dependence of the broadening Γ for E_1 and $E_1 + \Delta_1$ in pseudomorphic $Ge_{1-y}Sn_y$ alloys. 141

67 RSM plots of the out-of plane versus the in-plane reciprocal lattice vectors for the $Ge_{1-x}Sn_x$ samples A, B, G and H measured in inverse microns. The vertical line in each plot represents 100% compressive strain, so a layer peak centered on this line would have a parallel lattice constant equal to that of the Ge substrate (see plot A). The diagonal black line represents complete relaxation, as a peak centered anywhere on this line would have equal parallel and perpendicular lattice constants. With increasing Sn content, the $Q_{\|}$ decreases, indicating an increase in the in-plane lattice constant compared to the Ge substrate. 148

68 Relaxation (a), RMS surface roughness (b) and Thickness (b) of the $Ge_{1-x}Sn_x$ samples plotted against the ω peak FWHM (full width at half-maximum). The calculated correlation R-squared values represent how well the measured data fits against a linear trend line (shown). As discussed in the text, the small value of R-Squared in (a) suggests that there is no correlation between relaxation and FWHM for these samples. 149

69 Atomic force microscopy (AFM) of the samples A, B, G and H (with Sn contents of 10, 8.4, 18.5, 18.3% respectively). Each image is 3×3 μm^2. RMS roughness for the samples shown (clockwise from top left): 0.69 nm, 3.77 nm, 0.71 nm, 1.0 nm. These images show the periodic roughness of the $Ge_{1-x}Sn_x$, caused by strain-induced buckling, depends on the $Ge_{1-x}Sn_x$ layer thickness. 153

70 Real (solid) and imaginary (dashed) parts of the complex dielectric function of samples B, D and H (with bulk Germanium for reference) determined from ellipsometry. The dielectric functions were determined by fitting the measured ellipsometric angles using a four-phase ambient-GeO_2-$Ge_{1-x}Sn_x$-Ge model. 154

71 Second derivatives of the real (ϵ_1) part of the dielectric function of sample F (17%) with respect to photon energy near the E_1 and $E_1+\Delta_1$ critical points. Symbols represent the experimental data and solid line shows the best fit with a two dimensional critical point assuming parabolic bands and constant dipole matrix elements. The statistical error of this model is on the order of one meV. 155

72 The lines represent the E_1 critical point energies for $Ge_{1-x}Sn_x$ on Ge as a function of Sn content as modeled by Deformation Potential Theory (DPT). The solid line is fully relaxed and the dashed line is pseudomorphically strained. Circles (blue) represent the E_1 energies determined from second-order Derivative Analysis (DA) of the ellipsometry spectral data, with a statistical error on the order of one meV. Squares (red) represent the expected E_1 energy for each sample taking into account the Sn content and the degree of relaxation determined from asymmetric x-ray reciprocal space maps. The inset shows the measured E_1 energy of bulk Ge (2.116 eV), where the theoretical lines for strained and relaxed $Ge_{1-x}Sn_x$ converge. For some samples, the measured E_1 energy (circles) is lower than the calculated energy (squares), indicating that the degree of relaxation might be larger near the sample surface. The observed red shift is about 20 meV/% Sn. 157

73 Real (solid) and imaginary (dashed) parts of the dielectric function of samples C (8% relaxed) and D (61% relaxed) with similar Sn contents (12.5% Sn) but different degrees of relaxation showing a very small red shift of the spectrum with strain relaxation. 158

1 Introduction

Germanium is a group IV element in the periodic table, predicted by Dmitri Mendeleev in 1869, and discovered by Clemens Winkler nearly two decades later in 1886 [1]. It is the key substrate element used during the early days of the development of the semiconductor transistors and integrated circuits before it was overruled by a more abundant and cheaper material silicon [2]. Germanium is one of the most widely used and thoroughly studied semiconductor materials, next to silicon in the optoelectronic industry. It is an indirect band gap semiconductor with a 0.66 eV band gap (L point) at room temperature. The direct transition band gap of 0.8 eV (1.5 μm) makes Ge an ideal candidate for near-infrared (NIR) light detectors used for optical communications (1.3-1.55 μm) and NIR photonics which are important for medical and biological applications [3]. The need for the participation of phonons for the radiactive electron-hole pair recombinations to conserve momentum, significantly reduces the rate of the electron transition, making Ge inefficient for the design of photonic devices such as photodetectors, LEDs, and lasers [4]. Therefore, the indirect nature of the fundamental band gap of Ge has limited the large scale integration of Ge optoelectronic devices with the existing Si technology.

However, the electronic band structure of Ge is a strong function of strain. It has been reported that at about 2% tensile strain, Ge becomes a direct band gap material [5], indicating widespread applications of Ge based optoelectronic devices, photodetectors, LEDs, and lasers. Alloying Ge with Sn also makes Ge a direct band gap material [6, 7, 8]. Therefore, band gap engineering of Ge by controlling strain, temperature, alloying with Si, Sn, and doping has attracted great interest

and the knowledge of the compositional, strain, and temperature dependence of the optical properties is important for the design of highly efficient Ge-based photonic devices. This dissertation focuses on the optical characterization of the compositional, strain, and temperature dependence of the optical properties of Ge-Si-Sn alloys on Ge/Si substrates using spectroscopic ellipsometry and high resolution X-ray diffraction. The tunable band gaps and the optical properties of Ge-Si-Sn alloy epilayers on Ge, Si substrates, grown by MBE/CVD are studied as a function of composition, strain and temperature and compared with theoretical predictions from deformation potential theory. The compositions, thicknesses, strain, and surface roughnesses of the alloy epilayers are characterized by X-ray diffraction (XRD), high resolution X-ray diffraction (HRXRD), X-ray reflectivity (XRR), and atomic force microscopy (AFM).

The accurate knowledge of the complex dielectric function (ϵ_1 and ϵ_2) of Ge and surface oxide (GeO_2) on Ge is of great important for the optical characterization of the Ge-based semiconductors devices. We developed a hybrid dry-wet preclean method for thermal oxidation of Ge. Thermal GeO_2 with different thicknesses, up to 136 nm were produced by annealing Ge wafers in pure O_2 up to 10 h and the complex dielectric functions of Ge and GeO_2 were determined from 0.5 to 6.6 eV using a multisample spectroscopic ellipsometry investigation. In chapter 4, we discuss the preclean and annealing techniques used for the thermal oxidation of Ge and the optical constants of the GeO_2 obtained via multisample analysis of the spectroscopic ellipsometry data. The accuracy of our optical constants are discussed and compared with literature data. The optical constants of Ge and GeO_2 determined via multisample analysis, as discussed in chapter 4, are used to model the dielectric functions of Ge related samples in this research.

Strain is an important parameter which can be used to tune the band gaps

in the energy band structure to achieve desired optical properties of a material. One way to control the strain on Ge is by growing a relaxed Ge epilayer at a high temperature (∼800 K) on a substrate with a different thermal expansion coefficient, such as Si. The Ge epilayer is fully relaxed at the growth temperature forming misfit dislocations. As temperature decreases, the Ge layer experiences a temperature dependent tensile biaxial stress, since the bulk Ge shrinks more than the Si substrate as temperature decreases. The strain on Ge, generated due to the thermal expansion mismatch, affects the optical properties of the Ge film grown on Si. Using spectroscopic ellipsometry, we measured the dielectric function of bulk Ge and epitaxial Ge on Si grown by ultra high vacuum chemical vapor deposition from 80 to 780 K and from 0.8 to 6.5 eV to investigate the strain dependence of the band gaps. The E_1 and $E_1+\Delta_1$ band gaps in the Ge epilayers on Si are redshifted compared to bulk Ge. This redshift can be described with a model taking into account the thermal expansion coefficients, stress, and strain determined using continuum elasticity theory, and the strain-induced shifts calculated from deformation potentials. The strain measured using high resolution X-ray diffraction reciprocal space maps is consistent with the predictions from the model. We discuss the temperature dependent electronic band structure and critical points of bulk Ge and Ge on Si in detail in chapter 5. The contribution of the thermal expansion coefficient and electron-phonon interaction to the temperature dependence of the band gaps and the effects of the strain, which is a function of temperature, is investigated.

Another way to control the strain is by alloying Ge with Si and/or Sn and growing a thin alloy layer pseudomorphically on a lattice mismatched substrate. We investigate the compositional and strain dependence of the direct and indirect band gaps of pseudomorphic $Ge_{1-x-y}Si_xSn_y$ alloys on Ge using deformation

potential theory. Calculations predict an indirect to direct band gap crossover for pseudomorphic $Ge_{1-x-y}Si_xSn_y$ alloys on Ge and no indirect to direct transition for pseudomorphic $Ge_{1-y}Sn_y$ alloys on Ge, for practically approachable Sn compositions (y>25%). The predictions for the compositional and strain dependence of the E_0, E_1 and $E_1+\Delta_1$ band gaps were validated for pseudomorphic $Ge_{1-y}Sn_y$ alloys grown on Ge by molecular beam epitaxy, using Fourier transform infrared and ultraviolet-visible ellipsometry in the 0.1-6.6 eV energy range for Sn contents up to 11%. The Sn composition, thickness and strain of the epilayers are measured using high resolution X-ray diffraction techniques. In chapter 6, we discuss the compositional and strain dependence of the band structure, optical properties of pseudomorphic $Ge_{1-x-y}Si_xSn_y$ alloys on Ge and compare with ellipsometry results. Effects of the substrate on the band structure and optical properties are investigated for $Ge_{1-x-y}Si_xSn_y$ pseudomorphically grown on Ge buffered Si substrate and on GaAs.

Our deformation potential theory calculations in chapter 6 predict that pseudomorphic (fully strained) $Ge_{1-y}Sn_y$ alloys on Ge will never become a direct band gap material for practically approachable Sn compositions. However, it will become a direct band gap semiconductor through relaxation of strain by forming misfit dislocations, for y∼6-11%, depending on the amount of Sn and degree of relaxation [6, 7, 9]. The defects and dislocations, formed during the relaxation, act as non-radiative recombination centers and negatively affect the performance of the devices. Therefore, we investigate the optical properties of partially relaxed $Ge_{1-y}Sn_y$ alloys on Ge up to 18.5% Sn using spectroscopic ellipsometry. The effects of the strain relaxation on the dielectric function of the $Ge_{1-y}Sn_y$, E_1, and $E_1+\Delta_1$ band gaps will be discussed in chapter 7.

2 Semiconductor materials

Silicon (Si) is the dominant semiconductor material used in semiconductor devices since 1960s, yet the first transistor discovered in 1947 was a Germanium (Ge) device [10]. Therefore, Si is the most throughly studied semiconductor in literature, almost everything about Si is well known. Germanium, a group IV element below Si in the periodic table, forms a diamond crystal structure similar to Si [11]. It is the principal component used in solid state devices next to Si, playing a major role in the semiconductor industry. There has been great interest in Ge for its applicability to its high speed electronic devices due to high carrier mobility and high optical absorption at telecommunication wavelengths ($\sim$ 1620 nm) [12]. Compatibility with the existing Si technology makes Ge an ideal candidate for the integration of Ge based devices on Si. The understanding of the electronic band structure and related optical properties is critical in materials science for the design of Ge-based photonic devices by controlling strain, alloy composition, and doping concentration. Germanium band structure has been calculated over the last few decades employing various techniques; using empirical pseudopotentials, [13] k·p method [14] tight binding approximations, [15, 16] and more recently first principles density functional theory calculations [17]. Therefore, electronic band structure, deformation potentials, band gaps, spin-orbit interactions, and symmetry points of Ge are well known. The electronic band structure of Ge, calculated using the "full-zone k·p method" by Cardona *et al.*, in Ref. [14] is shown in Fig. 1. As illustrated in the figure, Ge is an indirect band gap material, the conduction band minimum is at the L point in the Brillouin zone with an experimentally determined indirect band gap (E_g^L) of 0.66 eV at room temperature. The conduction band at the center of the Brillouin zone is 0.14 eV above the L point, the direct

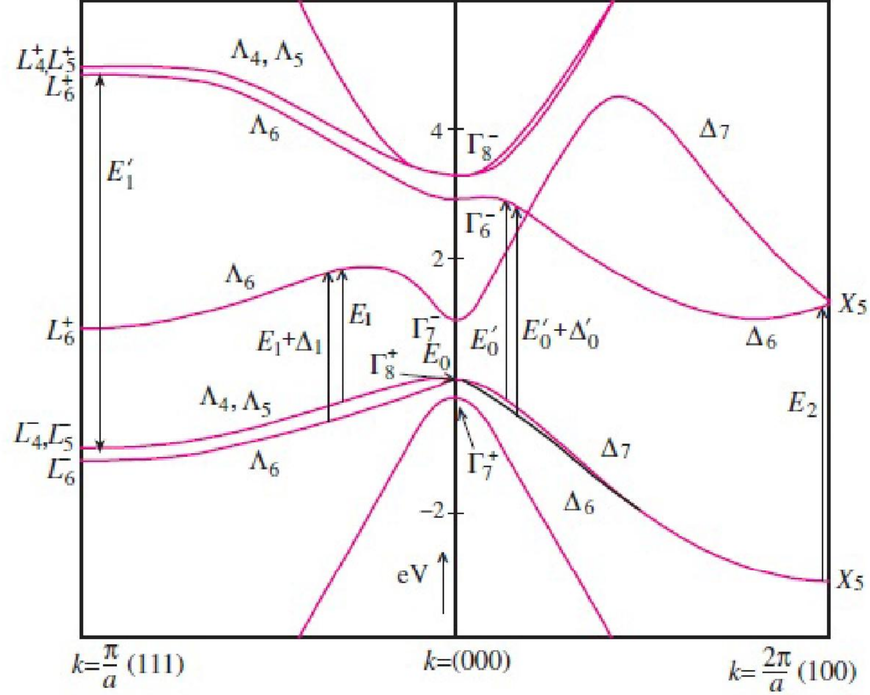

Figure 1: Band structure of bulk Ge calculated by "full-zone k·p method. [18] The conduction band minimum is at the L point in the Brillouin zone with an experimentally determined indirect band gap (E_g^L) of 0.66 eV. The conduction band at the center of the Brillouin zone is 0.14 eV above the L point, the direct band gap at the Γ point (E_g^Γ) is measured to be 0.8 eV.

band gap at the Γ point (E_g^Γ) is measured to be 0.8 eV (at room temperature) [5, 18, 19, 20, 21].

2.1 Interband transitions and critical points

An electron, in the occupied valence band can be excited into an unoccupied state in the conduction band by absorbing a photon. This process is called an interband transition. If the conduction band minimum and the valence band maximum occur at the same point in the Brillouin zone, the crystal momentum $\vec{k}$ is conserved $\left(E_v(\vec{k}) \rightarrow E_c(\vec{k})\right)$ and the transition is known as a direct transition,

as illustrated by vertical arrows in the band structure diagram of Ge in Fig. 1. Optical transitions between two bands with different momentum wave vectors are also possible with the involvement of a phonon ($\vec{k}_v = \vec{k}_c \pm \vec{q}_{phonon}$), and such transitions are known as indirect transitions. Usually, the indirect transitions are weaker than the direct transitions due to the requirement of the involvement of a phonon.

The probability of a direct electron transition for photon ($\hbar\omega$) absorption per unit time is given by Fermi's Golden rule [18, 22, 23],

$$R = \frac{2\pi}{\hbar} \sum_{\vec{k}_c, \vec{k}_v} |\langle v|H_{eR}|c\rangle|^2 \delta[E_c(\vec{k}_c) - E_v(\vec{k}_v) - \hbar\omega] \tag{1}$$

where $\delta[E_c(\vec{k}_c) - E_v(\vec{k}_v) - \hbar\omega]$ is the delta function implementing the condition of the energy conservation. $\hbar\omega$ is the energy quantum of the electromagnetic field, the transition can only occur if the energy of the field is exactly "tuned" to the transition. The matrix elements of the perturbation Hamiltonian H_{eR} describe the interaction between the photon and a Bloch electron between the initial and final states. This term is called the electron-radiation interaction Hamiltonian, which can be simplified by

$$|\langle v|H_{eR}|c\rangle|^2 = \left(\frac{e}{mc}\right)^2 |A|^2 |P_{cv}|^2 \tag{2}$$

to obtain:

$$R = \frac{2\pi}{\hbar} \left(\frac{e}{m\omega}\right)^2 \left|\frac{E(\omega)}{2}\right|^2 \sum_{\vec{k}} |P_{vc}|^2 \delta[E_c(\vec{k}) - E_v(\vec{k}) - \hbar\omega] \tag{3}$$

where,

$$\vec{A} = -\frac{E}{2e}\left\{\exp\left[i\left(\vec{q}\cdot\vec{r}\right)-\omega t\right]+\exp\left[-i\left(\vec{q}\cdot\vec{r}\right)-\omega t\right]\right\} \tag{4}$$

is the vector potential related to the Coulomb gauge (scalar potential ϕ=0 and $\vec{\nabla}\cdot\vec{A}$=0). The electric field $\vec{E}$=(-1/c)$\partial\vec{A}/\partial$t and the magnetic field $\vec{B}=\vec{\nabla}\times\vec{A}$. c is the velocity of light, m and e are the effective mass and the charge of the electron, respectively.

The transition rate per unit volume in the medium (R) is multiplied by the energy of each photon to obtain the power loss by the unit volume of the medium due to absorption (power loss=$R\hbar\omega$), which is equal to the rate of decrease in the energy of the incident beam. The rate of the energy decrease can be expressed in terms of the absorption coefficient (α) of the medium using Beer's law, [18, 24]

$$-\frac{dI}{dt} = -\left(\frac{dI}{dx}\right)\left(\frac{dx}{dt}\right) = \frac{c}{n}\alpha I = \frac{\epsilon_2\omega I}{n^2} = \frac{1}{8\pi}\epsilon_2\omega\left|E\left(\omega\right)\right|^2 \tag{5}$$

where $I = n^2\left|E(\omega)\right|^2/8\pi$ is the intensity of the incident beam and $-dI/dt$ gives the rate of decrease of the energy in the incident beam. n and ϵ_2 are the refractive index and the imaginary part of the dielectric function ($\epsilon = \epsilon_1 + i\epsilon_2$) of the medium respectively. Therefore, by combining Eq. (3) and Eq. (5), the transition rate can be related to the imaginary part of the dielectric function ϵ_2 of the medium [18]:

$$\epsilon_2(\omega) = \left(\frac{2\pi e}{m\omega}\right)^2 \sum_{\vec{k}} |P_{vc}|^2 \delta[E_c(\vec{k}) - E_v(\vec{k}) - \hbar\omega] \tag{6}$$

An expression for the real part of the dielectric function ϵ_1 can be obtained by

Kramers-Kronig transformation [18, 25, 26]:

$$\epsilon_1(\omega) = 1 + \frac{4\pi e^2}{m}\left[\sum_{\vec{k}}\left(\frac{2}{m\hbar\omega_{cv}}\right)\frac{|P_{vc}|^2}{\omega_{cv}^2 - \omega^2}\right] \tag{7}$$

The joint density of states (JODS) between the conduction and valence bands $\mathrm{D}_j\,(E_{cv})$ is defined as the number of energy states per unit volume per unit energy range, which occur with an energy difference between the conduction and valence band equal to the photon energy $\hbar\omega$. Introducing a constant energy surface S such that the energy difference $E_c - E_v$ is the photon energy $\hbar\omega$ [18, 27, 28],

$$d^3k = dk_n dS = dS\left[\frac{d\,(E_c - E_v)}{|\vec{\nabla}_k\,(E_c - E_v)\,|}\right] \tag{8}$$

Therefore,

$$D_j\,(E_{cv}) = \frac{2}{8\pi^3}\int\int\int \frac{dS\;d\,(E_c - E_v)\,\delta[E_c(\vec{k}) - E_v(\vec{k}) - \hbar\omega]}{|\vec{\nabla}_k\,(E_c - E_v)\,|}. \tag{9}$$

After carrying out the integral over $d\,(E_c - E_v)$, the joint density of states $D_j\,(E_{cv})$ can be written as,

$$D_j\,(E_{cv}) = \frac{2}{8\pi^3}\int\int \frac{dS}{|\vec{\nabla}_k\,(E_c - E_v)\,|} \tag{10}$$

Our special interest of JDOS are on those points in the Brillouin zone where the $(E_c - E_v)$ are stationary and $\vec{\nabla}_k\,(E_c - E_v)$ vanishes, making large contributions to JDOS. Van Hove reported these points in the Brillouin zone as critical points and the corresponding singularities in the JDOS are known as Van Hove singularities

[29].

Assuming that $\vec{k}_0$ is a critical point (known as a Van Hove singularity) in three dimensional space, the energy band separation, $\left[E_c\left(\vec{k}\right) - E_v\left(\vec{k}\right)\right]$ can be expanded in a Taylor series around the critical point $\vec{k}_0$ [18],

$$E_c\left(\vec{k}\right) - E_v\left(\vec{k}\right) \approx E_g\left(\vec{k}_0\right) + \sum_{i=1}^{3} a_i \left(k_i - k_{0i}\right)^2, \tag{11}$$

where $E_g\left(\vec{k}_0\right)$ is the energy gap at the critical point, $a_i = \frac{\partial^2}{\partial k_i^2}\left[E_c\left(\vec{k}_0\right) - E_v\left(\vec{k}_0\right)\right]$, the summation is taken over three directions x, y and z. Depending on the sign of the coefficient a_i, the band separations $\left[E_c\left(\vec{k}\right) - E_v\left(\vec{k}\right)\right]$ are increasing or decreasing when we move away from the critical point. Therefore, critical points are classified according to the number of negative coefficients a_i in Eq. (11). For example, there will be four types of critical points labeled, M_0, M_1, M_2, and M_3 in three dimensional space. Different types of critical points in one, two, and three dimensional space, with the functional form of the joint density of states D_j are listed in Table 2.1. As shown by the expressions in Eq. (3) and (6), photons with energy $\hbar\omega = E_c - E_v$, effectively induce electron transitions at the critical points, making large contributions to the transition probability, and to the JDOS. Therefore, critical points, usually at high symmetry points in the Brillouin zone, create additional features in the frequency dependent optical spectra. The corresponding singularities of the imaginary part of the dielectric function ϵ_2 near the critical points in one, two and three dimensions are schematically illustrated in Fig. 2.

As an example, the real (ϵ_1) and imaginary (ϵ_1) parts of the dielectric function of bulk Ge, obtained using spectroscopic ellipsometry at room temperature, are shown in Fig. 3. By comparing the electronic band structure of Ge in Fig. 1 and experimental dielectric function of Ge in Fig. 3, it is possible to iden-

Table 1: Different types of critical points in one, two and three dimensions with the corresponding joint density of states D_j [18].

Type		D_j	
		$E < E_0$	$E > E_0$
Three dimensions	M_0	0	$(E - E_0)^{1/2}$
	M_1	$C - (E_0 - E)^{1/2}$	C
	M_2	C	C- $(E - E_0)^{1/2}$
	M_3	$(E_0 - E)^{1/2}$	0
Two dimensions	M_0	0	C
	M_1	$-\ln(E_0 - E)^{1/2}$	$-\ln(E - E_0)^{1/2}$
	M_2	C	0
One dimension	M_0	0	$(E - E_0)^{-1/2}$
	M_1	$(E - E_0)^{-1/2}$	0

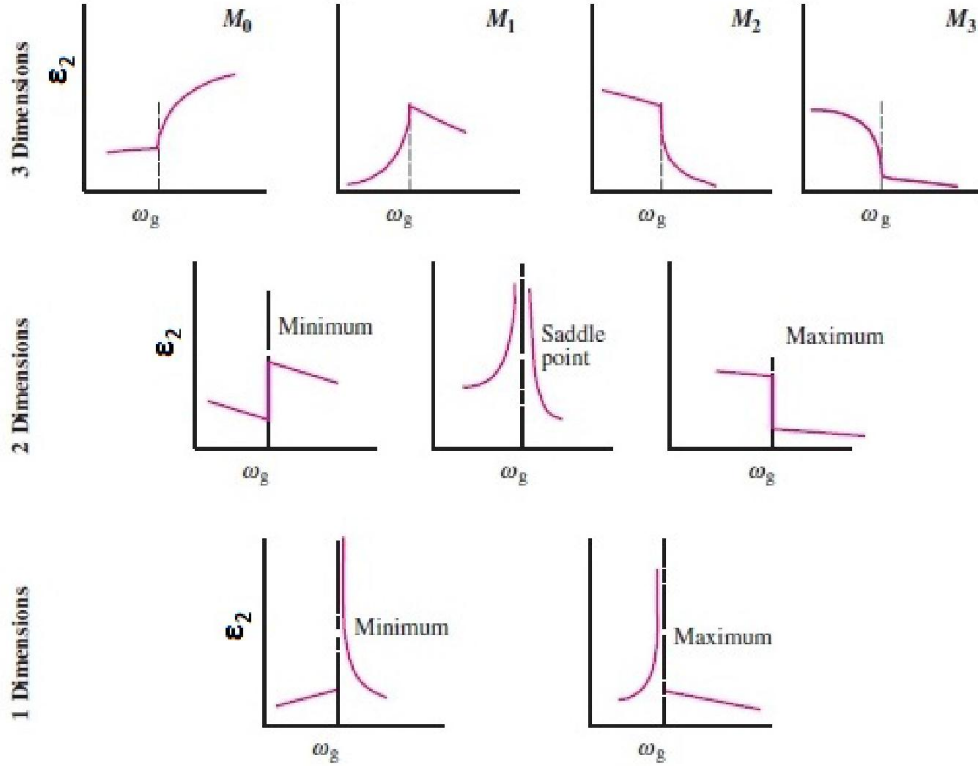

Figure 2: Schematic representation of the frequency dependence of the imaginary part of the dielectric function ϵ_2 near interband critical points in one, two and three dimensions [18].

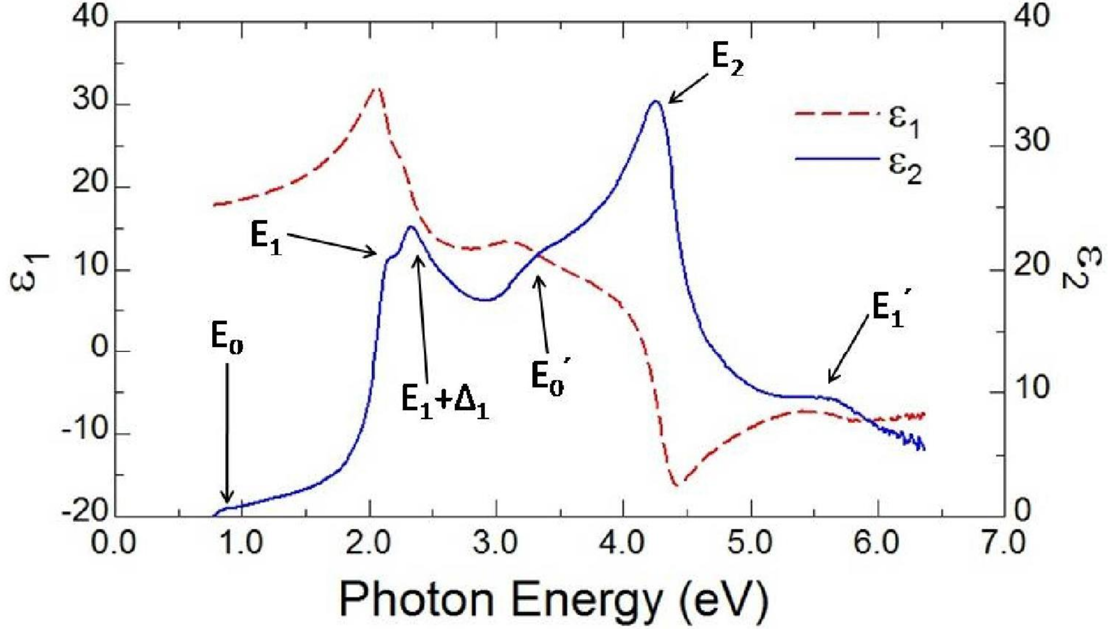

Figure 3: Real (ϵ_1, dashed) and imaginary (ϵ_2, solid) parts of the dielectric function of bulk Ge at room temperature obtained using spectroscopic ellipsometry (This work).

tify the electron transitions in the Brillouin zone corresponding to the particular critical points which is responsible for the structures (peaks) present in the optical spectra. Considering the electronic band structure, it can be seen that the lowest direct transition occurs at the Γ point, $\vec{k} = 0$, where the condition $\left[E_c\left(\vec{k}=0\right) - E_v\left(\vec{k}=0\right) = \hbar\omega\right]$ is satisfied, giving rise to the E_0 critical point at 0.8 eV in the dielectric function. For photon energies $\hbar\omega < E_0$, there is no absorption and therefore, ϵ_2 becomes zero below the lowest direct absorption edge. Both the conduction and valence bands have extrema at the L symmetry point, where the bands are parallel along the [111] direction in the Brillouin zone. The energy separation between the conduction band and the valence band $[E_c - E_v]$ is constant for a large region along the [111] direction. The E_1 critical point arises in the JDOS, making a large contribution to the dielectric function at around

2.2 eV. Since the negative longitudinal mass $1/a_1$, defined in Eq. (11), is large, E_1 critical point is modeled as a two dimensional M_0 critical point [30]. Large spin-orbit interactions of the valence band at L point split the E_1 structure into the E_1 and $E_1 + \Delta_1$ critical points, where Δ_1 (~0.198 eV, 2/3 of the spin-orbit splitting Δ_0 at the Γ point) is the spin-orbit splitting of the valence bands at the L point. The critical point associated with the electron transition occurring over a large region of the conduction and valence bands extrema near the X point along the [100] direction is known as the E_2 critical point and appears at 4.5 eV in the dielectric function. The weaker, broadened peak in ϵ_2 at ~3.3 eV, labeled as E_0', arises from the superimposed electron transitions between the valence band and higher conduction bands at the zone center (Γ point). The peak labeled as E_1', at ~5.5 eV involves with the superimposed electron transitions between the valence band and higher conduction bands at the L point along the [111] direction.

The electronic band structures of group IV semiconductors, Si, α-Sn (diamond crystal structure), and III-V semiconductors, like GaP, InP, etc (zinc blende crystal structure) are similar to the band structure of Ge as shown in the Fig. 1. They exhibit similar features (critical points) in the dielectric spectra [31, 32, 33, 34, 35, 36, 37]. Therefore, it is possible to identify the singularities in the JDOS (critical points) responsible for the structures present in the dielectric function for these materials, as discussed above. However, it should be noted that, only the E_0, E_1, and $E_1 + \Delta_1$ critical points can be definitely attributed to a particular type of a critical point (see Table 2.1), other higher energy critical points are often superimposed with several critical points and contain contributions from different types of critical points.

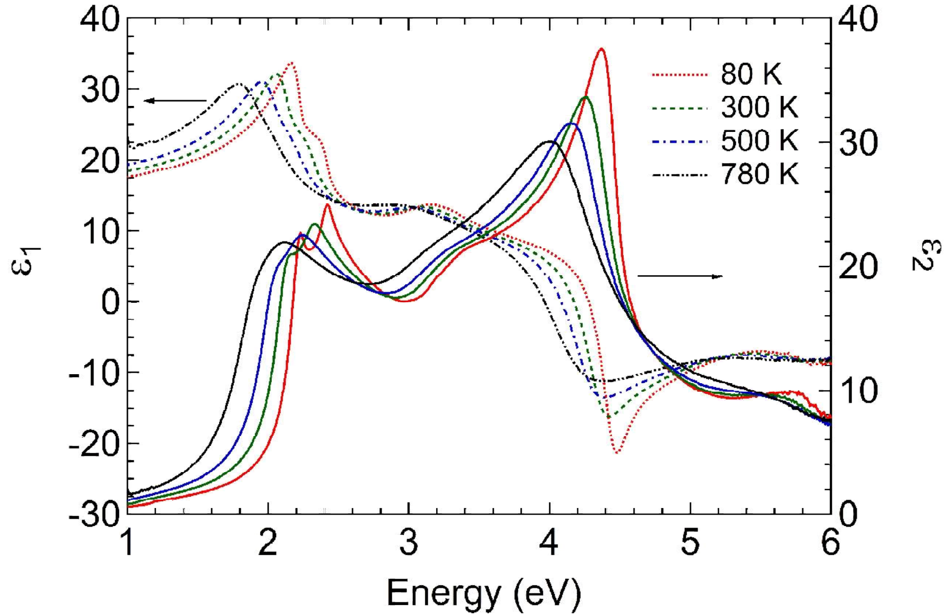

Figure 4: Real (ϵ_1, dashed) and imaginary (ϵ_2, solid) parts of the complex dielectric function of bulk Ge measured at temperatures between 80 K and 780 K (This work).

2.2 Temperature dependence of the critical points

The electronic band structure of Ge is a strong function of temperature [30] and there is also a close relationship between the band structure and the complex dielectric function of Ge. Therefore, the optical properties and critical points of Ge are also temperature dependent. The temperature dependence of the complex dielectric function (ϵ_1 and ϵ_2) measured using spectroscopic ellipsometry at temperatures between 80 K and 780 K is shown in Fig. 4. The dielectric function is shifted to lower energies (red shifted) and broadened critical points are observed as the temperature increases. The E_0 critical point, obtained via second derivative analysis of the dielectric function (will be discussed in next chapter) versus temperature is plotted in Fig. 5. The red shift of the E_0 transition with increasing temperature can be clearly observed from the temperature dependence of the E_0

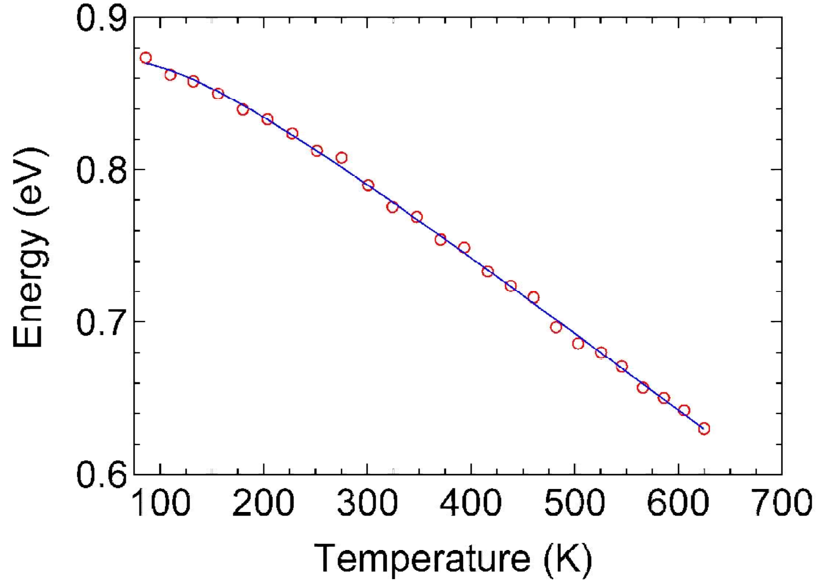

Figure 5: Temperature dependence of the E_0 critical point, obtained from second derivative analysis of the dielectric function (explained in the next chapter) of bulk Ge. The solid line shows the best fit of the data using Eq. (72) with parameters a=0.963 ±0.006 eV, b=0.090±0.006 eV and θ_B=347±27 K (This work).

critical point in the graph. In general, the temperature dependence of a band gap can be fitted with the semi-empirical Varshni equation [38]

$$\Delta E_g\left(T\right) = E_g^0 - \frac{\alpha T^2}{\left(T+\beta\right)} \tag{12}$$

where E_g^0 is the band gap at 0 K and α and β are fitting parameters characteristic to the given material. Although the Varshni equation describes the temperature dependence of the band gaps well with a small number of parameters, the theoretical basis behind the expression is weak. The expression predicts a linear temperature dependence in the high temperature regime and a quadratic dependence in the very low temperature regime. However, experiments finds a very weak temperature dependence of the band gaps at very low temperatures. There-

fore, Viña and coworkers have introduced a Bose-Einstein type expression for the temperature dependence of the band gaps, taking into account the average electron-phonon interactions [30].

The redshift of the band gaps with increasing temperature has two contributions, from thermal expansion of the crystal and from the renormalization of the electron energies due to electron-phonon interactions [39].

Investigation of the temperature dependent energy shift and broadening of the critical points allows to obtain important information about electron-phonon interactions. The temperature dependent energy shift of the band gap due to the thermal volume expansion can be written as [40, 41]

$$\Delta E_{th}\left(T\right) = D \int_{0}^{T} \alpha\left(T'\right) dT', \tag{13}$$

where $\alpha\left(T\right)$ is the linear thermal expansion coefficient of the material. D is the hydrostatic deformation potential for the corresponding band gap which is defined as the logarithmic volume derivative of the band gap, $D = \partial E/\partial \ln V = (-V\partial P/\partial V) \times (-\partial E/\partial P)$. Therefore, the net hydrostatic deformation potential can be related to the bulk modulus (B) and the pressure coefficient ($\partial E/\partial P$) by $D = B \times \partial E/\partial P$. The redshift of the band gap energy due to the electron-phonon interaction is proportional to the Bose-Einstein occupation factor for an (effective) phonon and often written as [30, 39]

$$E_{\mathrm{e-ph}}\left(T\right) = a' - b'\left[1 + 2/\left(e^{\theta'_B/T} - 1\right)\right], \tag{14}$$

where $k\theta'_B$ is the effective phonon energy and k is the Boltzmann constant, b' is the electron-phonon coupling strength, and a' is the unrenormalized transition

energy.

Experimentally, one measures the total energy shift (sum of the thermal expansion and electron-phonon contribution) and also describes it with the same empirical Bose-Einstein expression [30, 31, 32, 33]

$$E_{\text{total}}\left(T\right) = a - b\left[1 + 2/\left(e^{\theta_B/T} - 1\right)\right]. \tag{15}$$

The primed parameters can be obtained from the experiment by subtracting the thermal expansion contribution in Eq. (70) from the measured energy shifts and then fitting with Eq. (71).

2.3 Ge band gap engineering *via* strain and alloying

Germanium is an indirect band gap material, with the conduction band minimum at the L point, which is 140 meV below the conduction band minimum at the Γ point (see Fig. 1). As previously discussed, since the indirect electron transitions have to interact with a phonon to conserve momentum, the rate of the electron transitions is very low. The direct nature of the fundamental band gap of a material promises much more efficient electron-hole pair recombination, which is particularly important for the design of photonic devices, especially for the development of Ge-based optoelectronic devices. Due to these reasons, the indirect nature of the fundamental band gap of Ge has limited the large scale integration of Ge based optoelectronic devices on Si substrate. The electronic band structure of Ge is a strong function of strain as well as temperature. The energy position of the conduction band at the Γ point rapidly decreases as a function of the applied stress compared to the L point. Therefore, it has been predicted that,

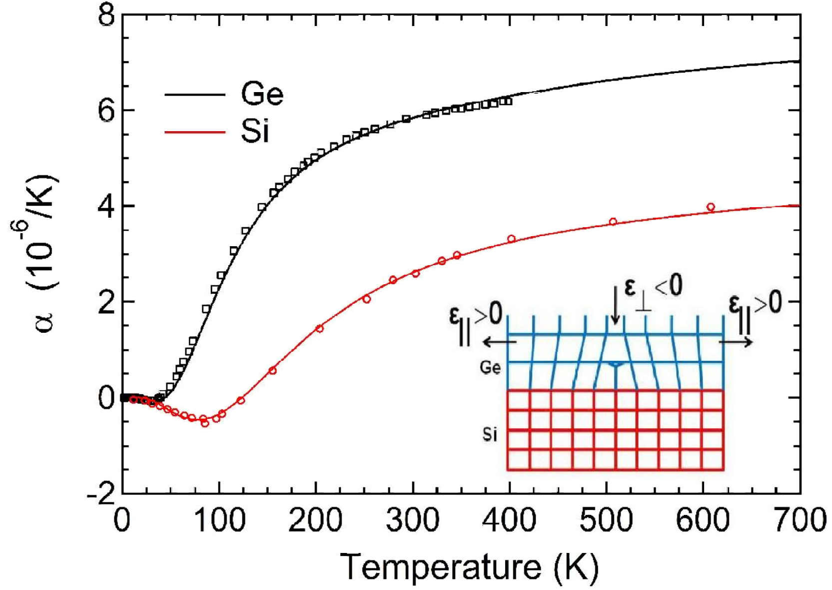

Figure 6: Temperature dependence of the linear thermal expansion coefficients of Si (α_{Si}) and Ge (α_{Ge}) modeled by Eq. (62) taken from ref. [42]. Experimental data (symbols) were taken from Ref. [44, 45, 46, 47, 48].

at about 1.4% tensile strain, Ge becomes a direct band gap material, indicating a possibility of widespread applications of Ge-based photonic devices such as lasers and modulators [5, 20, 21].

One way to control the strain on Ge is by growing a relaxed Ge epilayer at a high growth temperature (∼800 K) on a substrate with a different thermal expansion coefficient, such as Si. The temperature dependent thermal expansion coefficient of Ge (α_{Ge}) is about two times larger than the thermal expansion coefficient of Si (α_{Si}), see Fig. 6 [42]. As temperature decreases, the Ge epilayer experiences a temperature dependent tensile biaxial stress, since the bulk Ge shrinks more than the Si substrate with decreasing temperature, as illustrated in inset of the Fig. 6. The tensile in-plane strain $\epsilon_{\|}$(T) induced in the Ge epilayer due to the difference in thermal expansion coefficients of Si and Ge can be calculated, assuming no strain relaxation occurs while cooling down to lower temperatures

from the growth temperature T_g [12],

$$\epsilon_{\parallel}(T) = \int_{T}^{T_{\mathrm{g}}} [\alpha_{Ge}(T') - \alpha_{Si}(T')]dT' \tag{16}$$

where $\alpha_{Ge}(T)$ and $\alpha_{Si}(T)$ are linear thermal expansion coefficients of Ge and Si. The linear thermal expansion coefficient $\alpha(T)$ of Si and Ge can be expressed as [42]

$$\alpha(T) = \sum\nolimits_{i=1}^{4} \chi_i \frac{(\theta_i/T)^2 \exp(\theta_i/T)}{[\exp(\theta_i/T) - 1]^2} \tag{17}$$

where χ_i and θ_i are fitting parameters taken from ref. [42].

The Ge epilayer on Si substrate is elastically deformed under biaxial stress. The compressive out-of-plane strain $\epsilon_{\perp}(T)$ is related to the tensile in-plane strain $\epsilon_{\parallel}(T)$ by

$$\epsilon_{\perp}(T) = -2\frac{C_{12}}{C_{11}}(T)\,\epsilon_{\parallel}(T) \tag{18}$$

where the temperature dependence of the elastic moduli ratio $C_{12}/C_{11}(T)$ was taken from Ref. [43]

$$\frac{C_{12}}{C_{11}}(T) = 0.37492 - 3.7 \times 10^{-6}(T - 273.14)\,. \tag{19}$$

The temperature dependence of the hydrostatic strain $\epsilon_H(T)$ and the shear strain $\epsilon_S(T)$ components are [49]

$$\epsilon_H(T) = \frac{[\epsilon_{\perp}(T) + 2\epsilon_{\parallel}(T)]}{3} \quad \text{and} \quad \epsilon_S(T) = \frac{[\epsilon_{\perp}(T) - \epsilon_{\parallel}(T)]}{3}. \tag{20}$$

The hydrostatic strain shifts the conduction and valence bands relative to their

unstrained position, while the shear strain splits the bands removing degeneracies. The hydrostatic shift $\Delta E_H\left(T\right)$ and the shear shifts $\Delta E_S\left(T\right)$ of the conduction and valence bands of the biaxially strained Ge can be obtained from the experimental pressure dependence of the particular band gap, known as deformation potentials. From the definition of the hydrostatic deformation potential $D = \partial E/\partial \ln V = (V\partial E/\partial V)$, the energy shift due to the hydrostatic strain can be expressed as [49]

$$\Delta E = D\frac{\Delta V}{V} = D\mathrm{Tr}\epsilon = 3D\epsilon_H \qquad (21)$$

where the relative volume change $\Delta V/V$ of the material under biaxial stress is equal to the trace of the strain tensor Trϵ, which is given by $3\epsilon_H$. The energy shift due to the splitting of the band for a valley $\hat{n}$, for (001) biaxial stress is [49]

$$\Delta E = U_n\hat{n}\left(\epsilon - \frac{1}{3}\mathrm{Tr}\epsilon\right)\hat{n} = U_n\hat{n}\begin{bmatrix}\epsilon_S & 0 & 0\\ 0 & \epsilon_S & 0\\ 0 & 0 & 2\epsilon_S\end{bmatrix}\hat{n} \qquad (22)$$

where U_n is the shear deformation for the particular valley $\hat{n}$.

Therefore, strain dependence of the band gaps and related optical properties can be obtained using deformation potential theory. The strain depndence of the conduction and valence bands, band gaps and related parameters will be discussed in more detail in chapter 5 and chapter 6.

Another way of controlling strain in order to tune the Ge band structure is by alloying Ge with Si and/or Sn and growing a thin alloy layer on a lattice mismatched substrate. The lattice parameter of Sn (a_{Sn}=6.489 Å) [50] is about 14% larger than the lattice parameter of Ge (a_{Ge}=5.658 Å) [51]. Si (a_{Si}=5.431 Å)

[52] is about 4% smaller. The lattice parameter of relaxed $Ge_{1-x-y}Si_xSn_y$ alloys can be calculated using,

$$\begin{aligned} a^{rel}_{Ge_{1-x-y}Si_xSn_y} &= xa_{Si} + ya_{Sn} + (1-x-y)a_{Ge} \\ &+\theta_{GeSn}(1-x-y)y + \theta_{GeSi}(1-y-x)x \\ &+\theta_{SiSn}xy \end{aligned} \tag{23}$$

where the bowing parameters $\theta_{i,j}$ (i, j=Ge, Si, Sn) describe the deviation of the lattice parameter from the linear interpolation (Vegards' law) [53, 54]. Although extensive work has been done to characterize the compositional dependence of the lattice parameters of $Ge_{1-y}Sn_y$ alloys, a large discrepancy exists in the literature over the values of θ_{GeSn} [55, 56, 57, 58]. According to most recent findings [57, 58, 59], the bowing parameter θ_{GeSn} is very small and Vegard's law (θ_{GeSn}=0) can be used to accurately calculate the lattice parameters of GeSn alloys. The bowing parameter for lattice constant of $Ge_{1-x}Si_x$, θ_{GeSi} is -0.026 [60] and that of $Si_{1-x}Sn_x$, θ_{SiSn} was assumed to be zero, justified by the low Si and Sn content.

The calculated lattice parameter of relaxed $Ge_{1-x-y}Si_xSn_y$ using Eq. (76) is shown in Fig. 7, as a function of Si (x) and Ge (y) compositions. Figure 7 shows that the lattice parameter of relaxed $Ge_{1-x-y}Si_xSn_y$ is increasing with Sn composition y and decreasing with Si content x as expected. Depending on the Si and Sn compositions, the lattice parameter of relaxed $Ge_{1-x-y}Si_xSn_y$ will be larger, equal (lattice matched) or smaller than the lattice parameter of the Ge substrate. Under pseudomorphic growth conditions, the Ge substrate acts as a template for the growth of a thin alloy layer. $Ge_{1-x-y}Si_xSn_y$ on Ge experiences a biaxial stress along the interface due to the lattice mismatch between the ternary alloy layer and the Ge substrate, creating an in-plane strain parallel to the surface. The in-plane

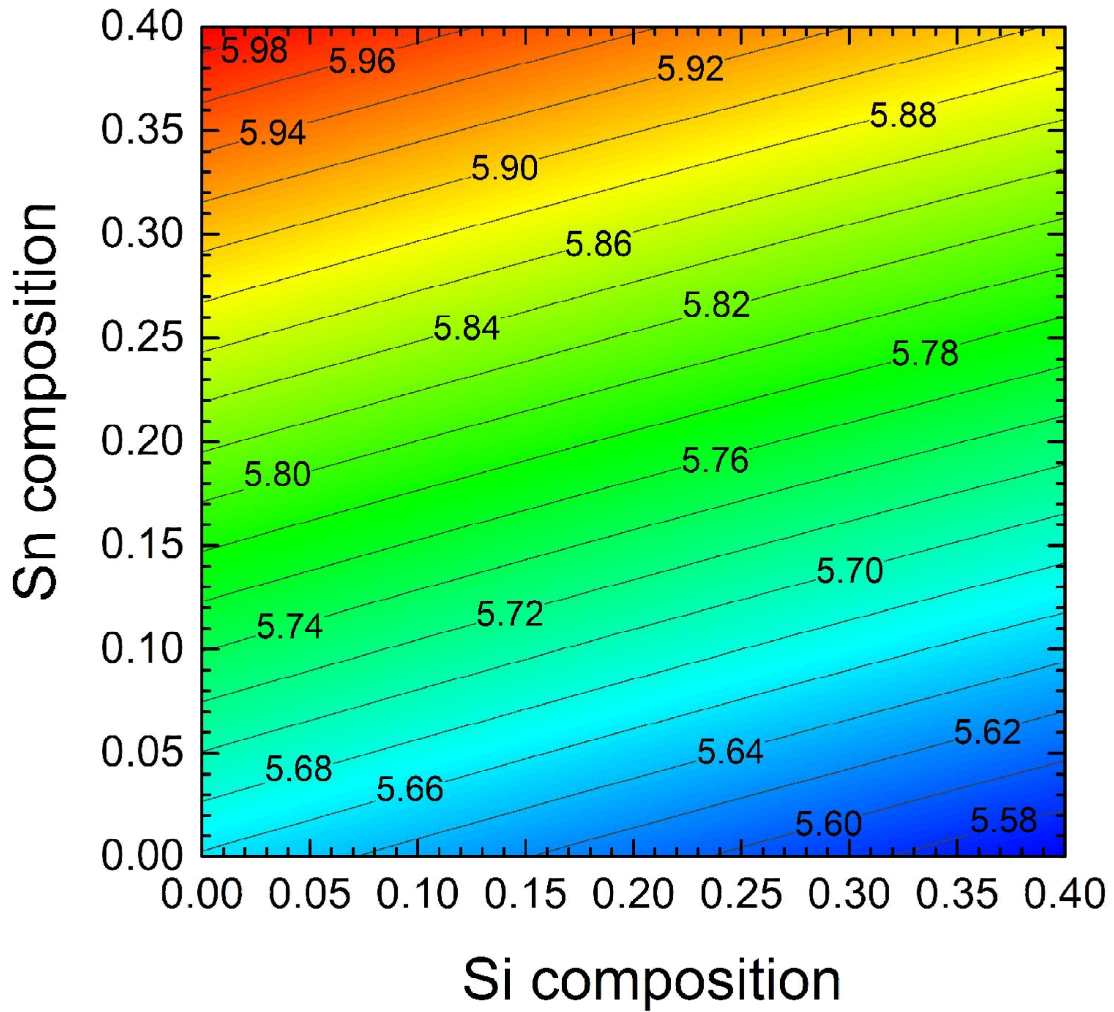

Figure 7: Compositional dependence of the lattice parameter of relaxed $Ge_{1-x-y}Si_xSn_y$ alloys, calculated using Eq. (76) (this work).

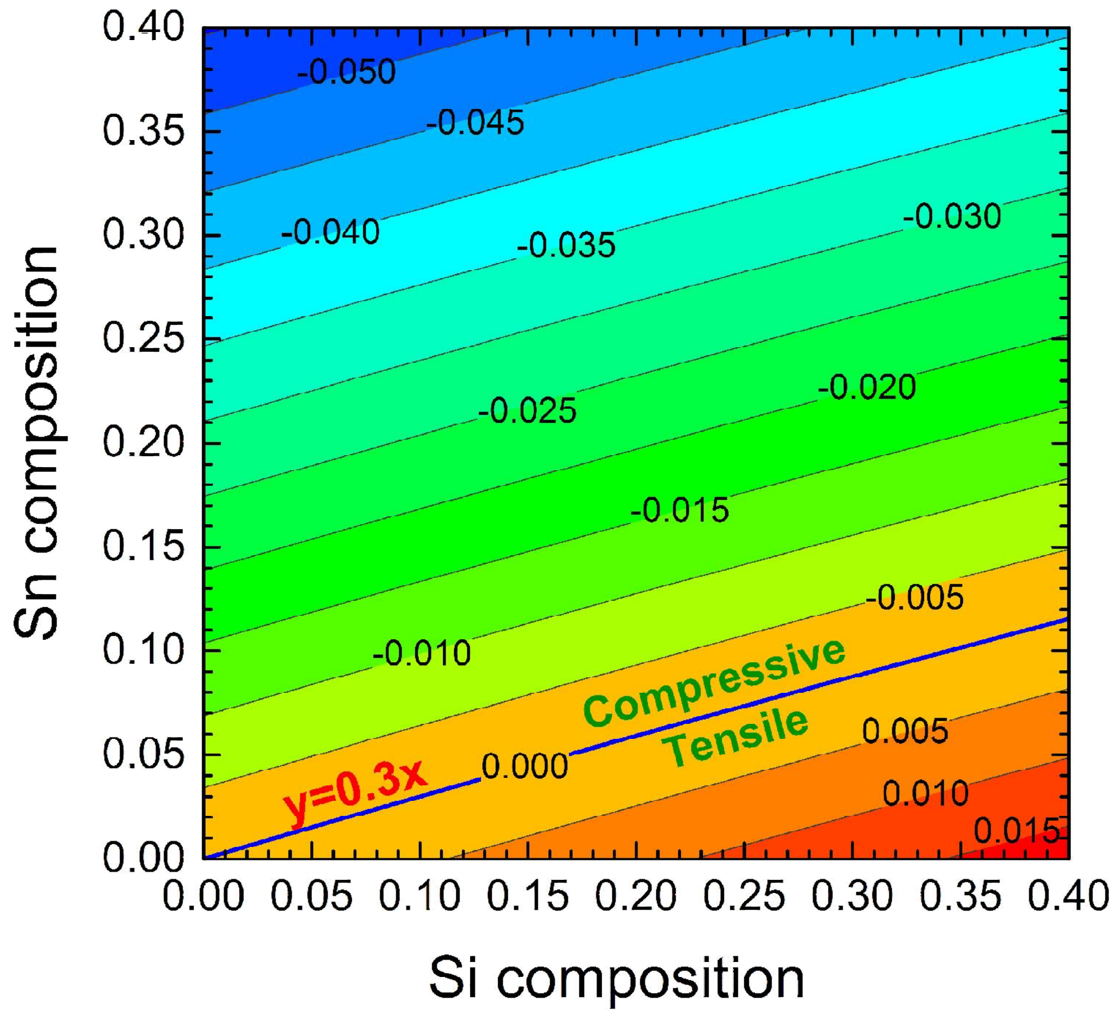

Figure 8: Compositional dependence of the in-plane strain $\epsilon_{\parallel}(x,y)$ on pseudomorphic $Ge_{1-x-y}Si_xSn_y$ on Ge, calculated using Eq. (77) (this work).

strain, on the epilayer can be calculated,

$$\epsilon_{\parallel}(x,y) = \frac{a_{Ge} - a^{rel}_{Ge_{1-x-y}Si_xSn_y}}{a^{rel}_{Ge_{1-x-y}Si_xSn_y}} \tag{24}$$

where a_{Ge} is the Ge substrate lattice parameter. The compositional dependence of the calculated in-plane strain $\epsilon_{\parallel}(x,y)$ is shown in Fig. 8. The thick solid line, $y = 0.3x$ indicates the lattice matched compositions of the $\mathrm{Ge}_{1-x-y}\mathrm{Si}_x\mathrm{Sn}_y$ on the Ge substrate. It is consistent with the previously reported value $y = 0.27x$ [68]. The small discrepancy is caused by the different values used in bowing parameters in Vegard's law when calculating the lattice parameters. The electronic and optical properties of strain free $\mathrm{Ge}_{1-x-y}\mathrm{Si}_x\mathrm{Sn}_y$ can be tuned along this lattice matched line. The lattice matched line, $y = 0.3x$, also shows a transition of $\mathrm{Ge}_{1-x-y}\mathrm{Si}_x\mathrm{Sn}_y$ on Ge from a positively strained (tensile) region to a negatively strained (compressive) region.

The ternary alloy layer is tetragonally deformed on the Ge substrate. The out-of-plane strain $\epsilon_{\perp}(x,y)$ is related to $\epsilon_{\parallel}(x,y)$ using the ratio of the elastic constants C_{12}/C_{11} by [49]:

$$\epsilon_{\perp}(x,y) = -2\left(\frac{C_{12}}{C_{11}}\right)^{Ge_{1-x-y}Si_xSn_y} \epsilon_{\parallel}(x,y)\,. \tag{25}$$

The compositional dependence of the elastic constants were taken from the literature [49, 61, 62]

$$C^{GeSiSn}_{mn} = xC^{Si}_{mn} + yC^{Sn}_{mn} + (1-x-y)C^{Ge}_{mn}. \tag{26}$$

The biaxial strain has two components: the hydrostatic strain component ϵ_H shifts the energy band positions and the shear strain component ϵ_S lifts the degeneracy of the electronic bands. The compositional dependence of the ϵ_H and the ϵ_S components are [49]:

$$\epsilon_H(x,y) = \frac{\left[\epsilon_\perp(x,y) + 2\epsilon_\parallel(x,y)\right]}{3} \tag{27}$$

$$\epsilon_S(x,y) = \frac{\left[\epsilon_\perp(x,y) - \epsilon_\parallel(x,y)\right]}{3}. \tag{28}$$

In the absence of strain, the heavy hole (v_1) and the light hole (v_2) bands are degenerate at the Γ point. Spin-orbit interactions lift the heavy hole and light hole bands with respect to the split-off (SO) band (v_3). The shear strain lifts the degeneracy of the valence band edge, leading to an additional splitting. The energy positions of the top three valence bands, v_1, v_2 and v_3 at the Γ point can be expressed as [49, 63, 64, 65]

$$E_{v_1} = -\frac{\Delta_0}{2} + \frac{3}{2}b\epsilon_S + \frac{1}{2}\sqrt{\Delta_0^2 + 6\Delta_0 b\epsilon_S + (9b\epsilon_S)^2} \tag{29}$$

$$E_{v_2} = -3b\epsilon_S \tag{30}$$

$$E_{v_3} = -\frac{\Delta_0}{2} + \frac{3}{2}b\epsilon_S - \frac{1}{2}\sqrt{\Delta_0^2 + 6\Delta_0 b\epsilon_S + (9b\epsilon_S)^2}. \tag{31}$$

where b is the biaxial deformation potential for the valence band and Δ_0 is the spin-orbit splitting of the valence band at the Γ point. The compositional dependence of the Δ_0 was obtained by linearly interpolating the three end values of Δ_0, see Table 6.

$$\Delta_0^{GeSiSn} = x\Delta_0^{Si} + y\Delta_0^{Sn} + (1-x-y)\Delta_0^{Ge}. \tag{32}$$

Several groups have reported the compositional dependence of the E_0^{Γ}, E_{ind}^{X}, E_{ind}^{L}, E_1 and $E_1 + \Delta_1$ band gaps of the relaxed $Ge_{1-x-y}Si_xSn_y$. The compositional dependence of the room temperature band gap E_i^{GeSiSn} of the relaxed $Ge_{1-x-y}Si_xSn_y$ alloys can be expressed as [66, 67, 68, 69]:

$$\begin{aligned} E_i^{GeSiSn}(x,y) = E_i^{Ge}(1-x-y) + E_i^{Si}x + E_i^{Sn}y \\ -b_i^{GeSn}y(1-x-y) - b_i^{GeSi}x(1-x-y) \\ -b_i^{SiSn}xy, \end{aligned} \tag{33}$$

where E_i^{Ge}, E_i^{Si} and E_i^{Sn} are the corresponding band gaps of the end components, and $b_i^{j,k}$ (j, k=Ge, Si, Sn) is the bowing parameter defining the deviation of the band gap from the linear interpolation. The effects of the ϵ_H and ϵ_S on the energy band positions of the conduction band can be calculated by adding the deformation potential term to the compositional dependence of the (unstrained) conduction band. The compositional dependence of the unstrained conduction band positions can be obtained from the compositional dependence of the corresponding band gaps of the relaxed alloys at the room temperature. The energy shift of the conduction band at the Γ point, ΔE_c^{Γ} and at the L point, ΔE_c^{L} due to the hydrostatic deformation can be calculated using the following expressions [5, 70, 71, 72]:

$$\Delta E_c^{\Gamma} = 3a_{\Gamma_2^-}\epsilon_H \tag{34}$$

$$\Delta E_c^{L} = 3\left[\Xi_d + \frac{1}{3}\Xi_u - a_{\Gamma_5^+}\right]^L \epsilon_H \tag{35}$$

where $a_{\Gamma_2^-}$ and $\left[\Xi_d + \frac{1}{3}\Xi_u - a_{\Gamma_5^+}\right]^L$ are the hydrostatic deformation potentials for the conduction band at the Γ and L points, respectively. The positions of the

conduction band at the Γ point and at the L point were calculated using the compositional dependence of the corresponding band gaps of the relaxed alloys, taking into account the bowing parameters (see Table 6).

The shear strain splits the conduction band at the X point into a doublet- $\Delta E_c^{(\Delta 2)}$ and a quadruplet- $\Delta E_c^{(\Delta 4)}$. The hydrostatic strain shifts the split-off bands. The effects of the shear strain and the hydrostatic strain on the conduction band at the X symmetry point can be expressed as [5, 70, 71, 72]:

$$\begin{aligned} \Delta E_c^{X(\Delta 2)} &= 2\epsilon_S \Xi_u^{\Delta} + 3\left[\Xi_d + \frac{1}{3}\Xi_u - a_{\Gamma_5^+}\right]^X \epsilon_H \\ \Delta E_c^{X(\Delta 4)} &= -\epsilon_S \Xi_u^{\Delta} + 3\left[\Xi_d + \frac{1}{3}\Xi_u - a_{\Gamma_5^+}\right]^X \epsilon_H, \end{aligned} \tag{36}$$

where Ξ_u^{Δ} is the shear deformation potential for the conduction band minimum at Δ and $\left[\Xi_d + \frac{1}{3}\Xi_u - a_{\Gamma_5^+}\right]^X$ is the hydrostatic deformation potential of the conduction band at the X point.

Combining the compositional dependence of the band gaps of the relaxed (unstrained) ternary alloys, given by Eq. (75), with the energy shift and the splitting of the conduction and valence bands using deformation potential theory, the compositional dependence of the band gaps of the pseudomorphic $Ge_{1-x-y}Si_xSn_y$ on Ge at the Γ, L and the X symmetry points can be obtained. All the parameters used for the calculation are listed in Table 6. The compositional and strain dependence of the band structure, indirect-direct crossover, and related parameters will be discussed in chapter 6.

3 Sample preparation and characterization techniques

3.1 Chemical vapor deposition (CVD)

The Ge on Si sample discussed in chapter 5, was prepared by the group of Kouvetakis at Arizona State University using chemical vapor deposition (CVD). Ge films were deposited on Si(100) wafers using reactant mixtures of tetragermane (Ge_4H_{10}) and H_2. Si substrates were cleaned using a standard cleaning procedure as described in Ref. [73] and loaded into the reactor for degassing at 500°C which was maintained at 10^{-10} Torr background pressure. Then, substrates were flashed at 850°C to remove surface oxide contaminants. Thereafter, deposition of the Ge layers were started immediately by introducing precursors (mixture of Ge_4H_{10} and H_2) into the CVD chamber at 370-425°C temperatures and at a total pressure of 10^{-4} Torr. The growth rate varied between 17 and 30 nm/min depending on the growth temperature. The growth of the Ge layers was continued until the desired thickness (∼1500 nm) was obtained. After the completion of the growth, samples were annealed in situ at 680°C for 3 min to improve the alignment of crystal mosaics. Atomic force microscopy confirmed the smooth defects free surface morphology of the Ge layers on Si with RMS roughness of 0.5-0.7 nm and the thickness was confirmed by the spectroscopic ellipsometry. X-ray diffraction of (224) reciprocal space maps indicate cubic Ge layers on Si and no residual compressive strain. Additional information about the sample growth and related parameters is given in Ref. [73].

3.2 Molecular beam epitaxy (MBE)

Pseudomorphic and partially relaxed $Ge_{1-y}Sn_y$ on Ge, discussed in chapter 6 and chapter 7 were grown by Kolodzey group in the Department of Electrical and Computer Engineering at the University of Delaware [58, 74]. All $Ge_{1-y}Sn_y$ alloy samples were grown on Ge using a modified EPI 620 MBE system with a base pressure of 1.3x10^{-8} Pa and utilizing Knudsen thermal effusion cells with pyrolytic Boron Nitride (pBN) crucibles for both Ge and Sn. Intrinsic (001) Ge substrates were prepared using a wet chemical cleaning based on the procedure outlined in Hovis *et al.*,[75] before quickly being loaded into the MBE introduction chamber and taken to ultra-high vacuum. The substrates were slowly heated to 450°C overnight, then taken to 650°C for one hour before individually being transferred into the main MBE growth chamber. Each wafer was flash heated to 850°C for 10 minutes, then cooled to the growth temperature of between 150°C and 250°C (as measured via thermocouple) prior to opening the Ge and Sn cell shutters for growth. The growth temperature was varied with Sn content to avoid surface segregation. The Sn composition was varied by changing the Sn effusion cell temperature while keeping the Ge cell temperature constant across all growths, achieving a growth rate of 0.62 to 0.7 nm/min. More details about the substrate precleaning, sample growth procedures and characterization can be found in Refs. [58, 74].

3.3 Spectroscopic ellipsometry

The accurate knowledge of optical constants of materials is of great importance for the design of optoelectronic devices. Spectroscopic ellipsometry is an optical measurement technique used to characterize the optical properties of ma-

terials (thin films and bulk). It is a widely used optical metrology technique in the semiconductor industry. In spectroscopic ellipsometry, the change of the polarization state of the light reflected form the surface of a sample is measured. The reflected light usually becomes elliptically polarized, giving the name of the technique "ellipsometry".

Depending on the oscillatory direction of the electric fields, light is classified into p- and s-polarized light waves. In p-polarization, electric fields of the light waves oscillate in the plane of incidence. Electric fields oscillate perpendicular to the plane of incidence in s- polarized light. Due to the difference in dipole radiation, p- and s- polarized light waves behave differently when light is reflected by a sample at oblique incidence. The amplitude reflection coefficients, r_p and r_s, of the p- and s-polarized light waves are given by Fresnel's equations [76, 77]

$$r_p = \frac{E_{rp}}{E_{ip}} = \frac{N_t \cos\theta_i - N_i \cos\theta_t}{N_t \cos\theta_i + N_i \cos\theta_t} \tag{37}$$

$$r_s = \frac{E_{rs}}{E_{is}} = \frac{N_i \cos\theta_i - N_t \cos\theta_t}{N_i \cos\theta_i + N_t \cos\theta_t} \tag{38}$$

where N_i and N_t show the complex refractive index defined by $N = n - ik$ for the ambient medium and the substrate. θ_i and θ_t are angle of incidence and transmission respectively.

3.3.1 Data acquisition

Ellipsometry measures two values, Ψ and Δ, known as ellipsometric angles, which represent the amplitude reflection ratio ($\mathrm{r}_p/\mathrm{r}_s$) and the phase difference ($\delta_p - \delta_s$) between the p- and s-polarized light waves (see Fig. 9). The ellipsometric

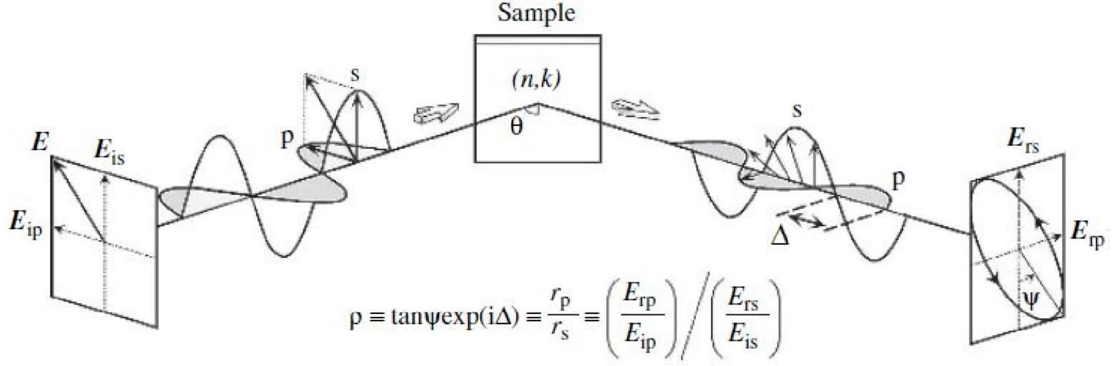

Figure 9: Schematic overview of the measurement principle of spectroscopic ellipsometry. [76]

angles, Ψ and Δ measured from ellipsometry are defined as [76, 77]

$$\rho = \tan\Psi \exp(i\Delta) = \frac{r_p}{r_s} \tag{39}$$

For the simplest system, light reflection at an air/sample interface, assuming that the sample is a bulk material with infinite thickness, using Eq. (37)- Eq. (39), it can be shown that the amplitude reflection ratio Ψ is characterized by the refractive index n and the phase difference Δ can be described by the extinction coefficient k of the material. The complex dielectric function of the material ϵ can be expressed as $\epsilon = N^2$, the absorption coefficient α can be obtained by the relation $\alpha = 4\pi k/\lambda$, where λ is the wavelength of the light.

The dielectric function, obtained directly from the measured ellipsometric angles Ψ and Δ is known as the pseudodielectric function $\langle\epsilon\rangle$ of the material and calculated from a model assuming a perfectly flat substrate (no surface roughness) with infinite thickness. If the dielectric constant of the ambient air is 1, the pseudodielectric function of the bulk substrate $\langle\epsilon\rangle$ can be obtained from the measured

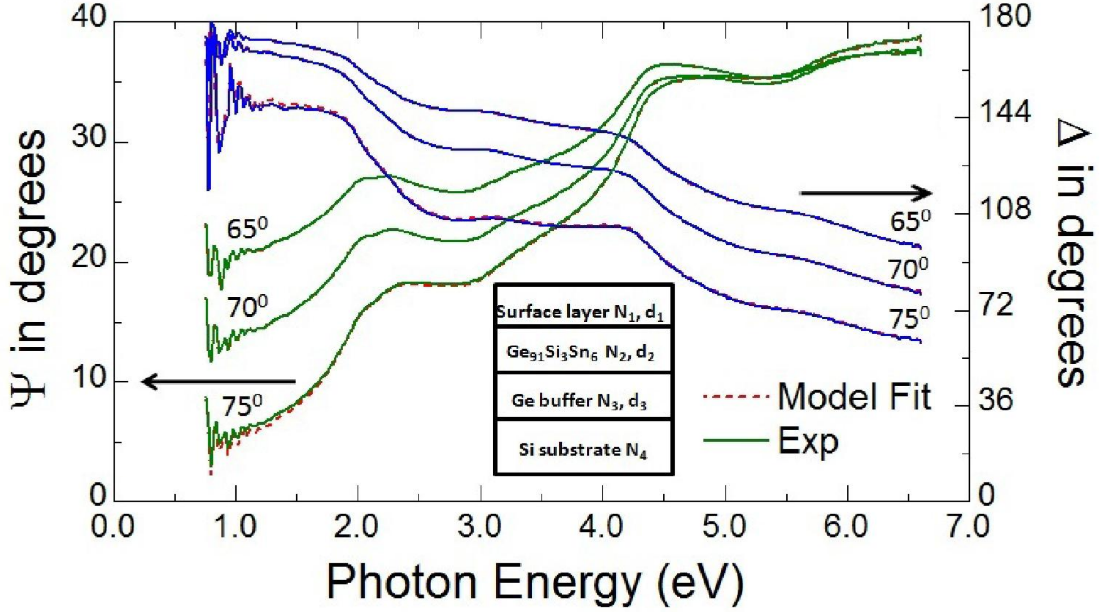

Figure 10: Experimental data (solid) of ellipsometric angles Ψ and Δ for $Ge_{91}Si_3Sn_6$ on Ge buffered Si versus photon energy. The model data (dashed) obtained, assuming a multilayer system as illustrated in the inset is also shown (this work).

ellipsometry angles, $\rho = \tan\Psi \exp(i\Delta)$ and the angle of incident θ_i, [76, 77]

$$\langle \epsilon \rangle = \langle N^2 \rangle = \sin^2\theta_i \left[1 + \tan^2\theta_i \left(\frac{1-\rho}{1+\rho} \right) \right] \tag{40}$$

In general, spectroscopic ellipsometry measures the Ψ and Δ spectra for photon energy ($\hbar\omega$), it is rather difficult to interpret or explain results from directly measured spectra. Hence, a construction of a model is required for data analysis and the electronic properties, optical properties and film thickness of the sample can be extracted from the model. Experimentally obtained ellipsometric angles Ψ and Δ for $Ge_{91}Si_3Sn_6$ on Ge buffered Si sample at 65°, 70° and 75° angle of incident are shown in Fig. 10. The pseudodielectric function of the sample, (assuming a

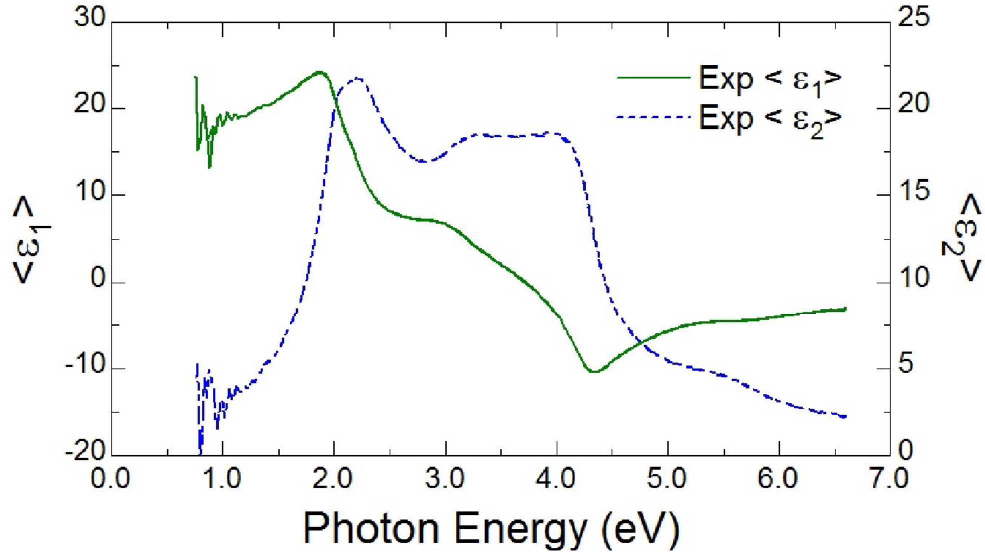

Figure 11: Pseudodielectric function $\langle\epsilon_1\rangle$ (solid) and $\langle\epsilon_2\rangle$ (dashed) for $Ge_{91}Si_3Sn_6$ on Ge buffered Si versus photon energy obtained from measured ellipsometric angles Ψ and Δ (this work).

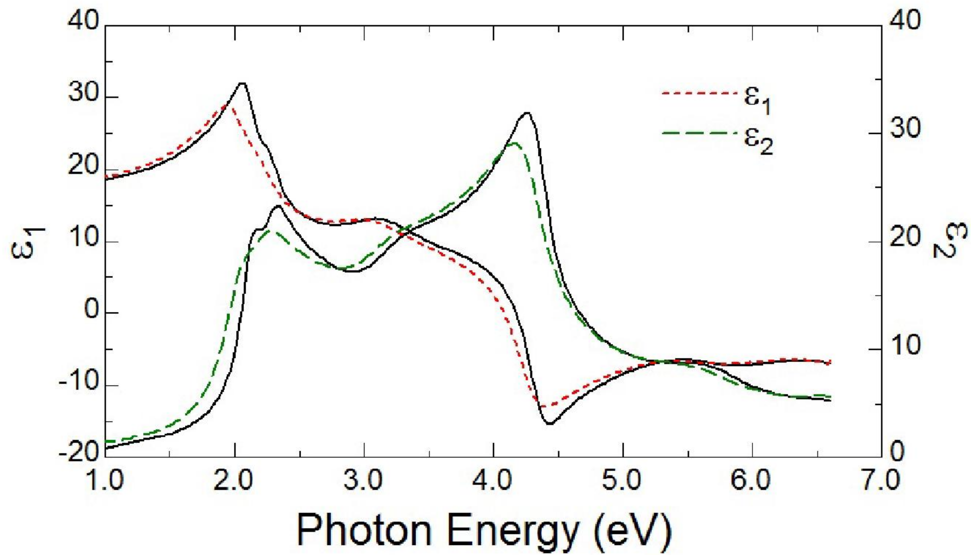

Figure 12: Real (ϵ_1, short-dashed) and imaginary (ϵ_2, long-dashed) parts of the dielectric function of $Ge_{91}Si_3Sn_6$ obtained from a point-by-point fit. Solid lines represent the dielectric function of Ge (this work).

flat infinitely thick substrate) obtained from measured Ψ and Δ spectra using Eq. (40) is shown in Fig. 11.

3.3.2 Modeling ellipsometry data

To obtain the electronic and optical properties, film thickness, and surface roughness of the sample, it is necessary to build an optical model to interpret the experimentally measured spectra. A multilayer optical model consisting of a surface layer/$Ge_{91}Si_3Sn_6$ film/Ge buffer/Si substrate, as shown in the inset of the Fig. 10 can be used to model experimental ellipsometric angles Ψ and Δ where ρ can be expressed as $\tan\Psi\exp(i\Delta) = \rho\,(N_1, N_2, N_3, N_4, d_1, d_2, d_3, \theta_0)$ using the variables used in the model. N_1, N_2, N_3, and N_4 denote the complex refractive index of the surface layer, $Ge_{91}Si_3Sn_6$ thin film, Ge buffer and Si substrate, respectively. d_1, d_2, d_3 denote the thicknesses of the surface layer, $Ge_{91}Si_3Sn_6$ thin film and Ge buffer. θ_0 is the angle of incidence. The surface layer with the surface roughness is modeled as a GeO_2 layer where the optical constants are known and available in tabulated form [78, 79]. The optical constants of the Ge buffer and Si substrate are also well known and published in the literature [80, 81, 82, 83]. The thickness of the surface layer, d_1 is inversely proportional to the amplitude of the E_2 peak appearing at around 4 eV. It can also be accurately extracted from the absorption (Δ) below the band gap of the material. When the light absorption in a thin film is very low, optical interference occurs, giving rise to interference fringes. The thickness interference fringes due to the superimposed optical wave are clearly seen in the optical spectra shown in Fig. 11 at low photon energies (between 0.7 and 1.2 eV) where the light absorption is relatively small and the thickness of the $Ge_{91}Si_3Sn_6$ thin film (d_2) and the Ge buffer (d_3) can be extracted

from the spacing of the interference fringes. Hence, the only unknown parameters are the optical constants of the $Ge_{91}Si_3Sn_6$ thin film N_2, which can be obtained from the measured Ψ and Δ spectra by fitting the model to the experimental data.

The dielectric functions of $Ge_{91}Si_3Sn_6$ were described using a parametric oscillator model [82], which imposes Kramers-Kronig consistency between the real and imaginary parts of ϵ. In the first step of the fit, the oxide, $Ge_{91}Si_3Sn_6$ and Ge buffer layer thicknesses and all parameters in the parametric oscillator model for $Ge_{91}Si_3Sn_6$ were adjusted to obtain a good fit with the experimental data. The dashed lines in Fig. 10 represent the modeled ellipsometry angles (Ψ and Δ) from the parametric oscillator model which is nearly indistinguishable from the experimental data. In the second step, all parameters were kept fixed at the values obtained in the first step, and the data were fitted again at each measured photon energy by taking the values of ϵ_1 and ϵ_2 for $Ge_{91}Si_3Sn_6$ as adjustable parameters (known as point-by-point fit) to obtain the final tabulated (non-parametric) dielectric function of $Ge_{91}Si_3Sn_6$. This final non-parametric dielectric function, shown in Fig. 12 is very close to the parametric dielectric function obtained in the first step, therefore we confirmed that results from the second step, shown were still Kramers-Kronig consistent. The complex dielectric functions of $Ge_{91}Si_3Sn_6$ show features similar to bulk Ge, indicating a diamond crystal structure composed of tetrahedrally coordinated atoms. The red shifting of the dielectric function along with the broadening of critical points (with respect to bulk Ge) can be clearly seen as a result of the alloying and the strain effects of Si and Sn on the Ge band structure.

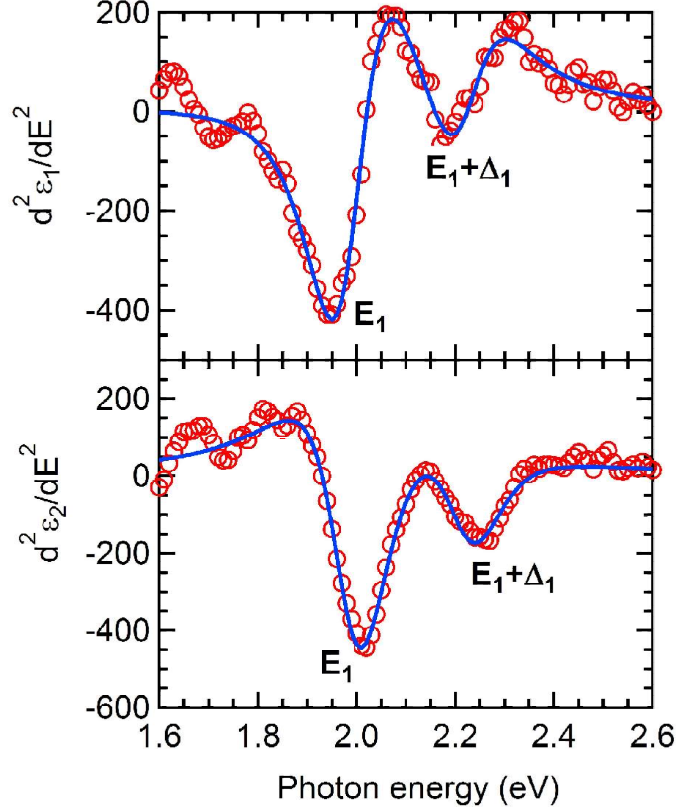

Figure 13: Second derivatives of the real (ϵ_1) and imaginary (ϵ_2) part of the dielectric function of $Ge_{91}Si_3Sn_6$ with respect to photon energy near the E_1 and $E_1 + \Delta_1$ critical points. Symbols represent the experimental data and the solid line shows the best fit with a two dimensional critical point assuming parabolic bands and constant dipole matrix elements (this work).

3.3.3 Second derivative analysis

The main focus in this thesis was to investigate the compositional, strain, and temperature dependence of the critical points (CPs) associated with the electronic band structure. The E_1 and $E_1 + \Delta_1$ CPs can be described using an expression for a mixture of a two-dimensional minimum and a saddle point [30]

$$\epsilon\left(\hbar\omega\right) = C - A\ln\left(\hbar\omega - E_g - i\Gamma\right)e^{i\phi}, \tag{41}$$

where $\hbar\omega$ is the photon energy, A is the amplitude, E_g is the CP energy, Γ is the broadening parameter, and ϕ is the excitonic phase angle which describes the amount of mixing. The contribution of the CPs to the dielectric function can be enhanced by analyzing the second derivatives of ϵ. The real and imaginary parts of the tabulated dielectric function obtained by point-by-point fitting were numerically differentiated and smoothed using ten Savitzky-Golay coefficients for second-order derivatives with a polynomial degree of three to obtain a good signal to noise ratio without distorting the line shape [84]. The second derivative spectra of the dielectric function for the $Ge_{91}Si_3Sn_6$ were fitted using Eq. (41) and A, E_g, ϕ, and Γ were treated as fit parameters. The second derivative spectrum of the $Ge_{91}Si_3Sn_6$ with the best fit of a 2D critical point is shown in Fig. 13. Both E_1 and $E_1+\Delta_1$ were fitted simultaneously and the excitonic phase angle ϕ was forced to take the same value for both CPs.

3.3.4 Temperature dependent measurements inside the cryostat

The temperature dependent measurements of the samples were performed inside a commercial, ultra-high vacuum (UHV) cryostat (Janis ST-400) as shown in Fig. 14. A type-E thermocouple built-in the cold finger, in conjunction with a Lakeshore 331 temperature controller was used to control the temperature of the cold finger. Since the built-in thermocouple and the heater in the copper cold finger are about 10 cm away from the sample holder, we attached another type-E thermocouple onto the sample surface, between the top surface of the sample and the metal holding clamp, see Fig. 15, in order to accurately measure the temperature of the sample surface. In order to achieve a better thermal equilibrium between the sample holder, the sample surface, and the thermocouple, a gold-

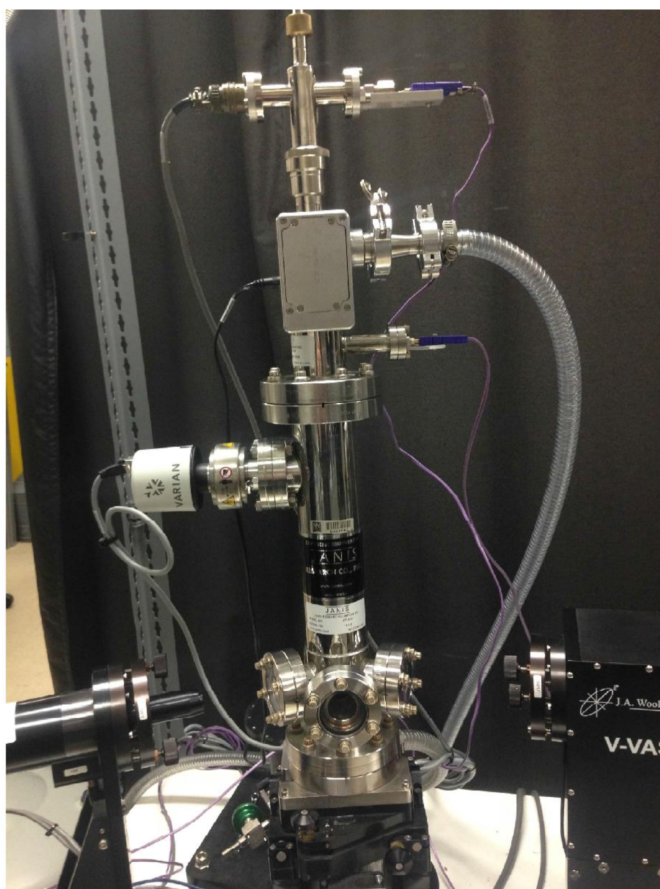

Figure 14: A view of the ellipsometry cryostat mounted on the J.A. Woollam variable angle-of-incidence ellipsometer.

Figure 15: The sample holder with a sample held by two horizontal metal clamping strips. The thermocouple is clamped between the front sample surface and the upper clamping strip in order to measure the temperature of the sample surface accurately.

plated coper heat shield was used to cover the sample holder and the cold finger. The temperature reading of the thermocouple on the front surface of a bulk Ge sample is 785 K, while the built-in thermocouple next to the heater reads 800 K. At liquid helium temperature, built-in thermocouple next the heater, reads 77 K and the thermocouple on surface of the bulk Ge reads 80 K. The temperature dependent measurements were performed on our samples at a 70° incidence angle from 0.8 to 6.6 eV in the UHV cryostat, shown in Fig. 14, from 80 K to 785 K. The details of the sample cleaning, measurement procedure inside the cryostat are explained in chapter 4.

3.4 High resolution X-ray diffraction

X-ray diffraction is a nondestructive technique used to characterize the crystal structure, crystalline quality, relaxation condition, lattice parameters and thickness of the epilayers on substrates. A PANalytical Empyrean diffractometer, operated at 45 keV and 40 mA, was used for the high resolution X-ray diffraction (HRXRD) analysis described in this thesis. Our high resolution configuration consists of a two bounce hybrid monochromator (2xGe(220)), which offers a well-collimated beam of monochromatic Cu Kα_1 radiation (1.5406 Å) and a three-bounce Ge (220) analyzer in front of the Xe proportional detector. Symmetric $\omega - 2\theta$ diffraction curves and $\omega - 2\theta/2\theta$ reciprocal space maps (RSMs) were performed for symmetrical (004) and asymmetrical ($\bar{2}\bar{2}4$) reflections at room temperature to investigate the pseudomorphic nature, crystalline quality, lattice parameters, and layer thickness of the samples.

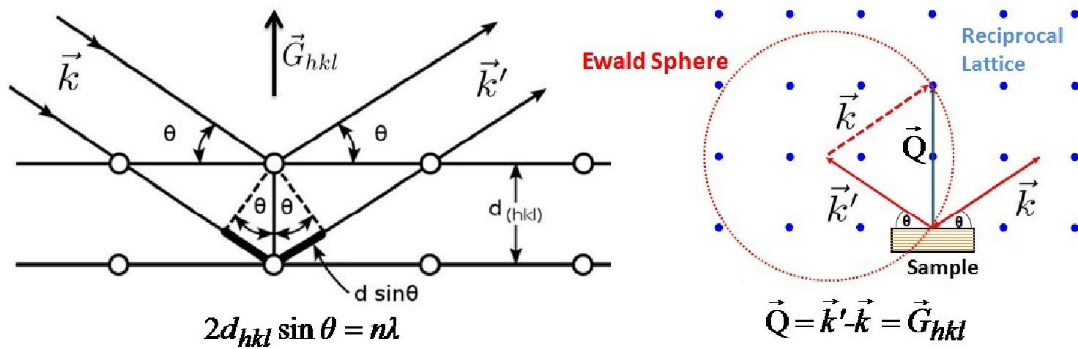

Figure 16: Schematic representation of $\omega - 2\theta$ symmetric scans. An initial plane wave with wave vector $\vec{k}$ is irradiated on the sample surface with an angle $\omega(=\theta)$ and the outgoing scattered waves $\vec{k}'$ are analyzed under the same angle [85].

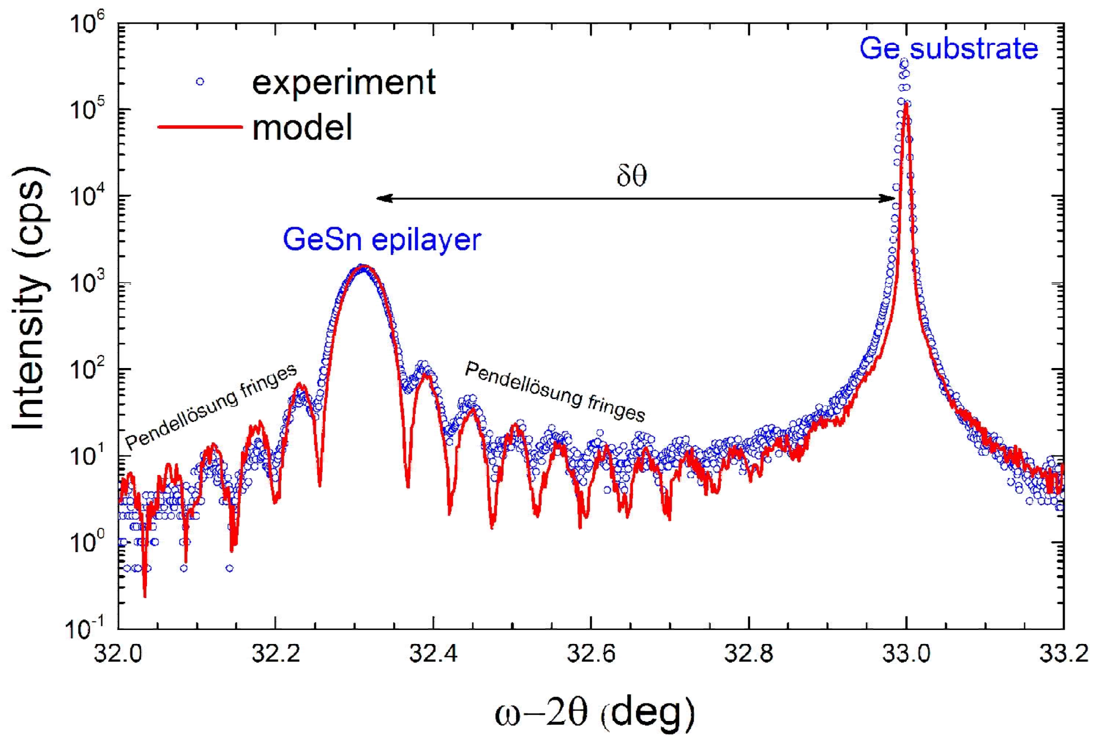

Figure 17: Logarithmic intensity versus diffraction angle for the symmetric (004) $\omega - 2\theta$ reflections of the pseudomorphic $Ge_{93.2}Sn_{6.8}$ on Ge. Symbols represent the experimental data and the solid line shows the model (this work).

3.4.1 Diffraction from epilayers

In a single $\omega - 2\theta$ symmetric scan, an initial plane wave with wave vector $\vec{k}$ is irradiated on the sample surface at an angle $\omega(=\theta)$ and the outgoing scattered waves $\vec{k}'$ are analyzed under the same angle. When the scattering vector $\vec{Q}$, $\left(\vec{Q} = \vec{k}' - \vec{k}\right)$ is equal to a reciprocal lattice vector $\vec{G}_{hkl}$, a diffraction pattern can be seen for the corresponding (hkl) Bragg reflections as illustrated in Fig. 16. It allows to scan the Bragg reflections along a line to get the positions of the substrate and the epilayer peaks. The corresponding peak positions can be used to extract the out-of-plane (perpendicular) lattice parameters ($a_\perp$) of the substrate and the epilayers using Bragg's law, $2d_{hkl}\sin\theta = n\lambda$, where $d_{hkl} = a_\perp/\sqrt{h^2+k^2+l^2}$ for a cubic structure.

Symmetric $\omega - 2\theta$ diffraction scans were performed for symmetrical (004) reflections at room temperature. The substrate peak with its known Bragg angle was used as a reference for analyzing the layer peaks in each sample. Before starting the measurements, samples were first aligned to the substrate (004) symmetric reflection and positions of the epilayer peaks were measured relative to the substrate peak. A symmetric $\omega - 2\theta$ scan of (004) reflections of pseudomorphic $Ge_{93.2}Sn_{6.8}$ on Ge is shown in Fig. 17. The measurement showed two peaks, the sharp peak at the higher angle, corresponding to the Ge substrate, and the broader lower angle peak, corresponding to the $Ge_{93.2}Sn_{6.8}$ alloy. The Bragg peaks for $Ge_{1-y}Sn_y$ alloys shifted to smaller angles with increasing Sn composition, indicating an increase in the perpendicular lattice constant in the presence of compressive strain, which was attributed to the incorporation of larger Sn atoms in the Ge lattice. The peak separation $\delta\theta$ is related to the ratio $a_{\mathrm{Ge}}/a_\perp$. Assuming that the epilayer is not tilted relative to the Ge substrate, which we confirmed by (004) symmetric reciprocal

space maps (RSMs), $a_\perp$ can be calculated from[86] $a_{\mathrm{Ge}}/a_\perp = 1 + \delta\theta \cot\theta$, where θ is the Bragg angle of bulk Ge. From the out-of-plane lattice constant $a_\perp$ and the in-plane lattice constant $a_\parallel = a_{\mathrm{Ge}}$ (pseudomorphic condition), we calculated the in-plane strain

$$\epsilon_\parallel = \frac{a_\parallel - a_\perp}{a_\perp + 2\left(\frac{C_{12}}{C_{11}}\right)^{\mathrm{Ge}_{1-y}\mathrm{Sn}_y} a_\parallel} \tag{42}$$

and the relaxed lattice constant

$$a^{\mathrm{rel}}_{\mathrm{Ge}_{1-y}\mathrm{Sn}_y} = \frac{a_\parallel}{\epsilon_\parallel + 1}, \tag{43}$$

from which the tin content y could be determined using the known compositional dependence of the lattice parameters of bulk $\mathrm{Ge}_{1-y}\mathrm{Sn}_y$ alloys given by Eq. (76), known as Vegard's law. Assuming the bulk Ge elastic constant ratio (C_{12}/C_{11}) as the starting point, Eq. (42) and Eq. (43) can be solved to obtain the initial Sn composition in the alloy epilayer. Based on the calculated Sn composition, the $C_{12}/C_{11}(y)$ for $\mathrm{Ge}_{1-y}\mathrm{Sn}_y$ can be obtained from the compositional dependence of the elastic constants by using Eq. (79) and the calculation is repeated iteratively until y is converged.

In addition to the Bragg peaks of the substrate and the epilayer, all samples showed (004) Pendellösung fringes around the epilayer peak due to the finite thickness of the $\mathrm{Ge}_{1-y}\mathrm{Sn}_y$ epilayer, indicating a uniform thickness of a high quality (coherent) epilayer. The spacing between the fringes can be related to the thickness of the epilayer and can be used to extract the thickness using [58, 86, 87]

$$\lambda = 2t\Delta\theta_t \cos\theta \tag{44}$$

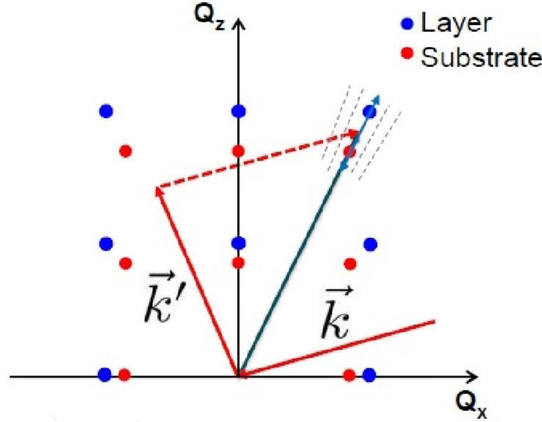

Figure 18: Schematic representation of reciprocal space mapping, where several $\omega - 2\theta$ scans are performed with stepped ω to cover an area of the Bragg peaks for the epilayer and the substrate [85].

where λ is the X-ray wavelength, t is the thickness of the epilayer, $\Delta\theta_t$ is the separation between the epilayer and the first interference fringe and θ is the Bragg angle of the epilayer.

3.4.2 Reciprocal space maps

In reciprocal space maps (RSMs), instead of a single $\omega - 2\theta$ scan, several $\omega - 2\theta$ scans are performed with stepped ω to cover an area of the Bragg peaks for the epilayer and the substrate, as illustrated in Fig. 18. Apart from the in-plane ($a_\parallel$) and out-of-plane ($a_\perp$) lattice parameters, the pseudomorphic nature, partial relaxation and the tilt of the epilayer on the substrate can be obtained from RSMs. As illustrated in Fig. 19, for a fully relaxed epilayer on a substrate, Bragg reflections of the epilayer lie on a line going through the origin and the substrate reflection. When the epilayer is pseudomorphically grown (fully strained) on a substrate, the epilayer Bragg reflections lie on a vertical line going through the substrate reflections. Bragg reflections of partially relaxed epilayers lie on the

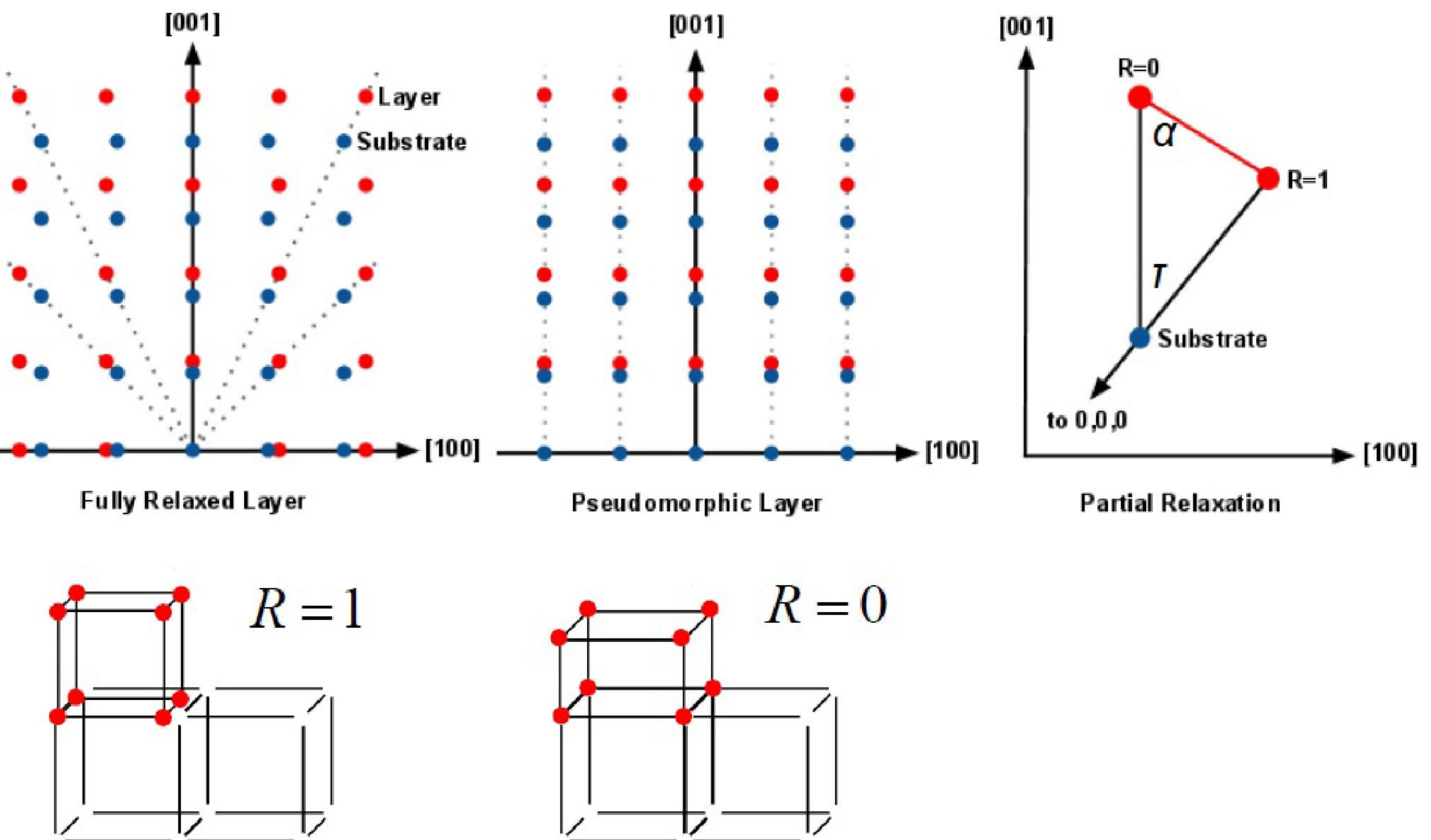

Figure 19: Schematic representation of RSMs of a fully relaxed, pseudomorphic (fully strained), and partially relaxed epilayers on a substrate [85].

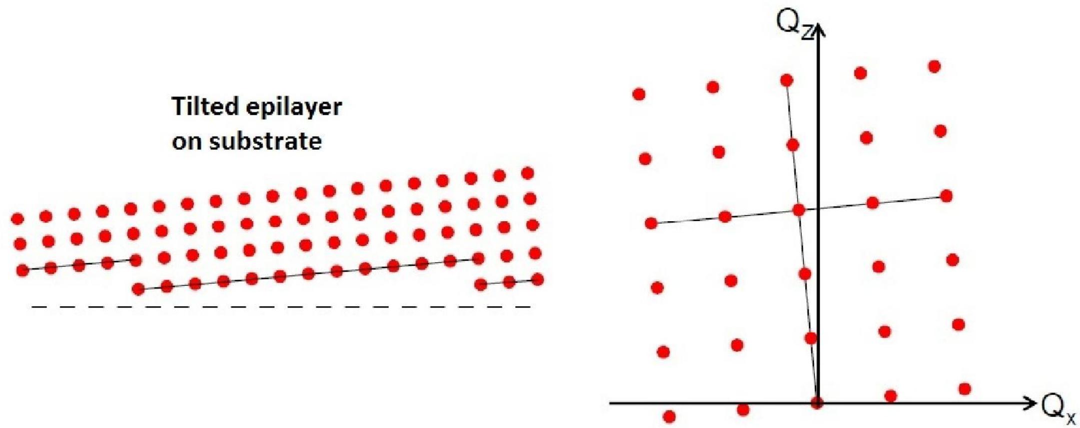

Figure 20: Schematic representation of a tilted epilayer relative to the substrate. Tilting causes a rotation of the epilayer reflections about the origin in reciprocal space [85].

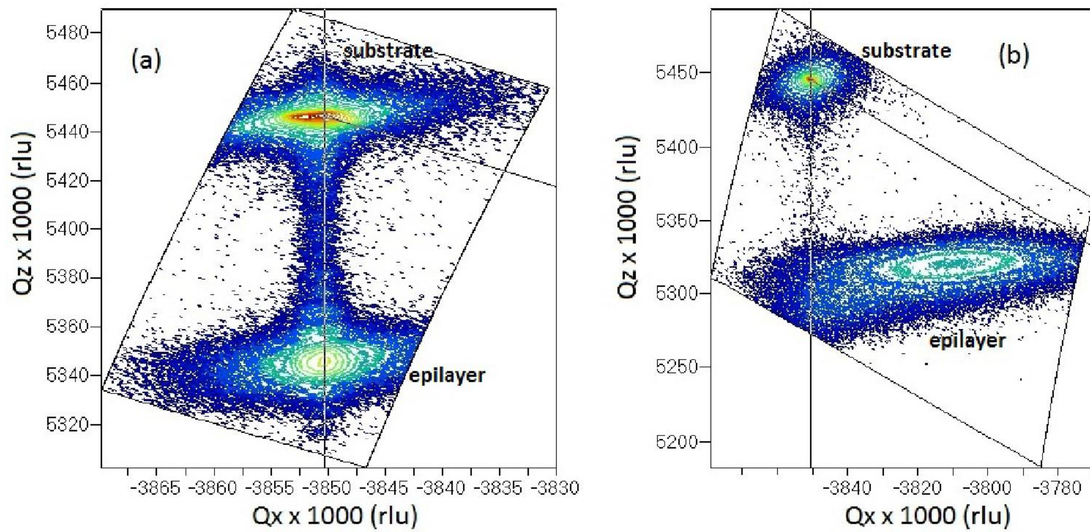

Figure 21: Reciprocal space maps around $(\bar{2}\bar{2}4)$ reflections of (a) fully strained $Ge_{93.2}Sn_{6.8}$ and (b) partially (60%) relaxed $Ge_{87.5}Sn_{12.5}$ on Ge. Solid lines show the fully strained and fully relaxed conditions (this work).

relaxation line connecting the fully strained and fully relaxed points. If the epilayer is tilted relative to the substrate, the the epilayer Bragg reflections are rotated about the origin, as shown in Fig. 20.

In this research, symmetric (004) RSMs were performed to investigate the tilt of the epilayers on substrates. Asymmetric ($\bar{2}\bar{2}4$) grazing exit RSMs were performed to extract the perpendicular and parallel lattice parameters of the epilayers simultaneously and to evaluate the pseudomorphic nature (or partial relaxation) of the epilayers on substrates. In the RSM, the intensity of the diffracted beam is plotted as a function of the reciprocal lattice vectors along the [110] and [001] ($\mathrm{Q}_{\|}$ and $\mathrm{Q}_{\perp}$) directions, as contours of equal intensity. The $\mathrm{Q}_{\|}$ and $\mathrm{Q}_{\perp}$ vectors are related to the reciprocals of the in-plane and out-of-plane lattice constants, respectively, and are typically given in terms of reciprocal lattice units (rlu) that are calculated from the angular positions ω and 2θ using the following equations [58]:

$$Q_{\|}(\mathrm{rlu}) = \sin\theta \times \sin(\theta - \omega) \tag{45}$$

$$Q_{\perp}(\mathrm{rlu}) = \sin\theta \times \cos(\theta - \omega) \tag{46}$$

The $Q_{\|}$ and $Q_{\perp}$ along the [110] and [001] directions, extracted from the ($\bar{2}\bar{2}4$) RSMs are related to the out-of-plane

$$a_{\perp} = \frac{Q_{\perp \mathrm{substrate}} - Q_{\perp \mathrm{epilayer}}}{Q_{\perp \mathrm{epilayer}}} a_{\mathrm{substrate}} + a_{\mathrm{substrate}} \tag{47}$$

and in-plane lattice parameters [88]

$$a_{\|} = \frac{Q_{\| \mathrm{substrate}} - Q_{\| \mathrm{epilayer}}}{Q_{\| \mathrm{epilayer}}} a_{\mathrm{substrate}} + a_{\mathrm{substrate}}. \tag{48}$$

The degree of relaxation (R) of the epilayer on substrate can be calculated using,

$$R = \frac{\left(a_{\parallel \text{epilayer}} - a_{\text{substrate}}\right)}{\left(a_{\text{epilayer}}^{relaxed} - a_{\text{substrate}}\right)} \tag{49}$$

Therefore, using Eqs. (42), (43), and (76) iteratively, the relaxed lattice parameter, alloy composition, strain, and degree of relaxation of the epilayer can be obtained as explained above. Reciprocal space maps around asymmetric ($\bar{2}\bar{2}4$) reflections of (a) fully strained $Ge_{93.2}Sn_{6.8}$ and (b) partially (60%) relaxed $Ge_{87.5}Sn_{12.5}$ on Ge are shown in Fig. 21. Solid lines show the fully strained and fully relaxed conditions.

3.5 X-ray reflectivity

Accurate measurements of thickness, surface and interface roughness and electron density distribution of epilayers are important since this relates to the structure of the multilayer sample which is used to model optical constants. X-ray reflectivity (XRR) is a nondestructive technique used to characterize thicknesses, interface and surface roughnesses of multilayer samples with a resolution on the order of a few Å. At X-ray wavelengths, the refractive index of most materials is slightly less than one, thus the X-rays are totally reflected from smooth surfaces for grazing incidence angles lower than the critical angle θ_c of the material. When the incident angle is larger than the θ_c the reflectivity decreases quickly with the increment of the incident angle. X-ray reflectivity takes advantage of this effect and measures the intensity of X-rays reflected from the surface as a function of angle at a given wavelength by running $\omega - 2\theta$ scans, yielding the reflectivity

curve, R(Q), where Q $= 4\pi \sin\theta/\lambda$, [89]

$$R(Q) = \frac{1}{4L_x L_y \sin\theta} \iint_{\Delta\Omega} \left(\frac{d\sigma}{d\Omega}\right)_{el} d\Omega \quad \propto \quad \frac{16\pi^2}{Q^2} \left| \int_{-\infty}^{\infty} \beta\left(z\right) e^{-izQ} dz \right|^2 \tag{50}$$

where $4L_x L_y \sin\theta$ is the area of the sample illuminated perpendicular to the incoming beam and the elastic differential cross section $(d\sigma/d\Omega)_{el}$ is given by the Fourier transform of the scattering length density (SLD) function β known as the depth profile. Integrating by parts, Eq. (50) yields, [89]

$$R(Q) \approx \frac{16\pi^2}{Q^4} \left| \int_{-\infty}^{\infty} \frac{d\beta}{dz} e^{-izQ} dz \right|^2 . \tag{51}$$

Considering a simple situation involving a uniform layer (thickness L, SLD β_L) on a substrate (SLD β_S) and assuming infinitely smooth surface and interface, the depth profile $\beta\left(z\right)$ of the system is equal to; β_S for z $<$ -L, β_L for -L $<$ z $<$ 0, and zero for z $>$ 0. The derivative of the depth profile is a pair of δ functions, dβ/dz $=(\beta_L - \beta_S)\,\delta\left(z + L\right) + \beta_L \delta\left(z\right)$. Therefore, Eq. (51) can be solved for the reflectivity curve [89]

$$R(Q) \approx \frac{16\pi^2}{Q^4} \left[\beta_L^2 + \left(\beta_L - \beta_S\right)^2 - 2\beta_L\left(\beta_L - \beta_S\right)\cos\left(LQ\right)\right] . \tag{52}$$

Therefore, the specular reflectivity spectrum R(Q) is a sinusoidal function, decaying with Q^{-4} and the period of the oscillations is related to the thickness of the layer by, ΔQ$= 2\pi$/L [89].

However, in practice the SLD β at the boundary diffuses and the roughness at the surface or interface is modeled as a Gaussian function. Therefore, the

derivative of the depth profile is also a Gaussian [89],

$$\frac{d\beta}{dz} = -\frac{\beta_i}{\sigma\sqrt{2\pi}} \exp\left(-\frac{z^2}{2\sigma^2}\right) \tag{53}$$

and using Eq. (50), Eq. (53) and the convolution theorem the reflectivity is predicted to be [89]

$$R(Q) \approx \frac{16\pi^2\beta_i^2}{Q^4}\left[\frac{5}{4} - \cos(LQ)\right]\beta_i \exp\left(-\frac{Q^2\sigma^2}{2}\right), \tag{54}$$

where β_i becomes β_L if the roughness occurs at the air/layer interface and β_i becomes β_S if the roughness occurs at the layer/substrate interface. The reflectivity R(Q) will decay more rapidly with increasing Q compared to smooth surfaces and interfaces.

All the XRR measurements in this work were performed using a PANalytical high resolution diffractometer operated at 45 keV and 40 mA. A hybrid monochromator (2xGe(220)) which offers a well-collimated beam of monochromatic Cu Kα_1 radiation (1.5406 Å) with a 1/32^0 divergence slit were used in the incident beam optics and a Soller slit of 0.04 rad with parallel plate collimator (0.27^0) and Xe proportional detector were used in the diffracted beam path. A Programmable (pneumatic) Ni beam attenuator was attached to the front of the Xe proportional detector to avoid overloading the detector at high intensities. With this geometry, the spectrum of the reflected intensity versus incidence angle was measured. The reflectivity spectrum (R) vs Q =(4π/λ)sinθ for a GeO_2 layer on Ge substrate is shown in Fig. 22 with the theoretical model curve (solid line). The area corrections (known as foot-print correction) have been made at incident angles (θ_i) smaller than the critical angle (θ_c), where the irradiated area exceeds the sample

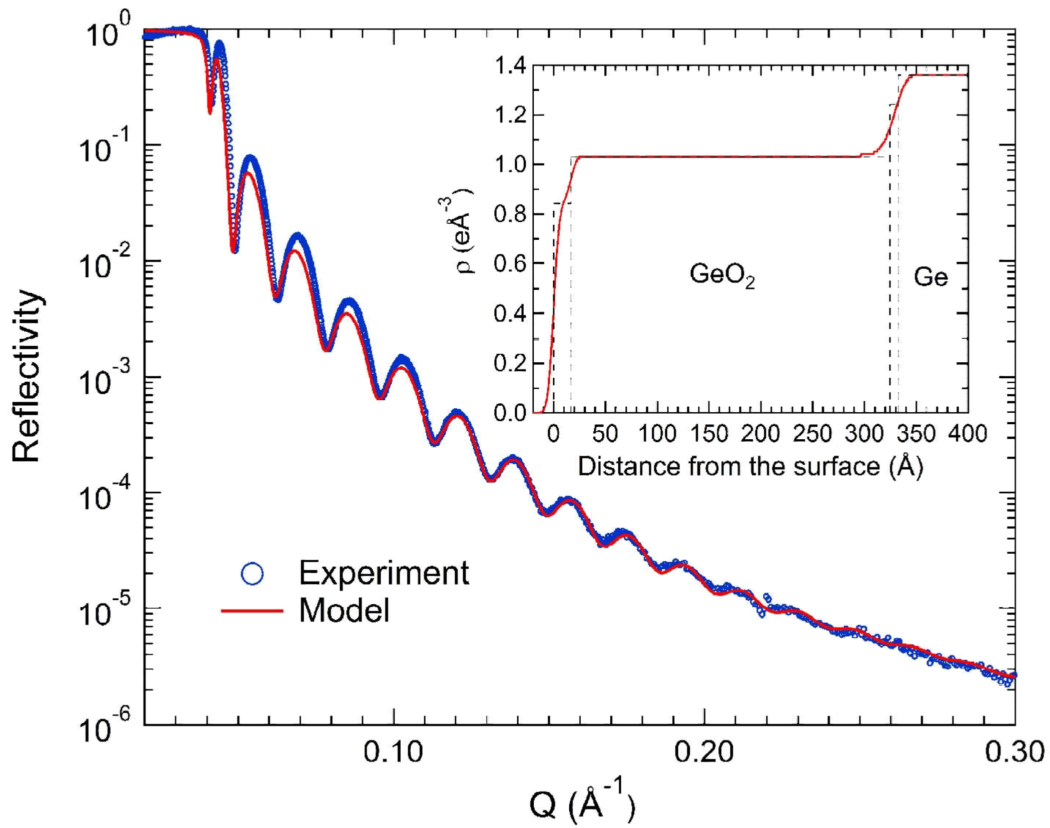

Figure 22: X-ray reflectivity spectrum of a 33 nm thick GeO_2 layer on Ge (○: experimental data, line: model). Electron density profile versus depth obtained from the model for the same sample is shown in the inset (this work).

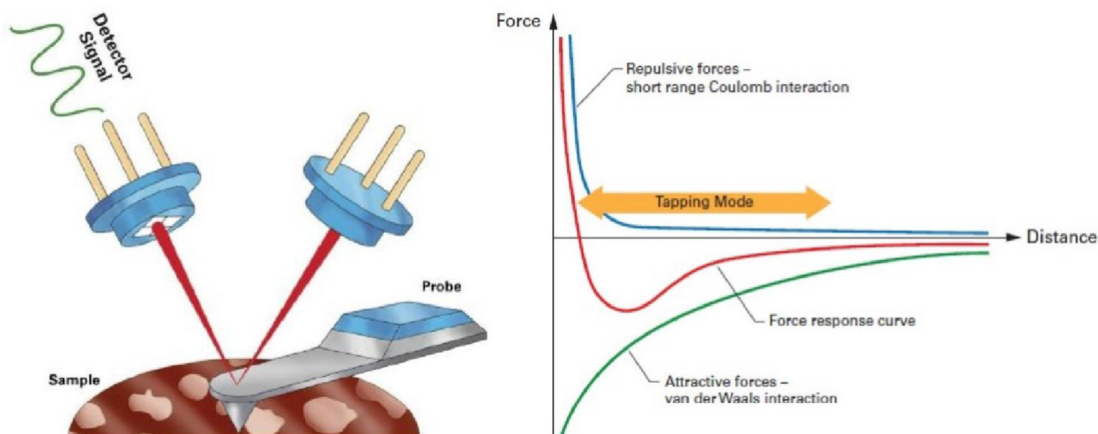

Figure 23: Left: Schematic of an AFM detection system, showing the laser beam (light source), tip, cantilever, and photodiode detector. Right: The force between the tip of the oscillating cantilever and the surface as a function of the distance between them [93].

size, assuming that the relative reflectivity must be equal to 1 due to total external reflection. A simple layer model GeO_2/Ge was used to model the reflectivity spectrum. The calculated reflectivity was fitted with the experimental data using the Parratt's recursion formula [90] implemented in the Motofit package [91] in IGOR Pro [92] analysis program.

3.6 Atomic force microscopy

Atomic force microscopy (AFM) is a powerful surface analytical tool widely used in materials science to obtain topographical images, chemical, mechanical, and magnetic properties of sample surfaces down to molecular/atomic level resolution [94, 95]. A sharp tip attached to a cantilever, scanned across the surface of the sample as shown in Fig. 23. The interaction between the tip and the surface causes cantilever to deflect towards or away from the surface. A variety of interactions are present between the surface and the tip, depending on the distance between them. For an example, if the tip is very close (a few Å) to the

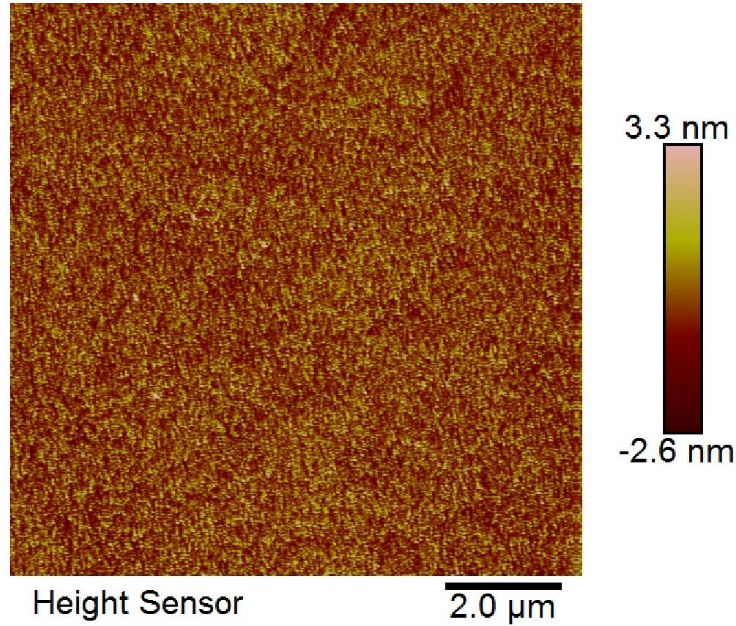

Figure 24: Atomic force microscopy image of the $Ge_{89}Sn_{11}$ on Ge surface showing an RMS roughness of 0.8 nm (this work).

sample surface, a very strong repulsive force will occur between the tip and the surface, due to the overlapping of the electronic orbitals. When the tip is at a few nanometers away from the surface, the Van der Waals interactions cause an attractive force between the tip and the surface (see Fig. 23). The deflection of the cantilever, caused by the forces between the tip and the sample surface, is monitored by a laser and a photodiode detector array to generate a topographical image of the surface. Laser and photodiode provide excellent spatial resolution and high sensitivity in two dimension.

AFM imaging can be performed in different modes: contact mode and (non-contact) tapping mode. In contact mode imaging, the deflection of the cantilever is kept fixed during the scan. The scanning is highly influenced by frictional and adhesive forces. The drawback is that high forces exerted on the surface can cause damage to the sample, resulting in a distorted image. In tapping mode

operation, the tip is oscillated and touches the surface only for a short period of time, avoiding a large lateral force and drag across the sample surface. Tapping mode provides better image resolution with no surface alternation [93].

A Bruker FastScan Dimension AFM system with a TESPA probe in non-contact tapping mode was used to characterize the sample surfaces. AFM scans were performed across a 10×10 μm^2 area of the samples, the scans were repeated on multiple areas of a given sample in order to verify the surface morphology. Figure 24 shows a 10×10 μm^2 area AFM image of a $Ge_{89}Sn_{11}$ on Ge sample. The color scale on the right of the figure represents the height of the structures on the sample surface and the surface morphology of the $Ge_{89}Sn_{11}$ is described by the root mean square (RMS) roughness.

4 Optical constants of germanium and thermally grown germanium dioxide from 0.5 to 6.6 eV via a multi-sample ellipsometry investigation

Timothy N. Nunley, Nalin S. Fernando, Nuwanjula Samarasingha, Jaime M. Moya, Cayla M. Nelson, Amber A. Medina, Stefan Zollner

Department of Physics, New Mexico State University, MSC 3D, P.O. Box 30001, Las Cruces, NM 88003-8001, USA

4.1 Abstract

Thermal GeO_2 oxides up to 136 nm thickness were produced by annealing Ge wafers in pure oxygen at 550°C and 270 kPa pressure for up to ten hours. The oxidation kinetics followed the Deal-Grove Law. Using multi-sample spectroscopic ellipsometry of a series of five thermal oxides with different thicknesses, the complex dielectric functions of Ge and GeO_2 were determined from 0.5 to 6.6 eV, for thin-film metrology applications in Ge-based microelectronics and photonics. The dispersion of the GeO_2 layer was modeled with a simple Tauc-Lorentz oscillator model, but a more complicated dispersion with eight parametric oscillators was required for Ge. A reasonable fit to the ellipsometric angles could be obtained by assuming that all thermal oxides can be described by the same dielectric function, regardless of thickness, but a slight improvement was achieved by allowing for a lower density oxide near the surface of the thickest films. The authors compare their results with literature data for Ge and bulk and thin-film GeO_2.

4.2 Introduction

Optical constants (complex refractive index n, complex dielectric function ϵ, reflection and absorption coefficients R and α) of materials are of great importance for optical metrology in the semiconductor industry [96, 97]. A high-performance complementary-metal-oxide-semiconductor (CMOS) process flow with eleven layers of metal requires about 75 photolayers and may contain up to 100 thickness measurements, most of them performed using spectroscopic ellipsometry [98]. This technique has been described in various books with increasing levels of sophistication [76, 99, 100, 101].

Since most microelectronic devices are built on a Si wafer, the optical constants of Si and SiO_2 are the most important ones and have been determined with greater accuracy than other materials [82]. They are often referred to as *Woollam silicon* and used almost universally for thickness measurements in factories around the world. For many materials, optical constants have been tabulated by Palik [102] and Adachi [103]. Optical constants of intrinsic materials are related to their vibrational and electronic properties [18, 104, 105, 106, 107].

Optical constants are determined using different techniques: Below [108] or near [109, 110] the band gap of a semiconductor, the absorption coefficient α and refractive index n are determined using transmission and minimum-deviation prism [111] measurements, respectively. These techniques (and data resulting from them) are still the most useful today and have not been replaced by more modern methods, such as spectroscopic ellipsometry, which is not suitable for measuring small absorption coefficients below about 10^3 cm^{-1} see Refs. [112, 113]. Above the band gap, transmission measurements on thin films can be successful [114]. Since about 1960, the complex dielectric function above the band gap has

been determined by reflectance followed by Kramers-Kronig transformation, [115] but such results are often plagued by systematic errors due to surface overlayers (including surface roughness) and the limited spectral range of the measurement.

More recently, the optical constants of semiconductors have been determined by spectroscopic ellipsometry. Early instrument designs suffered from the rotating-analyzer artifact [30, 116] and could not measure small absorption coefficients accurately. This accuracy was improved by instruments employing a polarization modulator [83] or a computer-controller Berek waveplate compensator [82]. Even the most precise spectroscopic ellipsometers are unable to compete with transmission or minimum-deviation prism measurements to determine the optical constants below the band gap. We note that transmission measurements must be performed using two-side polished wafers, while ellipsometry measurements are better taken on single-side polished wafers, because reflections from a polished (or insufficiently roughened) back surface interact incoherently with the reflection from the front surface, thus causing depolarization of the reflected light beam [76].

Ellipsometry measurements on bulk semiconductors are difficult to interpret because semiconductor wafers are usually covered by native oxides and have a slightly rough surface. Modeling ellipsometry data from a real semiconductor surface requires precise knowledge of the optical constants of the substrate (for example, Ge), the surface layer (native oxide and roughness), and the thickness of the surface layer. There are too many unknowns in the model to determine all of them in measurements of a single sample.

Aspnes and Studna [116] addressed this problem for Ge by minimizing the surface layer thickness with wet chemical etching (using a bromine solution in methanol, buffered hydrofluoric acid, followed by a water rinse) and thus optimizing the height of the absorption near the E_2 critical point at 4.26 eV. They

achieved an $<\epsilon_2>$ peak value of 30.6 at 4.26 eV, which is still only a lower bound for the true value of ϵ_2 for Ge at this energy because it was not corrected for the oxide or roughness layer. Cleaving a bulk Ge crystal in ultra high vacuum [117] or cleaning the surface through ion bombardment [80] followed by annealing to produce clean 2×8 or 2×1 reconstructed surfaces also introduces uncertainties because of the distortion of the polarization state by windows [76] and because of surface roughness, ion bombardment damage, and epioptical effects, which make the optical constants dependent on surface orientation [118] or surface passivation.

A different approach was taken by Jellison [83]. whose intent of wafer cleaning was to remove carbon-based surface contamination (with acetone, methanol, and peroxide, followed by a water rinse), but not the surface oxide itself. The thickness of the remaining stable native oxide was then determined with an ellipsometric measurement slightly above the direct band gap, where the absorption of Ge is small. This is known as the Jellison-Sales method for transparent glasses [119]. It works well, if the optical constants of the surface overlayer are known precisely, but fails otherwise. Jellison found an ϵ_2 peak value of 31.8 at 4.24 eV, slightly higher than the result from Aspnes and Studna [116] because of the native oxide layer correction.

Finally, Herzinger *et al.,* [82] describe a method to determine the optical constants of semiconductors, if the optical constants of the substrate, those of the oxide overlayer, and the layer thickness are all unknown. This method requires a series of samples consisting of the same substrate and the same oxide, where only the oxide thickness is varied. Ellipsometry measurements of several such samples with oxide thicknesses ranging from very thin (only native oxide) to as thick as possible (limited by the rate of oxidation) yield the optical constants of the substrate, those of the oxide, and the thicknesses of all layers. The only assumption

used by this method is that the optical constants of the oxide do not vary with thickness (or from one sample to another). The validity of this assumption can be checked by inspecting the goodness of fit for all samples.

This method has only been used for Si so far [82], where uniform and repeatable thermal oxides with arbitrary thicknesses are easily produced with well established silicon manufacturing techniques [120]. It has led to universally accepted values for the optical constants of Si (100) and its thermal oxide [82]. The purpose of this paper is to use the same method to determine the optical constants of bulk Ge with a (100) surface orientation and those of thermally grown GeO_2. Precise knowledge of Ge optical constants is important for the development of Ge-based p-type metal-oxide-semiconductor (PMOS) devices, which have attracted much attention recently [121]. The optical constants of thin Ge layers may, of course, be different from those of bulk Ge, but that is beyond the scope of this article.

This article is organized as follows: We first describe our experimental methods to clean the Ge substrate, prepare thermal GeO_2 oxides, and ellipsometry data acquisition and analysis. Next, we present our results for GeO_2 on Ge in a three-phase (ambient/oxide/substrate) model, followed by a discussion if this model can be improved by including a thin interfacial layer between the GeO_2 and the substrate or by allowing the GeO_2 refractive index to vary between samples. Finally, we discuss our overall results and compare our findings to previous data.

4.3 Thermal oxidation of Ge

As-received Ge bulk wafers were cleaved into 20×20 mm^2 pieces. These pieces were then subjected to an ozone clean in a Novascan PSD Pro series digital UV ozone system utilizing a Hg vapor lamp. This clean was performed in an oxygen-

enriched environment, achieved by allowing ultrapure (99.98%) oxygen to flow through the system for several minutes before sealing the chamber with the Hg lamp on and the sample on a heating stage held at 150°C for 60 min, followed by a 30-minute period of incubation with the lamp off and the sample cooling to room temperature. After the ozone clean, samples were cleaned ultrasonically for 20 min in deionized water, followed by 20 min in isopropanol.

The intent of this hybrid dry/wet clean is to remove carbon-containing surface contaminants from the wafer and reduce the native oxide thickness, but leave a thin stable oxide on the wafer [83] as a seed oxide for thermal oxidation. Unlike Ref. [78], we did not use harsh chemicals (bromine or hydrofluoric acid) before oxidation to avoid roughening or contaminating the surface. Some elements of our clean, especially the use of reactive oxygen species, are similar to those of Ref. [122]. Photoemission studies have shown that exposure to UV light leads to a predominance of the Ge^{4+} oxidation state [123].

After cleaning, the samples were placed in an ULVAC-RIKO MILA-5000 infrared lamp heating system for rapid thermal annealing. Samples were annealed in ultrapure oxygen with 170 kPa gauge pressure (270 kPa absolute), as measured by the gas regulator, at 1 L/min flow at 550°C for several hours, as needed to achieve the desired oxide thickness [78]. Table 2 lists the annealing times for several samples as well as their thicknesses and other parameters.

GeO_2 is hygroscopic and water soluble [124]. Therefore, ellipsometry measurements were performed within a few days after oxidation. Furthermore, thermal GeO_2 desorbs by reaction with the Ge substrate and diffusion of oxygen vacancies generated at the Ge/GeO_2 interface [125]. Higher oxidation temperatures and lower oxygen pressures promote GeO_2 desorption. We selected an oxidation temperature of 550°C, because it allows a suitable thermal oxide growth rate with

minimal oxide desorption and lowest interface trap density [126, 127, 128]. The oxidation pressure of 2.7 atm also enhances oxidation and suppresses thermal oxide desorption, compared to atmospheric pressure [124].

The resulting GeO_2/Ge layers were brown*, yellow-brown, and light blue* in appearance *(with increasing thickness)*, with reasonably uniform thickness and occasional spots. Optimizing the clean was crucial to the success of our annealing experiments. We found that thermal oxidation (see Table 2 and Fig. 25) follows the Deal-Grove model [120]

$$d^2 + Ad = B\,(t + \tau)\,, \tag{55}$$

where d is the oxide thickness (determined from ellipsometry as described below), t the oxidation time, and A, B, and τ are parameters that depend on the oxidation conditions, such as temperature, pressure, and gas composition. As shown by the dashed lines in Fig. 25, the oxide thickness depends nearly quadratically on oxidation time, i.e., $d^2 \approx B\,(t + \tau)$. Including the linear term Ad (solid line) becomes important for thinner oxides and higher pressures. The oxidation is much faster at higher pressure.

We characterized our layers using grazing-incidence x-ray reflectance (XRR) as shown in Fig. 26. These XRR spectra show a double critical angle for the Ge substrate (1.35 e/Å^3 density) and the GeO_2 layer with a lower density (1.03 eV/Å^3). *The* interference fringes (if present) indicate uniform oxide layers with a well-defined electron density. We could only find such fringes for the thinner oxide layers, where XRR thickness and ellipsometry thickness agree to within 1 nm (which could be explained with surface roughness). From fitting the XRR spectra for thinner oxides, we are able to determine the electron density as a function of

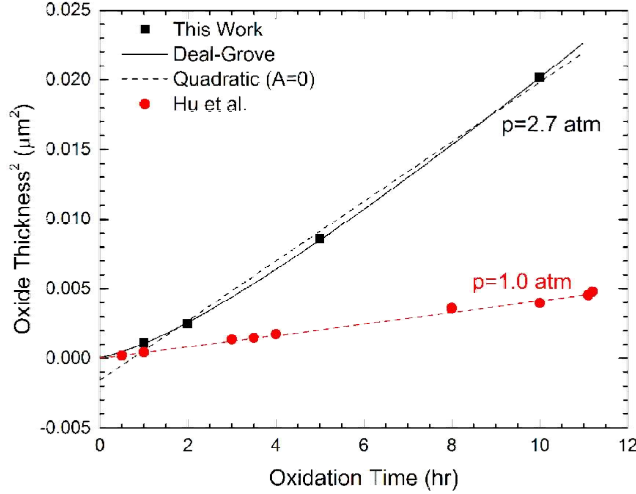

Figure 25: Thermal oxide thickness versus oxidation time at atmospheric pressure (Ref. [78]) and at 2.7 atm (this work). The solid line shows the best fit to Eq. (55), while the dashed lines assume a quadratic dependence of the thickness on oxidation time (A=0).

depth, also shown in Fig. 26. Thicker oxide layers do not show interference fringes, perhaps due to thickness non-uniformity or a density gradient in the oxide.

Symmetric ω-2θ powder x-ray diffraction scans on a sealed-tube instrument with 1.8 kW power are similar for all samples and only show background and the 2×Ge(002) and Ge (004) substrate peaks. We did not find the amorphous GeO_2 diffraction peak at 2θ=25° seen on rf sputtered GeO_2 films [129], which were up to 100 times thicker than our thermally grown oxides. Unpolarized Raman spectra with 532 nm laser excitation are similar for all of our samples and only show first- and second-order Raman peaks from the Ge substrate and no significant peaks that might be attributed to GeO_2. FTIR ellipsometry and transmission results to investigate the infrared active phonons of these oxides will be discussed elsewhere.

Table 2: List of GeO_2 oxides produced by thermal oxidation of Ge substrates at 2.7 atm oxygen pressure at 550°C. d is the oxide thickness from ellipsometry, t the oxidation time, Δd the relative thickness non-uniformity determined from the ellipsometry depolarization spectra, d_{XRR} the thickness determined by x-ray reflectance (XRR) (samples 4 and 5 were fit with a fixed thickness), and $<\rho>$ the electron density determined by XRR. Ellipsometry results are from two models (uniform and graded) as discussed in Sec. 4.5 (MSE=14) and 4.6 (MSE=6.9). Probable errors are given in parentheses.

		Uniform		Graded			
No.	t (hr)	d (nm)	Δd (%)	d (nm)	Δd (%)	d_{XRR} (nm)	$<\rho>$ (e/Å^3)
1	0	2.31(1)	NA	2.31(1)	NA	NA	NA
2	1	34.01(3)	8.0(2)	35.32(2)	6.0(1)	33.3	1.03
3	2	52.18(3)	6.0(1)	53.31(2)	6.0(1)	50.2	1.03
4	5	88.62(5)	8.0(2)	92.11(5)	7.0(1)	92.5(f)	1.00
5	10	135.94(6)	1.5(1)	141.69(5)	1.0(1)	142(f)	1.01

Table 3: Deal-Grove parameters A, B, and τ from Eq. (55) for thermal oxidation of Ge in pure O_2 at temperature T and pressure p. Probable errors are given in parentheses.

T (°C)	p (kPa)	A (nm)	B (nm^2/hr)	τ (hr)	
550	100	0	432	0	From Ref. [78]
550	270	90(37)	3225(440)	0.22(32)	this work

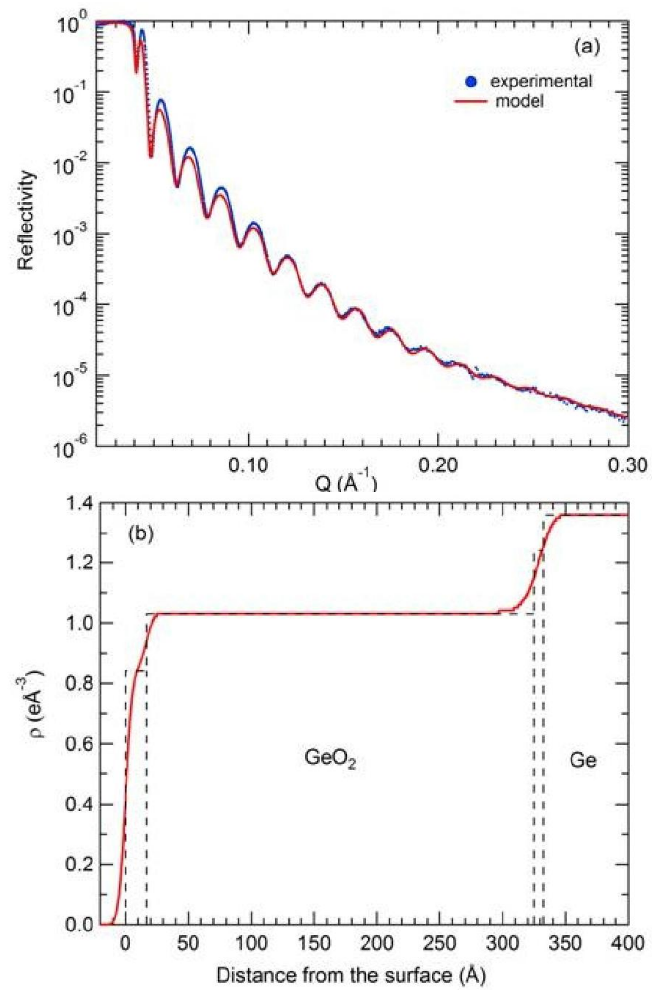

Figure 26: (a) Grazing-incidence x-ray reflectance spectrum (red: model; blue: data) and (b) electron density versus depth for sample 2 (33 nm thickness).

4.4 Ellipsometry measurements and data analysis

We acquired the ellipsometric angles ψ and Δ and the depolarization spectra from 0.5 to 6.6 eV with 0.01 eV steps on a J.A. Woollam vertical variable-angle-of-incidence rotating-analyzer ellipsometer with a computer-controlled Berek wave-plate compensator [130]. To reduce experimental errors, all data were obtained by averaging two-zone measurements with equal and opposite polarizer angles. Data were acquired for four angles of incidence (ϕ_0=60°, 65°, 70°, and 75°). Larger incidence angles would be desirable to have data near the Brewster regime for bulk Ge, but such measurements are not practical because of the finite sample size and nonuniform oxide thickness. The magnitude of the polarizer angle was kept equal to ψ at each wavelength, but no less than 5°. The time needed to acquire data for one sample was several hours.

Monochromatic light was produced by an HS-190 double monochromator equipped with three sets of gratings for the near-infrared (NIR), visible (VIS), and quartz-ultraviolet (QUV) portion of the spectral range. The linear dispersion of the monochromator is 2.3 nm/mm in the VIS/QUV and 4.6 nm/mm in the NIR, leading to spectral bandwidths of no more than 4 and 8 nm, respectively, for a maximum slit width of 1.7 mm.

For the spectral range from 0.76 to 6.6 eV, we used a UV-enhanced optical fiber and a 75 W Xe short-arc lamp (Hamamatsu L10873) to produce the incident monochromatic beam. We also measured from 0.5 to 3.0 eV using an IR-enhanced optical fiber and a 100 W quartz-tungsten-halogen lamp (Ushio, with a TDK-Lambda ZUP20-20 power supply), also mounted on the HS-190 monochromator using a slightly modified reflector insert capable of holding and powering the tungsten lamp. This IR setup slightly extends the spectral range downward to

0.5 eV and avoids the strong peaks of the Xe lamp and the opaque region of the UV fiber from 0.88 to 0.92 eV. Data obtained with both setups were merged and showed good agreement in the region of spectral overlap. As one might expect, only the Ge wafer with the thinnest (native) oxide layer showed a slightly unstable oxide due to ongoing oxidation.

The ellipsometric angles (ψ and Δ) and the Fresnel reflectance ratio $\rho = e^{i\Delta} \tan \psi$ are related to the pseudo-refractive index $<n>$ and the pseudo-dielectric function $<\epsilon>=<n>^2$ of the sample through [76, 99]

$$\rho = \frac{(\langle n \rangle \cos \phi_0 - \cos \phi_1)(\cos \phi_0 + \langle n \rangle \cos \phi_1)}{(\langle n \rangle \cos \phi_0 + \cos \phi_1)(\cos \phi_0 - \langle n \rangle \cos \phi_1)}, \tag{56}$$

where ϕ_0 is the angle of incidence and ϕ_1 the angle of refraction. For an ideal sample without surface overlayers, $<n>$ and $<\epsilon>$ are equal to the refractive index n and the dielectric function $\epsilon = n^2$. The ellipsometric angles for a sample consisting of one or more layers on a substrate can be calculated if the optical constants for all materials are known (or assumed to follow a model) [76, 99, 100, 101].

The complex dielectric function ϵ for an amorphous oxide like thermally grown GeO_2 is usually described by the Tauc-Lorentz model, where the imaginary part of ϵ as a function of photon energy E is given by [76, 100, 131]

$$\epsilon_2(E) = \frac{A E_0 \Gamma (E - E_g)^2}{E\left[(E^2 - E_0^2)^2 + \Gamma^2 E^2\right]} \tag{57}$$

for $E > E_g$ and vanishes below E_g. The real part is obtained by Kramers-Kronig transform. This model contains the following parameters: E_g is the Tauc gap, the onset of absorption. The Lorentz oscillator [132] resonance energy is E_0, its

amplitude A, and its broadening Γ.

In addition, we use two poles [99] (unbroadened Lorentz oscillators)

$$\epsilon(E) = \frac{A}{E_0^2 - E^2} \tag{58}$$

(where the resonance energies are often chosen arbitrarily as 0.01 and 11 eV) to describe the influence of absorption peaks below or above our spectral range on the dispersion. For crystalline, tetragonal (rutile) GeO_2, the dominant transverse optical phonon modes for the ordinary (E_u) and extraordinary (A_{2u}) beams have energies of 41 and 65 meV, respectively [133]. Glassy germania [134, 135] also has a significantly higher IR absorption band located at 111 meV. An IR pole at 0.05 eV was chosen for our model.

Finding a parametric model for semiconductors like Ge with a finite number of adjustable parameters requires some thought. In principle, the analytical properties of the complex dielectric function imply that it can be written as a product defined by its poles and zeroes in the complex plane, which can be approximated as a sum of Lorentzians. Seven Lorentzians [136] are sufficient to fit ϵ for GaAs between 1.5 and 5.0 eV, but more terms are needed outside of this range. More flexibility can be introduced by allowing Lorentzians with a complex amplitude [132].

A different approach was taken by Aspnes [137], who calculated the absorption of semiconductors assuming parabolic bands and constant dipole matrix elements. This critical-point parabolic-band model gives a good description of the derivatives of the dielectric function, but fails to describe ϵ away from the critical point singularities, where the nonparabolicity and the $\vec{k}$-dependence of the dipole matrix element have to be taken into account [138].

More general models for ϵ can be constructed from the superposition of critical point structures, which are composed of continuous polynomial sections with Gaussian broadening [82, 138, 139]. The details of such models are complicated and not relevant for our work, but they describe the dispersion of the dielectric function and its derivatives in a Kramers-Kronig-consistent fashion with a reasonable number of parameters (about 40, compared to 1200 values for ϵ). To be specific, we describe ϵ for Ge with the Herzinger-Johs parametric oscillator model [139] as implemented in the WVASE32 software package [130]. We also included a UV pole at 11 eV, but no IR pole because IR lattice absorption is weak for a nonpolar material like Ge [108]. The number of free parameters can be reduced by keeping some of the shape parameters for Ge the same as those chosen previously [139] for GaAs.

Quoting from Ref. [132], no attempts are made to give a physical meaning to the models. We use them primarily to achieve a flexible Kramers-Kronig-consistent description of the dispersion of real materials with a manageable number of parameters. In some cases, fit parameters such as energies or broadenings are related to actual materials properties (such as band gaps), but such agreement is often accidental and should not be over-interpreted. Only the dispersion of the complex dielectric function and the layer thicknesses are actual outcomes of our fit, but none of the oscillator parameters in this analysis.

Once the model has been built, one varies the parameters using the Levenberg-Marquardt algorithm to minimize the mean-squared error

$$\mathrm{MSE} = \sqrt{\frac{1}{3N-M}\sum_{i=1}^{3N}\left|\frac{\rho_i^{\mathrm{mod}}-\rho_i^{\mathrm{exp}}}{\Delta\rho_i^{\mathrm{exp}}}\right|^2}, \tag{59}$$

where N is the number of data points (all photon energies, incidence angles, and samples), M the number of parameters, ρ_i^{exp} the three experimental quantities (ellipsometric angles ψ and Δ and depolarization) at each data point, ρ_i^{mod} the quantities calculated from the model, and $\Delta\rho_i^{\text{exp}}$ the experimental errors.

4.5 Results for GeO_2 on Ge with uniform layer fits

The ellipsometric angles and the depolarization for all five Ge/GeO_2 samples were acquired from 0.5 to 6.6 eV as described earlier. This results in ten data sets in the NIR/VIS and VIS/QUV spectral range. All data were loaded into our software and fitted simultaneously.

Figures 27 and 28 show the ellipsometric angles and the pseudodielectric function $<\epsilon>$ for the sample with the thinnest oxide layer (about 2 nm native oxide). Two data sets from 0.5 to 3.0 eV and from 0.76 to 6.6 eV taken on the same day, but under slightly different conditions, were merged in these figures. The differences between the two data sets are no more than 2% of $<\epsilon>$. Most likely, these differences are due to slight non-uniformity across the wafer surface or due to changes in surface conditions between the measurements. The depolarization for this sample is below 0.4% (except at the extreme ends of the spectral range due to noise) and peaks near 3.5 eV. There is no sign of depolarization due to backside reflections below the indirect band gap [110] (E_i=0.66 eV).

The ellipsometric angle ψ is largest for ϕ_0=60° and decreases towards larger incidence angles, see Fig. 27. ψ becomes zero at the Brewster angle (76° for Ge at 2.5 μm). ψ increases gradually towards larger photon energies. The E_1, $E_1+\Delta_1$, E_0, E_2, and E_1 critical points [30] are clearly visible. Δ is near 180° in the IR and drops towards larger photon energies, as the absorption increases. There is a

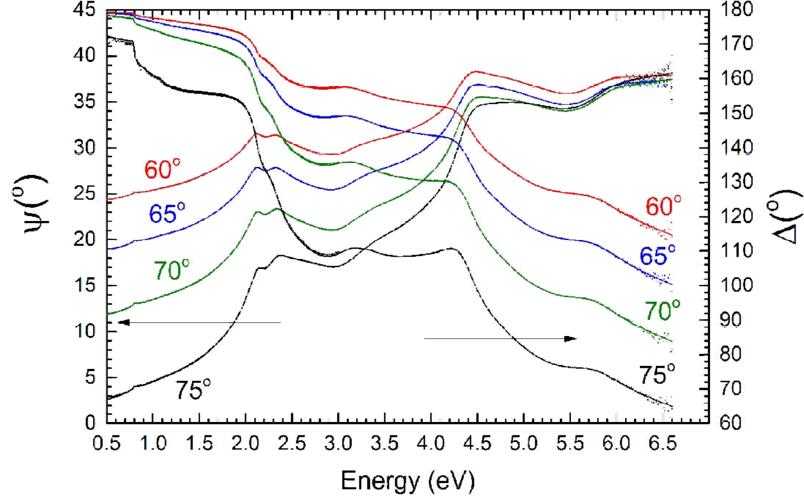

Figure 27: Ellipsometric angles ψ and Δ (symbols) at four angles of incidence (60°, 65°, 70°, 75°) for a Ge wafer with native oxide, after the standard clean described in Sec. 4.3. Two data sets from 0.5 to 3.0 eV and from 0.76 to 6.6 eV were merged. Lines: Data calculated from our model.

sharp drop near the direct gap E_0=0.8 eV and additional drops at critical points with higher energies. Δ also decreases with increasing ϕ_0.

Below the direct gap, Δ should be 180° in the absence of a surface layer, because the absorption nearly vanishes. Instead, $\Delta \approx 170°$ for ϕ_0=75° below 0.8 eV. For both Ge and GeO_2, the refractive index at 2.5 μm (in the transparent region) is fairly well established as 4.07 (Ge) and 1.57 (GeO_2), respectively [102, 111, 140, 141]. Therefore, we are able to calculate that the native oxide thickness for this sample must be about 23 Å. This native oxide thickness is consistent with our peak value of $<\epsilon_2>$=22.6 near 4.2 eV, see Fig. 28, considerably below the literature peak values [116, 83] of 31−32 for bare Ge. We therefore fix the native oxide thickness at 23 Å for our initial fits of sample 1.

Figures 29, 30, and 31 show the ellipsometric angles and depolarization spectra for Ge wafers with thermally grown oxides of 34, 89, and 136 nm thickness. For the

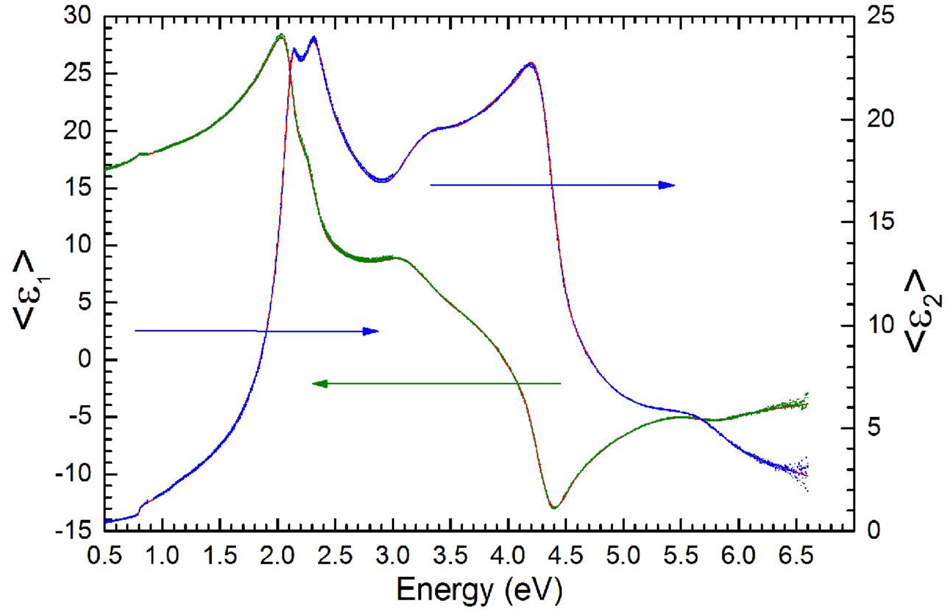

Figure 28: Same data as in Fig. 27 for four angles of incidence, but displayed as a complex pseudodielectric function with real part $<\epsilon_1>$ (green) and imaginary part $<\epsilon_2>$ (blue). Data from our model are shown in red.

34 nm sample, ψ shows a strong interference fringe near 4.8 eV, while the 89 nm sample shows two interferences fringes at 2.5 and 6.0 eV. The thickest (136 nm) sample shows three interference fringes. At the same energies as the ψ fringes, we also see maxima in the depolarization, which can become quite strong (up to 40%). We model the depolarization with a constant monochromator bandwidth of 4 nm and by selecting a thickness nonuniformity (see Table 2) to match the magnitude of the largest depolarization peak in the UV [142]. Small lateral variations of the refractive index have the same effect as thickness nonuniformity.

Even at 6.1 eV, the ψ interference fringes are still quite strong, indicating that the absorption coefficient of GeO_2 is still small at this energy. The magnitude of the ψ fringes is significantly influenced by depolarization. For example, for the same absorption coefficient (3×10^4 cm^{-1} at 6.1 eV), the peak value of ψ would be 76° for an ideal situation (without depolarization), but this peak is reduced to

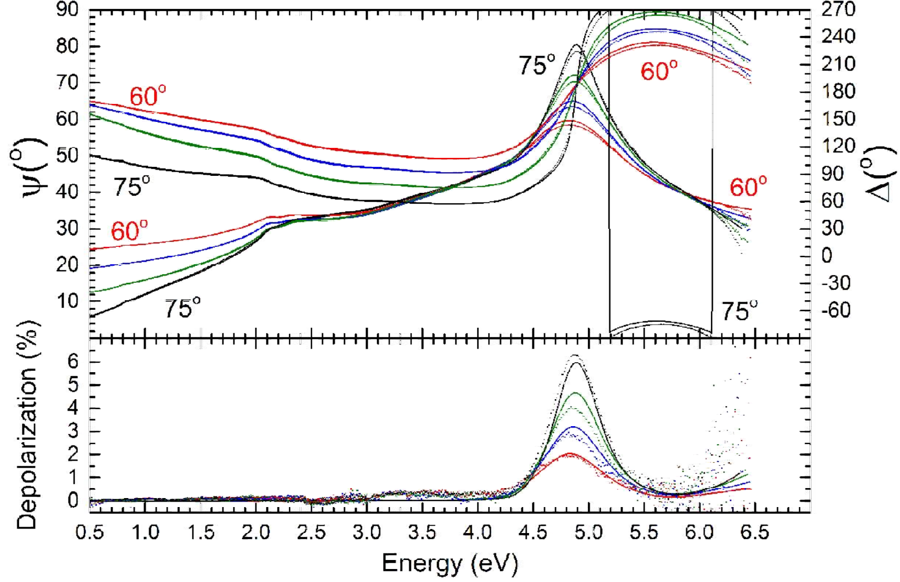

Figure 29: Ellipsometric angles (ψ, Δ) and depolarization (symbols) for 34 nm GeO_2 on Ge. Our model with a uniform oxide (lines) is nearly indistiguishable from the experimental data.

63−65° under non-ideal (depolarizing) conditions for our films and experimental setup. Depolarizing effects therefore make it difficult to place an exact value on the absorption coefficient of GeO_2.

We are finally ready to start the fit, using the Tauc-Lorentz parameters fitted to the GeO_2 optical constants [78, 140] and parametric oscillator parameters for Ge from the WVASE32 software as starting values. The shape parameters for the E_0, $E_0 + \Delta_0$, E_1, and $E_1 + \Delta_1$ critical points were fixed at the same values as for GaAs. We also fixed Δ_0=0.297 eV and the broadenings for E_0 (10 meV) and $E_0 + \Delta_0$ (20 meV) based on historical transmission measurements [143].

The material parameters obtained from our best model are given in Tables S-1 and S-2 as supplemental information [144]. The dielectric functions for Ge and GeO_2 are shown in Figs. 32 and 33 and also tabulated [144] in Tables S-3 and S-4.

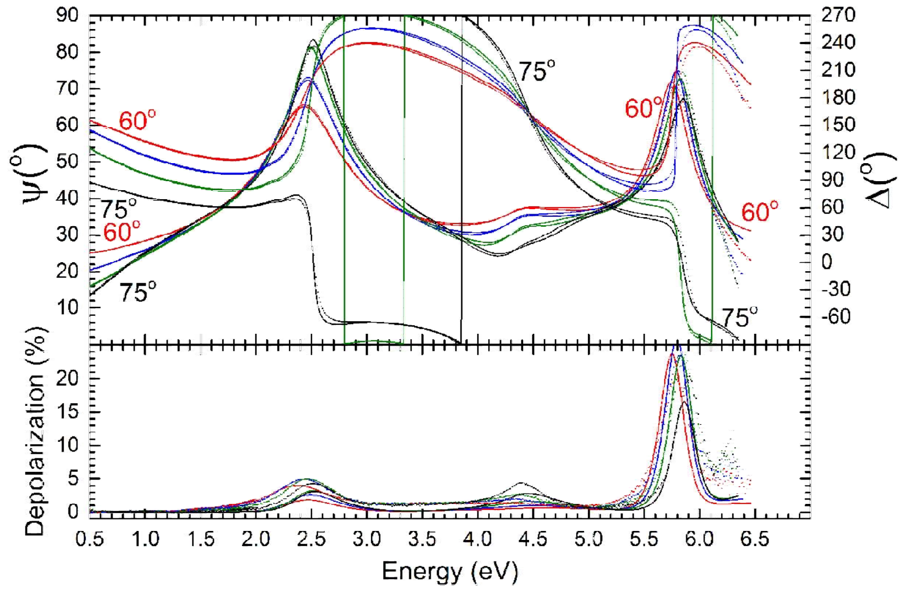

Figure 30: As Fig. 29, but for a Ge wafer with 89 nm GeO_2.

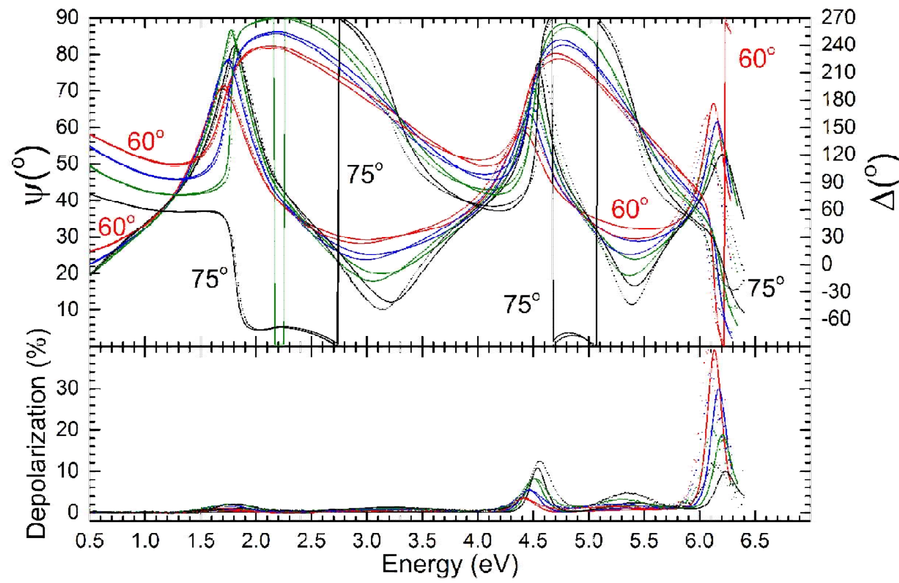

Figure 31: As Fig. 29, but for a Ge wafer with 136 nm GeO_2. The uniform layer model (lines) matches the maxima of ψ, but not the minima. This is a clear indication for a gradient in the refractive index of the GeO_2 film.

The mean-squared error (MSE) including all five samples in Table 2 was found to be 14. This means that the average deviation between data and model is about 14 times the experimental errors. Half of the MSE is from the thickest oxide layer as will be discussed later. Our model gives a near-perfect fit (MSE=0.9) for the Ge substrate with native oxide, but deviations are larger for the thicker oxides. The MSE is just slightly larger (MSE=18) for a non-absorbing model for GeO_2 using two UV poles. We suspect that the largest sources of deviation for the thicker oxide samples are the depolarization and errors in the ellipsometric angles (especially in the UV) due to thickness variations across the samples.

To estimate the accuracy of the GeO_2 optical constants shown in Fig. 33, we proceed as follows: The black lines in Fig. 34 show the best fit to all samples with a uniform Tauc-Lorentz layer for the GeO_2 oxide. This fit also determines the thicknesses of all oxides, see Table 2. Next, we only fit the 89 nm oxide with an uncorrelated all-wavelength inversion of the ellipsometric angles at fixed thickness, where Kramers-Kronig consistence is not enforced. (This is also known as a point-by-point fit.) The results of this fit are shown by symbols in Fig. 34. We then perform the same fit for another sample with 136 nm thickness and also show the results by symbols. We can see that the differences between the Tauc-Lorentz fit to all samples (assuming uniform identical oxide layers) and the single-sample point-by-point fits are quite large (up to 10% for ϵ_1). Furthermore, we see oscillations in the data, which are probably artifacts due to incomplete removal of interference fringes. Values of ϵ_2<0.1 are probably not reliable, but it appears that there is some absorption in the oxide above 6 eV. It has been reported [145] that the absorption coefficient of GeO_2 depends on the details of preparation. Therefore, it is possible that poor agreement between data and model in the deep UV are due to sample-to-sample variations, which we have ignored in our model.

4.6 Results for GeO_2 on Ge with non-uniform layer fits

Since the quality of our fit with a three-phase (ambient-film-substrate) model is only moderate (MSE=14), we discuss how the fit might be improved by adding more complexity to our model. We focus on the UV spectral region, where the discrepancy between data and model is largest. (For sample 1, the native oxide, the differences between the measured ellipsometric angles and the model are much less than 1°. The differences reach several degrees or even more for thicker oxides, especially in the UV.) First, we note that adding additional oscillators in the UV spectral region for GeO_2 (beyond the Tauc-Lorentz oscillator and poles at 11 and 0.05 eV) does not reduce the overall MSE.

Next, we allow the density of the thickest oxides to vary between the bottom and top by adding a variable-density layer on top (effective medium layer with variable thickness and variable void fraction). This reduces the MSE to 8.3 and somewhat improves the fit in the UV for the thicker oxides. The void fraction in this layer is quite low (near 20%) and the thickness large, several tens of nm. This model would also account for surface roughness as a special case (with a 50% void fraction), which does not appear to be a major factor due to the low void fraction resulting from the fit. Similar results can be obtained by describing the oxide as an effective medium, where the void fraction follows a power law with a large exponent (about 5) and reaches about 30% near the surface. Finally, our best model (MSE=6.9) adds an additional Gaussian oscillator for GeO_2 in the UV, which leads to a kink in the absorption as shown in Fig. 34.

As a generalization of this effective-medium-approximation (EMA) model, we can also describe the oxides with a graded-layer model, where the complex refractive index depends on thickness through a power law with a variable exponent.

The refractive index in such oxide models is typically about 20% lower at the surface than at the substrate/oxide interface and the exponent quite high (indicating that the low-density region is confined to the top 20% of the film).

We also added an interfacial layer with variable thickness (kept the same for all samples), which consists of a 50/50 mixture of the bulk and film optical constants described within the Bruggeman EMA. The rationale for this model is that some electrons in the bulk Ge might leak out into the oxide (have a finite probability to be located in the GeO_2 barrier). It has also been shown theoretically [146] for the Si/SiO_2 interface that the first 7-10 Å of the oxide have a different structure and density than thick oxides. Using this intermix model [82], which assumes a higher electron density near the interface than in a thick oxide, did not improve our fits and therefore we discarded this possibility.

4.7 Discussion

Since a three-layer (ambient-oxide-substrate) model with uniform GeO_2 layers gives good agreement with our ellipsometry data and cannot be improved much by introducing more complexity, we consider the results from our uniform three-layer fit the final results from this work. Results for the complex dielectric function, complex refractive index, absorption coefficient, and normal-incidence reflectance for Ge and GeO_2 as a function of photon energy and wavelength are given in Tables S-3 and S-4 of the supplemental materials [144],

The complex dielectric function of Ge from our fit together with literature results [116, 83] and an unpublished data set [130] are shown in Fig. 32. Our ϵ_2 maximum of 31.3 at 4.25 eV is between the results of Ref. [116] and Ref. [83] and slightly lower than the unpublished Nebraska result [130] of ϵ_2=32.3. Since

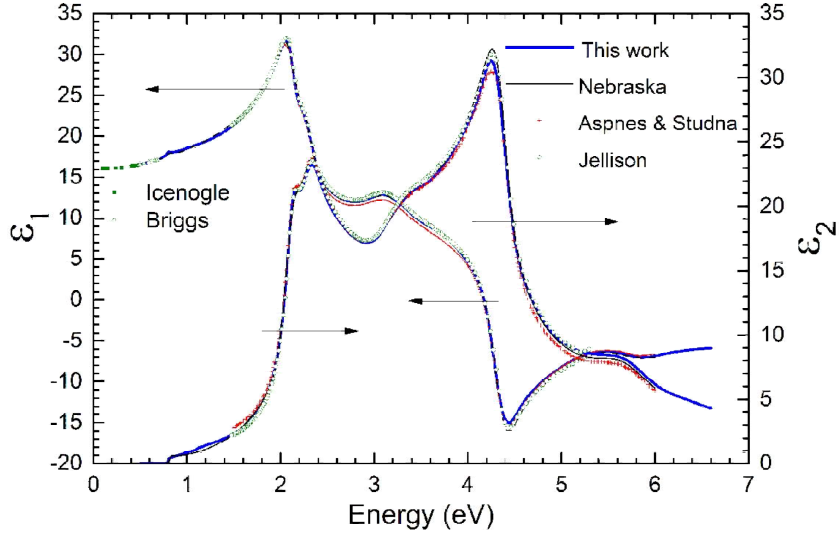

Figure 32: Complex dielectric function for Ge from a fit to our ellipsometry results in comparison with literature data [83, 102, 111, 116, 130].

we determined the oxide thickness for our thinnest sample (native oxide) using the Jellison-Sales method [119] with measurements below the Ge band gap, we believe that our results are highly accurate. At 0.5 eV, below the band gap, our refractive index n=4.07 is identical to minimum-deviation prism results [111, 102]. The maxima and minima of our spectra related to critical points and interband transitions [30] have been discussed elsewhere [81].

Figure 33 shows the dielectric function for GeO_2 from our fit in comparison with prior data [78, 140]. The results for thermal oxides produced by Hu *et al.* [78] cover the energy range from 1.5 to 5.5 eV, while Devyatykh *et al.* [140] measured bulk crystals from 0.5 to 2.5 eV using the minimum-deviation prism method.

Our value of ϵ_1 at 0.5 eV for the oxide film equals 2.4 (corresponding to n=1.55), which is about 4% lower than prior results [78, 140]. Our values do not depend much on the details of our Tauc-Lorentz model (such as the strength

of the IR pole, the Tauc gap, or including a density gradient). Therefore, it is possible that our GeO_2 oxides indeed have a lower density (resulting in a lower refractive index) than films and crystals produced by others, perhaps related to our fast high-pressure oxidation conditions (see Fig. 25). For the Si/SiO_2 system, it is known that oxides with lower density have a lower refractive index [147, 148, 149, 150]. Variations of the index of a silicate glass by 5-10% are common (even without adding heavy metals to increase the index). On the other hand, Fig. 34 also demonstrates that the accuracy of our GeO_2 refractive index measurement is only about 5%, because an oscillator fit may yield a different result than a direct point-by-point inversion. Pajasova [141] provided accurate measurements of the refractive index n for bulk glassy GeO_2 in the transparent region from 0.4 to 2.5 μm using the minimum-deviation prism measurements. She found that n decreases from 1.57 at 1 μm to 1.56 at 2.5 μm (ϵ_1=2.43), quite similar to our values.

Pajasovas [141] results for ϵ_2 of GeO_2 are less accurate, because they were obtained from Kramers-Kronig transformation of reflectance data, but they clearly indicate strong absorption peaks at 6.6 and 10.7 eV, outside of our spectral range. From measurements on RF-sputtered GeO_2 films with 0.77 to 6 μm thickness [129], the onset of strong absorption was found to be about 5.95 eV. Below the main band gap, there is an absorption peak with a magnitude of about 200 cm^{-1} centered at 5.06 eV, which was found in bulk crystals [145] as well as in thin films [129]. This peak depends on preparation conditions and disappears after annealing at high temperatures of bulk specimens or films on fused silica [129]. This below-gap absorption has been attributed to oxygen vacancies [145], which are also expected in our thermal oxides due to oxide decomposition [124]. In our absorption coefficient data derived from ϵ for GeO_2, we determine α=2$\times$10^4 cm^{-1}

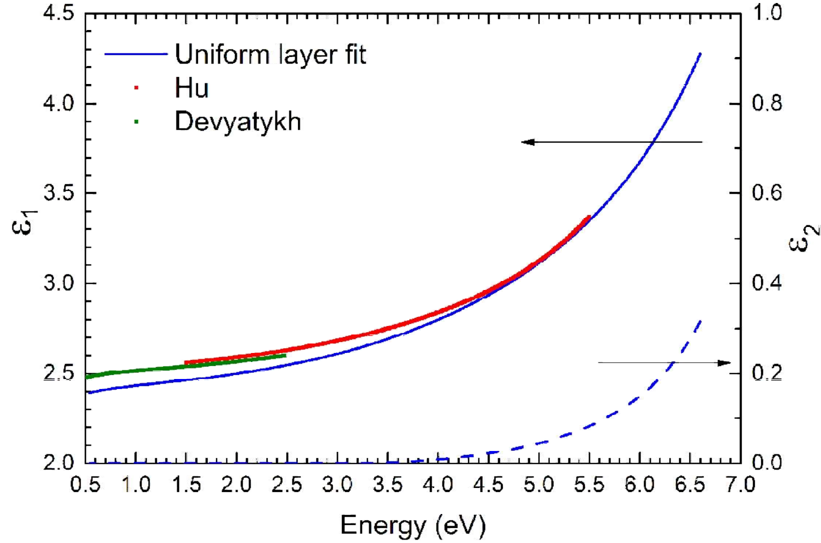

Figure 33: Complex dielectric function for GeO_2 from the uniform layer fit to our ellipsometry results in comparison with literature data [78, 140].

(the threshold of our sensitivity, compare Fig. 34) at 6 eV, considerably larger than α=0.5×10^4 cm^{-1} found by transmission measurements on sputtered films. [129] It is common for spectroscopic ellipsometry measurements to overestimate small absorption coefficients [112, 113].

4.8 Summary

We developed a hybrid dry-wet preclean for thermal oxidation of Ge and produced thermal oxides on Ge at 550°C and 270 kPa O_2 pressure, with oxide thicknesses ranging from 34 to 136 nm and oxidation times up to 10 hours. Multi-sample ellipsometry analysis of these oxides determined the dielectric functions of Ge and GeO_2 from 0.5 to 6.6 eV. We carefully discuss the accuracy of our results and compare with prior data.

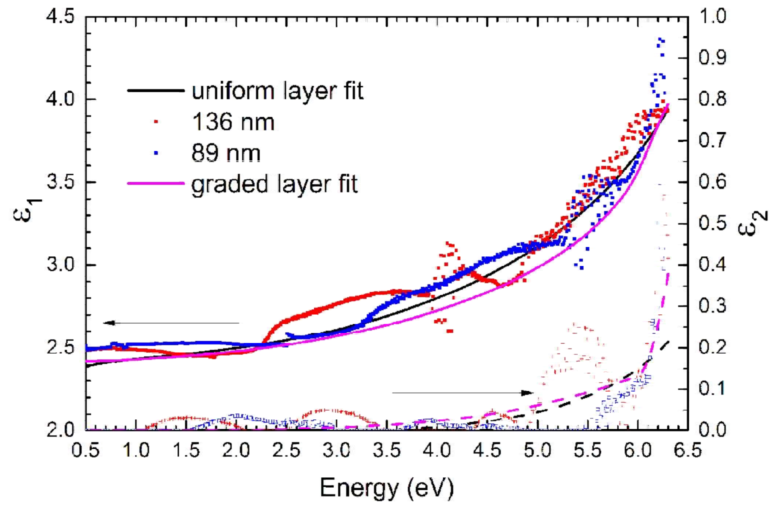

Figure 34: To estimate the accuracy of the optical constants for GeO_2, we plot the dielectric function obtained from various methods: From a Tauc-Lorentz fit to all data assuming uniform oxide density, from fits of single samples (89 nm and 136 nm thickness) with uniform density, and a two-oscillator fit (Tauc-Lorentz and Gaussian) to all data allowing a density gradient for the thicker oxides.

Acknowledgments

This work was supported by the Air Force Office of Scientific Research (FA9550-13-1-0022) and by the Army Research Office (W911NF-14-1-0072). Support during 2016 was provided by the National Science Foundation (DMR-1505172). J.M.M. and A.A.M. acknowledge support from the New Mexico Alliance for Minority Participation (NM-AMP).

5 Temperature dependence of the interband critical points of bulk Ge and strained Ge on Si

Nalin S. Fernando, T. Nathan Nunley, Ayana Ghosh, Cayla M. Nelson, Jacqueline A. Cooke, Amber A. Medina, Stefan Zollner

Department of Physics, New Mexico State University, MSC 3D, P.O. Box 30001, Las Cruces, NM 88003, USA

Chi Xu, Jose Menendez

Department of Physics, Arizona State University, Tempe, AZ 85287, USA

John Kouvetakis

School of Molecular Science, Arizona State University, Tempe, AZ 85287, USA

5.1 Abstract

Epitaxial Ge layers on a Si substrate experience a tensile biaxial stress due to the difference between the thermal expansion coefficients of the Ge epilayer and the Si substrate, which can be measured using asymmetric x-ray diffraction reciprocal space maps. This stress depends on temperature and affects the band structure, interband critical points, and optical spectra. This manuscripts reports careful measurements of the temperature dependence of the dielectric function and the interband critical point parameters of bulk Ge and Ge epilayers on Si using spectroscopic ellipsometry from 80 to 780 K and from 0.8 to 6.5 eV. The authors find a temperature-dependent redshift of the E_1 and $E_1 + \Delta_1$ critical points in Ge on Si (relative to bulk Ge). This redshift can be described well with a model based on thermal expansion coefficients, continuum elasticity theory, and the deformation potential theory for interband transitions. The interband transitions leading to E_0' and E_2 critical points have lower symmetry and therefore

are not affected by the stress.

5.2 Introduction

There is a close relationship between the optical constants, especially the complex dielectric function ϵ, of semiconductors and their electronic band structure [105]. The dielectric function spectra [83, 116], usually measured by spectroscopic ellipsometry [76, 77, 151, 152], show distinctive peaks, called interband critical points (CPs), which are associated with energy differences between the conduction and valence bands at characteristic points or regions in the Brillouin zone [105]. For example, the dielectric function of Ge displays two peaks called E_1 and $E_1 + \Delta_1$ near 2 eV due to interband optical transitions at the L-point of the Brillouin zone and along the Λ-direction [30].

These CPs depend on temperature [30], alloy composition [153, 154, 155], doping [156, 157, 158], pressure [159, 160], and strain [161, 162] and therefore can be used for characterization and process control [49, 98]. CP changes can also be exploited for electronic and optoelectronic applications. For example, tensile biaxial stress lowers the direct gap of Ge [3] and increases the near-infrared absorption coefficient [163], which enhances the efficiency of Ge-based photodetectors [12]. At sufficiently large tensile biaxial stress, Ge epitaxial layers on Si show direct-gap photoluminescence [164] and optical amplification [165]. By contrast, unstrained layers of $Ge_{1-y}Sn_y$ alloys also exhibit a direct band gap [166, 167] for $y>0.07$, which allows fabrication of semiconductor lasers [168].

We previously reported [79] accurate measurements of the Ge dielectric function from 0.5 to 6.6 eV at room temperature. The subject of the present manuscript is to discuss the temperature dependence of the CP parameters of Ge between 80

and 800 K. Especially, we focus on CP differences between bulk Ge and epitaxial Ge layers grown on Si, which are under tensile biaxial stress because of the thermal expansion coefficient mismatch between the Ge epilayer and the Si substrate.

5.3 Sample preparation and characterization

Bulk undoped Ge wafers with (100) surface orientation and a resistivity greater than 40 Ωcm were obtained commercially [169] and cleaved into 20×20 mm^2 pieces, then cleaned using a hybrid dry/wet process as described elsewhere [79]. The purpose of the clean is to create a thin stable native oxide layer with about 2−3 nm thickness. No strong acids were used to remove the native oxide completely. For comparison with bulk Ge, we also prepared thick relaxed Ge epitaxial layers on Si.

Undoped layers of Ge with a thickness of about 1500 nm were deposited on Si (100) using ultrahigh vacuum chemical vapor deposition (UHV-CVD) [73]. We used tetragermane (Ge_4H_{10}) as the precursor, diluted in hydrogen at a 1:20 ratio. Growth occurred at temperatures between 350 and 400°C at a total pressure of 10^{-4} Torr. The growth rate varied between 17 and 30 nm/min depending on the growth temperature. After the completion of the growth, samples were annealed *in situ* at 680°C for 3 min to improve the alignment of crystal mosaics. Before ellipsometry measurements, these samples were also cleaned ultrasonically with water and isopropanol.

The Ge layer thickness was verified by spectroscopic ellipsometry [170] from the spacing of the interference fringes at low photon energies (between 0.8 and 1.2 eV), see Fig. 35. Films were smooth and defect-free with a surface roughness of about 0.5 nm as determined using atomic force microscopy. X-ray diffraction studies

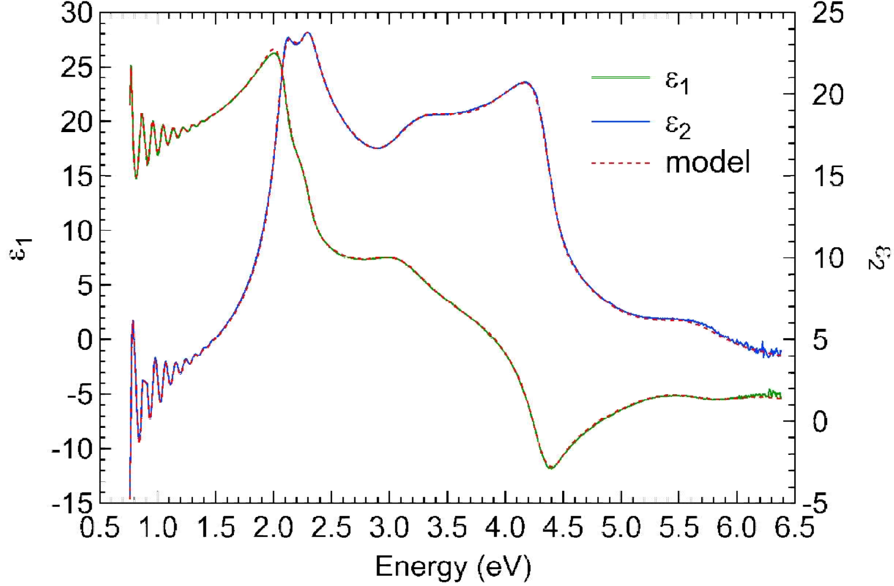

Figure 35: Pseudodielectric function of a Ge epitaxial layer on Si at 300 K (solid: data; dashed: model). Interference fringes between 0.8 and 1.2 eV allow the determination of the Ge epilayer thickness (1460 nm). The native oxide thickness obtained from the fit is 3.1 nm.

show sharp (004) diffraction peaks from the Si substrate and the Ge epilayer, see Fig. 36 (inset). The full width at half maximum of the Ge (004) rocking curve is only 120". Additional information about these samples and their applications for photodiodes is given in [73].

Using asymmetric ($\bar{2}\bar{2}4$) grazing exit x-ray reciprocal space maps [86, 87] (see Fig. 36) we determined the out-of-plane lattice constant to be 5.652±1 Å. In comparison to the bulk Ge lattice constant of 5.658 Å, that results in a compressive out-of-plane strain of $\epsilon_{\perp}=-0.11\%$. We also determined the in-plane lattice constant to be 5.666±2 Å, which corresponds to a tensile in-plane strain of $\epsilon_{\|}=0.14\%$. Considering the large error bars for these small strains, these results are consistent

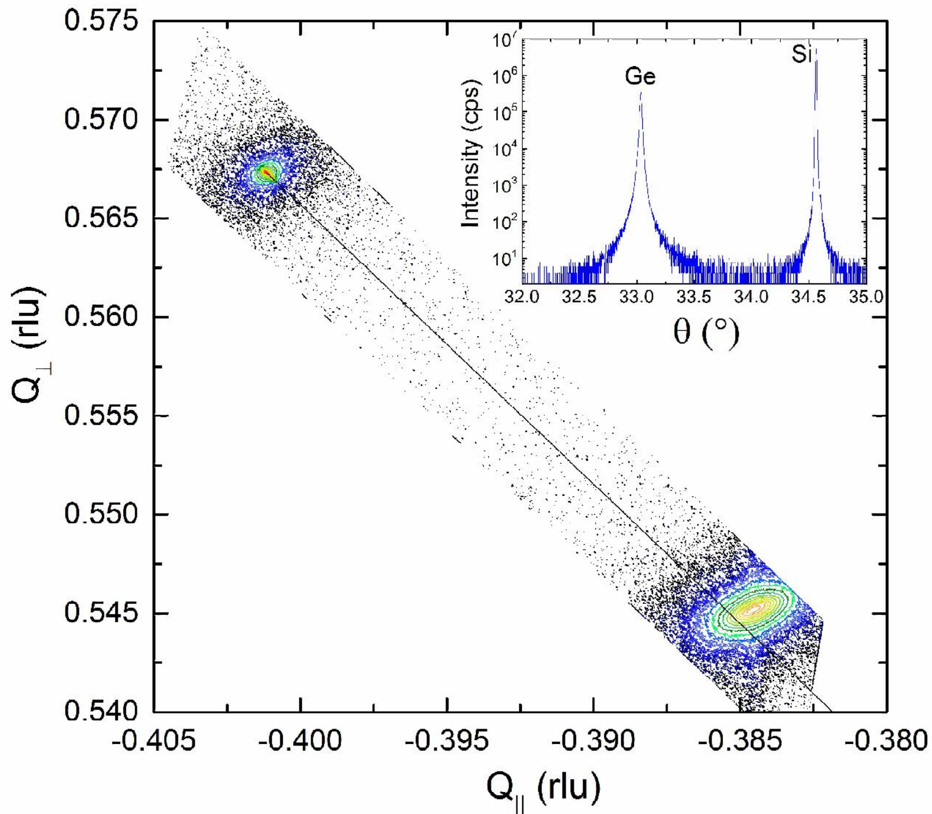

Figure 36: Inset: Logarithmic intensity versus diffraction angle for the symmetric (004) ω-2θ x-ray reflections of Ge on Si, showing a strong peak from the Si substrate at ω=34.5° and a weaker peak from the Ge epilayer at 33°. Main graph: High-resolution x-ray diffraction ($\bar{2}\bar{2}4$) grazing exit reciprocal space map of Ge on Si. The relaxation line (solid) shows that the Ge epilayer is not fully relaxed relative to the Si substrate. The residual in-plane strain $\epsilon_{||}$ is 0.14±0.04% (tensile) and the out-of-plane strain $\epsilon_{\perp}$ is -0.11±0.03% (compressive) as a result of the difference in thermal expansion of Ge and Si.

with elasticity theory [87]

$$\epsilon_{\perp}(T) = -2\frac{C_{12}}{C_{11}}(T)\,\epsilon_{\parallel}(T) \approx -0.75\epsilon_{\parallel}(T)\,, \tag{60}$$

where the temperature-dependent ratio of the elastic moduli is [43]

$$\frac{C_{12}}{C_{11}}(T) = 0.37492 - 3.7 \times 10^{-6}\ \mathrm{K}^{-1}(T - 273\ \mathrm{K})\,. \tag{61}$$

The Ge epilayers on Si are under tensile biaxial stress because of the different thermal expansion coefficients for Si and Ge [171]. For the purposes of our investigation, we assume that the Ge epilayers are fully relaxed on the Si substrate at the growth temperature T_g through the formation of misfit dislocations near the interface between the epilayer and the substrate. Since the thermal expansion coefficient for bulk Ge is roughly twice that of Si [171], the Ge epilayer wants to contract much faster than the Si substrate as the sample is cooled down to room temperature [163]. Assuming no additional misfit dislocation form during the cool-down step, the thermal expansion mismatch leads to a tensile biaxial stress of the Ge layer along the wafer surface at room temperature. This stress increases the in-plane lattice constant and decreases the out-of-plane lattice constant according to elasticity theory, as found in our x-ray diffraction analysis [86, 87].

Determining the “growth temperature” T_g in this simple model is not straightforward, since growth occurs in several steps at diferent temperatures followed by *in situ* annealing [73]. One might argue that the epilayer is anchored to the Si substrate during the initial stages of growth (near 650 K). One might also expect that the strain-free condition is reached at a higher temperature during the anneal step. Given this ambiguity, we perform different model calculations with T_g

between 700 K and 850 K, which we consider lower and upper bounds for the growth temperature.

5.4 Thermal expansion mismatch

To model the biaxial stress in our samples as a function of temperature, we express the linear thermal expansion coefficient for Si and Ge as [42]

$$\alpha\left(T\right)=\sum_{i=1}^{4}\chi_i\frac{\left(\theta_i/T\right)^2\exp\left(\theta_i/T\right)}{\left[\exp\left(\theta_i/T\right)-1\right]^2}, \tag{62}$$

where χ_i and θ_i are parameters taken from [42]. (A good fit to the thermal expansion coefficients can also be obtained with a model containing only two adjustable parameters [43].)

The tensile in-plane strain $\epsilon_{\|}$(T) induced in a Ge epilayer on Si due to the thermal expansion mismatch between Si and Ge can then be calculated [12], assuming no strain relaxation occurs while cooling down from the growth temperature T_g:

$$\epsilon_{\|}\left(T\right)=\int_{T}^{T_{\mathrm{g}}}\left[\alpha_{\mathrm{Ge}}\left(T'\right)-\alpha_{\mathrm{Si}}\left(T'\right)\right]dT'. \tag{63}$$

The corresponding out-of-plane strain is given by Eq. (60). Calculated values for the strain tensor components are shown in Fig. 37 along with values measured by x-ray diffraction (compare Fig. 36). The agreement of our model with the strain measured at room temperature is good.

To calculate the CP energies as a function of strain, we introduce the hydro-

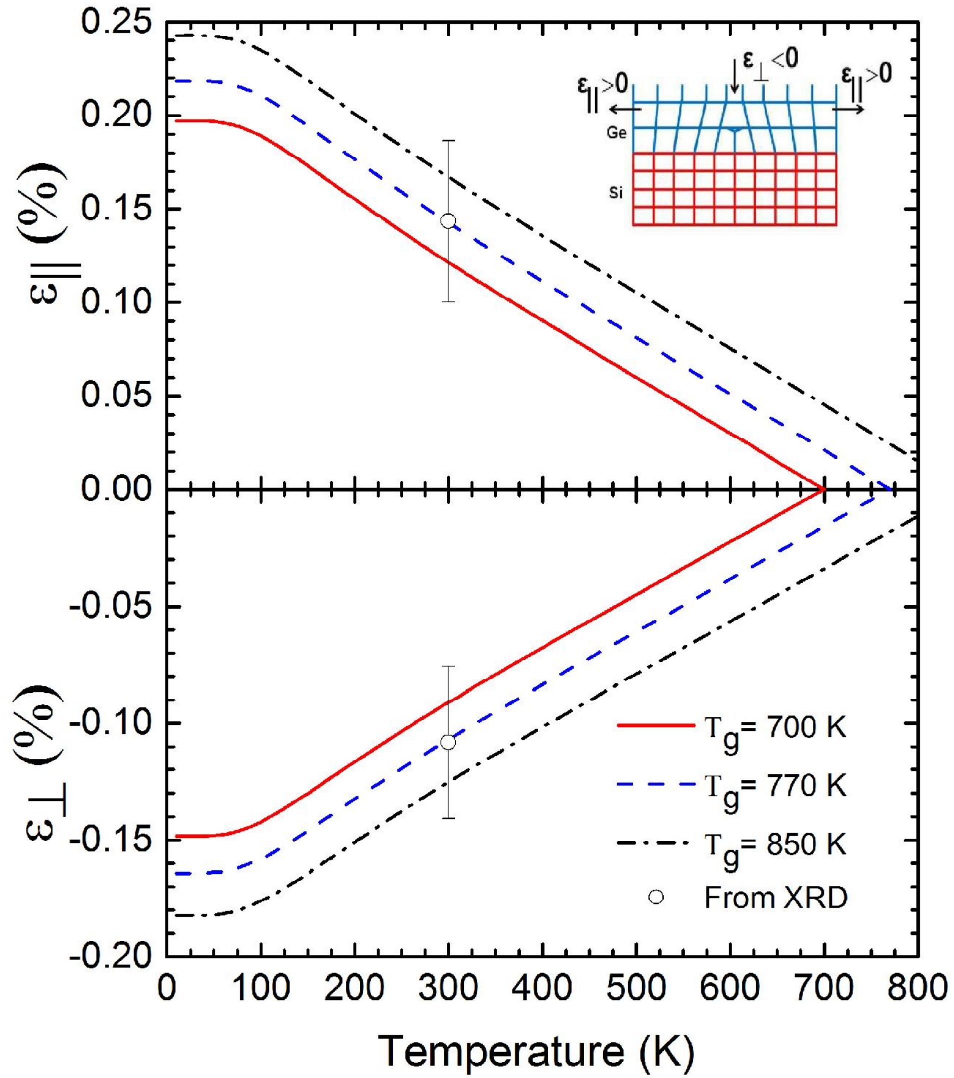

Figure 37: Temperature dependence of the in-plane strain $\epsilon_{\|}$ and the out-of-plane strain $\epsilon_{\perp}$ in the Ge epilayer caused by the thermal expansion mismatch between the Si substrate and the Ge layer as shown in the inset. Ge experiences a temperature dependent biaxial tensile stress which leads to a tensile in-plane strain calculated using Eq. (63) from the thermal expansion coefficients of Si and Ge assuming different growth temperatures T_g. The resulting out-of-plane strain is compressive (negative). $\circ$: Strain components derived from high resolution x-ray diffraction $(\bar{2}\bar{2}4)$ grazing exit reciprocal space map at 300 K.

static and shear strains [49]

$$\epsilon_H = \left[\epsilon_\perp + 2\epsilon_\parallel\right]/3 \quad \text{and} \quad \epsilon_S = \left[\epsilon_\perp - \epsilon_\parallel\right]/3. \tag{64}$$

The hydrostatic and shear shifts [49] ΔE_H and ΔE_S of the E_1 and $E_1 + \Delta_1$ CPs define the hydrostatic and shear deformation potentials D_1^1 and D_3^3 by [49]

$$\Delta E_H = \sqrt{3} D_1^1 \epsilon_H \quad \text{and} \quad \Delta E_S = \sqrt{6} D_3^3 \epsilon_S, \tag{65}$$

resulting in [49]

$$E_1^s = E_1^o\left(T\right) + \frac{\Delta_1}{2} + \Delta E_H - \sqrt{\frac{\left(\Delta_1\right)^2}{4} + \left(\Delta E_S\right)^2} \tag{66}$$

$$\left(E_1 + \Delta_1\right)^s = E_1^o\left(T\right) + \frac{\Delta_1}{2} + \Delta E_H + \sqrt{\frac{\left(\Delta_1\right)^2}{4} + \left(\Delta E_S\right)^2}, \tag{67}$$

where the superscripts s and 0 denote the CP energies in strained and unstrained Ge, respectively. The temperature independent quantity Δ_1 is the spin-orbit splitting of the valence band of unstrained Ge at the L point, taken as our experimental value of 0.198 eV.

5.5 Ellipsometric measurements and data processing

We measured the pseudodielectric function of our samples at a 70° incidence angle from 0.8 to 6.6 eV (with 10 meV steps) in a UHV cryostat at temperatures from 80 K to 785 K using an ellipsometer [170] described elsewhere [172] to investigate the temperature dependence of the CP parameters of Ge on Si in

comparison with bulk Ge. The samples were attached to a copper cold finger using metal clamps. A type-E thermocouple in a stainless steel sheeth was attached to the front surface of the sample to read the temperature of the sample accurately. A gold-coated copper radiation shield covered the sample and cold finger to minimize heat loss. The sample was heated to 600 K for an hour to allow the sample to degas, which slightly reduces the (native oxide) surface layer thickness. Then it was cooled down to 80 K and heated again to 400 K to minimize the formation of an ice layer on the surface of the sample during measurements at low temperatures. This achieved a base pressure below 10^{-8} Torr.

The temperature-dependent dielectric functions of bulk Ge and Ge on Si were obtained in a two-step fitting procedure. Two multilayer models, GeO_2-Ge and GeO_2-Ge-Si, were used to fit the experimental data. Dielectric functions for GeO_2 and Si at 300 K were taken from the literature [79, 82]. Their temperature dependence does not have a big impact on the analysis. The dielectric functions of bulk Ge and Ge on Si were described using a parametric oscillator model [79, 82] which imposes Kramers-Kronig consistency between the real and imaginary parts of the dielectric function. In the first step of the fit, the oxide layer thickness, the Ge layer thickness on Si, and all parameters in the parametric oscillator model were adjusted. In the second step, the thicknesses were kept fixed at the values obtained in the first step, and the data were fit again by adjusting the values of ϵ for Ge at each photon energy (known as point-by-point fit) to obtain the final tabulated dielectric function of Ge (or Ge on Si). We obtained a 1-3 nm thick GeO_2 surface oxide layer for both samples when modeling room temperature experimental data. During measurements between 600 and 800 K, the oxide thickness is reduced by up to 6 Å. For consistency, we did not vary the oxide thickness during our temperature-dependent point-by-point fits for the purposes

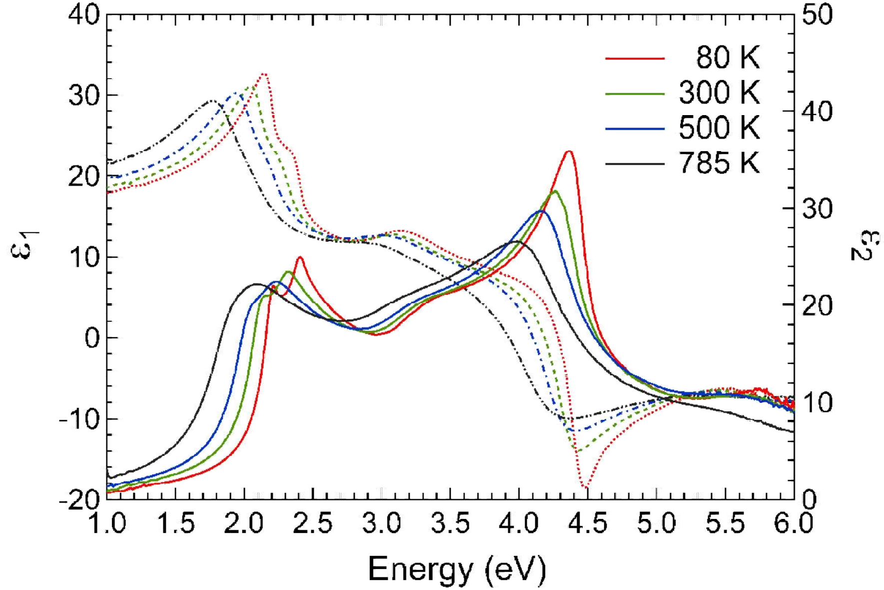

Figure 38: Real (ϵ_1, dashed) and imaginary (ϵ_2, solid) parts of the dielectric function of Ge on Si at temperatures between 80 K and 785 K.

of CP analysis. According to our analysis, the $E_1\left(T\right)$ and $E_1+\Delta_1\left(T\right)$ CP energies are not sensitive to the thickness of the oxide layer, which is consistent with the literature [173]. Fixing the oxide thickness reduces variations in the magnitude of the CPs. The dielectric function of Ge on Si at temperatures between 80 and 785 K is shown in Fig. 38.

The dielectric function in the vicinity of the E_1 and $E_1+\Delta_1$ CPs can be described using an expression for a mixture of a two-dimensional minimum and a saddle point [30]

$$\epsilon\left(\omega\right)=C-A\ln\left(\omega-E_g-i\Gamma\right)e^{i\phi}, \tag{68}$$

where ω is the photon energy, A the dimensionless amplitude, E_g the CP energy, Γ the broadening parameter, and ϕ the excitonic phase angle, which describes the amount of mixing. The contribution of the CPs to the dielectric function can be enhanced and the non-resonant background C (from other CPs) removed

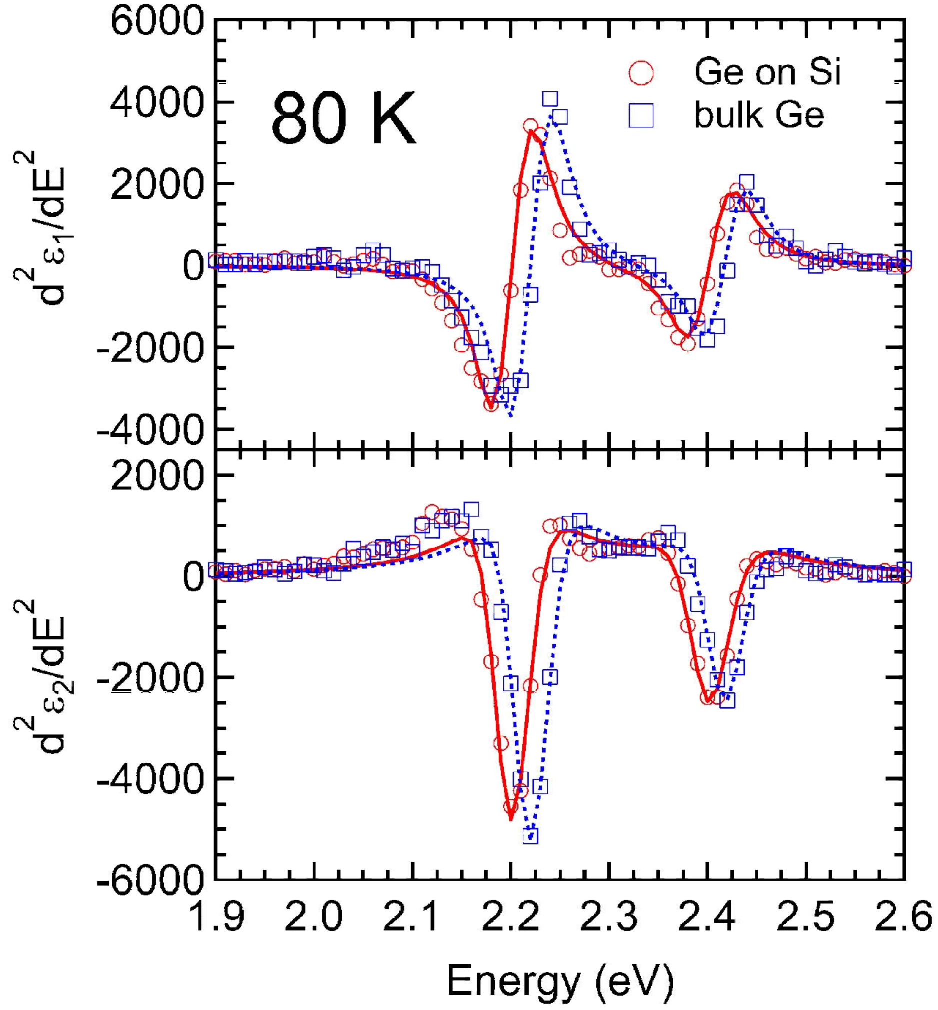

Figure 39: Second derivatives of the real (ϵ_1) and imaginary (ϵ_2) parts of the dielectric function of Ge on Si (solid) and bulk Ge (dotted) with respect to photon energy near the E_1 and $E_1+\Delta_1$ CPs at 80 K. Symbols (∘: Ge on Si, □: bulk Ge) represent the experimental data, the lines the best fit with a two dimensional minimum critical point using Eq. (68).

by analyzing second derivatives [30]. The real and imaginary parts of the dielectric function obtained by point-by-point fitting at different temperatures were numerically differentiated and smoothed using Savitzky-Golay [84] coefficients for second-order derivatives with a cubic polynomial. The number of smoothing coefficients depended on temperature: 8, 10, and 12 smoothing coefficients were used in the temperature ranges below 500 K, 525-600 K, and above 625 K, respectively, to obtain a good signal to noise ratio without distorting the line shape. The second derivative spectra of the dielectric function of the bulk Ge and Ge on Si were fit using Eq. (68), with results shown in Fig. 39. Both the E_1 and $E_1 + \Delta_1$ structures were fitted simultaneously, and the excitonic phase angle ϕ was forced to take the same value for both E_1 and $E_1 + \Delta_1$. It is quite clear from Fig. 39 that the CPs are red-shifted for Ge on Si compared to bulk Ge due to the biaxial tensile stress.

5.6 Results and discussion for E_1 and $E_1 + \Delta_1$

Our derivative line-shape analysis yields the E_1 and $E_1 + \Delta_1$ CP parameters as a function of temperature, which are shown in Fig. 40 (energy), Fig. 41 (amplitude), Fig. 42 (phase angle), and Fig. 43 (broadening). One source of the errors associated with the CP parameters are random statistical errors coming from the second derivative analysis. The statistical errors of the energy, amplitude (A), phase angle (ϕ) and broadening (Γ) are on the order of 1 meV, 0.1, 0.2° and 1 meV respectively. These errors are much smaller than the fluctuations observed in our data. Therefore, there should be some other systematic errors, inherited to the experimental data and the model, which are difficult to quantify. One such source of the errors could be the effects of the surface layer. Thickness nonuni-

formity and the instability of the surface oxide layer during the measurements at high at temperatures (above 600 K) affect the dielectric function, making the surface layer correction less accurate in the optical model. Increased noise with increasing temperature due to the black body radiation from the sample also affects the CP parameters obtained from the second derivative analysis. The influence of one bad data point can become significant in the second derivative spectrum and can affect the amplitude and the broadening of the line shape of the CP. The observed random fluctuations of the CP parameters with increasing temperature may caused by these factors. Figure 44 shows that the spin-orbit splitting Δ_1, if treated as a fitting parameter, is independent of temperature and fluctuates between 195 and 200 meV due to random measurement and fitting errors. Our measured Δ_1 is significantly larger than the value of 187 meV reported in [30], but consistent with measurements by others [30, 174].

Figure 40 clearly demonstrates that the E_1 and $E_1+\Delta_1$ CP energies are about the same for bulk Ge and Ge on Si near 700 K. At lower temperatures, the CPs of Ge on Si are redshifted (i.e., lower in energy) compared to those of bulk Ge at the same temperature. The redshift increases towards lower temperatures, because the biaxial stress increases. There might be a small blueshift above 700 K, which is on the order of the experimental errors.

The differences of the E_1 and $E_1 + \Delta_1$ energies between bulk Ge and Ge on Si as a function of temperature are shown in Fig. 45. This redshift is 15−20 meV at low temperatures and gradually becomes smaller near 700 K. At very high temperatures, the shift becomes negative. These shifts can be modeled using the continuum elasticity theory for the biaxial stress due to thermal expansion mismatch, as explained earlier. From the strain tensor shown in Fig. 37, we

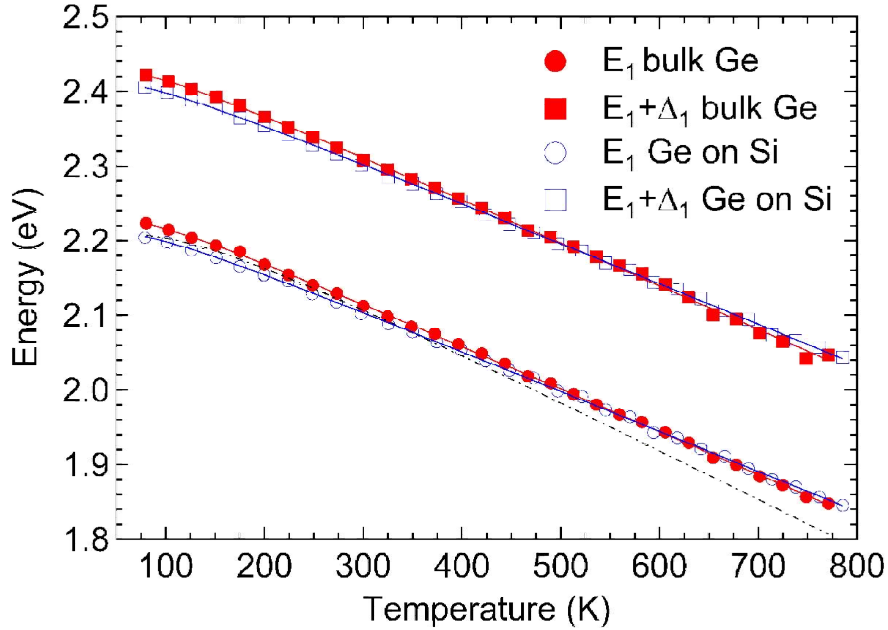

Figure 40: Temperature dependence of the E_1 (•, ∘) and $E_1+\Delta_1$ (■, □) energies of bulk Ge (solid) and Ge on Si (open). The statistical errors of the CP energies determined from the second derivatives are on the order of 1 meV. Solid lines show the best fit of the data using Eq. (72) with parameters given in Table 4. The dash-dotted line shows the results from [30] for comparison.

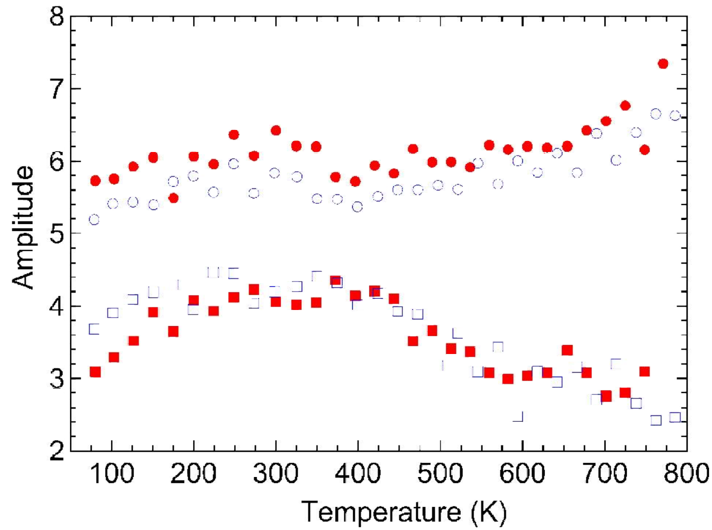

Figure 41: Temperature dependence of the dimensionless amplitudes (A) of the E_1 (•, ∘) and $E_1+\Delta_1$ (■, □) transitions of bulk Ge (solid) and Ge on Si (open).

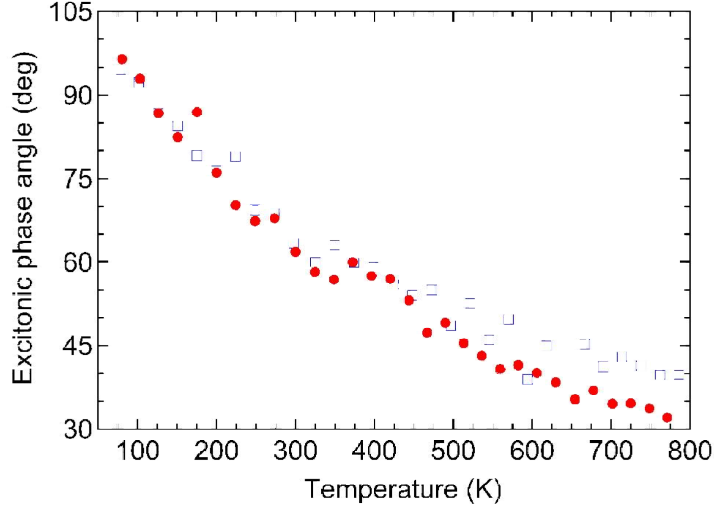

Figure 42: Temperature dependence of the excitonic phase angle (ϕ) defined in Eq. (68) for the E_1 transitions of bulk Ge (●) and Ge on Si (□). We assumed that $E_1 + \Delta_1$ had the same phase angle as E_1.

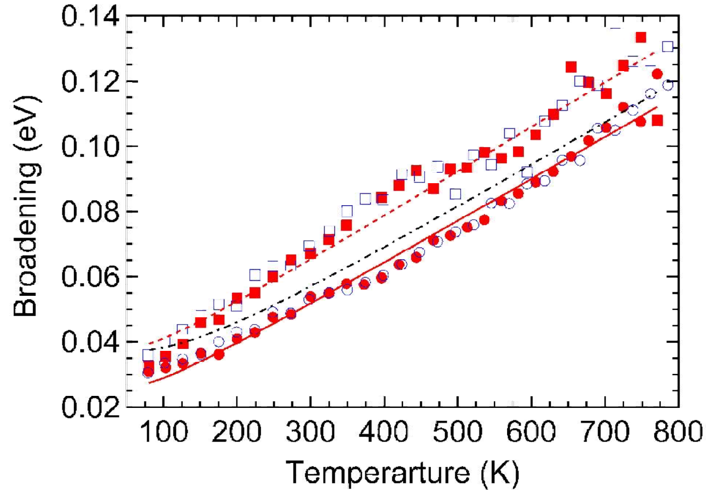

Figure 43: Temperature dependence of the E_1 (●, ○) and E_1+Δ_1 (■, □) broadening parameter Γ defined in Eq. (68) for bulk Ge (solid) and Ge on Si (open). The dash-dotted line shows the results for E_1 of bulk Ge from [30] for comparison. The solid and dashed lines show the best fit to Eq. (73) with parameters in Table 5.

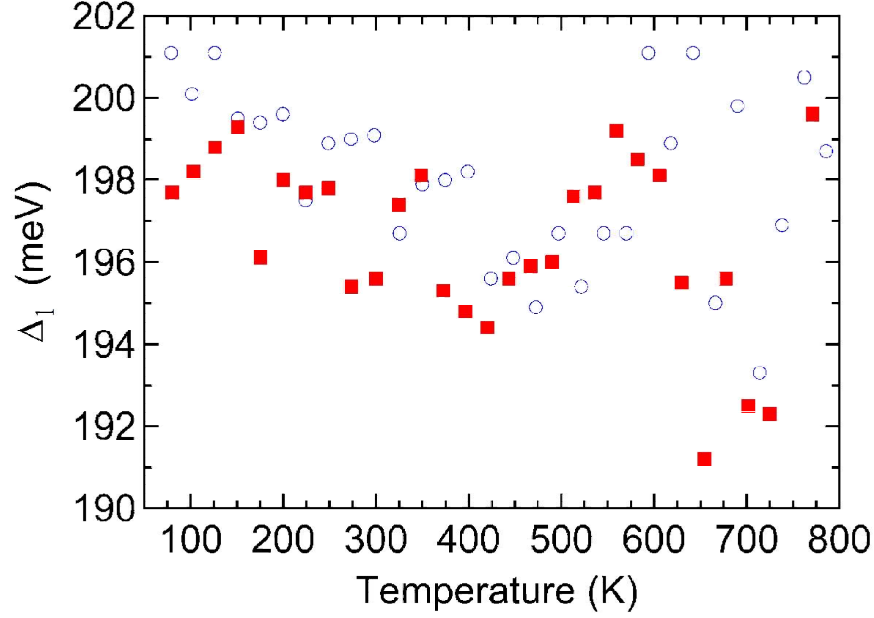

Figure 44: Temperature dependence of the spin orbit splitting Δ_1 of the valence band for bulk Ge (■) and Ge on Si (○).

calculate the E_1 redshift

$$\Delta E_1 \;=\; \frac{\Delta_1}{2} + \Delta E_H - \sqrt{(\Delta_1)^2/4 + (\Delta E_S)^2} \qquad (69)$$

for an assumed growth temperature T_g between 700 and 850 K. These results, shown by the lines in Fig. 45, show the correct trend, but the calculated slope of the temperature shift is smaller than the slope of the measured data. It appears as if the tensile stress determined from our CP energy differences is 30-50% larger than the stress calculated from the thermal expansion coefficients.

It is well known that most CPs redshift with increasing temperature [30, 39, 175]. This can easily be seen in Fig. 40. Our measured redshift is smaller than that obtained in [30]. We trust that our temperature measurements are more accurate, since we have mounted our thermocouple directly on the sample surface.

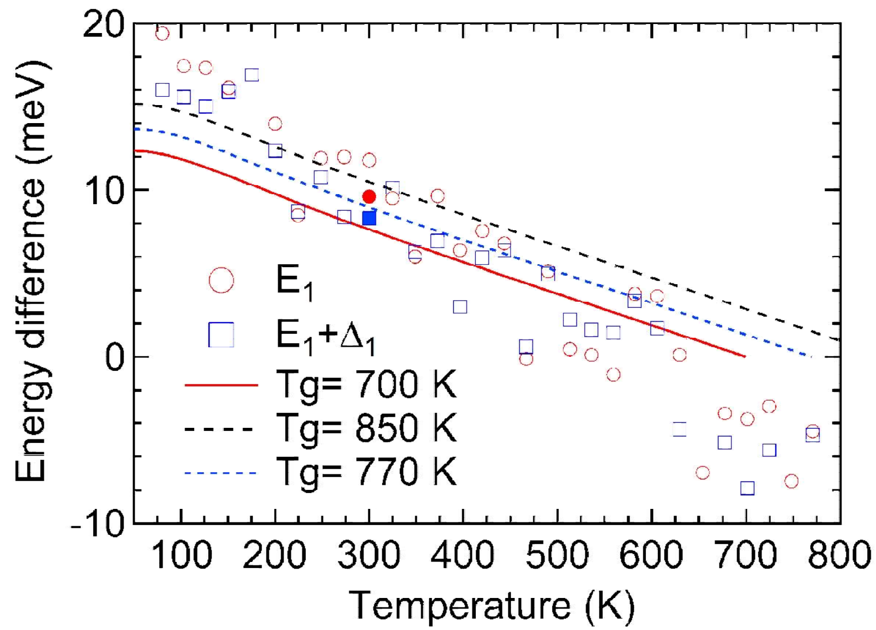

Figure 45: Energy difference of the E_1 (∘) and $E_1+\Delta_1$ (□) critical point energies between bulk Ge and Ge on Si. Lines show the predicted energy difference for three growth temperatures T_g using Eqs. (89) and (90). • and ■ represent the calculated energy difference of the E_1 and $E_1+\Delta_1$ critical point energies using the measured XRD strain at 300 K.

This redshift has two contributions, from thermal expansion of the crystal and from the renormalization of the electron energies due to electron-phonon interactions [39]. The temperature dependent energy shift due to the thermal volume expansion follows from Eq. (65) and can be written as

$$\Delta E_{th}\left(T\right) = \sqrt{3} D_1^1 \int_0^T \alpha\left(T'\right) dT'. \tag{70}$$

The redshift due to electron-phonon interaction is proportional to the Bose-Einstein occupation factor for an (effective) phonon and often written as [30, 39]

$$E_{\mathrm{e-ph}}\left(T\right) = a' - b'\left[1 + 2/\left(e^{\theta'_B/T} - 1\right)\right], \tag{71}$$

where $k\theta'_B$ is the effective phonon energy, b' the electron-phonon coupling strength, and a' the unrenormalized transition energy.

Experimentally, one measures the total energy shift (sum of thermal expansion and electron-phonon contributions), and also describes it with the same empirical Bose-Einstein expression

$$E_{\mathrm{total}}\left(T\right) = a - b\left[1 + 2/\left(e^{\theta_B/T} - 1\right)\right]. \tag{72}$$

The primed parameters can be obtained from the experiment by subtracting the thermal expansion contribution in Eq. (70) from the measured energy shifts and then fitting with Eq. (71).

In Table 4, we list the primed and unprimed Bose-Einstein parameters describing the temperature shifts for the E_1 and $E_1 + \Delta_1$ transitions in comparison with

Table 4: Values of the parameters a, b, and θ_B obtained by fitting the E_1 and E_1+Δ_1 critical point energy vs temperature to Eq. (72) and the values of the parameters a', b$'$, and θ'_B which describe the temperature dependence of the E_1 and E_1+Δ_1 taking into account the effects of the thermal expansion using Eq. (71). Parameters marked (f) were fixed during the fit.

Bulk Ge	a (eV)	b (eV)	θ_B (K)
E_1	2.295±0.002	0.063±0.004	218±14
$E_1 + \Delta_1$	2.494±0.002	0.064±0.001	218 (f)
E_1 (Ref. [30])	2.33±0.03	0.12±0.04	360±120
E'_0	3.18±0.02	0.05±0.02	313±107
E'_0 (Ref. [30])	3.23±0.02	0.08±0.03	484±136
E_2	4.505±0.006	0.05±0.01	217±41
E_2 (Ref. [30])	4.63±0.05	0.17±0.06	499±127
Ge on Si			
E_1	2.273±0.001	0.0591±0.0009	218 (f)
$E_1 + \Delta_1$	2.472±0.001	0.0593±0.0002	218 (f)
E'_0	3.165±0.006	0.051±0.002	313(f)
E_2	4.496±0.003	0.052±0.001	217(f)

Bulk Ge	a' (eV)	b$'$ (eV)	θ'_B (K)
$E_1 - \Delta E_{th}$	2.275±0.002	0.039±0.005	166±21
$(E_1 + \Delta_1) - \Delta E_{th}$	2.474±0.002	0.040±0.0002	166 (f)
$E_2 - \Delta E_{th}$	4.488±0.005	0.03±0.01	167±58
Ge on Si			
$E_1 - \Delta E_{th}$	2.253±0.001	0.0363±0.0002	166 (f)
$(E_1 + \Delta_1) - \Delta E_{th}$	2.452±0.001	0.0366±0.0002	166 (f)
$E_2 - \Delta E_{th}$	4.479±0.002	0.0328±0.0004	167 (f)

previous results [30]. Our electron-phonon coupling parameter b and our effective phonon energy $k\theta_B$ are both smaller than in [30], thus compensating each other. This difference compared to [30] also affects the unrenormalized band gap parameter a. Since the optical phonon energy of Ge is 37 meV, any temperature θ_B lower than 430 K is physically meaningful. Lower values indicate increasing importance of acoustic phonons for electron-phonon mediated band gap renormalization.

The broadenings of the E_1 and $E_1 + \Delta_1$ CPs (see Fig. 43) are very similar for bulk Ge and Ge on Si. The broadenings for $E_1+\Delta_1$ are larger than for E_1, because electrons and holes with higher energy have a larger phase space to scatter into [176]. Our broadenings are similar to [30].

Similar to Eq. (72), the broadenings can also be fitted with a Bose-Einstein factor [30]

$$\Gamma\left(T\right) = \Gamma_1 + \Gamma_0\left[1 + 2/\left(e^{\theta_B/T} - 1\right)\right]. \quad (73)$$

The results from a fit to our measured broadenings is shown in Table 5 in comparison with literature data [30]. Just like for the energy shifts, we find a smaller electron-phonon coupling constant Γ_0 and also a smaller effective phonon energy $k_B\theta_B$ than in [30]. A parameter-free theory for the temperature dependence of the broadenings [176] predicts an effective phonon temperature θ_B for the E_1 broadenings between 230 and 390 K and a coupling constant Γ_0 between 20 and 40 meV.

The dimensionless CP amplitudes calculated from Eq. (68) and shown in Fig. 41 are about 5-6 for E_1 and 3-4 for $E_1 + \Delta_1$. Their temperature dependence is weak. The agreement with [30] is reasonable. The details of the numerical fitting procedure (especially calulating the Savitzky-Golay derivatives) have a strong impact on the amplitudes and broadenings, but not so much on the energies. An

Table 5: Bose-Einstein parameters to describe the critical-point broadenings using Eq. (73). The phonon energy parameter θ_B was fixed to be the same as in Table 4. Parameters marked (f) were fixed during the fit.

Bulk Ge	Γ_1 (meV)	Γ_0 (meV)	θ_B (K)
E_1	11±1	14.2±0.3	218(f)
E_1 (Ref. [30])	12±9	25±3	376(f)
$E_1 + \Delta_1$	22±3	15.1±0.6	218(f)
$E_1 + \Delta_1$ (Ref. [30])	9±8	43±5	484 (sic)
E_2	38±2	22.1±0.5	217(f)
E_2 (Ref. [30])	8±5	69±3	499(f)
Ge on Si			
E_1	12.5±1	13.9±0.3	218(f)
$E_1 + \Delta_1$	25±2	14.8±0.5	218(f)
E_2	39±2	22.9±0.4	217(f)

uncorrelated electron model for the amplitudes (ignoring excitonic effects) yields [30]

$$A_{E_1} \approx A_{E_1+\Delta_1} \approx \frac{44}{aE_1^2}\left(E_1 + \Delta_1/3\right) \approx 3\ldots4, \tag{74}$$

where a is the Ge lattice constant in Å and the energies are specified in eV, in good agreement with our experiments. The difference in the amplitudes for E_1 and $E_1 + \Delta_1$ might be explained by terms linear in $k_\perp$, see Refs. [30] and [177]. Excitonic effects might also enhance the strength of the E_1 amplitudes [178].

In the absence of excitonic effects and surface overlayers, we expect a phase angle of 90° for a two-dimensional saddle point [179]. Deviations from this value explained by excitonic effects and other (often questionable) reasons [138]. At low temperatures, we indeed find the expected phase angle ϕ=90°, but it drops quickly towards higher energies. This was also observed in [30].

5.7 Higher-energy critical points E_0' and E_2

For completeness, we also determined the temperature dependence of the E_0' and E_2 CP parameters for bulk Ge and Ge on Si. The E_2 structure was fitted as a single CP with 12−18 Savitzky-Golay coefficients, depending on temperature. Since the E_0' structure is influenced by the tails of the $E_1 + \Delta_1$ and E_2 CPs, all four structures had to be fitted simultaneously with 17−21 coefficients. The E_0' CP is very weak and therefore requires more smoothing (using a larger number of coefficients). The results are shown in Figs. 46 through 53. The main value of these results is in helping to find a parametric description for the temperature dependence of the dielectric function of Ge, which has technological applications [180].

The E_0' CP energy decreases with increasing temperatures for both bulk Ge and Ge on Si, see Fig. 46. The Bose-Einstein parameters are shown in Table 4. We find a clear redshift by about 20 meV for the Ge on Si layer compared to bulk Ge, which is constant between 80 and 500 K. At higher temperatures, the data become too noisy to determine accurate E_0' values. Since this E_0' redshift is independent of temperature, it is therefore also independent of the strain in the Ge on Si samples. Therefore, the most likely explanation for the redshift is an artifact of the fitting procedure. The amplitude of the E_0' CP drops by 50% towards higher temperatures, see Fig. 47. The E_0' phase angle remains constant near 150° up to 600 K, as shown in Fig. 48. The temperature dependence of the E_0' broadenings in Fig. 49 cannot be described with Eq. (73) and this CP is therefore omitted from Table 5.

The temperature dependence of the E_2 CP energy shows the expected behavior, see Fig. 50, without a significant difference between bulk Ge and Ge on Si.

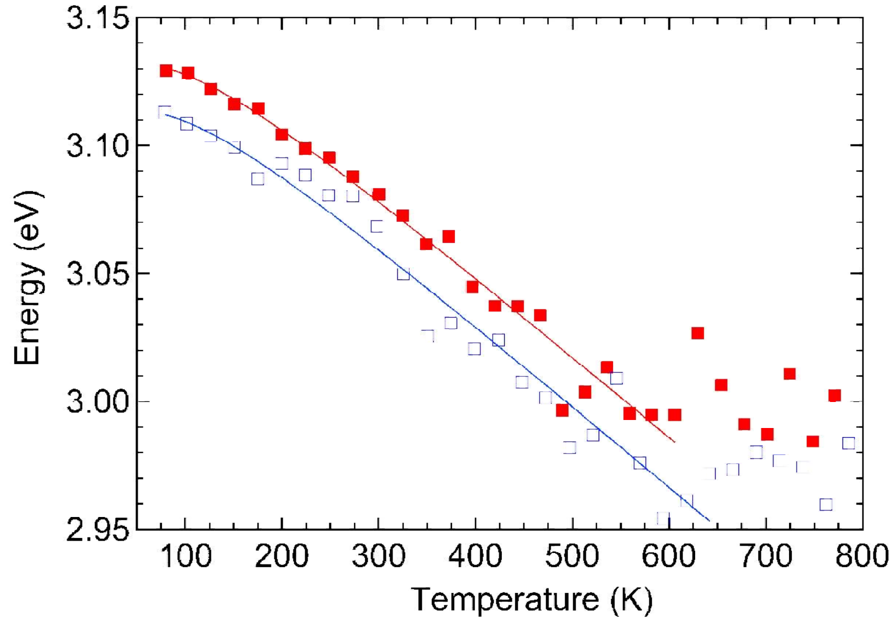

Figure 46: Temperature dependence of the E'_0 energies of bulk Ge (solid) and Ge on Si (open). Solid lines show the best fit of the data using Eq. (72) with parameters given in Table 4.

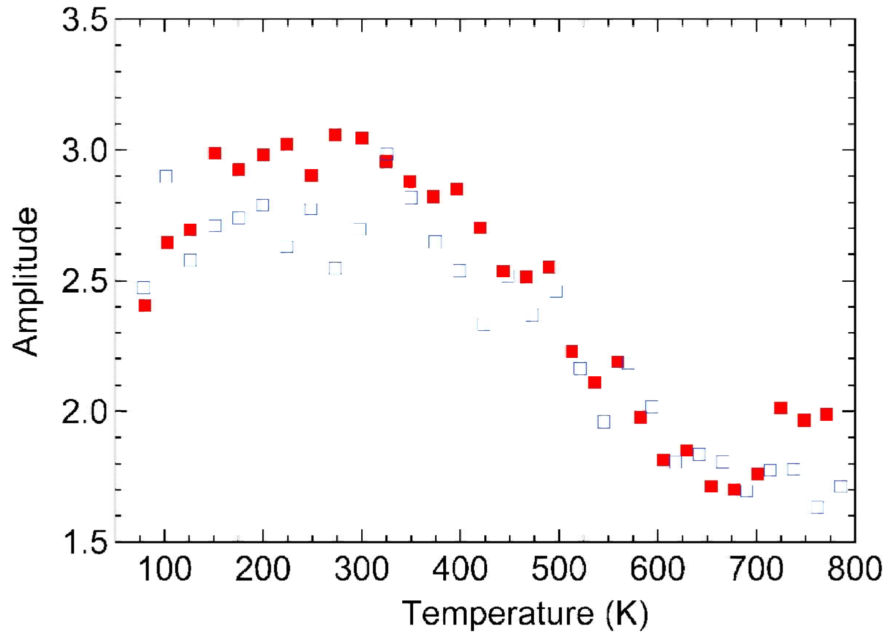

Figure 47: (Color online) Temperature dependence of the amplitudes (A) of the E'_0 transitions of bulk Ge (solid) and Ge on Si (open).

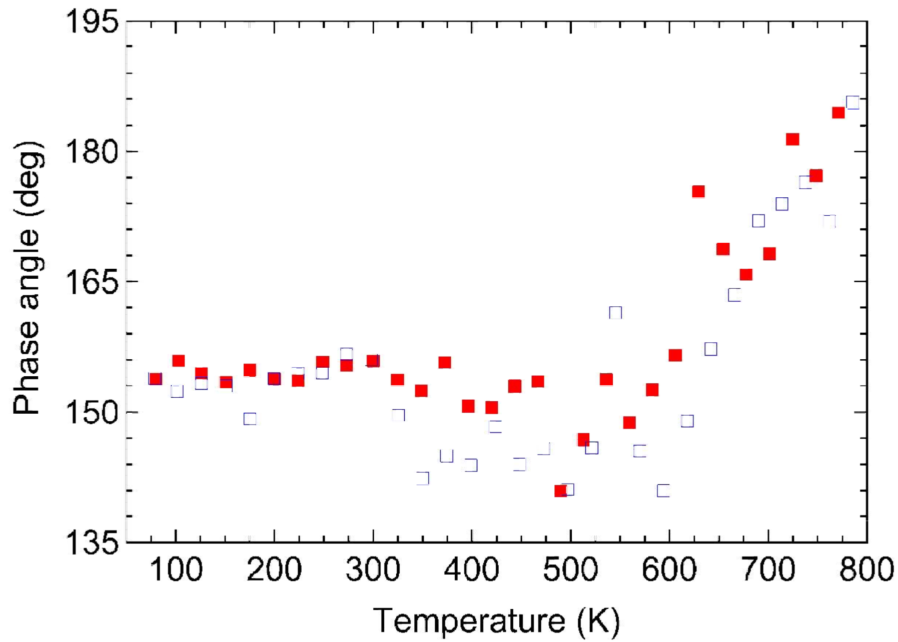

Figure 48: Temperature dependence of the excitonic phase angle (ϕ) defined in Eq. (68) for the E_0' transitions of bulk Ge (solid) and Ge on Si (open).

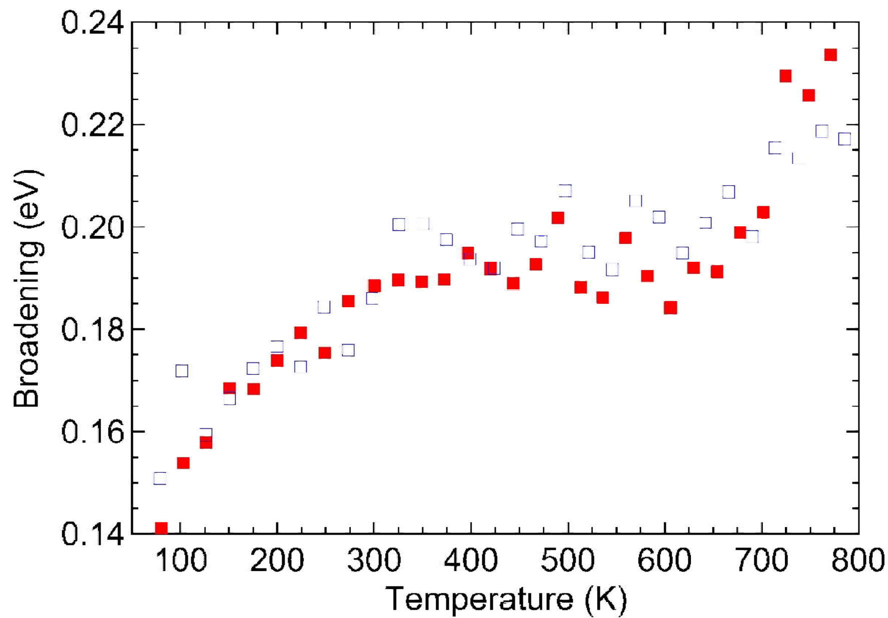

Figure 49: Temperature dependence of the E_0' broadening parameter Γ defined in Eq. (68) for bulk Ge (solid) and Ge on Si (open).

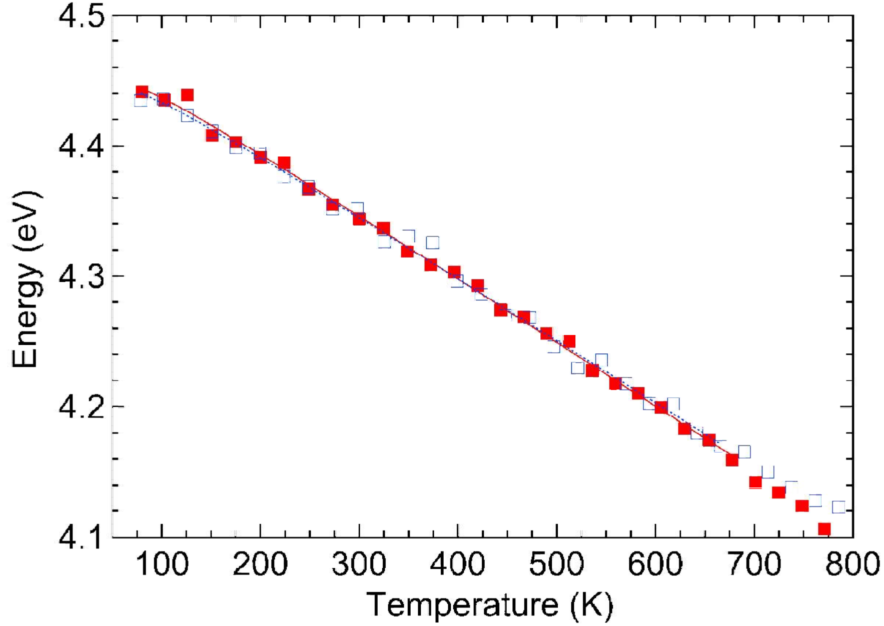

Figure 50: Temperature dependence of the E_2 energies of bulk Ge (solid) and Ge on Si (open). Solid lines show the best fit of the data using Eq. (72) with parameters given in Table 4.

The Bose-Einstein parameters for the E_2 energy are shown in Table 4. The amplitude and phase angle drop slightly with increasing temperature, see Figs. 51 and 52. The E_2 broadening increases with increasing temperature, see Fig. 53, and can be described with Eq. (73) using the parameters shown in Table 5. Our broadenings are slightly smaller than those found in [30].

5.8 Conclusion

Using spectroscopic ellipsometry, we measured the dielectric function of bulk Ge and epitaxial Ge on Si grown by UHV-CVD from 80 to 780 K and from 0.8 to 6.5 eV. By fitting the Savitzky-Golay derivatives of the spectra to analytical lineshapes, we determined the temperature-dependent critical-point parameters (energy, broadening, amplitude, and phase angle) of the E_1, $E_1+\Delta_1$, E_0'. and E_2

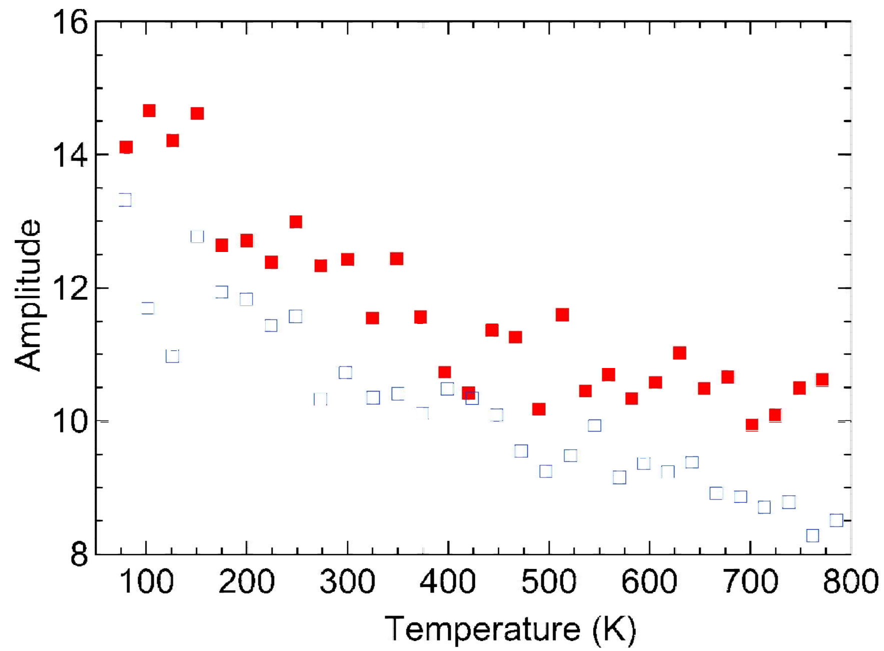

Figure 51: Temperature dependence of the amplitudes (A) of the E_2 transitions of bulk Ge (solid) and Ge on Si (open).

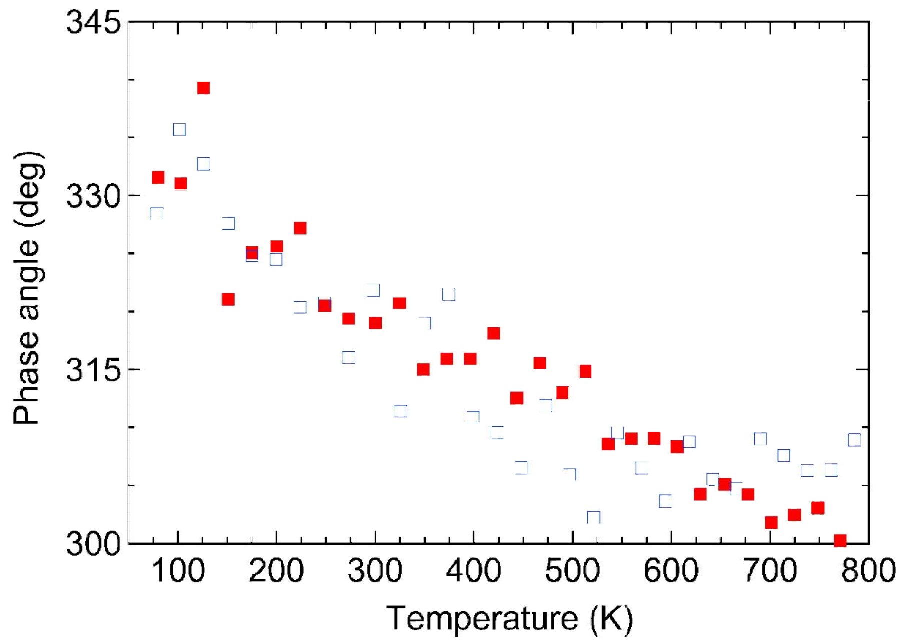

Figure 52: Temperature dependence of the excitonic phase angle (ϕ) defined in Eq. (68) for the E_2 transitions of bulk Ge (solid) and Ge on Si (open).

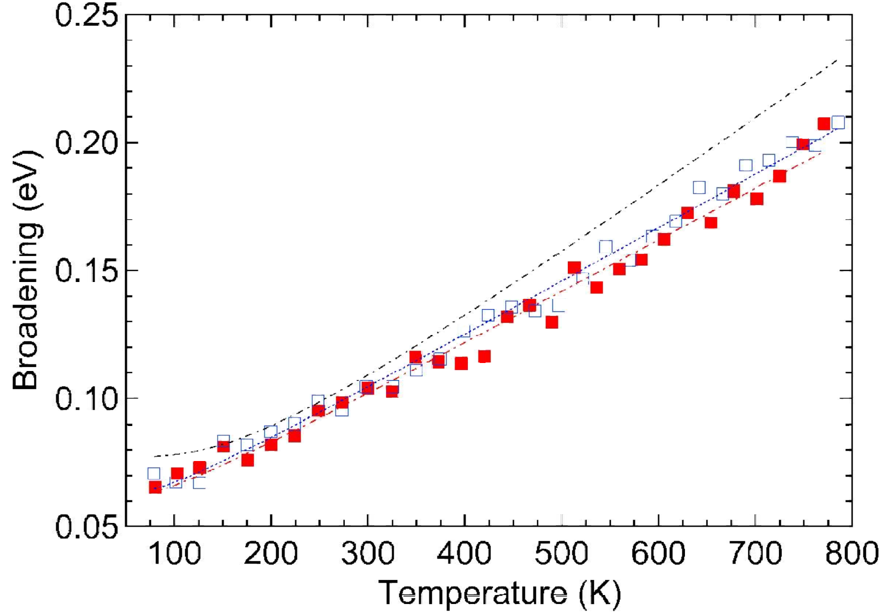

Figure 53: Temperature dependence of the E_2 broadening parameter Γ defined in Eq. (68) for bulk Ge (solid) and Ge on Si (open). The dash-dotted line shows the results of bulk Ge from [30] for comparison.

interband transitions.

The E_1 and $E_1+\Delta_1$ critical points in Ge epilayers on Si are redshifted compared to bulk Ge because of the temperature-dependent biaxial stress caused by the thermal expansion mismatch between Si and Ge. This redshift can be described with a model taking into account the thermal expansion coefficients, stress and strain determined using continuum elasticity theory, and the strain-induced shifts calculated from deformation potentials for the E_1 critical point.

This work follows our previous results [79] for the dielectric function of bulk Ge at 300 K. Future work will focus on the temperature dependence of the dielectric function for bulk Ge and a detailed analysis of the E_0 and $E_0+\Delta_0$ critical points, taking into account excitonic effects using the Tanguy model [181].

Acknowledgments

This work was supported by the Air Force Office of Scientific Research (FA9550-13-1-0022) and by the Army Research Office (W911NF-14-1-0072). A.A.M. acknowledges support from the New Mexico Alliance for Minority Participation (NM-AMP). Support during 2016 was provided by the National Science Foundation (DMR-1505172).

6 Band gap and strain engineering of pseudomorphic $Ge_{1-x-y}Si_xSn_y$ alloys on Ge and GaAs for photonic applications

Nalin S. Fernando, Stefan Zollner

Department of Physics, New Mexico State University, MSC 3D, P.O. Box 30001, Las Cruces, NM 88003

Ryan Hickey, John Hart, Ramsey Hazbun, Dainan Zhang, James Kolodzey

Department of Electrical and Computer Engineering, University of Delaware, 140 Evans Hall, Newark, DE 19716

Stefan Schoeche, James N. Hilfiker

J.A.Woollam Co., Inc., 645 M Street, Suite 102, Lincoln, NE 68508

6.1 Abstract

The authors report the compositional dependence of the direct and indirect band gaps of pseudomorphic $Ge_{1-x-y}Si_xSn_y$ alloys on Ge with [001] surface orientation determined from deformation potential theory and spectroscopic ellipsometry measurements. The effects of alloying Ge with Si and Sn and the strain dependence of the band gaps at the Γ, Δ, and L conduction band minima are discussed. Deformation potential theory predicts an indirect to direct crossover in pseudomorphic $Ge_{1-y-x}Si_xSn_y$ alloys on Ge only for very high Sn concentrations between 15 and 20%. No indirect to direct transition in pseudomorphic $Ge_{1-y}Sn_y$ alloys (x=0) on Ge is found for practically approachable Sn compositions (y<25%). The predictions for the compositional dependence of the E_0, E_1, and $E_1+\Delta_1$ band gaps were validated for pseudomorphic $Ge_{1-y}Sn_y$ alloys on Ge using spectroscopic ellipsometry. The complex pseudodielectric functions of pseudomorphic $Ge_{1-y}Sn_y$

alloys grown on Ge by molecular beam epitaxy were determined from Fourier transform infrared and ultraviolet-visible ellipsometry in the 0.1−6.6 eV energy range for Sn contents up to 11%, to investigate the compositional dependence of the band gaps. Critical point energies and related parameters were obtained by analyzing the second derivative spectra of the dielectric function of the $Ge_{1-y}Sn_y$ epilayer. Sn composition, thickness, and strain of the $Ge_{1-y}Sn_y$ epilayers on Ge are characterized by high resolution X-ray diffraction. The E_0, E_1, and $E_1 + \Delta_1$ band gaps of pseudomorphic $Ge_{1-y}Sn_y$ alloys on Ge obtained from ellipsometry are in good agreement with the theoretical predictions.

6.2 Introduction

The modern optoelectronic industry has been ruled by group IV semiconductors, mainly by cheap, stable, and widely available Si technology. One of the major issues with the currently existing Si and group IV semiconductor technology is that C, Si, and Ge are indirect band gap materials, while Sn is a semi-metal. The indirect nature of the fundamental band gap precludes the use of group IV semiconductor materials in the active layers for the design of optoelectronic devices, such as laser diodes, LEDs, amplifiers, photodetectors and modulators [182, 183]. Therefore, the need for a truly direct band gap to maximize the performance of devices, has limited the large scale integration of optoelectronic devices on the well established Si platform [184].

The Ge band structure is a strong function of strain: it has been predicted that the 0.140 eV separation of the L and Γ valleys of the conduction band can be overcome by introducing a ∼2% tensile strain and Ge becomes a direct band gap material [5, 21]. However, introducing a 2% tensile strain on Ge by thermal

expansion mismatch or by lattice mismatch is not practical.

The successful use of group III-V and II-VI alloy compounds for the design of optoelectronic devices paved the way to think about a new class of direct band gap alloy materials, containing Sn and group IV semiconductors. The optical properties of the group-IV alloy compounds containing C have been thoroughly studied [49]. The low solubility, large lattice mismatch, and the perturbation induced in the band structure restricted the applications of alloys containing C [49, 185]. Tight binding and pseudopotential band structure calculation predicted that $Ge_{1-y}Sn_y$ will become a direct band gap material for Sn contents >20% [186, 187]. More recent first principle calculations, using density functional theory (DFT) reported lower Sn (6-8%) contents for the indirect-direct band gap crossover, indicating the possibility of widespread applications of Ge-Sn based optoelectronic devices, integrated on Si platform [188, 189]. However, the low solubility of Sn in Ge (less than 1%), unstablity of the α-Sn cubic phase above 13° C, large lattice mismatch between Ge and Sn, and surface segregation of Sn atoms in Ge at high temperatures make the synthesis of $Ge_{1-y}Sn_y$ much more difficult [190]. Non equilibrium growth techniques, such as molecular beam epitaxy (MBE) and chemical vapor deposition (CVD) are needed for the successful growth of good crystalline quality, epitaxial $Ge_{1-y}Sn_y$ alloys on Ge/Si substrates.

He *at al.*, demonstrated the optical properties of $Ge_{1-y}Sn_y$ alloys up to 15% Sn for the first time and reported the tunable band gap (absorption features) and an indirect-direct transition of $Ge_{1-y}Sn_y$ [6]. Over a decade of research, with the improvements of the CVD and MBE techniques, allowed to grow high quality epitaxial $Ge_{1-y}Sn_y$ alloys up to 20% of Sn on Ge, Ge-buffered Si and Si substrates [55, 56, 57, 58]. A significant amount of research has been performed by the Kouvetakis group at Arizona State University to characterize the optical

properties of $Ge_{1-y}Sn_y$ alloys focusing on the design of Ge based photonic devices [55]. An indirect to direct transition has been reported for relaxed $Ge_{1-y}Sn_y$ on Si at about 6-11% Sn, depending on the growth conditions and the residual strain on the epilayer [6, 7, 8]. The strain, generated due to the lattice mismatch between the epilayer and the substrate, is relieved by creating dislocations and defects above a critical thickness. The defects and dislocations act as non-radiative recombination centers for the carriers in the medium, degrading the performance and the ability to control the band gaps of the devices. Therefore, the light emission of the $Ge_{1-y}Sn_y$ devices is too weak for practical applications. Under pseudomorphic growth, the substrate acts as a template for the growth of the epilayer. The in-plane ($a_{\|}$) lattice parameter of the alloy is forced to be equal to the substrate lattice parameter. The pseudomorphic growth is important to keep low defects densities and no dislocations, which significantly improves the performance of the devices, by reducing the non-radiative recombinations. Due to the large lattice mismatch between the substrate and the alloy, it is not possible to grow a pseudomorphic $Ge_{1-y}Sn_y$ on Si, a buffer layer such as Ge, $Ge_{1-x}Si_x$ or $Ge_{1-y}Sn_y$ is required for the epitaxial growth.

Initially proposed by Soref *et al.*, incorporation of Si into $Ge_{1-y}Sn_y$ minimizes the lattice mismatch between the Ge/Si substrate and the alloy, improving the thermal stability [191]. Ternary $Ge_{1-x-y}Si_xSn_y$ alloys allow to decouple the lattice parameter and the band structure, creating new opportunities to tune the band gap above and below the bad gap of Ge (0 to 1 eV), covering a wide range of operating wavelength of optoelectronic devices. Lattice mismatch and strain have become an important tool in band gap engineering, controlling the band gap allows to optimize the performance of the devices. Therefore $Ge_{1-x-y}Si_xSn_y$ may become the first direct band gap material fully integrated on Si technology.

Novel CVD routes designed and developed by the Kouvetakis group have allowed to grow high quality $Ge_{1-x-y}Si_xSn_y$ on Ge as well as on Si, with no dislocations propagating into the film [185, 192, 193]. Several groups have performed experiments as well as theoretical calculations to investigate the compositional and strain dependence of the optical properties [194, 195, 196, 197]. Although extensive experiments have been performed to characterize the optical and structural properties of $Ge_{1-x-y}Si_xSn_y$, most of them are remain unexplored.

Therefore, more studies are needed to understand and explore the unknown properties of $Ge_{1-x-y}Si_xSn_y$ ternary alloys for the application of direct band optoelectronic devices integrated on Si. First principle calculations are complicated, time consuming, and required sophisticated computing power. The deformation potential theory, which is based on experimental observations, is considered as a simple and accurate tool use to investigate the strain dependence of the band gaps. In this work, we have employed deformation potential theory to investigate the strain and compositional dependence of the conduction bands valleys at the Γ, L, and Δ symmetry points, and the three top valence bands at Γ. Considering the strain and alloying effects, the direct and indirect band gaps can be investigated to obtain the critical Si and Sn compositions for indirect-direct transitions.

6.3 Continuum elasticity and deformation potential theory

Several groups have reported the compositional dependence of the various band gaps of relaxed $Ge_{1-x-y}Si_xSn_y$ alloys at room temperature [66, 67, 68, 69, 194, 196, 197] . E_0^Γ is the direct band gap at the Γ-point. E_i^L and E_i^Δ are the indirect band gaps between the the valence band (VB) maximum at Γ and the conduction band (CB) minima at the L-point and along Δ. E_1 and $E_1 + \Delta_1$ are

the direct band gaps at or near the L-point split by spin-orbit interactions of the VB. The compositional dependence of the various room temperature band gaps of the relaxed (unstrained) $Ge_{1-x-y}Si_xSn_y$ alloys can be expressed as

$$\begin{aligned} E^{\mathrm{Ge}_{1-x-y}\mathrm{Si}_x\mathrm{Sn}_y}(x,y) = E^{\mathrm{Ge}}(1-x-y) + E^{\mathrm{Si}}x + E^{\mathrm{Sn}}y - \\ -b^{\mathrm{GeSn}}y(1-x-y) - b^{\mathrm{GeSi}}x(1-x-y) \\ -b^{\mathrm{SiSn}}xy, \end{aligned} \tag{75}$$

where E^j are the corresponding band gaps of the elements and b^{jk} (j, k=Si, Ge, Sn) the bowing parameters defining the deviation of the band gap from the linear interpolation. Gaps and bowing parameters are given in Table 6 for the various gaps.

By definition, we always use the VB maximum as our zero energy level. Under hydrostatic strain, this choice implies that the absolute deformation potential for the VB a_{VB} is zero. Theory shows that a_{VB} is small and its sign is not known. Under shear strain, when the VB splits, we still use the highest VB maximum as our energy reference level, which leads to an unphysical value of a_{VB}. The actual value of a_{VB} does not matter for our results, since we only report band gaps and splittings.

The compositional dependence of the CBs can then be obtained from the dependence of the corresponding band gaps of the alloys. To take into account how these bands and band gaps are changed in pseudomorphic alloys, we must first calculate the strain tensor caused by the lattice mismatch using continuum elasticity theory. Then, we calculate band gap shifts and splittings using deformation potentials.

The lattice parameters of relaxed $Ge_{1-x-y}Si_xSn_y$ alloys were calculated using a

linear interpolation (Vegard's Law) from the lattice parameters a_j of the elements

$$\begin{aligned} a^{\mathrm{rel}}_{\mathrm{Ge}_{1-x-y}\mathrm{Si}_x\mathrm{Sn}_y} = x a_{\mathrm{Si}} + y a_{\mathrm{Sn}} + (1-x-y) a_{\mathrm{Ge}} + \\ + \theta_{\mathrm{GeSn}}(1-x-y)y + \theta_{\mathrm{GeSi}}(1-x-y)x \\ + \theta_{\mathrm{SiSn}} xy \end{aligned} \tag{76}$$

with small quadratic deviations from linearity described by the bowing parameters θ_{jk}. Although extensive work has been done to characterize the compositional dependence of the lattice parameters of $\mathrm{Ge}_{1-y}\mathrm{Sn}_y$ alloys, a large discrepancy exists in the literature over the values of θ_{GeSn} [55, 56, 57, 58]. According to most recent findings, [57, 58, 59] the bowing parameter θ_{GeSn} is very small and Vegard's Law (θ_{GeSn}=0) can be used to accurately calculate the lattice parameters of $\mathrm{Ge}_{1-y}\mathrm{Sn}_y$ alloys. The bowing parameter for the lattice constant of $\mathrm{Ge}_{1-x}\mathrm{Si}_x$ alloys $\theta_{\mathrm{GeSi}}=-0.026$ (see Ref. [60]); and θ_{SiSn} was assumed to be zero, justified by the low Si and Sn content.

Depending on composition, the lattice parameter of relaxed $\mathrm{Ge}_{1-x-y}\mathrm{Si}_x\mathrm{Sn}_y$ will be larger, equal to (lattice matched to Ge), or smaller than the lattice parameter of the Ge substrate. Under pseudomorphic growth conditions, $\mathrm{Ge}_{1-x-y}\mathrm{Si}_x\mathrm{Sn}_y$ on Ge experiences a biaxial stress along the interface due to the lattice mismatch between the alloy layer and the Ge substrate, creating an in-plane strain given by

$$\epsilon_{\parallel}(x,y) = \frac{a_{\mathrm{Ge}} - a^{\mathrm{rel}}_{\mathrm{Ge}_{1-x-y}\mathrm{Si}_x\mathrm{Sn}_y}}{a^{\mathrm{rel}}_{\mathrm{Ge}_{1-x-y}\mathrm{Si}_x\mathrm{Sn}_y}}. \tag{77}$$

Within continuum elasticity theory and for [001] surface orientation, the pseudomorphic alloy layer is tetragonally deformed on the Ge substrate and the out-of-

plane strain

$$\epsilon_{\perp}(x,y) = -2\left(\frac{C_{12}}{C_{11}}\right)^{\mathrm{Ge}_{1-x-y}\mathrm{Si}_x\mathrm{Sn}_y} \epsilon_{\parallel}(x,y) \tag{78}$$

is related to $\epsilon_{\parallel}(x,y)$ through the ratio of the elastic constants C_{12}/C_{11}. For the elements, the elastic constants C_{mn} were taken from the literature [49, 61, 62], see Table 6, and scaled linearly with composition

$$C_{mn}^{\mathrm{Ge}_{1-x-y}\mathrm{Si}_x\mathrm{Sn}_y} = xC_{mn}^{\mathrm{Si}} + yC_{mn}^{\mathrm{Sn}} + (1-x-y)C_{mn}^{\mathrm{Ge}}. \tag{79}$$

The strain resulting from biaxial stress in the (100) surface has two components: The hydrostatic strain ϵ_H shifts the CB positions and the [001] shear strain ϵ_S lifts the degeneracy of the electronic bands. They are related to the in-plane and out-of-plane strain through [49]

$$\epsilon_H(x,y) = \left[\epsilon_{\perp}(x,y) + 2\epsilon_{\parallel}(x,y)\right]/3 \quad \text{and} \tag{80}$$

$$\epsilon_S(x,y) = \left[\epsilon_{\perp}(x,y) - \epsilon_{\parallel}(x,y)\right]/3. \tag{81}$$

In the absence of shear strain, the heavy (v_1) and light hole (v_2) bands are degenerate at the Γ point. Spin-orbit interactions separate the heavy and light hole bands from the split-off band (v_3). The [001] shear strain lifts the degeneracy of the VB edge, leading to an additional splitting. The energy positions of the

Table 6: Deformation potentials, band gaps, and bowing parameters for Ge, Si, and Sn and their alloys used in the model, in units of eV. Deformation potential parameters a, b, $\left[\Xi_d + \frac{1}{3}\Xi_u\right]^L$, Ξ_u^Δ, and $\left[\Xi_d + \frac{1}{3}\Xi_u\right]^\Delta$ were taken from Refs. [5, 49, 72, 202]. The band gaps E_0^Γ, E_i^L, E_i^Δ and related parameters were taken from Refs. [9, 68, 66, 67, 203, 204, 205]. The E_1, $E_1 + \Delta_1$ band gaps and related parameters were taken from Refs. [66, 69]. The asterisk indicates that the value of Ge was used for our calculations. Elastic constants C_{ij} are in units of GPa from Ref. [49, 55].

	Ge	Si	Sn	b_{GeSi}	b_{GeSn}	b_{SiSn}
a	-9.75	-10.12	-9.75*	-	-	-
b	-2.3	-2.2	-2.3*	-	-	-
$\left[\Xi_d + \frac{1}{3}\Xi_u\right]^L$	-3.6	-3.6*	-3.6*	-	-	-
Ξ_u^Δ	9.0	8.6	9.0*	-	-	-
$\left[\Xi_d + \frac{1}{3}\Xi_u\right]^\Delta$	1.31	1.5	1.31*	-	-	-
E_0^Γ	0.796	4.090	-0.413	0.210	2.46	13.2
E_i^L	0.655	1.930	0.006	0.0	1.03	0.0
E_i^Δ	0.900	1.120	0.900	0.21	0.21	0.0
E_1	2.120	-	1.270	-	1.650	-
$E_1 + \Delta_1$	2.310	-	1.770	-	1.050	-
Δ_0	0.300	0.043	0.800	-	-	-
C_{11}	128.5	166.0	69.0	-	-	-
C_{12}	48.3	63.9	29.3	-	-	-

top three VBs at the Γ point can be expressed as [49, 63, 64, 65]

$$E_{v_1} = -\frac{\Delta_0}{2} + \frac{3}{2}b\epsilon_S + \frac{1}{2}\sqrt{\Delta_0^2 + 6\Delta_0 b\epsilon_S + (9b\epsilon_S)^2}, \tag{82}$$

$$E_{v_2} = -3b\epsilon_S, \tag{83}$$

$$E_{v_3} = -\frac{\Delta_0}{2} + \frac{3}{2}b\epsilon_S - \frac{1}{2}\sqrt{\Delta_0^2 + 6\Delta_0 b\epsilon_S + (9b\epsilon_S)^2}. \tag{84}$$

The sign of the shear strain ϵ_S determines whether v_1 or v_2 is the highest VB. Note that the [001] shear deformation potential b for the VB has a negative value. Δ_0 is the spin-orbit splitting of the VB at the Γ point. Its compositional dependence was obtained by linearly interpolating the elemental end values, see Table 6:

$$\Delta_0^{\mathrm{Ge}_{1-x-y}\mathrm{Si}_x\mathrm{Sn}_y} = x\Delta_0^{\mathrm{Si}} + y\Delta_0^{\mathrm{Sn}} + (1-x-y)\Delta_0^{\mathrm{Ge}}. \tag{85}$$

The energy shifts of the CB at the Γ and L points due to the hydrostatic deformation can be calculated using [5, 70, 71, 72]

$$\Delta E_c^{\Gamma} = 3a\epsilon_H \quad \text{and} \quad \Delta E_c^{L} = 3\left[\Xi_d + \frac{1}{3}\Xi_u\right]^L \epsilon_H, \tag{86}$$

where a and $\left[\Xi_d + \frac{1}{3}\Xi_u\right]^L$ are the hydrostatic deformation potentials for the CB at the Γ and L points, respectively. The [001] shear strain does not split the CB at Γ (because it is non-degenerate) and at the L-point.

At the Δ-minimum, however, we have to consider both hydrostatic and shear contributions. The [001] shear strain splits the CB at the six Δ minima into a doublet and a quadruplet, in addition to the hydrostatic strain shift. The energies

can be expressed as [5, 70, 71, 72]

$$\Delta E_c^{\Delta 2} = 2\epsilon_S \Xi_u^{\Delta} + 3\left[\Xi_d + \frac{1}{3}\Xi_u\right]^{\Delta} \epsilon_H \quad \text{and} \tag{87}$$

$$\Delta E_c^{\Delta 4} = -\epsilon_S \Xi_u^{\Delta} + 3\left[\Xi_d + \frac{1}{3}\Xi_u\right]^{\Delta} \epsilon_H, \tag{88}$$

where Ξ_u^{Δ} is the [001] shear deformation potential and $\left[\Xi_d + \frac{1}{3}\Xi_u\right]^{\Delta}$ the hydrostatic deformation potential of the CB at the Δ minima.

Combining the compositional dependence of the band gaps of the relaxed (unstrained) ternary alloys, given by Eq. (75), with the energy shifts and splittings of the CBs and VBs under strain using deformation potential theory, the compositional dependence of the band gaps of pseudomorphic $Ge_{1-x-y}Si_xSn_y$ on Ge at the Γ, L, and Δ CB minima can be obtained. All parameters used for the calculation are listed in Table 6. Results are shown in Fig. 54.

The band gaps at the Γ, L, and Δ minima as a function of Si and Sn compositions show a similar qualitative behavior: The band gaps are widening with increasing Si and narrowing with increasing Sn content, as expected. The thick solid line, $y = 0.3x$, indicates the lattice matched compositions of $Ge_{1-x-y}Si_xSn_y$ on Ge, consistent with the previously reported value $y = 0.27x$ (see Ref. [68]). The small discrepancy is caused by slightly different bowing parameters used in the calculation of the lattice parameters. This line separates a positively strained (tensile) region from a negatively strained (compressive) region. A Ge-like band gap between 0.66 and 0.82 eV can be obtained for unstrained $Ge_{1-x-y}Si_xSn_y$ by varying the Si and Sn content.

A singularity of the band gaps is observed as the sign of the in-plane strain changes from tensile to compressive. As mentioned earlier, the sign of the in-

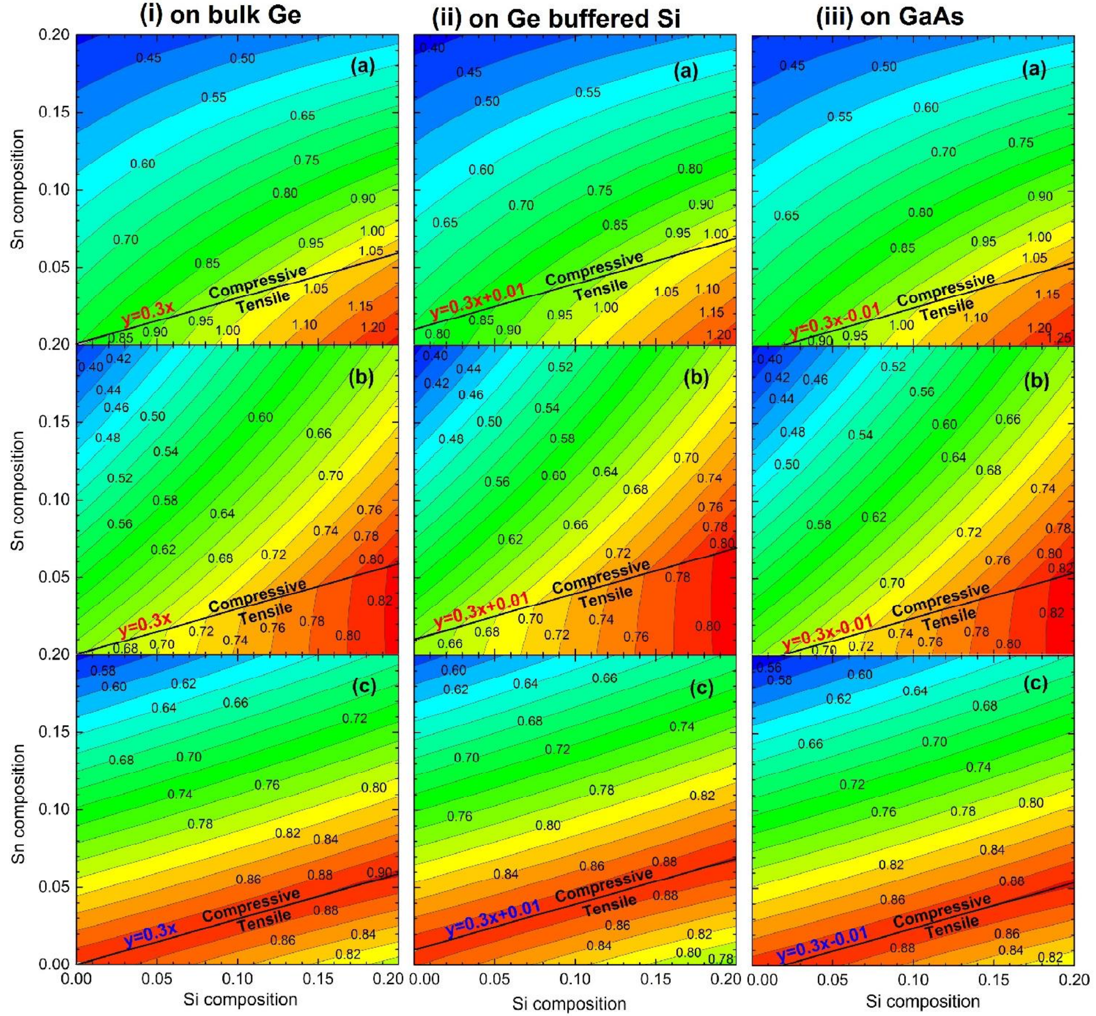

Figure 54: Band structure maps (energy in eV versus composition) of pseudomorphic $Ge_{1-x-y}Si_xSn_y$ alloys (i) on Ge for band gaps at the (a) Γ, (b) L, and (c) Δ CB minima, (ii) grown on a thick Ge buffer on a Si substrate, at the (a) Γ, (b) L, and (c) Δ CB minima. The Ge buffer is assumed to have been grown at 770 K. We assume full relaxation of the buffer at the growth temperature, but no additional relaxation when cooling down to room temperature, resulting in a tensile biaxial stress of the Ge buffer, and (iii) on GaAs substrate at the (a) Γ, (b) L, and (c) Δ CB minima.

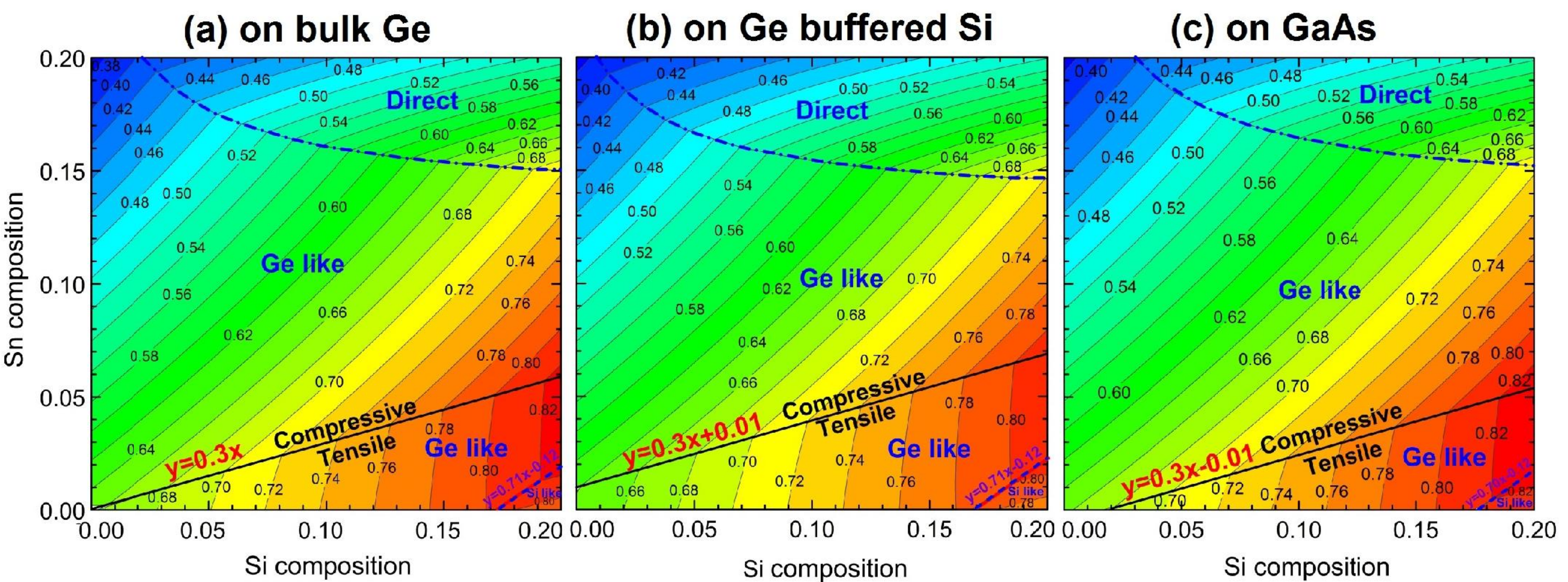

Figure 55: Compositional dependence of the lowest band gap (either direct or indirect) of pseudomorphic $Ge_{1-x-y}Si_xSn_y$ alloys (a) on Ge, (b) on Ge buffered Si, and (c) on GaAs.

plane strain determines whether v_1 or v_2 is the highest VB. The light hole v_2, given by Eq. (83), is the highest VB for compressively strained pseudomorphic $Ge_{1-x-y}Si_xSn_y$ alloys on Ge, while the heavy hole v_1, given by Eq. (82), becomes the highest VB under tensile in-plane strain. Also, the $\Delta 4$ quadruplet is lower in energy compared to the $\Delta 2$ doublet in the compressively strained region, while tensile strain makes the $\Delta 2$ energy lower. Therefore, the band gap E_i^{Δ} at the Δ minimum is associated with the $\Delta 4$ quadruplet under compressive strain, while the $\Delta 2$ doublet determines E_i^{Δ} in tensile pseudomorphic $Ge_{1-x-y}Si_xSn_y$ on Ge. Hence, the behavior of the highest VB and the lowest CB at the Δ minimum with respect to strain explain the singularity in the predicted band gaps when the sign of the strain changes.

The smallest band gap, either direct or indirect, of pseudomorphic $Ge_{1-x-y}Si_xSn_y$ alloys on Ge is shown in Fig. 55. The dashed-dotted curve between 15 and 20% tin represents an indirect to direct band gap crossover: Above this line, pseudomorphic $Ge_{1-x-y}Si_xSn_y$ on Ge becomes a direct band gap material. This condition requires a very large Sn content, which has not yet been achieved experimentally due to the low solubility of Sn in Ge and Si. The dashed line, $y = 0.71x - 0.12$, shows a transition of the smallest band gap from the L valley (Ge like) to the Δ valley of the CB (Si like). The smallest band gap is associated with the L-valley of the CB (Ge like) in the region bounded by the dashed-dotted and dashed lines.

As a special case, we consider pseudomorphic $Ge_{1-y}Sn_y$ alloys grown pseudomorphically on Ge (x=0), see Fig. 56. This figure shows the position of the top three VB maxima calculated from Eqs. (82)-(84) and the various band gaps E_0^{Γ}, E_i^L, $E_i^{\Delta 2}$, and $E_i^{\Delta 4}$ from Eqs. (75) and (86)-(88) versus Sn content We clearly see that the indirect gap E_i^L is lower than the direct gap E_0^{Γ} for y<25%, indicating that pseudomorphic $Ge_{1-y}Sn_y$ alloys on Ge will not become a direct band gap

material for practically achievable Sn compositions, which is consistent with the models recently reported [9, 206].

There is strong interest in growing $Ge_{1-x-y}Si_xSn_y$ alloys on Ge buffered Si substrates instead of directly on a Ge substrate [73]. The Ge buffer on Si is under tensile biaxial stress because of the different thermal expansion coefficients of Si and Ge, [201] which can be accurately modeled, assuming full relaxation of the Ge buffer at the growth temperature T_g (of the buffer) and no additional relaxation while cooling down [81]. The thermal strain increases the in-plane lattice parameter of the Ge buffer, which in turn affects the strain of the pseudomorphic $Ge_{1-x-y}Si_xSn_y$ alloy layer grown on top of the Ge buffer. This reduces the compressive strain in the pseudomorphic $Ge_{1-x-y}Si_xSn_y$ on the Ge buffer and thus lowers the critical Si and Sn contents needed to achieve a direct band gap material. Increasing the growth temperature of the Ge buffer increases its tensile strain, which reduces the critical Sn content more, but even the highest possible growth temperature of the Ge buffer (melting point of Ge, T_g=1200 K) reduces the critical Sn content for the indirect to direct transition by only 1%. In Figs. 54(ii) and 55(b), we show the band gaps of $Ge_{1-x-y}Si_xSn_y$ alloys grown pseudmorphically on Ge buffered Si substrates, where the Ge buffer was grown at T_g=770 K. For such alloys, the strain-free condition for the alloy composition becomes $y = 0.3x + 0.01$.

Similarly, one can also grow $Ge_{1-x-y}Si_xSn_y$ alloys pseudomorphically on a bulk GaAs substrate. Since the GaAs lattice constant is slightly smaller than that of Ge, growth on GaAs reduces the tensile strain or increases the compressive strain of $Ge_{1-x-y}Si_xSn_y$ alloys compared to growth on bulk Ge. For such alloys on GaAs, the strain-free condition for the alloy composition becomes $y = 0.3x - 0.01$. In Figs. 54(iii) and 55(c), we show the band gaps of $Ge_{1-x-y}Si_xSn_y$ alloys grown

pseudomorphically on bulk GaAs. To achieve a direct band gap in pseudomorphic $Ge_{1-x-y}Si_xSn_y$ alloys on GaAs, a slightly higher tin content is required than for similar pseudomorphic alloys grown on bulk Ge.

Finally, we also discuss the compositional dependence of the E_1 and $E_1+\Delta_1$ interband transitions in pseudomorphic $Ge_{1-y}Sn_y$ alloys (x=0) on Ge. These transitions occur at the L-point of the Brillouin zone and along the Λ direction. They are easily observed in the optical constants of Ge and related materials using spectroscopic ellipsometry measurements [81]. The strain dependence of these transitions is given by [49, 69, 198, 200]

$$E_1^s = E_1^o + \frac{\Delta_1}{2} + \Delta E_H - \sqrt{\frac{(\Delta_1)^2}{4} + (\Delta E_S)^2} \quad (89)$$

$$(E_1 + \Delta_1)^s = (E_1 + \Delta_1)^o - \frac{\Delta_1}{2} + \Delta E_H + \sqrt{\frac{(\Delta_1)^2}{4} + (\Delta E_S)^2}, \quad (90)$$

where the superscripts s and 0 denote the band gaps of the strained and relaxed alloys, respectively. The spin-orbit splitting Δ_1 of the VB at the L point is taken as the difference between the E_1 and $E_1 + \Delta_1$ energies with parameters in Table 6. ΔE_H and ΔE_S are the energy shifts due to hydrostatic and shear strain, respectively, calculated using

$$\Delta E_H = \sqrt{3} D_1^1 \epsilon_H \quad \text{and} \quad \Delta E_S = \sqrt{6} D_3^3 \epsilon_S, \quad (91)$$

where D_1^1=−5.4 eV and D_3^3=−3.8 eV are the hydrostatic and shear deformation potentials for $Ge_{1-y}Sn_y$ alloys taken from Ref. [69] (significantly lower than for bulk Ge). The sign of D_3^3 affects the intensities of the two critical points [49] (as discussed below) and therefore we follow the sign convention from Ref. [49].

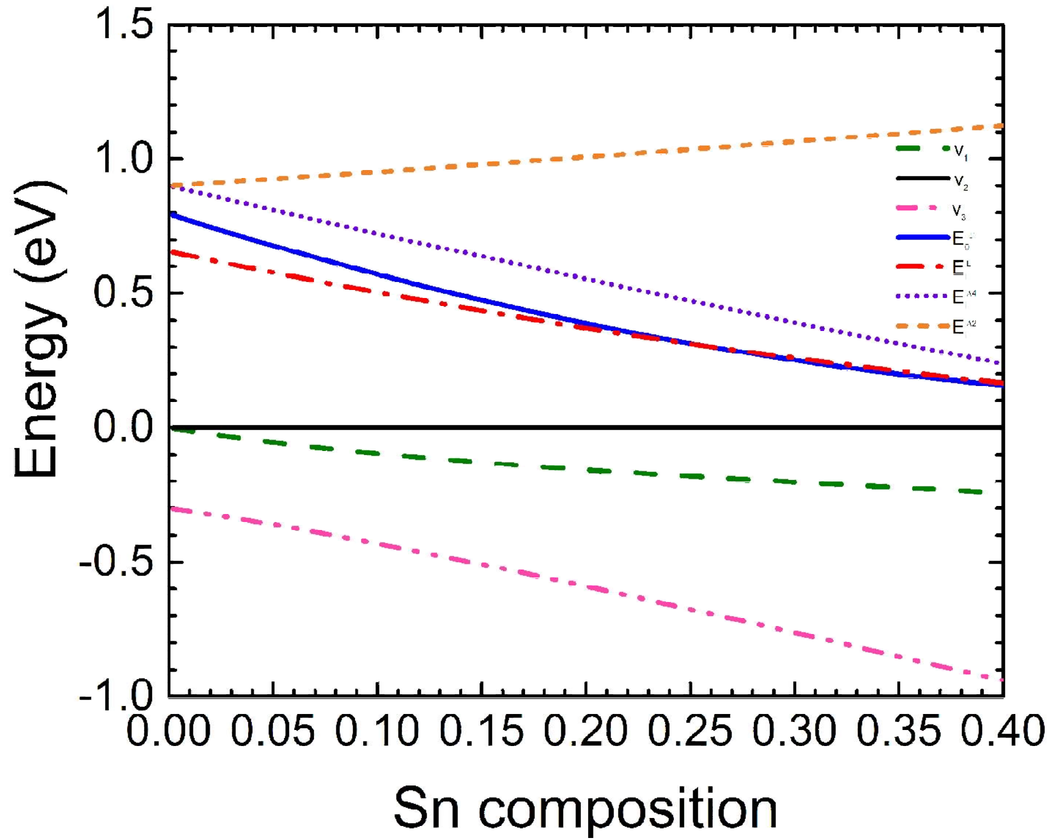

Figure 56: Energies of the three top valence bands at the Γ point (v_1, v_2, v_3), the conduction band minimum at the Γ point (E_c^Γ) and at the L point (E_c^L) in pseudomorphic $Ge_{1-y}Sn_y$ alloys grown on Ge as a function of Sn content calculated using Eqs. (82)-(88). The reference energy (0 eV) was chosen as the valence band maximum for any composition and shear strain.

The band gaps of the relaxed alloys and other parameters were taken from the literature and are listed in Table 6. As explained below, our own experimental values for these deformation potentials are slightly different, but agree within the errors, and therefore we used the parameters established in Ref. [69] for our calculations.

6.4 Pseudomorphic $Ge_{1-y}Sn_y$ alloys on Ge: Sample preparation and characterization

To avoid the complexity of the ternary $Ge_{1-x-y}Si_xSn_y$ system with too many compositional parameters to be determined precisely, pseudomorphic $Ge_{1-y}Sn_y$ binary alloy layers on Ge were prepared by molecular beam epitaxy (MBE) to validate the theory described in the previous section. These epilayers were grown using a modified EPI 620 MBE system with a base pressure of 1.3×10^{-8} Pa and utilizing Knudsen thermal effusion cells with pyrolytic BN crucibles for both Ge and Sn. Intrinsic (001) Ge substrates were prepared by wet chemical cleaning [75] before quickly being loaded into the MBE introduction chamber and taken to ultra-high vacuum. The substrates were slowly heated to 450°C overnight, then taken to 650°C for one hour before individually being transferred into the main MBE growth chamber. Each wafer was flash heated to 850°C for 10 min, then cooled to the growth temperature between 150°C and 250°C (as measured via thermocouple) prior to opening the Ge and Sn cell shutters for growth. The Sn composition was varied by changing the Sn effusion cell temperature while keeping the Ge cell temperature constant across all growths, achieving a growth rate of 0.6 to 0.7 nm/min.

A PANalytical Empyrean diffractometer, operated at 45 kV and 40 mA, was used for the high resolution X-ray diffraction (HRXRD) analysis of $Ge_{1-y}Sn_y$ epitaxial layers. Our high resolution configuration consists of a two-bounce Ge(220) hybrid monochromator, which offers a high-intensity well-collimated beam of monochromatic Cu $K\alpha_1$ radiation (1.5406 Å) and a three-bounce Ge (220) analyzer in front of the Xe proportional detector. We acquired symmetric (004) $\omega - 2\theta$ diffraction curves and $2\theta/\omega - 2\theta$ reciprocal space maps (RSMs) for sym-

metric (004) and asymmetric ($\bar{2}\bar{2}4$) grazing exit reflections at room temperature to investigate the pseudomorphic nature, crystalline quality, lattice parameters, and thicknesses of the layers.

The optical properties of the $Ge_{1-y}Sn_y$ alloys were characterized using spectroscopic ellipsometry with a combination of two ellipsometers for different spectral ranges. The ellipsometric angles ψ and Δ were acquired from 0.5 to 6.6 eV with 0.01 eV steps at four angles of incidence (60°, 65°, 70°, 75°) on a J.A. Woollam vertical variable angle-of-incidence rotating-analyzer ellipsometer [170] with a computer-controlled Berek waveplate compensator, as described elsewhere [172]. To reduce experimental errors, all data were obtained by averaging two-zone measurements with equal and opposite polarizer angles. In the infrared spectral range from 250 to 7000 cm^{-1}, we measured on a Woollam FTIR-VASE ellipsometer, which is based on a fixed analyzer (0° and 180°) and polarizer (±45°) and a rotating compensator, at the same four angles of incidence. In the FTIR experiments, the spectral resolution was set to 16 cm^{-1} with long signal averaging (three measurement cycles, each with 15 spectra per compensator revolution, and 20 scans per spectrum) to improve the signal to noise ratio. The ellipsometric angles (ψ and Δ) and the Fresnel reflectance ratio $\rho = e^{i\Delta}\tan\psi$ are related to the pseudo-refractive index $\hat{n}$ and the pseudo-dielectric function $\hat{\epsilon} = \hat{n}^2$ of the sample through

$$\rho = \frac{(\hat{n}\cos\phi_0 - \cos\phi_1)(\cos\phi_0 + \hat{n}\cos\phi_1)}{(\hat{n}\cos\phi_0 + \cos\phi_1)(\cos\phi_0 - \hat{n}\cos\phi_1)}, \tag{92}$$

where ϕ_0 is the angle of incidence and ϕ_1 the angle of refraction.

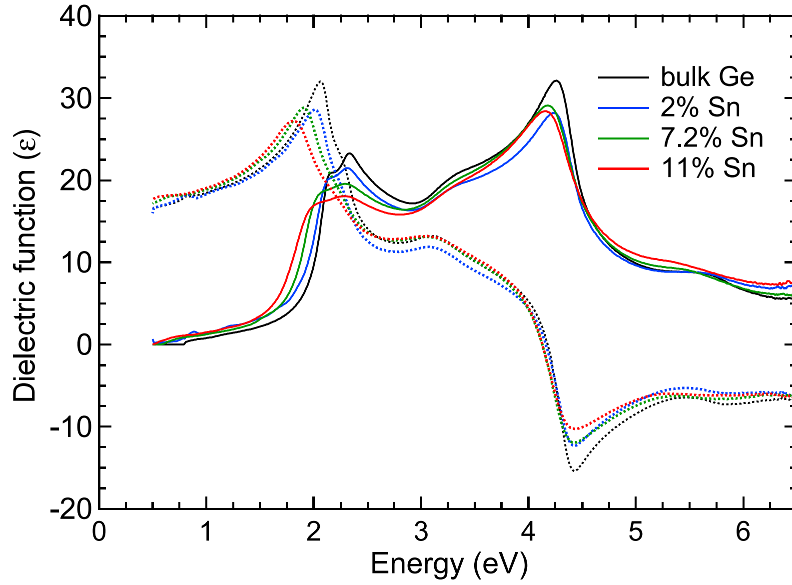

Figure 57: Real (dashed) and imaginary (solid) parts of the complex dielectric function of pseudomorphic $Ge_{1-y}Sn_y$ on Ge versus photon energy determined from ellipsometry.

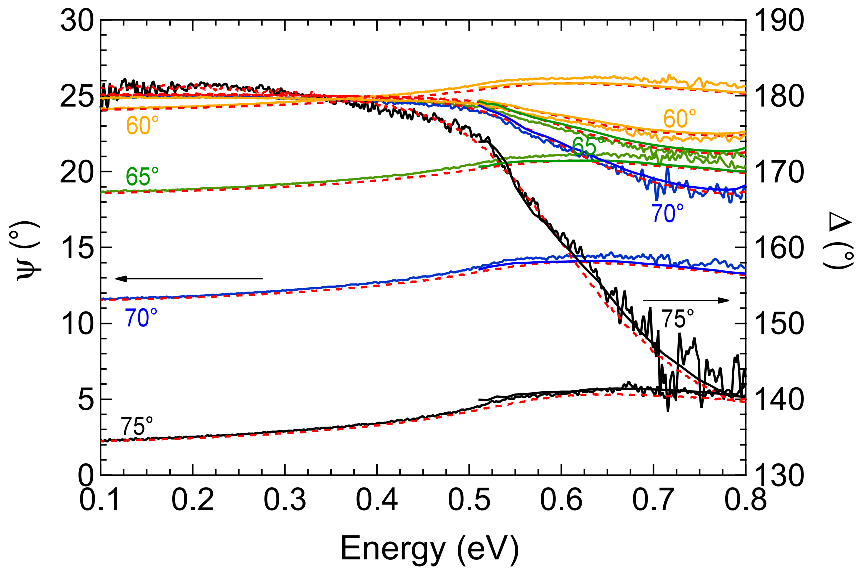

Figure 58: Experimental data (solid) and model (dashed) of the ellipsometric angles Ψ and Δ for pseudomorphic $Ge_{0.89}Sn_{0.11}$ on Ge versus photon energy in the infrared region obtained by merging data from two instruments.

6.5 Ellipsometry data analysis

The dielectric functions $\epsilon(\hbar\omega)$ of pseudomorphic $Ge_{1-y}Sn_y$ alloys on Ge were obtained by analyzing the ellipsometric angles with a multilayer model (GeO_2 /$Ge_{1-y}Sn_y$ /Ge). $\epsilon(\hbar\omega)$ for GeO_2 and Ge was used in tabulated form [79]. The dielectric functions of $Ge_{1-y}Sn_y$ were described with a parametric oscillator model citeHeJo98, which imposes Kramers-Kronig consistency between the real and imaginary parts of ϵ. In the first step of the fit, the oxide and $Ge_{1-y}Sn_y$ layer thicknesses and all parameters in the parametric oscillator model for $Ge_{1-y}Sn_y$ were adjusted. In the second step, all parameters were kept fixed at the values obtained in the first step, and the data were fitted again at each measured photon energy by taking the values of ϵ_1 and ϵ_2 for $Ge_{1-y}Sn_y$ as adjustable parameters (known as point-by-point fit) to obtain the final tabulated dielectric function of $Ge_{1-y}Sn_y$. We confirmed that the results from the second step, shown in Fig. 57, were still Kramers-Kronig consistent. Redshifting of the dielectric function and broadened critical points (CPs) with respect to bulk Ge with increasing Sn percentage indicates the alloying and strain effects of Sn on the Ge band structure.

Our main focus here was to investigate the compositional dependence of the CPs associated with the E_0, E_1, and $E_1+\Delta_1$ optical transitions. The E_1 and $E_1+\Delta_1$ CPs can be described using an expression for a mixture of a two-dimensional minimum and a saddle point [30]

$$\epsilon(\hbar\omega) = C - A\ln(\hbar\omega - E_g - i\Gamma)\, e^{i\phi}, \tag{93}$$

where $\hbar\omega$ is the photon energy, A the amplitude, E_g the CP energy, Γ the broadening parameter, and ϕ the excitonic phase angle, which describes the amount of

mixing. The contribution of the CPs to the dielectric function can be enhanced by analyzing the second derivatives of ϵ. The real and imaginary parts of the tabulated dielectric function obtained by point-by-point fitting were numerically differentiated and smoothed using ten Savitzky-Golay coefficients for second-order derivatives with a polynomial degree of three to obtain a good signal to noise ratio without distorting the line shape [84]. The second derivative spectra of the dielectric function for the $Ge_{1-y}Sn_y$ were fitted using Eq. (93). Both E_1 and $E_1 + \Delta_1$ were fitted simultaneously and the excitonic phase angle ϕ was forced to take the same value for both CPs.

The poor signal to noise ratio of the ellipsometric angles ψ and Δ obtained from FTIR ellipsometry between 0.1 and 0.9 eV makes the second derivative analysis of the tabulated dielectric function impractical. A different approach has to be followed to extract the compositional dependence of the E_0 band gap: Following of D'Costa *et al.,* [66] we calculated the second derivatives of the parametric dielectric function: For a given sample, two data sets from 0.5 to 3 eV and from 0.1 to 0.9 eV, taken on two instruments under slightly different conditions, were fitted simultaneously using a single model to obtain the parametric dielectric function of the $Ge_{1-y}Sn_y$ alloy layer, assuming two slightly different surface oxide thicknesses. This parametric dielectric function was then used for the second derivative line shape analysis and fitted with a three dimensional critical point [66]

$$\epsilon\left(\hbar\omega\right) = C - Ae^{i\phi}\left(\hbar\omega - E_g + i\Gamma\right)^{1/2}. \tag{94}$$

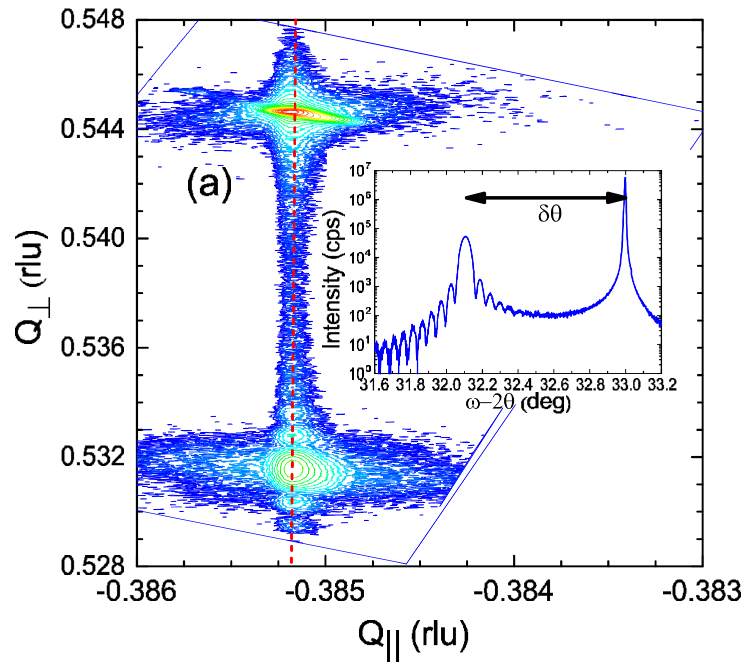

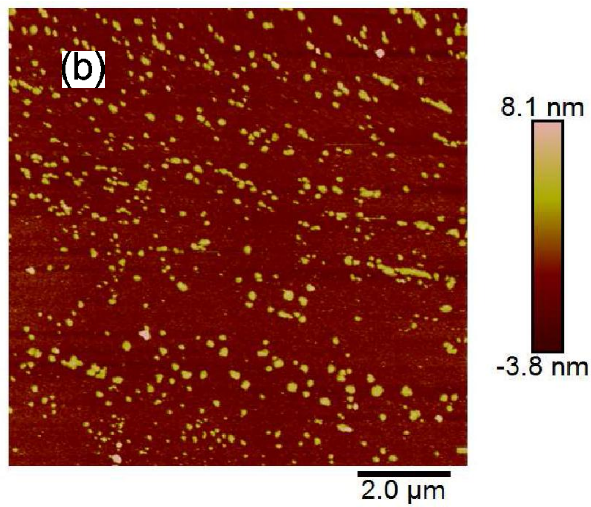

Figure 59: (a) High-resolution X-ray diffraction $(\bar{2}\bar{2}4)$ grazing exit reciprocal space map showing contours of equal intensity of a $Ge_{0.904}Sn_{0.096}$ layer on Ge. The Ge substrate and the $Ge_{1-y}Sn_y$ layer peaks have the same $Q_{\|}$ indicating that the epilayer is fully strained. Inset: Logarithmic intensity versus diffraction angle for the symmetric (004) ω-2θ X-ray reflections. (b) Atomic force microscopy image of the GeSn surface showing an RMS roughness of 1.6 nm.

6.6 Results and discussion

High resolution X-ray diffraction was used to characterize the crystalline quality, composition, strain, and thickness of the $\mathrm{Ge}_{1-y}\mathrm{Sn}_y$ epilayers on Ge. $\omega - 2\theta$ scans of symmetric (004) reflections showed two peaks, see the inset in Fig. 59(a). The sharp peak near 33.0° arises from the Ge substrate. The broader peak corresponding to the $\mathrm{Ge}_{1-y}\mathrm{Sn}_y$ epilayer is shifted to lower angles (away from the Ge peak) as the Sn composition increases, as a result of the increased out-of-plane lattice constant $a_\perp$ of the epilayer due to composition and biaxial compressive stress. The peak separation $\delta\theta$ is related to the ratio $a_{\mathrm{Ge}}/a_\perp$. Assuming that the epilayer is not tilted relative to the Ge substrate, which we confirmed by (004) symmetric reciprocal space maps (RSMs), $a_\perp$ can be calculated from [86] $a_{\mathrm{Ge}}/a_\perp = 1+\delta\theta \cot\theta$, where θ is the Bragg angle of bulk Ge. From the out-of-plane lattice constant $a_\perp$ and the in-plane lattice constant $a_\parallel = a_{\mathrm{Ge}}$ (pseudomorphic condition), we calculated the in-plane strain

$$\epsilon_\parallel = \frac{a_\parallel - a_\perp}{a_\perp + 2\left(\frac{C_{12}}{C_{11}}\right)^{\mathrm{Ge}_{1-y}\mathrm{Sn}_y} a_\parallel} \tag{95}$$

and the relaxed lattice constant

$$a^{\mathrm{rel}}_{\mathrm{Ge}_{1-y}\mathrm{Sn}_y} = \frac{a_\parallel}{\epsilon_\parallel + 1}, \tag{96}$$

from which the tin content y could be determined using Vegard's Law, see Eq. (76) and the solid line in Fig. (60). The resulting value y is plotted along the horizontal axis in our figures showing experimental results and also listed in Table 7.

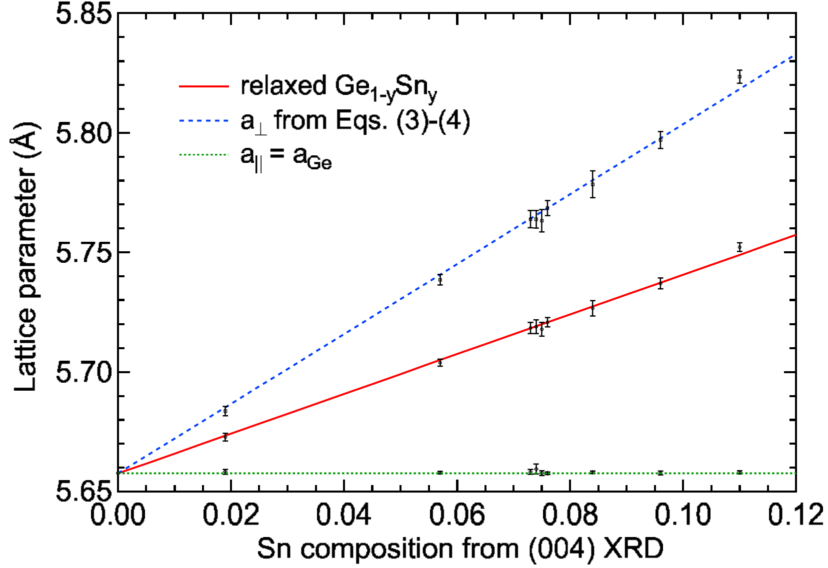

Figure 60: Compositional dependence of the lattice parameter of relaxed $Ge_{1-y}Sn_y$ alloys calculated from Vegard's Law shown in Eq. (76) (solid) and out-of-plane lattice parameter $a_\perp$ of pseudomorphic $Ge_{1-y}Sn_y$ alloys on Ge (dashed) from Eqs. (76)-(78). The dotted line shows the Ge lattice constant. Symbols show the in-plane and out-of-plane lattice constants $a_\perp$ and $a_\parallel$ determined from $(\bar{2}\bar{2}4)$ grazing exit reciprocal space maps and the relaxed lattice constant from Eqs. (95)-(96).

All samples showed (004) Pendellösung fringes around the epilayer peak, indicating a uniform thickness of a high quality (coherent) $Ge_{1-y}Sn_y$ epilayer. The spacing between the fringes can be used to extract the thickness of the epilayer [58, 86, 87], in good agreement with spectroscopic ellipsometry, see Table 7.

Asymmetric $(\bar{2}\bar{2}4)$ grazing exit $\omega - 2\theta/2\theta$ RSMs, shown in Fig. 59(a), were also acquired to extract the reciprocal lattice coordinates $Q_\parallel$ and $Q_\perp$ along the [110] and [001] directions of the $Ge_{1-y}Sn_y$ epilayers and to investigate the degree of relaxation of the epilayer on Ge. The Ge substrate and the epilayer peaks have the same $Q_\parallel$, indicating that the $Ge_{1-y}Sn_y$ epilayer is fully strained to the Ge substrate. The AFM characterization of the surface roughness for the same sample is shown in Fig. 59(b). The sample has an RMS roughness of 1.6 nm,

indicating the reliability of the optical characterization techniques used in this paper.

The $Q_{\|}$ and $Q_{\perp}$ maxima are related to the out-of-plane [88]

$$a_{\perp} = \frac{Q_{\perp \mathrm{Ge}} - Q_{\perp \mathrm{GeSn}}}{Q_{\perp \mathrm{GeSn}}} a_{\mathrm{Ge}} + a_{\mathrm{Ge}} \tag{97}$$

and in-plane lattice parameters [88]

$$a_{\|} = \frac{Q_{\| \mathrm{Ge}} - Q_{\| \mathrm{GeSn}}}{Q_{\| \mathrm{GeSn}}} a_{\mathrm{Ge}} + a_{\mathrm{Ge}}, \tag{98}$$

which are shown by symbols in Fig. 60. The pseudomorphic condition ($a_{\|} = a_{\mathrm{Ge}}$) is satisfied very well. Overall, the ($\bar{2}\bar{2}4$) XRD results are consistent with the (004) XRD results, which we used to determine composition. Therefore, the relaxed lattice constants calculated from Eqs. (95)-(96) shown by symbols agree well with Vegard's Law (solid line).

The sign and magnetitude of the in-plane, out-of-plane, hydrostatic, and shear strain calculated from Eqs. (76)-(78) and (80)-(81) are shown by lines in Fig. 61. Strains determined from the in-plane and out-of-plane lattice parameters measured by ($\bar{2}\bar{2}4$) XRD are also shown (symbols). These pseudomorphic $\mathrm{Ge}_{1-y}\mathrm{Sn}_y$ alloys are described well by continuum elasticity theory with the elastic constants given by Eq. (79).

The measured Sn composition and thickness from (004) XRD and the in-plane strain $\epsilon_{\|}$ and out-of-plane strain $\epsilon_{\perp}$ from ($\bar{2}\bar{2}4$) RSMs for pseudomorphic $\mathrm{Ge}_{1-y}\mathrm{Sn}_y$ alloys on Ge samples are summarized in Table 7.

The compositional dependence of the direct and indirect band gaps derived from the bands (in Fig. 56) is shown in Fig. 62 (lines). The E_0 band gaps mea-

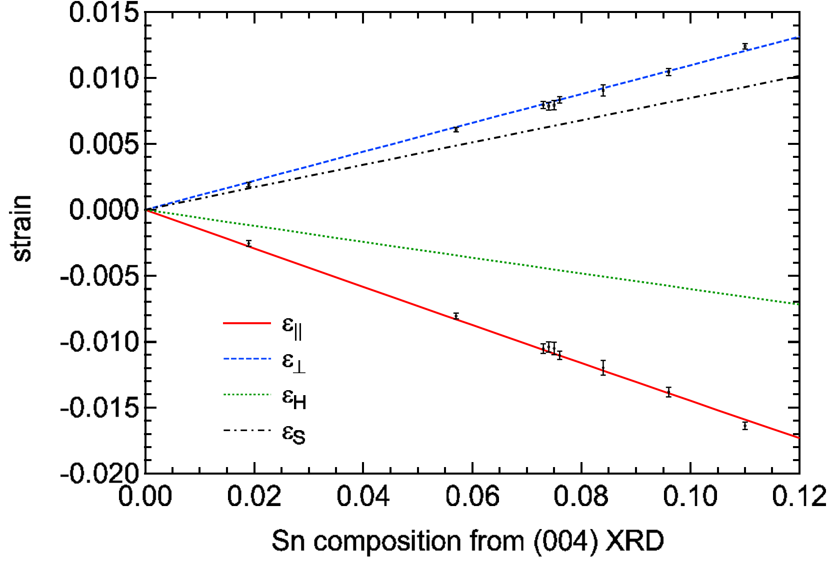

Figure 61: Lines show the compositional dependence of the in-plane $\epsilon_{\parallel}$, out-of-plane $\epsilon_{\perp}$, hydrostatic ϵ_H, and shear strain ϵ_S for pseudomorphic $Ge_{1-y}Sn_y$ alloys on Ge calculated using Eqs. (77)-(78) and (80)-(81). In-plane (∘) and out-of-plane strain (□) results derived from ($\bar{2}\bar{2}4$) XRD.

sured by FTIR ellipsometry (∘) are in excellent agreement with the theoretical predictions. The slight discrepancy with the values reported in Ref. [200] (+), where a Ge buffer layer on Si is used to grow $Ge_{1-y}Sn_y$, may be due to the tensile strain caused by the thermal expansion mismatch between the Ge buffer and the Si substrate. The resulting strain affects the lattice parameter of the Ge buffer and reduces the compressive strain of the pseudomorphic $Ge_{1-y}Sn_y$ epilayer (dotted).

The compositional dependence of the E_1 and E_1+Δ_1 energies of pseudomorphic $Ge_{1-y}Sn_y$ alloys on Ge, predicted from Eqs. (89)-(90), is shown in Fig. 63 (dashed). Both are blue shifted compared to relaxed $Ge_{1-y}Sn_y$ alloys (solid); the blue shift is larger for the E_1+Δ_1 critical point (CP). Our experimental results from ellipsometry are shown by symbols and also listed in Table 7. The statistical errors of the CP energies are on the order of 1 meV. The agreement is good if the deformation potentials from Ref. [69] are used in the calculation (dashed), but it

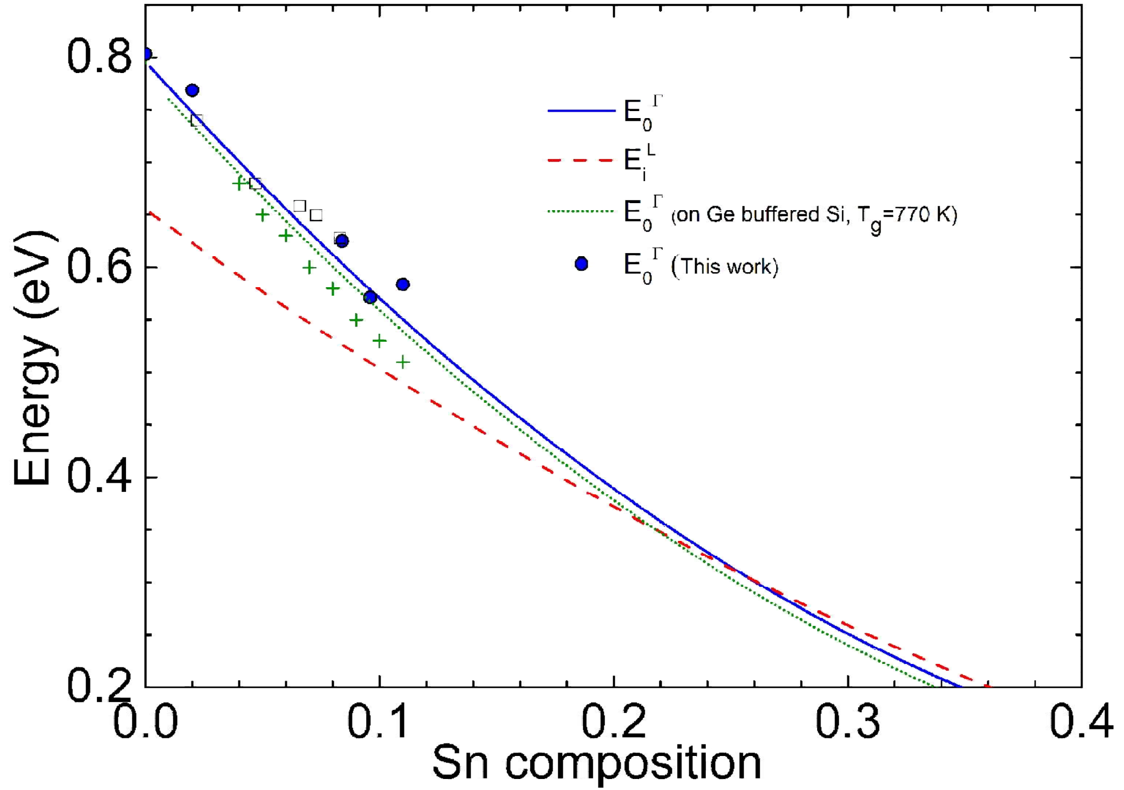

Figure 62: Compositional dependence of the direct (solid) and indirect (dashed) band gaps of pseudomorphic $Ge_{1-y}Sn_y$ alloys grown on bulk Ge at 300 K, calculated from Eqs. (83) and (86), derived from Fig. 56. The dotted line shows the direct gap for $Ge_{1-y}Sn_y$ grown on a Ge buffer on Si, see Fig. 54(b). □: Direct band gap of pseudomorphic $Ge_{1-y}Sn_y$ on Ge taken from Ref. [199]. +: Direct band gap of pseudomorphic $Ge_{1-y}Sn_y$ grown on relaxed Ge on Si from ellipsometry [200].

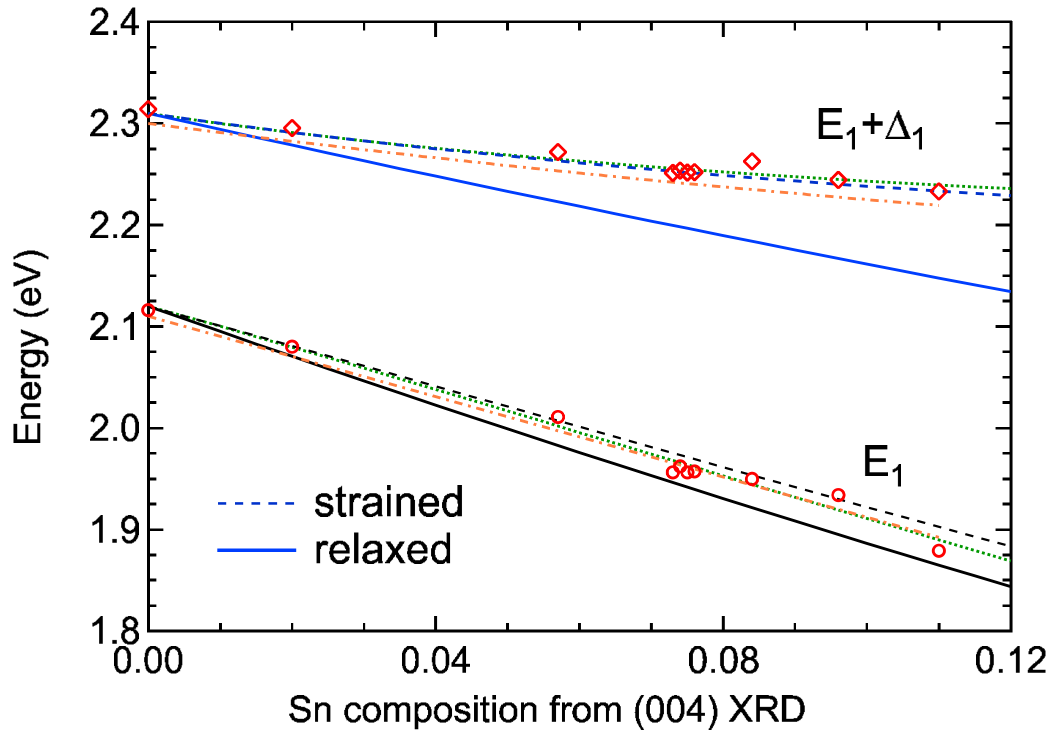

Figure 63: Compositional dependence of the E_1 ($\circ$) and $E_1+\Delta_1$ ($\diamondsuit$) critical point energies of pseudomorphic $Ge_{1-y}Sn_y$ alloys grown on Ge from ellipsometry (derivative analysis). The statistical errors of the CP energies are on the order of 1 meV. The solid lines are E_1 (black) and $E_1+\Delta_1$ (blue) for relaxed $Ge_{1-y}Sn_y$ alloys. The dashed lines are for E_1 (black) and $E_1+\Delta_1$ (blue) of pseudomorphically strained $Ge_{1-y}Sn_y$ alloys grown on Ge calculated using deformation potential theory.

can be improved slightly with revised values of D_1^1=5.1 ± 0.3 eV and D_3^3=4.5 ± 0.1 eV. Within the errors, our deformation potentials are the same as those in Ref. [69].

The small deviation of the E_1 CP of the 11% Sn sample from the prediction may be caused by a thickness interference fringe in the pseudo-dielectric function, which could be removed only partially by our data analysis techniques. It therefore influences the second derivative spectrum of the dielectric function used to determine the CP energies.

Our data analysis also determines the other CP parameters (amplitude, broadening, and phase angle), which are shown in Figs. 64, 65, and 66. Amplitude, broadening, and excitonic phase angle are in good agreement with the prior experimental data, shown by lines in figures [198]. Broadening of both E_1 and $E_1+\Delta_1$ CPs are increasing with increasing Sn composition due to the increased alloy scattering. The phase angles of all the alloys are lower than the phase angle of Ge, indicating a reduced excitonic effect with incorporation of Sn in the Ge lattice. The statistical errors of the critical point parameters energy, amplitude, phase angle, and broadening are on the order of 0.1 meV, 0.1, 0.1° and 1 meV, respectively. In addition to the factors discussed in the previous chapter, partial removal of the thickness interference fringes from the multilayer model also distorts the CP line shapes, affecting the CP parameters obtained from the second derivative spectrum. Therefore, random fluctuations of our data may be caused by these systematic errors which are difficult to quantify.

Table 7: Sn composition y and thickness t from (004) XRD; in-plane ($\epsilon_{\parallel}$) and out-of-plane strain ($\epsilon_{\perp}$) from ($\bar{2}\bar{2}4$) reciprocal space maps. Band gaps E_0^{Γ}, E_1, $E_1+\Delta_1$, and thickness from spectroscopic ellipsometry (SE). Also growth temperature T_g.

Sample	SampleID	y % (HRXRD)	T_g (C°)	t (nm) (HRXRD)	$\epsilon_{\parallel}$ (%) (HRXRD)	$\epsilon_{\perp}$ (%) (HRXRD)	E_0^{Γ} (eV) (SE)	E_1 (eV) (SE)	$E_1+\Delta_1$ (eV) (SE)	t (nm) (SE)
A	Ge	0.0	-	-	-	-	0.789	2.116	2.314	-
B	SGC581	1.9±0.1	250		-0.26±0.02	0.19±0.02		2.080	2.295	344±2
C	SGC586	5.7±0.1	200	150±10	-0.81±0.02	0.61±0.02		2.011	2.272	146±4
D	SGC687	7.3±0.1	200	91±4	-1.05±0.04	0.79±0.03		1.956	2.251	92±3
E	SGC686	7.4±0.1	175	100±10	-1.04±0.04	0.79±0.03	0.634	1.962	2.254	
F	SGC685	7.5±0.1	150	82±2	-1.05±0.05	0.79±0.04		1.956	2.252	84±2
G	SGC689	7.6±0.1	250	80±4	-1.10±0.03	0.83±0.02	0.650	1.957	2.252	90±1
H	SGS005	8.4±0.1	150	54±3	-1.20±0.05	0.90±0.04		1.950	2.263	54±1
I	SGC693	9.6±0.1	150	97±3	-1.38±0.04	1.04±0.03	0.600	1.934	2.244	104±1
J	SGC684	11.0±0.1	150	110±10	-1.64±0.03	1.24±0.02	0.555	1.879	2.233	109±1

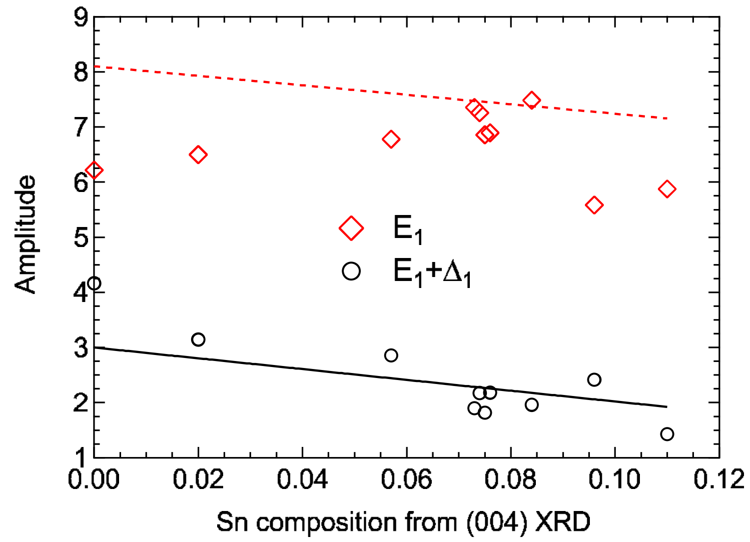

Figure 64: Compositional dependence of amplitudes (A) for E_1 and $E_1 + \Delta_1$ in pseudomorphic $Ge_{1-y}Sn_y$ alloys.

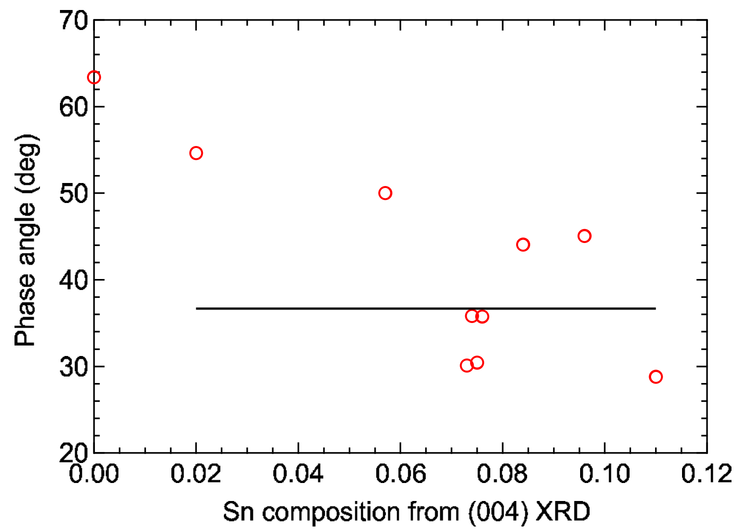

Figure 65: Compositional dependence of the exitonic phase angle ϕ for E_1 in pseudomorphic $Ge_{1-y}Sn_y$ alloys.

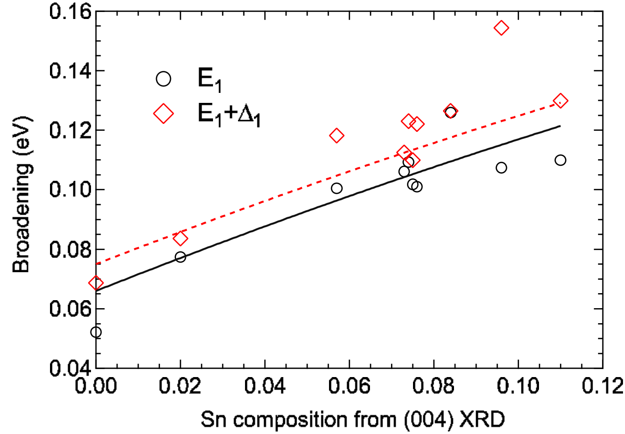

Figure 66: Compositional dependence of the broadening Γ for E_1 and $E_1 + \Delta_1$ in pseudomorphic $Ge_{1-y}Sn_y$ alloys.

6.7 Conclusion

In summary, the compositional dependence of the band gaps of pseudomorphic $Ge_{1-x-y}Si_xSn_y$ alloys on Ge was calculated using deformation potential theory. We predict an indirect to direct band gap transition only for very large Sn compositions. Specifically, no indirect to direct cross-over can be achieved for pseudomorphic $Ge_{1-y}Sn_y$ on Ge with practically approachable Sn ($y < 25\%$) compositions.

Our predictions were confirmed for $Ge_{1-y}Sn_y$ alloys (x=0) using spectroscopic ellipsometry. The complex pseudodielectric functions of pseudomorphic $Ge_{1-y}Sn_y$ alloys grown on Ge by MBE were measured using FTIR and UV-visible ellipsometry in the 0.1-6.6 eV energy range for Sn contents up to 11%, to investigate the compositional dependence of the band gaps. Critical point energies and related parameters were obtained by analyzing the second derivative spectrum of the dielectric function. The E_0^Γ, E_1 and $E_1 + \Delta_1$ band gaps of pseudomorphic $Ge_{1-y}Sn_y$ alloys measured from ellipsometry are in good agreement with the theoretical predictions from continuum-elasticity theory and deformation potentials.

Acknowledgments

This work was supported by the Air Force Office of Scientific Research (FA9550-13-1-00222) and by the Army Research Office (W911NF-14-1-0072). Support during 2016 was provided by the National Science Foundation (DMR-1505172).

7 Properties of pseudomorphic and relaxed $\text{Germanium}_{1-x}\text{Tin}_x$ alloys (x < 0.185) grown by MBE

Ryan Hickey

Department of Electrical and Computer Engineering, University of Delaware, 140 Evans Hall, Newark, DE 19716

Nalin S. Fernando, Stefan Zollner

Department of Physics, New Mexico State University, MSC 3D, P.O. Box 30001, Las Cruces, NM 88003

John Hart, Ramsey Hazbun, Dainan Zhang, James Kolodzey

Department of Electrical and Computer Engineering, University of Delaware, 140 Evans Hall, Newark, DE 19716

7.1 Abstract

Epitaxial layers of $Ge_{1-x}Sn_x$ with Sn compositions up to 18.5% were grown on Ge (100) substrates via solid-source molecular beam epitaxy. Crystallographic information was determined by high resolution X-ray diffraction, and composition was verified by Rutherford backscattering. The surface roughness, measured via atomic force microscopy and variable angle spectroscopic ellipsometry, was found to scale with the layer thickness and the Sn concentration. X-ray rocking curve peak broadening, however, was found not to trend with strain relaxation. The optical response of the $Ge_{1-x}Sn_x$ alloys was measured by spectroscopic ellipsometry. With increasing Sn content, the E_1 and $E_1+\Delta_1$ critical points shifted to lower energies, and closely matched the deformation potential theory calculations for both pseudomorphic and relaxed $Ge_{1-x}Sn_x$ layers. The dielectric functions of

the high Sn and strain relaxed material was similar to bulk germanium, but with slightly lower energies.

7.2 Introduction

Semiconducting $Ge_{1-x}Sn_x$ alloys have been under active investigation for creating direct-bandgap CMOS compatible optical devices [183]. Recent experimental results have shown promising detectors [210] and emitters [211, 212] with Sn concentrations up to 12.6% [168]. With the growing interest in group-IV photonics for telecommunications and infrared imaging [183, 213, 214], the ability to reliably produce Silicon-compatible optoelectronic materials using $Ge_{1-x}Sn_x$ is an important area of ongoing research. The large (14.7%) lattice mismatch between cubic α-Sn (6.489 Å) and Ge (5.658 Å) results in a $Ge_{1-x}Sn_x$ alloy with a bulk (relaxed) lattice parameter determined by Vegards law [58]. On a Germanium substrate, the alloy strain increases with Sn content, which inevitably leads to a critical thickness above which the pseudomorphic $Ge_{1-x}Sn_x$ relaxes strain through mechanisms that may include the formation of misfit dislocations and Sn precipitation. In addition, the higher Sn contents reduce the thermal stability of the alloy, promoting relaxation and composition segregation [215] at progressively lower process temperatures. Multiple theoretical models have predicted $Ge_{1-x}Sn_x$ alloys to transition to a direct bandgap material at Sn compositions above about 6% [66], and with experimental evidence of a shift to direct bandgap at 6-8% [216]. More recent theories, however, suggest that pseudomorphic $Ge_{1-x}Sn_x$ that is compressively strained to Ge remains indirect in bandgap for any composition, and only through relaxation will the $Ge_{1-x}Sn_x$ become direct at Sn concentrations as low as 6% Sn, depending on the amount of relaxation [217, 218]. Unfortunately, the

low thermal stability of $Ge_{1-x}Sn_x$ makes the standard method of thermal annealing to reduce defects introduced from strain relaxation difficult [190]. Therefore, in order to produce direct bandgap $Ge_{1-x}Sn_x$ for optical applications, it will be necessary to grow relaxed layers of high quality material with minimal thermal processing. In this paper, we experimentally investigate the properties of both strained and partially relaxed $Ge_{1-x}Sn_x$ layers with up to 18.5% Sn, to determine the effects of relaxation on material and optical properties.

7.3 Preparation and Growth

The $Ge_{1-x}Sn_x$ alloys were grown using a multi-chamber EPI model 620 molecular beam epitaxy (MBE) system utilizing solid source Knudsen thermal effusion cells. The cells were loaded with triple zone-refined Ge and Sn (6N, United Mineral and Chemical Corporation) in pyrolytic Boron Nitride (pBN) crucibles as described elsewhere [58, 214]. The growth chamber is pumped with both a closed loop cryopump system (CTI Cryogenics CT-8F, 4000L/s) and a Varian (400l/s) ion pump, which take the MBE growth chamber to a base pressure of 1.3×10^{-8} Pascal (10^{-10} Torr).

The substrates used for this study were single-side polished 76.2mm diameter undoped (001) oriented Germanium substrates with a resistivity of 40 Ωcm. Because the native oxide of Germanium doesn't sufficiently passivate the wafer surface, extreme care must be taken when cleaning the substrates to mitigate contamination, optimize material quality, and to remove the unwanted surface GeO prior to growth. The Ge substrate cleaning procedure is based on that outlined in Hovis et al., [75]. The wafers are first rinsed in running DI water (18.23 MΩ), then submerged in dilute Hydrofluoric acid $HF:H_2O$ (1:20) for five minutes.

They are again rinsed in DI water and placed in $HCl:H_2O$ (1:4) for one minute to remove any remaining surface oxide. Next the wafers are dipped in H_2O_2 for thirty seconds then $HCl:H_2O$ (1:4) for one minute, repeating these last two steps so that they are performed three times in total. This process iteratively oxidizes and strips the wafer surface, removing surface contaminants in the process. Immediately following the last acid step, the wafers are placed in a solution of $NH_4OH:H_2O_2:H_2O$ (1:2:20) for 20 seconds to form a final protective oxide (GeO_2) layer. The wafers are removed from the final solution and quickly blown dry with high-purity nitrogen, and moved into the MBE introduction chamber within 30 seconds. This wafer cleaning technique was tested by growing a 100nm thick Ge layer on a Ge wafer cleaned using the above procedure, after which atomic force microscopy (AFM) and secondary ion mass spectrometry (SIMS) were used to characterize the layer. The SIMS showed low interfacial C and O doses, and the RMS surface roughness was found to be just 63 pm.

After about 45 minutes when the load lock pressure reached 5.5×10^{-6} Pascal, the wafers were transferred to a preparation chamber, and heated to 450 °C overnight, followed by a one-hour bake at 650 °C. The wafers were then transferred to the growth chamber and flashed to 850 °C for 10 minutes to remove the surface oxide before being cooled to growth temperature. This last step was found necessary to produce a flat surface morphology and to prevent Sn segregation. The substrate growth temperature varied depending on the Sn content of the $Ge_{1-x}Sn_x$ layer to be grown. For the reported samples A through D (less than 15% Sn) reported here, the substrate temperature was 150 °C (measured by a thermocouple behind the substrate), while samples E and F (higher Sn) were grown at 120 °C. In order to grow samples G and H (Sn contents above 18%), the substrate heater was turned off and the wafer was allowed to cool to 90 °C, at

which point the effusion cell shutters were opened. Radiative heating from the Ge and Sn sources slowly increased the substrate temperature to approximately 115 °C over the course of 30 minutes, after which the temperature remained stable for the remainder of the growth. This relatively low temperature at the beginning of the growth was found to help mitigate possible Sn segregation.

7.4 Analysis

7.4.1 X-ray diffraction

Crystallographic data were collected via high resolution X-Ray diffraction (HR-XRD) using a Philips/Panalytical X'Pert MRD system. The incident beam path consists of a multi-layer parabolic mirror for focusing the beam, and a Bartels Ge (220) four-crystal monochromator to isolate the Cu Kα_1 X-ray line (λ=1.54056 Å). This configuration provided a collimated beam with a divergence of 12 arc seconds incident on the sample, which is mounted on a triple axis goniometer. The diffracted beam then traveled to a three-crystal Ge analyzer using (220) plane reflections to isolate the coherent component of the diffracted beam before reaching the detector. The thickness of the strained $Ge_{1-x}Sn_x$ layers was extracted from the Pendellösung interference fringes from symmetric (004) rocking curve ($\omega - 2\theta$) scans, while the thickness of the relaxed layers was inferred from the calibrated MBE growth rate and from Rutherford Backscattering Spectrometry (RBS) data. Asymmetric (224) Triple-Crystal Reciprocal space measurements (RSMs) showed the out-of plane ([001] direction) $Q_\perp$, and the in-plane ([110] direction) $Q_\parallel$ reciprocal lattice vectors for the $Ge_{1-x}Sn_x$ samples. The RSM plots in Fig. 67 show the diffraction contours of the $Ge_{1-x}Sn_x$ layers (lower contour peak in each plot) relative to the diffraction peak of the substrate (upper contour peak).

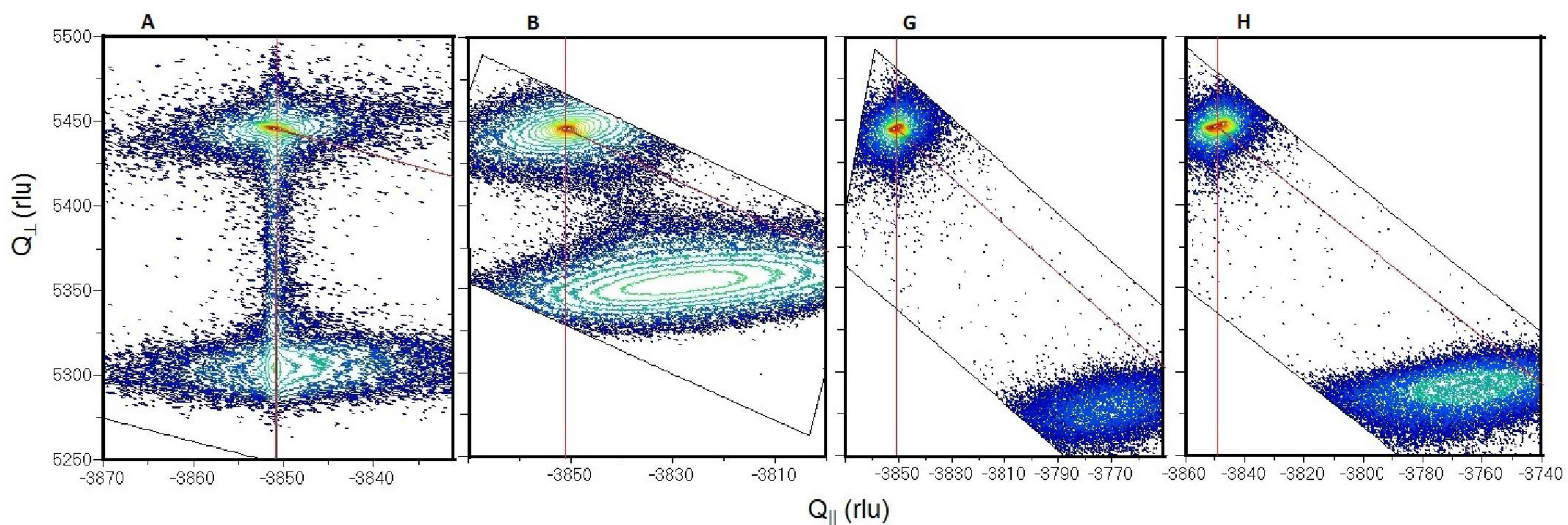

Figure 67: RSM plots of the out-of plane versus the in-plane reciprocal lattice vectors for the $Ge_{1-x}Sn_x$ samples A, B, G and H measured in inverse microns. The vertical line in each plot represents 100% compressive strain, so a layer peak centered on this line would have a parallel lattice constant equal to that of the Ge substrate (see plot A). The diagonal black line represents complete relaxation, as a peak centered anywhere on this line would have equal parallel and perpendicular lattice constants. With increasing Sn content, the $Q_\parallel$ decreases, indicating an increase in the in-plane lattice constant compared to the Ge substrate.

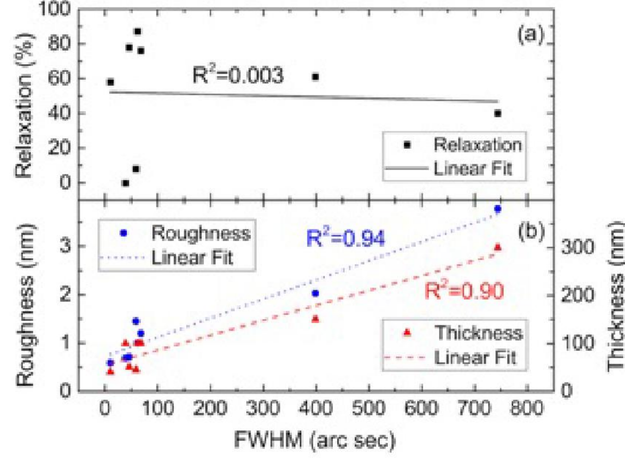

Figure 68: Relaxation (a), RMS surface roughness (b) and Thickness (b) of the $Ge_{1-x}Sn_x$ samples plotted against the ω peak FWHM (full width at half-maximum). The calculated correlation R-squared values represent how well the measured data fits against a linear trend line (shown). As discussed in the text, the small value of R-Squared in (a) suggests that there is no correlation between relaxation and FWHM for these samples.

The separation in both $Q_{\parallel}$ and $Q_{\perp}$ between these two peaks represents the relative lattice mismatch, which are extracted from the RSMs using a semi-automatic peak search with Panalytical software. The reciprocal lattice vectors can be used to find the $Ge_{1-x}Sn_x$ lattice constants: [219]

$$a_{\perp GeSn} = \frac{Q_{\perp \mathrm{Ge}} - Q_{\perp \mathrm{GeSn}}}{Q_{\perp \mathrm{GeSn}}} a_{\mathrm{Ge}} + a_{\mathrm{Ge}} \tag{99}$$

$$a_{\parallel GeSn} = \frac{Q_{\parallel \mathrm{Ge}} - Q_{\parallel \mathrm{GeSn}}}{Q_{\parallel \mathrm{GeSn}}} a_{\mathrm{Ge}} + a_{\mathrm{Ge}}. \tag{100}$$

where $a_{\perp GeSn}$ is the lattice constant of the GeSn in the growth direction (out of plane), $a_{\parallel GeSn}$ is the bulk lattice constant parallel [011] to the growth direction (in plane), and a_{Ge} is the lattice constant of the substrate (5.6579 Å). In order to properly account for tetragonal distortion of the $Ge_{1-x}Sn_x$ layers, the elastic

constants of Ge (C_{11}= 126 GPa, C_{12}=44 GPa) [220] and cubic Sn (C_{11}= 72.5 GPa, C_{12}=29.7 GPa) [58] used to calculate the respective [100] Poisson's ratios ν=C12/(C11+C12) where ν is the [100] Poisson's ratio and C_{11} and C_{12} are elastic constants, resulting in a ν_{Ge} of 0.26 and a ν_{Sn} of 0.29. The $Ge_{1-x}Sn_x$ Poisson's ratio is interpolated from the composition estimated from growth conditions to calculate the respective [100] Poissons ratios of the $Ge_{1-x}Sn_x$ alloy. [221] Using the component lattice constants from Eqs. (99), (100) and the interpolated Poisson's ratio, the bulk lattice constant of relaxed $Ge_{1-x}Sn_x$ can be calculated:

$$a_{0GeSn} = a_{\perp GeSn} + \frac{2\nu_{GeSn}\left(a_{\parallel GeSn} - a_{\perp GeSn}\right)}{1 + \nu_{GeSn}} \tag{101}$$

The lattice constants of $Ge_{1-x}Sn_x$ from Eqs. (99), (100) and (101) can now be used to find the strain tensor of the $Ge_{1-x}Sn_x$ [222] alloy layer:

$$\epsilon_{\perp GeSn} = \frac{a_{\perp GeSn} - a_{0GeSn}}{a_{0GeSn}} \tag{102}$$

$$\epsilon_{\parallel GeSn} = \frac{a_{\parallel GeSn} - a_{0GeSn}}{a_{0GeSn}} \tag{103}$$

where $\epsilon_{\perp}$ and $\epsilon_{\parallel}$ are the out-of-plane and in-plane strain, respectively, as seen in Table 8. The lattice constants can also be used to calculate the relaxation R_{GeSn}=($a_{\parallel GeSn}$))-a_{Ge})/(a_{0GeSn}-a_{Ge}) of the $Ge_{1-x}Sn_x$ layer [219, 223]. The broadened elliptical shape of some of the $Ge_{1-x}Sn_x$ contour peaks in Fig. 67 is a result of relaxation, which increases the in-plane lattice constant, causing $Q_{\parallel}$ to decrease [224]. The Sn concentration x=(a_{oGeSn}-a_{Ge})/(a_{Sn}-a_{Ge}) is determined from the GeSn bulk lattice constant using Vegard's law. The accuracy of using the linear interpolation for alloy concentration has previously been investigated, and the

bowing parameter for the alloy lattice constant was very small (under 10^{-3} nm), and contributed to a compositional variation of less than 0.1% for the alloys in this series [58, 59, 57]. Channeling RBS was performed on sample G (18.5% Sn), which verified the accuracy of these composition calculations. In addition, the RBS channeled backscattered yield ratios (not plotted here) of $\chi_{min,Ge}$=0.26 and $\chi_{min,Sn}$=0.24, showed that over 95% of the Sn was substitutional in the lattice8.

Symmetric Triple-Crystal ω X-ray rocking curves aligned to the $Ge_{1-x}Sn_x$ layer peak were performed to calculate the full width at half maximum (FWHM) (see Table 8), measured in arc seconds. The width of this peak is affected by a number of parameters, including layer thickness, defectivity, mosaic tilt and surface roughness. Figure 68 is a plot of the FWHM against relaxation, roughness, and thickness, which shows no correlation between the FWHM and relaxation, but a definite correlation with roughness and thickness.

7.4.2 Atomic force microscopy

Atomic Force microscopy (AFM) measurements were performed using a Bruker MultiMode 8 instrument with a Veeco NanoScope V controller. Prior to measurements, the system was calibrated using a Digital Instruments AFM reference standard. The RMS roughness (see Table 8) was calculated across a 3×3 μm^2 area scan. Scans were repeated on multiple areas of a given sample, which verified uniformity across the sample. The AFM scans for samples A, B, G and H are shown in Fig. 69. The AFM images revealed a periodic surface roughness, with a lateral correlation length of approximately 50-90 nm. The effects of composition, thickness and strain on roughness will be discussed in the next section.

Table 8: List of materials parameters for the eight samples in this series. Sn concentration, relaxation, in and out of plane strain, thickness and FWHM of the (004) xrd peak were calculated from XRD as described in the text. The RMS roughness was determined via AFM scans over a 3×3 μm surface region. The spectroscopic ellipsometry (VASE) roughness is a calculated from a peak-to-valley surface layer model, which includes the thickness of a native oxide layer.

Sample	Thickness (nm)	Sn (%)	Relaxation (%)	GeSn $\epsilon_{\parallel}$ (%)	GeSn $\epsilon_{\perp}$ (%)	004 ω FWHM (arc sec)	VASE Roughness (nm)	AFM Roughness (nm)
(A)	100	10	0	-1.51	1.14	39	3.5	0.69
(B)	300	8.4	41	-0.73	0.55	744	6.5	3.77
(C)	45	12.5	8	-1.65	1.25	56	3.1	1.45
(D)	150	12.5	61	-0.70	0.53	399	3.9	2.03
(E)	40	15.6	58	-0.93	0.71	10	3.4	0.59
(F)	100	17.0	76	-0.59	0.45	68	3.2	1.2
(G)	50	18.5	78	-0.56	0.43	46	4.6	0.71
(H)	100	18.3	87	-0.35	0.27	62	3.4	1.0

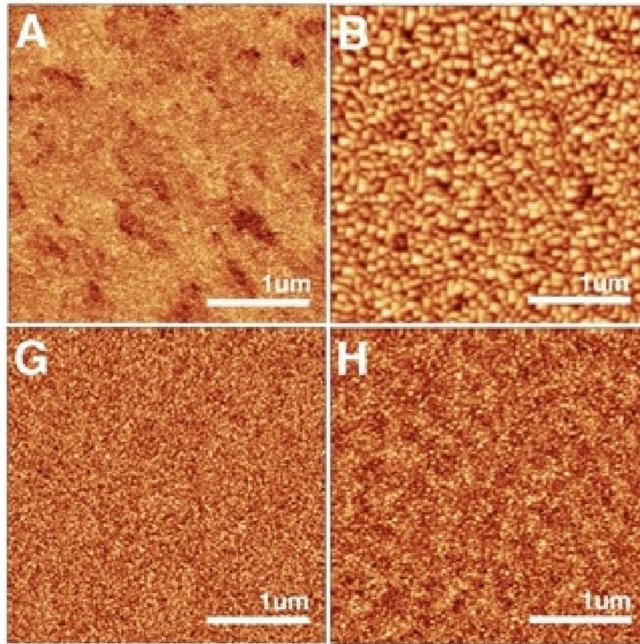

Figure 69: Atomic force microscopy (AFM) of the samples A, B, G and H (with Sn contents of 10, 8.4, 18.5, 18.3% respectively). Each image is 3×3 μm^2. RMS roughness for the samples shown (clockwise from top left): 0.69 nm, 3.77 nm, 0.71 nm, 1.0 nm. These images show the periodic roughness of the $Ge_{1-x}Sn_x$, caused by strain-induced buckling, depends on the $Ge_{1-x}Sn_x$ layer thickness.

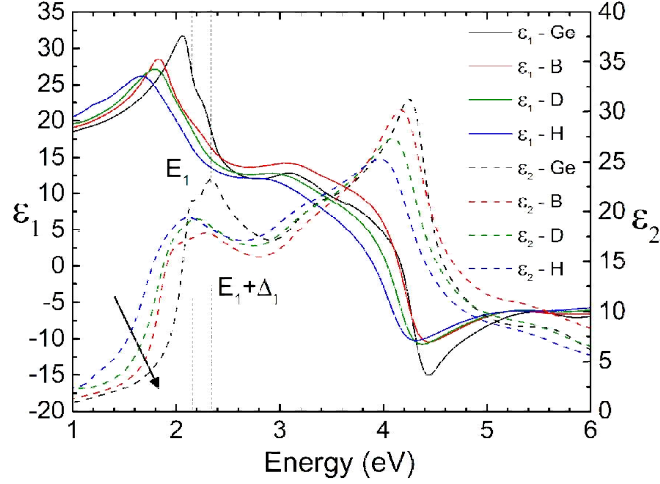

Figure 70: Real (solid) and imaginary (dashed) parts of the complex dielectric function of samples B, D and H (with bulk Germanium for reference) determined from ellipsometry. The dielectric functions were determined by fitting the measured ellipsometric angles using a four-phase ambient-GeO_2-$Ge_{1-x}Sn_x$-Ge model.

7.4.3 Spectroscopic ellipsometry

The optical response of the $Ge_{1-x}Sn_x$ alloys was characterized using variable angle spectroscopic ellipsometry (VASE) [174]. The ellipsometric angles, ψ and Δ were acquired from 0.7 to 6.6 eV photon energies with 0.01 eV steps at three angles of incidence (65°, 70°, 75°), on a J.A. Woollam V-VASE spectroscopic ellipsometer, utilizing a computer-controlled Berek waveplate compensator and a rotating variable-angle analyzer [172]. To reduce experimental errors, all data were obtained by averaging two measurements with equal and opposite polarizer angles. The dielectric functions of the $Ge_{1-x}Sn_x$ on Ge were obtained by modeling the ellipsometry data. A multilayer model including $GeO_2/Ge_{1-x}Sn_x/Ge$ was used for accurate treatment of the experimental data. The dielectric functions for the GeO_2 and Ge were used in tabulated form from published data [79, 81]. The dielectric functions of $Ge_{1-x}Sn_x$ were described using a parametric oscillator model [82]

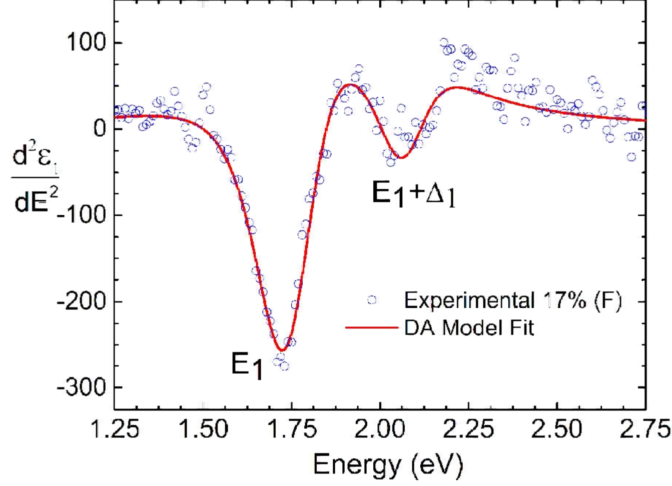

Figure 71: Second derivatives of the real (ϵ_1) part of the dielectric function of sample F (17%) with respect to photon energy near the E_1 and E_1+Δ_1 critical points. Symbols represent the experimental data and solid line shows the best fit with a two dimensional critical point assuming parabolic bands and constant dipole matrix elements. The statistical error of this model is on the order of one meV.

that imposes Kramers-Kronig consistency between the real and imaginary parts. In the first step of the model fitting, the layer thicknesses and the parametric oscillator parameters for the dielectric function of $Ge_{1-x}Sn_x$ were all treated as adjustable and varied until good agreement with the measured ellipsometric angles is achieved. In the second fitting step, the values obtained for the thicknesses were kept fixed as determined in the first step, and the ellipsometric angles were fitted again by taking the values of the dielectric function of $Ge_{1-x}Sn_x$ at each measured photon energy as adjustable parameters. The dielectric function obtained from this point-by-point fit is shown in Fig. 70 for alloys with different Sn contents. We confirmed that it is still Kramers-Kronig consistent. Note the red-shift of critical points for increasing Sn contents.

Additionally, analyzing the second derivatives can more accurately indicate the contribution of the critical points to the dielectric function. The real and imag-

inary parts of the tabulated dielectric function obtained by this point-by-point fitting were numerically differentiated and smoothed using ten Savitzky-Golay coefficients for second-order derivatives with a polynomial of degree three, to obtain a good signal to noise ratio without distorting the line shape [84]. The second-order derivative spectra of the dielectric function fitted using an expression for a 2D critical point assuming parabolic bands and constant dipole matrix elements [30]. The second derivative spectrum of sample F with the best fit of a 2D critical point is shown in Fig. 71 Both E_1 and $E_1+\Delta_1$ structures were fitted simultaneously, the excitonic phase angle θ was forced to take the same value for both the E_1 and $E_1+\Delta_1$ critical points.

7.5 Discussion

The measurement data from Table 8 show that the extent of relaxation and the surface roughness of the $Ge_{1-x}Sn_x$ films both increase with layer thickness as well as with the Sn concentration, as would be expected from calculations of critical thickness versus lattice mismatch [225]. The peak-to-valley roughness modeled by VASE, although larger than the AFM roughness because the VASE model includes the thickness of the surface oxide layer [226], follows the same trends as the roughness calculated from AFM. Similar periodic roughness has previously been reported for $Ge_{1-x}Sn_x$ alloy layers grown by MBE [227, 228, 229, 230]. The periodic roughness at the epitaxial surface is believed to be an effect of strain-induced lattice buckling caused by local gradients in the surface energy as reported by O. Gurdal *et al.*, [227]. Similar surface deformation caused by strain-induced kinetic roughening is also widely reported for other alloys such as pseudomorphic Silicon Germanium ($Si_{1-x}Ge_x$) strained to Silicon [231, 232, 233]. H. Lin *et al.*,

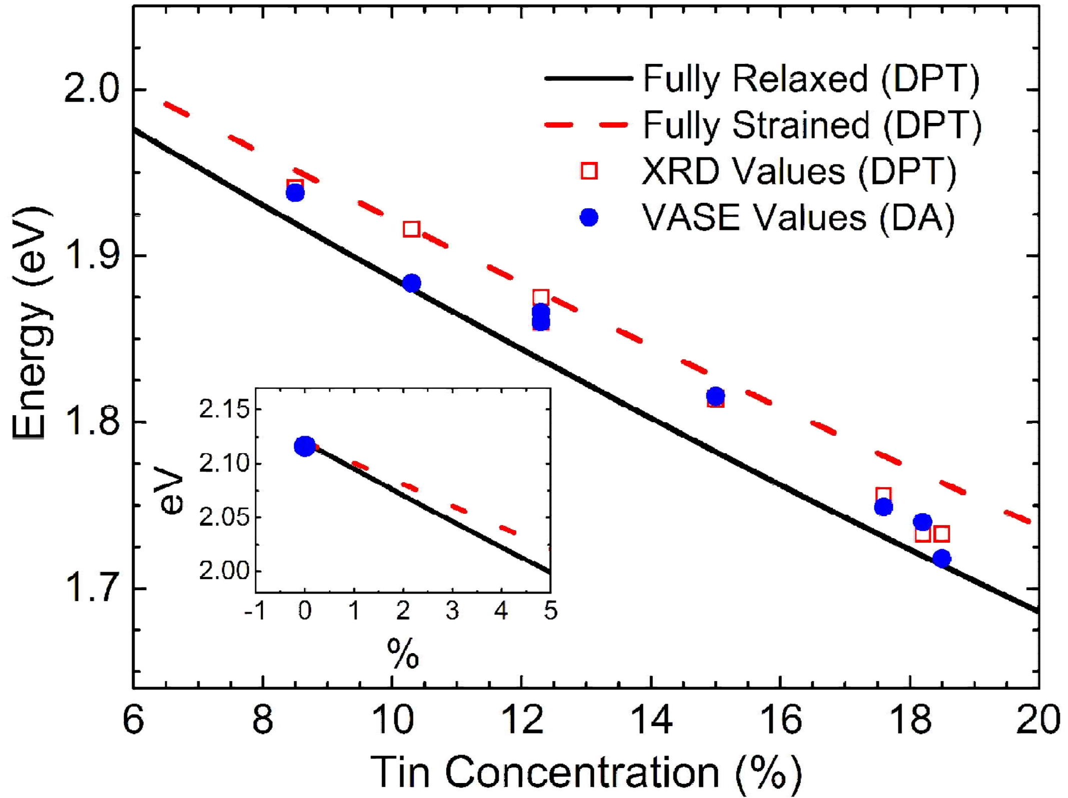

Figure 72: The lines represent the E_1 critical point energies for $Ge_{1-x}Sn_x$ on Ge as a function of Sn content as modeled by Deformation Potential Theory (DPT). The solid line is fully relaxed and the dashed line is pseudomorphically strained. Circles (blue) represent the E_1 energies determined from second-order Derivative Analysis (DA) of the ellipsometry spectral data, with a statistical error on the order of one meV. Squares (red) represent the expected E_1 energy for each sample taking into account the Sn content and the degree of relaxation determined from asymmetric x-ray reciprocal space maps. The inset shows the measured E_1 energy of bulk Ge (2.116 eV), where the theoretical lines for strained and relaxed $Ge_{1-x}Sn_x$ converge. For some samples, the measured E_1 energy (circles) is lower than the calculated energy (squares), indicating that the degree of relaxation might be larger near the sample surface. The observed red shift is about 20 meV/% Sn.

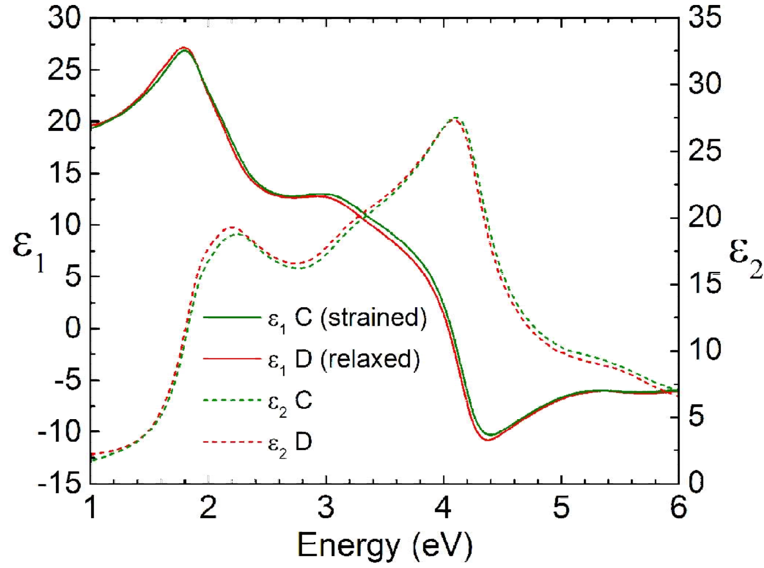

Figure 73: Real (solid) and imaginary (dashed) parts of the dielectric function of samples C (8% relaxed) and D (61% relaxed) with similar Sn contents (12.5% Sn) but different degrees of relaxation showing a very small red shift of the spectrum with strain relaxation.

reported comparable strain-induced surface roughness on unintentionally tensile-strained $Ge_{1-x}Sn_x$ [229]. These results suggest that the roughening is moderated by a strain field that is proportional to both the lattice-mismatch and the layer thickness. There could also be a contribution from statistical growth kinetics, where the low growth temperatures reduce the atomic mobility and hinder surface flattening. The FWHMs of the ω rocking curves are indicated in Fig. 68 plotted against relaxation, thickness and roughness, along with a linear fit for each. The thickness and roughness trend closely with the FWHM, with a R-squared value of 0.90 and 0.94 respectively. The relaxation however has a R-squared value of only 0.003, representing a low correlation between strain and the ω x-ray peak broadening. The data presented in Fig. 68(b) shows the FWHM increasing with thickness, which agrees with the Hirsch model that correlates the width of the

rocking curve (ω scan) to the dislocation density. The Hirsch model suggests a broadening of the rocking curve width, as the dislocation density increases for thicker films due to their increased relaxation [234, 235]. The data presented in Fig. 68, however, indicates no correlation between relaxation and the ω rocking curve, suggesting that the mechanism of strain relaxation in $Ge_{1-x}Sn_x$ alloys may not involve dislocations in the same manner as other mismatched heteroepitaxial semiconductors. A likely cause of the ω peak broadening is surface roughness, as the strain-induced deformation of the lattice at the surface can cause atypical reflections that would contribute to the observed width of the peak [236]. The complex dielectric functions of samples B, D and H in Fig. 70 show features similar to bulk Ge, indicating a diamond crystal structure composed of tetrahedrally coordinated atoms [174] and that the $Ge_{1-x}Sn_x$ epilayers are high quality, even at high Sn compositions and high degrees of relaxation obtained here. As the Sn concentration increases, the red shifting of the dielectric function along with the broadened of critical points (with respect to bulk Ge) as Sn concentration increases are a result of the alloying and the strain effects of Sn on the Ge band structure.

The compositional dependence of the E_1 critical points is plotted in Fig. 72 from both VASE (as determined by second-order Derivative Analysis [DA]) and XRD (predicted from Deformation Potential Theory [DPT] calculations), along with the DPT predictions for both fully strained and relaxed (dashed and solid lines, respectively) $Ge_{1-x}Sn_x$ [200, 198]. As the strain relaxation measured from XRD is incorporated into the DPT predictions of the E_1 critical point energy, the measured values of E_1 from VASE can be used as a comparative measure of relaxation between the two measurement techniques. The experimental and theoretical data are in overall good agreement, except for sample A which has

a larger discrepancy in energy between the RSM and VASE derived values. The discrepancy could be related to the larger critical thickness of sample A (due to the relatively low Sn content of 10%), where the lattice deformations due to increasing strain cause the $Ge_{1-x}Sn_x$ to relax kinetically at the surface [237], as opposed to the established Matthews and Blakeslee model of equilibrium relaxation in which mismatched layers are assumed to relax predominantly from the epitaxial interface [238]. In this kinetic relaxation model, the misfit dislocations would nucleate throughout the thickness of the layer instead of only at the substrate interface, creating a strain gradient proportional to lattice mismatch. The effect of this strain gradient would likely be most pronounced in the low Sn alloys, as larger critical thicknesses would yield layers that have thicker pseudomorphic regions [239, 240, 241]. As the light from the ellipsometry measurement has a penetration depth of a just a few tens of nanometers (based on the absorption coefficient from the imaginary part of the dielectric function from VASE) for the material measured, only the strain relaxation near the surface of the film is being analyzed during VASE. In contrast, HR-XRD is a relatively bulk measurement of the layer, which accounts for the strain throughout the entire thickness of the layer. Figure 73 compares the real and imaginary parts of the dielectric function of two samples (C & D) with similar Sn composition but different (8% and 61%) relaxations. There is a slight red shift in energy for the relaxed sample, in good agreement with DPT modeling. The similarity of the features indicates that both the strained and relaxed samples have similar optical response, with a slight red-shift for the relaxed layer, but that the strain relaxation mechanism does not affect the overall quality of the material.

7.6 Conclusion

We have demonstrated the growth of both pseudomorphic and relaxed $Ge_{1-x}Sn_x$ alloy layers on Ge substrates via solid source MBE, including wafer preparation and growth conditions, for a range of thicknesses and Sn compositions up to 18.5%. RBS showed very high (>95%) Sn substitutionality, with composition in good agreement with that calculated from HR-XRD. The width of the XRD rocking curve did not increase as a function of strain relaxation, indicating that the $Ge_{1-x}Sn_x$ may have a relaxation mechanism that differs from the dislocation creation that is reported for other common heteroepitaxial semiconductors. AFM was used to characterize the RMS surface roughness of the $Ge_{1-x}Sn_x$, which was found to increase with thickness, likely as a result of strain induced buckling of the lattice at the growth surface. The optical response of the samples was measured by spectroscopic ellipsometry and indicated a red shift in critical point energies with increasing Sn content (about 20 meV/% Sn) as well as with strain relaxation, in good agreement with theory. The ellipsometric measurements also showed the dielectric functions of all of the $Ge_{1-x}Sn_x$ alloys were qualitatively similar to bulk Ge, suggesting that the high Sn contents and strain relaxation isnt significantly reducing the crystal quality of the material. All of the characterizations reported here suggest that the relaxation mechanisms did not significantly degrade the morphology and optical constants of the relaxed $Ge_{1-x}Sn_x$ alloy layers compared with the strained layers. These results suggest that relaxed, high Sn $Ge_{1-x}Sn_x$ alloy layers can be grown by the MBE method to retain much of the crystal quality of the pseudomorphic, lower Sn content alloy layers, which is a promising finding for the development of strain-engineered direct bandgap $Ge_{1-x}Sn_x$.

Acknowledgements

This work was funded in part by grants from the Air Force (AFOSR award FA9550-14-1-0207 and award FA9550-13-1-0022), the Army Research Office (ARO award W911NF-12-1-0380), and by gifts from IBM Corporation and Thorlabs. Special thanks to T.N. Adam, R. Soref, Y.-K. Yeo, and S.-Q. (Fisher) Yu for valuable discussions.

8 Conclusion

$Ge_{1-x-y}Si_xSn_y$ alloys have emerged as a promising material for the design of Ge based optoelectronic devices (photovoltaic applications, IR detectors, IR lasers and LEDs) on current Si technology. They allow to tune the absorption edge by controlling the alloy composition and strain independently. Therefore, the accurate knowledge of the compositoinal and strain dependence of the optical constants (refractive index, dielectric function, absorption coefficients and reflectivity) are of great interest to optoelectronic industry. We characterize the compositional, strain and temperature dependence of the optical properties of Ge-Si-Sn alloys using spectroscopic ellipsometry and high resolution X-ray diffraction.

Usually, Ge and Ge-based alloys are covered with a native surface oxide and a roughness layer, which make it more challenging to interpret the ellipsometry measurements on these semiconductors. In order to accurately characterize the optical constants of native oxides on Ge, we produced thermal oxides (GeO_2) on Ge, with thicknesses from 34 to 136 nm by thermal oxidation of Ge. Optical constants of GeO_2 were determined and tabulated from 0.5 - 6.6 eV, using spectroscopic ellipsometry via multisample analysis. Surface oxides layers were also characterized using X-ray reflectance.

The temperature dependent dielectric functions of bulk Ge and Ge on Si, grown by CVD were measured from 80 - 780 K, from 0.8 - 6.6 eV, using spectroscopic ellipsometry. The temperature dependence of the E_1, $E_1+\Delta_1$, E_0' and E_2 critical points were determined from second derivative analysis. The E_1 and $E_1+\Delta_1$ critical points in the Ge epilayers on Si are redshifted compared to bulk Ge. A model, taking into account the thermal expansion coefficients, stress, and

strain determined using continuum elasticity theory, and the strain-induced shifts calculated from deformation potentials, was developed to explain the temperature dependent energy shift of the E_1 and $E_1+\Delta_1$ critical points.

The compositional dependence of the band gaps of pseudomorphic $Ge_{1-x-y}Si_xSn_y$ alloys on Ge were reported using deformation potential theory. Theory predicts an indirect to a direct band gap transition of pseudomorphic $Ge_{1-x-y}Si_xSn_y$ alloys on Ge for very high high Sn compositions, y>15% and no indirect to direct cross over for pseudomorphic $Ge_{1-y}Sn_y$ on Ge for practically approachable Sn ($y < 25\%$) compositions. The effects of the substrate on the indirect-direct transition were discussed for bulk Ge, Ge-buffered Si, and GaAs substrates. The predictions of the deformation potential theory were validated for $Ge_{1-y}Sn_y$ alloys (x=0) using spectroscopic ellipsometry. The complex pseudodielectric functions of pseudomorphic $Ge_{1-y}Sn_y$ alloys grown on Ge by MBE were measured using FTIR and UV-visible ellipsometry in the 0.1-6.6 eV energy range for Sn contents up to 11%, to investigate the compositional dependence of the band gaps. Critical point energies and related parameters were obtained by analyzing the second derivative spectrum of the dielectric function. The E_0^{Γ}, E_1 and $E_1 + \Delta_1$ band gaps of pseudomorphic $Ge_{1-y}Sn_y$ alloys measured from ellipsometry are in good agreement with the theoretical predictions.

The effects of strain relaxation of the $Ge_{1-y}Sn_y$ on Ge substrate on the optical properties were investigated up to 18.5% Sn and for thicknesses ranging from 40 - 300 nm. The Sn composition and degree of relaxation of the epilayers were determined from high-resolution X-ray diffraction reciprocal space maps. Taking into account the strain relaxation, measured from XRD, the compositional and strain dependence of the E_1 critical point were predicted using deformation potential theory. The optical response of the samples was measured by spectroscopic

ellipsometry and indicated a red shift in critical point energies with increasing Sn content (about 20meV/% Sn) as well as with strain relaxation, in good agreement with theory. The ellipsometric measurements also showed that the dielectric functions of the $Ge_{1-y}Sn_y$ alloys were qualitatively similar to bulk Ge, suggesting that the high Sn contents and strain relaxation do not significantly reduce the crystal quality of the material.

REFERENCES

[1] C. Winkler, Berichte der Deutschen Chemischen Gesellschaft. **19**, 210 (1886).

[2] C. Claeys, and E. Simoen, *Germanium-Based Technologies: From Materials to Devices*, (Elsevier, Oxford, 2007).

[3] Y. Ishikawa, K. Wada, D.D. Cannon, J. Liu, H.C. Luan, and L.C. Kimerling, Appl. Phys. Lett. **82**, 2044 (2003).

[4] E. Kasper, M. Kittler, M. Oehme, and T. Arguirov, Photon. Res. **1**, 69 (2013).

[5] M. El Kurdi, G. Fishman, S. Sauvage, and P. Boucaud, J. Appl. Phys. **107**, 013710 (2010).

[6] G. He and H.A. Atwater, Phys. Rev. Lett. **79**, 1937 (1997).

[7] J. Mathews, R.T. Beeler, J. Tolle, C. Xu, R. Roucka, J. Kouvetakis, and J. Menendez, Appl. Phys. Lett. **97**, 221912 (2010).

[8] C. Eckhardt, K. Hummer, and G. Kresse, Phys. Rev. B **89**, 165201 (2014).

[9] L. Jiang, J.D. Gallagher, C.L. Senaratne, T. Aoki, J. Mathews, J. Kouvetakis and J. Menendez, Semicond. Sci. Technol. **29**, 115028 (2014).

[10] S.M. Sze, *Semiconductor Devices: Pioneering Papers* (Teaneck, NJ: World Scientific Publishing Co., 1991).

[11] H.P. Singh, Acta Crystallogr., **24**, 469 (1968).

[12] D.D. Cannon, J. Liu, Y. Ishikawa, K. Wada, D.T. Danielson, S. Jongthammanurak, J. Michel, and L.C. Kimerling, Appl. Phys. Lett. **84**, 906 (2004).

[13] J.R. Chelikowsky and M.L. Cohen, Phys. Rev. B **14**, 556 (1976).

[14] M. Cardona and F.H. Pollak, Phys. Rev. **142**, 530 (1966).

[15] C. Tserbak, H.M. Polatoglou, and G. Theodorou, Phys. Rev. B **47**, 7104 (1993).

[16] Q.M. Ma, K.L. Wang, and J.N. Schulman, Phys. Rev. B **47**, 1936 (1993).

[17] T. Low, Ming-Fu Li, G. Samudra, Yee-Chia Yeo, Chunxiang Zhu, A. Chin, Dim-Lee Kwong, Electron Devices IEEE Transactions on, **52**, 2430 (2005).

[18] P.Y. Yu and M. Cardona, *Fundamentals of Semiconductors: Physics and Materials Properties*, 4th ed. (Springer, Berlin, 2010).

[19] M. de Kersauson, R. Jakomin, M. El Kurdi, G. Beaudoin, N. Zerounian, F. Aniel, S. Sauvage, I. Sagnes, and P. Boucaud, J. Appl. Phys. **108**, 023105 (2010).

[20] Y. Bai, K.E. Lee, C. Cheng, M.L. Lee and E.A. Fitzgerald, J. Appl. Phys. **104**, 084518 (2008).

[21] M.V. Fischetti and S.E. Laux, J. Appl. Phys. **80**, 2234 (1996).

[22] E. Fermi, *Nuclear Physics, formula VIII.2*, (University of Chicago Press., 1950).

[23] P.A.M. Dirac, Proceedings of the Royal Society of London, Series A **114**, 243 (1927).

[24] A. Beer, Annalen der Physik und Chemie. **86**, 78 (1852).

[25] H.A. Kramers, Atti Cong. Intern. Fisici, **2**, 545 (1927).

[26] R. de L. Kronig, J. Opt. Soc. Am. **12**, 547 (1926).

[27] N.W. Ashcroft, and N.D. Mermin, *Solid State Physics* (New York: Holt, Rinehart and Winston, 1976).

[28] D.W. Snoke, *Solid State Physics: Essential Concepts*, (Addison-Wesley, New York, 2008).

[29] L. Van Hove, Phys. Rev. **89**, 1189 (1953).

[30] L. Viña, S. Logothetidis, and M. Cardona, Phys. Rev. B **30**, 1979 (1984).

[31] P. Lautenschlager, M. Garriga, L. Viña and M. Cardona, Phys. Rev. B **36**, 4821 (1987).

[32] P. Lautenschlager, M. Garriga and M. Cardona, Phys. Rev. B **36**, 4813 (1987).

[33] P. Lautenschlager, M. Garriga, S. Logothetidis and M. Cardona, Phys. Rev. B **35**, 9174 (1987).

[34] S. Gopalan, P. Lautenschlager and M. Cardona, Phys. Rev. B **35**, 5577 (1987)

[35] M. Garriga, P. Lautenschlager, M. Cardona and K. Ploog, Solid State Communications **61**, 157 (1987).

[36] S. Zollner, M. Garriga, J. Humlicek, S. Gopalan and M. Cardona, Phys. Rev. B **43**, 4349 (1991).

[37] L. Viña, H. Hochst and M. Cardona, Phys. Rev. B **31**, 958 (1985).

[38] Y.P. Varshni, Physica **34**, 149 (1967).

[39] P. Lautenschlager, P.B. Allen, and M. Cardona, Phys. Rev. B **31**, 2163 (1985).

[40] Z. Hang, D. Yan, F.H. Pollak, G.D. Pettit, and J.M. Woodall, Phys. Rev. B **44**, 10 546 (1991).

[41] L. Malikova, W. Krystek, F.H. Pollak, N. Dai, A. Cavus, and M.C. Tamargo, Phys. Rev. B **44**, 1819 (1996).

[42] R.R. Reeber and K. Wang, Mater. Chem. Phys. **46**, 259 (1996).

[43] R. Roucka, Y.Y. Fang, J. Kouvetakis, A.V.G. Chizmeshya, and J. Menendez, Phys. Rev. B **81**, 245214 (2010).

[44] Y. Ma, J.S. Tse, Solid State Communications, **143**, 161 (2007).

[45] P.W. Sparks, C.A. Swenson, Phys. Rev. **163**, 779 (1967).

[46] D.F. Gibbons, Phys. Rev. **112**, 136 (1958).

[47] S.I. Novikova, Sov. Phys. Solid State **2**, 37 (1960).

[48] H. Ibach, Phys. Stat. Sol. **33**, 257 (1969).

[49] S. Zollner, in *Silicon-Germanium Carbon Alloys: Growth, Properties and Applications*, edited by S.T. Pantelides and S. Zollner (Taylor&Francis, New York, NY, 2002).

[50] O. Madelung, U. Rössler, and M. Schulz, *Grey tin (alpha-Sn), crystal structure, lattice parameter (pure Sn, Sn-IV alloys), thermal expansion*, (Springer, Berlin, Heidelberg, 2002), p. 1–6.

[51] J.F.C. Baker and M. Hart, Acta Cryst. A **31**, 364 (1975).

[52] E. Massa, G. Mana, U. Kuetgens, and L. Ferroglio, New J. Phys. **11**, 053013 (2009).

[53] L. Vegard, Zeitschrift fr Physik. **5**, 17 (1921).

[54] A.R. Denton, and N.W. Ashcroft, Phys. Rev. A. **43**, 3161 (1991).

[55] J. Kouvetakis, J. Menendez, and A.V.G. Chizmeshya, Annu. Rev. Mater. Res. **36**, 497 (2006).

[56] V.R. D'Costa, Y.Y. Fang, J. Mathews, R. Roucka, J. Tolle, J. Menendez, and J. Kouvetakis, Semicond. Sci. Technol. **24**, 115006 (2009).

[57] R. Beeler, R. Roucka, A.V.G. Chizmeshya, J. Kouvetakis, and J. Menendez, Phys. Rev. B **84**, 035204 (2011).

[58] N. Bhargava, M. Coppinger, J.P. Gupta, L. Wielunski, and J. Kolodzey, Appl. Phys. Lett. **103**, 041908 (2013).

[59] H. Lin, R. Chen, W.S. Lu, Y.J. Huo, T.I. Kamins, and J.S. Harris, Appl. Phys. Lett. **100**, 102109 (2012).

[60] J.P. Dismukes, R.J. Paff, and L. Ekstrom, J. Phys. Chem. **68**, 3021 (1964).

[61] H.J. McSkimin and P. Andreatch, J. Appl. Phys. **34**, 651 (1963).

[62] D.L. Price, J.M. Rowe, and R.M. Nicklow, Phys. Rev. B **3**, 1268 (1971).

[63] H.J. Osten, J. Appl. Phys. **84**, 2716 (1998).

[64] M. Chandrasekhar and F.H. Pollak, Phys. Rev. B **15**, 2127 (1977).

[65] F.H. Pollak and M. Cardona, Phys. Rev. **172**, 816 (1968).

[66] V.R. D'Costa, C.S. Cook, A.G. Birdwell, C.L. Littler, M. Canonico, S. Zollner, J. Kouvetakis, and J. Menendez, Phys. Rev. B **73**, 125207 (2006).

[67] R.T. Beeler, D.J. Smith, J. Kouvetakis, and J. Menendez, IEEE J. Photovoltaics **2**, 434 (2012).

[68] V.R. D'Costa, Y.Y. Fang, J. Tolle, J. Kouvetakis, and J. Menendez, Phys. Rev. Lett. **102**, 107403 (2009).

[69] V.R. D'Costa, W. Wang, Q. Zhou, E.S. Tok, and Y.C. Yeo, Appl. Phys. Lett. **104**, 022111 (2014).

[70] J. Menendez and J. Kouvetakis, Appl. Phys. Lett. **85**, 1175 (2004).

[71] C.G. Van De Walle, Phys. Rev. B **39**, 1871 (1989).

[72] A. Attiaoui and O. Moutanabbir, J. Appl. Phys. **116**, 063712 (2014).

[73] C. Xu, R.T. Beeler, L. Jiang, G. Grzybowski, A.V.G. Chizmeshya, J. Menéndez, and J. Kouvetakis, Semicond. Sci. Technol. **28**, 105001 (2013).

[74] R. Hickey, N. Fernando, S. Zollner, J. Hart, R. Hazbun, and J. Kolodzey, J. Vac. Sci. Technol. B **35**, 021205 (2017).

[75] J.S. Hovis, R.J. Hamers, and C.M. Greenlief, Surf. Sci. Lett. **440**, 815 (1999).

[76] H. Fujiwara, *Spectroscopic Ellipsometry: Principles and Applications*, (Wiley, Chichester, England, 2007).

[77] R.M.A. Azzam and N.M. Bashara, *Ellipsometry and Polarized Light*, (North-Holland, Amsterdam, 1977).

[78] Y.Z. Hu, J.-Th. Zettler, S. Chongsawangvirod, Y.Q. Wang, and E.A. Irene, Appl. Phys. Lett. **61**, 1098 (1992).

[79] T.N. Nunley, N.S. Fernando, N. Samarasingha, J.M. Moya, C.M. Nelson, A.A. Medina, and S. Zollner, J. Vac. Sci. Technol. B **34**, 061205 (2016).

[80] D.E. Aspnes and A.A. Studna, Surf. Sci. **96**, 294 (1980).

[81] N.S. Fernando, T.N. Nunley, A. Ghosh, C.M. Nelson, J.A. Cooke, A.A. Medina, S. Zollner, C. Xu, J. Menendez, and J. Kouvetakis, Appl. Surf. Sci. (2016).

[82] C.M. Herzinger, B. Johs, W.A. McGahan, J.A. Woollam, and W. Paulson, J. Appl. Phys. **83**, 3323 (1998).

[83] G.E. Jellison, Opt. Mater. **1**, 151 (1992).

[84] A. Savitzky and M.J.E. Golay, Anal. Chem. **36**, 1627 (1964).

[85] M. Hawkridge, *High resolution X-ray diffraction* (PANalytical, 2014).

[86] D.K. Bowen and B.K. Tanner, *High Resolution X-Ray Diffractometry and Topography* (Taylor & Francis, Bristol, PA, 1998).

[87] V. Holý, U. Pietsch, and T. Baumbach, *High-Resolution X-Ray Scattering from Thin Films and Multilayers* (Springer, Berlin, 1999).

[88] A. Navarro-Quezada, A.G. Rodriguez, M.A. Vidal, and H. Navarro-Contreras, J. Cryst. Growth **291**, 340 (2006).

[89] D.S. Sivia, *Elementary scattering theory : for X-ray and neutron users* (Oxford University Press, New York, 2011).

[90] L.G. Parratt, Phys. Rev. **95**, 359 (1954).

[91] A. Nelson, J. Appl. Cryst. **39**, 273 (2006).

[92] WaveMetrics Inc., Lake Oswego, OR, USA.

[93] Bruker Nano Surfaces, *Fundamentals of contact mode and tapping mode atomic force microscopy*, May 2012.

[94] G. Binnig, C.F. Quate, and Ch. Gerber, Phys. Rev. Lett. **56**, 930 (1986).

[95] Y. Martin, C.C. Williams, and H.K. Wickramasinghe, J. Appl. Phys. **61**, 4723 (1987).

[96] A. Diebold, *Handbook of Silicon Semiconductor Metrology* (Marcel Dekker, New York, 2001).

[97] T. Yoshizawa, *Handbook of Optical Metrology: Principles and Applications* (CRC Press, Boca Raton, FL, 2009).

[98] S. Zollner, in *Ellipsometry at the Nanoscale*, edited by M. Losurdo and K. Hingerl (Springer, Berlin, 2013), pp. 607-627.

[99] H.G. Tompkins and W.A. McGahan, *Spectroscopic Ellipsometry and Reflectometry: A Users Guide* (Wiley, New York, 1999).

[100] H.G. Tompkins and E.A. Irene, *Handbook of Ellipsometry* (Springer, Heidelberg, 2005).

[101] H.G. Tompkins and J.N. Hilfiker, *Spectroscopic Ellipsometry: Practical Application to Thin Film Characterization* (Momentum Press, New York, 2016).

[102] R.F. Potter in *Handbook of Optical Constants of Solids*, edited by E.D. Palik (Academic Press, San Diego, 1998), pp. 462-475.

[103] S. Adachi, *The Handbook on Optical Constants of Semiconductors* (World Scientific, Singapore, 2012).

[104] M. Fox, *Optical Properties of Solids*, 2nd ed. (Oxford University Press, Oxford, 2010).

[105] M.L. Cohen and J.R. Chelikowsky, *Electronic Structure and Optical Properties of Semiconductors* (Springer, Berlin, 1988).

[106] D.G. Seiler, S. Zollner, A.C. Diebold, and P.M. Amirtharaj, in *Handbook of Optics*, 3rd ed., edited by M. Bass (McGraw-Hill, New York, 2010), Vol. IV, Chap. 5, pp. 5.1-96.

[107] W.G. Spitzer, Semiconductors and Semimetals **3**, 17 (1967).

[108] R.J. Collins and H.Y. Fan, Phys. Rev. **93**, 674 (1954).

[109] W.C. Dash and R. Newman, Phys. Rev. **99**, 1151 (1955).

[110] G.G. Macfarlane, T.P. McLean, J.E. Quarrington, and V. Roberts, Phys. Rev. **108**, 1377 (1957); J. Phys. Chem. Solids **8**, 388 (1959).

[111] H.W. Icenogle, B.C. Platt, and W.L. Wolfe, Appl. Opt. **15**, 2348 (1976).

[112] T.N. Nunley, T.I. Willett-Gies, J.A. Cooke, F.S. Manciu, P. Marsik, C. Bernhard, and S. Zollner J. Vac. Sci. Technol. A **34**, 051507 (2016).

[113] A. Ghosh, C.M. Nelson, L.S. Abdallah, and S. Zollner J. Vac. Sci. Technol. A **33**, 061203 (2015).

[114] M. Cardona and G. Harbeke, J. Appl. Phys. **34**, 813 (1963).

[115] H.R. Philipp and E.A. Taft, Phys. Rev. **113**, 1002 (1959).

[116] D.E. Aspnes and A.A. Studna, Phys. Rev. B **27**, 985 (1983).

[117] M.K. Kelly, S. Zollner, and M. Cardona, Surf. Sci. **285**, 282 (1993).

[118] K.A. Bell, L. Mantese, U. Rossow, and D.E. Aspnes, Thin Solid Films **313-314**, 161 (1998).

[119] G.E. Jellison and B.C. Sales, Appl. Opt. **30**, 4310 (1991).

[120] B.E. Deal and A.S. Grove, J. Appl. Phys. **36**, 3770 (1965).

[121] G. Hellings, J. Mitard, G. Eneman, B. De Jaeger, D.P. Brunco, D. Shamiryan, T. Vandeweyer, M. Meuris, M.M. Heyns, and K. De Meyer, IEEE Electron Dev. Lett. **30**, 88 (2009).

[122] P. Ponath, A.B. Posadas, R.C. Hatch, and A.A. Demkov, J. Vac. Sci. Technol. B **31**, 031201 (2013).

[123] H. Adhikari, P.C. McIntyre, S. Sun, P. Pianetta, and C.E.D. Chidsey, Appl. Phys. Lett. **87**, 263109 (2005).

[124] S.R.M. da Silva, G.K. Rolim, G.V. Soares, I.J.R. Baumvol, C. Krug, L. Miotti, F.L. Freire, M.E.H.M. da Costa, and C. Radtke, Appl. Phys. Lett. **100**, 191907 (2012).

[125] K. Kita, S. Suzuki, H. Nomura, T. Takahashi, T. Nishimura, and A. Toriumi, Jpn. J. Appl. Phys. **47**, 2349 (2008).

[126] H. Matsubara, T. Sasada, M. Takenaka, and S. Takagi, Appl. Phys. Lett. **93**, 032104 (2008).

[127] J.T. Law and P.S. Meigs, J. Electrochem. Soc. **104**, 154 (1957).

[128] R.B. Bernstein and D. Cubicciotti, J. Am. Chem. Soc. **73**, 4112 (1951).

[129] P. Bohač, L. Jastrabik, D. Chvostova, and V. Železny, Vacuum **41**, 1466 (1990).

[130] J.A. Woollam Co., Inc., Lincoln, NE.

[131] G.E. Jellison and F.A. Modine, Appl. Phys. Lett. **69**, 371 (1996); **69**, 2137 (1996).

[132] J. Leng, J. Opsal, H. Chu, M. Senko, and D.E. Aspnes, J. Vac. Sci. Technol. A **16**, 1654 (1998).

[133] A. Kahan, J.W. Goodrum, R.S. Singh, and S.S. Mitra, J. Appl. Phys. **42**, 4444 (1971).

[134] E.R. Lippincott, A. Van Valkenburg, C.E. Weir, and E.N. Bunting, J. Res. Natl. Bur. Stand. **61**, 61 (1958).

[135] M. Hass, J. Phys. Chem. Solids **31** 415 (1970).

[136] M. Erman, J.B. Theeten, N. Vodjdani, and Y. Demay, J. Vac. Sci. Technol. B **1**, 328 (1983).

[137] D.E. Aspnes, in *Handbook on Semiconductors: Optical Properties of Solids*, edited by M. Balkanski (North-Holland, Amsterdam, 1980), vol. 2, p. 109.

[138] C.C. Kim, J.W. Garland, H. Abad, and P.M. Raccah, Phys. Rev. B **45**, 11749 (1992).

[139] C.M. Herzinger and B.D. Johs, U.S. Patent No. 5,796,983 (18 August 1998).

[140] G.G. Devyatykh, E.M. Dianov, N.S. Karpychev, S.M. Mazavin, V.M. Mashinskiĭ, V.B. Neustruev, A.V. Nokolaĭchik, A.M. Prokhorov, A.I. Ritus, N.I. Sokolov, and A.S. Yushin, Sov. J. Quantum Electron. **10**, 900 (1980).

[141] L. Pajasova, Czech. J. Phys. B **19**, 1265 (1969).

[142] G.E. Jellison and J.W. McCamy, Appl. Phys. Lett. **61**, 512 (1992).

[143] T.P. McLean and E.G.S. Paige, in *Report of the International Conference on the Physics of Semiconductors*, edited by A.C. Stickland (Institute of Physics, London, 1962), p. 450.

[144] See supplementary material at http://dx.doi.org/10.1116/1.4963075 for a listing of the oscillator parameters for Ge and GeO_2 and for tables of the optical constants of these materials.

[145] J.M. Jackson, M.E. Wells, G. Kordas, D.L. Kinser, R.A. Weeks, and R.H. Magruder, J. Appl. Phys. **58**, 2308 (1985).

[146] A.A. Demkov and O.F. Sankey, Phys. Rev. Lett. **83**, 2038 (1999).

[147] W.A. Pliskin, J. Vac. Sci. Technol. **14**, 1064 (1977).

[148] K. Taniguchi, M. Tanaka, C. Hamaguchi, and K. Imai, J. Appl. Phys. **67**, 2195 (1990).

[149] N. Kitamura, K. Fukumi, J. Nishii, and N. Ohno, J. Appl. Phys. **101**, 123533 (2007).

[150] W. Rzodkiewicz and A. Panas, Acta Physica Polonica A **116**, S-92 (2009).

[151] H.G. Tompkins and W.A. McGahan, *Spectroscopic Ellipsometry and Reflectometry: A User's Guide*, (Wiley, New York, NY, 1999).

[152] H.G. Tompkins and J.N. Hilfiker, *Spectroscopic Ellipsometry: Practical Application to Thin Film Characterization* (Momentum Press, New York, 2015).

[153] J. Humlíček, M. Garriga, M.I. Alonso, and M. Cardona, J. Appl. Phys. **65**, 2827 (1989).

[154] G.R. Muthinti, M. Medikonda, T. Adam, A. Reznicek, and A.C. Diebold, J. Appl. Phys. **112**, 053519 (2012).

[155] C. Xu, C.L. Senaratne, J. Kouvetakis, and J. Menéndez, Soild-State Electron. **110**, 76 (2015).

[156] L. Viña and M. Cardona, Phys. Rev. B **29**, 6739 (1984).

[157] D.E. Aspnes, A.A. Studna, and E. Kinsbron, Phys. Rev. B **29**, 768 (1984).

[158] G.E. Jellison, F.A. Modine, C.W. White, R.F. Wood, and R.T. Young, Phys. Rev. Lett. **46**, 1414 (1981).

[159] M. Cardona, W. Paul, and H. Brooks, J. Phys. Chem. Solids **8**, 204 (1959).

[160] A.R. Goñi, K. Syassen, and M. Cardona, Phys. Rev. B **41**, 10104 (1990).

[161] M. Chandrasekhar and F.H. Pollak, Phys. Rev. B **15**, 2127 (1977).

[162] P. Etchegoin, J. Kircher, M. Cardona, and C. Grein, Phys. Rev. B **45**, 11721 (1992).

[163] Y. Ishikawa, K. Wada, J. Liu, D.D. Cannon, H.C. Luan, J. Michel, and L.C. Kimerling, J. Appl. Phys. **98**, 013501 (2005).

[164] X. Sun, J. Liu, L.C. Kimerling, and J. Michel, Appl. Phys. Lett. **95**, 011911 (2009).

[165] J. Liu, X. Sun, R. Camacho-Aguilera, L.C. Kimerling, and J. Michel, Opt. Lett. **35**, 679 (2010).

[166] J.D. Gallagher, C. Xu, L. Jiang, J. Kouvetakis, and J. Menendez, Appl. Phys. Lett. **103**, 202104 (2013).

[167] J. Jiang, J.D. Gallagher, C.L. Senaratne, T. Aoki, J. Mathews, J. Kouvetakis, and J. Menendez, Semicond. Sci. Technol. **29**, 115028 (2014).

[168] S. Wirths, R. Geiger, N. von den Driesch, G. Mussler, T. Stoica, S. Mantl, Z. Ikonic, M. Luysberg, S. Chiussi, J.M. Hartmann, H. Sigg, J. Faist, D. Buca, and D. Grützmacher, Nat. Photon. **9**, 88 (2015).

[169] Wafer World, Inc., West Palm Beach, FL.

[170] J.A. Woollam Co., Inc., Lincoln, NE. Model V-VASE.

[171] D.F. Gibbons, Phys. Rev. **112**, 136 (1958).

[172] C.M. Nelson, M. Spies, L.S. Abdallah, S. Zollner, Y. Xu, and H. Luo, J. Vac. Sci. Technol. A **30**, 061404 (2012).

[173] T.H. Ghong, T.J. Kim, Y.W. Jung, Y.D. Kim, and D.E. Aspnes, J. Appl. Phys. **103**, 073502 (2008).

[174] K.E. Junge, R. Lange, J.M. Dolan, S. Zollner, M. Dashiell, B.A. Orner, and J. Kolodzey, Appl. Phys. Lett. **69**, 4084 (1996).

[175] M. Cardona and R.K. Kremer, Thin Solid Films **571**, 680 (2014).

[176] P. Lautenschlager, P.B. Allen, and M. Cardona, Phys. Rev. B **33**, 5501 (1986)

[177] M. Cardona, Phys. Rev. B **15**, 5999 (1977).

[178] P. Lautenschlager, M. Garriga, L. Viña, and M. Cardona, Phys. Rev. B **36**, 4821 (1987).

[179] M. Cardona, *Modulation Spectroscopy* (Academic Press, New York, 1969).

[180] B.J. Frey, D.B. Leviton, T.J. Madison, Proc. SPIE **6273**, 62732J (2006). DOI: 10.1117/12.672850.

[181] C. Tanguy, J. Appl. Phys. **80**, 4626 (1996).

[182] X. Sun, *Germanium-on-Silicon for Integrated Silicon Photonics* in Advanced Photonic Sciences, M. Fadhali (Ed.), (InTech, Croatia, 2012).

[183] R. Soref, Nat. Photon. **4**, 495 (2010).

[184] S. Wirths, R. Geiger, N. von den Driesch, G. Mussler, T. Stoica, S. Mantl, Z. Ikonic, M. Luysberg, S. Chiussi, J.M. Hartmann, H. Sigg, J. Faist, D. Buca, and D. Grützmacher, Nat. Photon. **9**, 88 (2015).

[185] J. Xie, A.V.G. Chizmeshya, J. Tolle, V.R.D'Costa, J. Menendez, and J. Kouvetakis, Chem. Mater. **22**, 3779 (2010).

[186] D.W. Jenkins and J.D. Dow, Phys. Rev. B **36**, 7994 (1987).

[187] K.A. Mader, A. Baldereschi, and H. von Kanel, Solid State Commun. **69**, 1123 (1989).

[188] S. Gupta, R. Chen, B. Magyari-Köpe, H. Lin, B. Yang, A. Nainani, J.S. Harris, and K.C. Saraswat, in Proceedings of the IEEE International Electron Devices Meeting (Institute of Electrical and Electronics Engineering Proceedings, 2011), p. 398.

[189] W.J. Yin, X.G. Gong, and S.H. Wei, Phys. Rev. B **78**, 161203 (2008).

[190] H. Li, Y.X. Cui, K.Y. Wu, W.K. Tseng, H.H. Cheng, and H. Chen, Appl. Phys. Lett. **102**, 251907 (2013).

[191] R.A. Soref and C.H. Perry, J. Appl. Phys. **69**, 539 (1991).

[192] J. Xie, J. Tolle, V.R. D'Costa, A.V.G. Chizmeshya, J. Menendez, and J. Kouvetakis, Appl. Phys. Lett. **95**, 181909 (2009).

[193] M. Bauer, C. Ritter, P.A. Crozier, J. Ren, J. Menendez, G. Wolf, and J. Kouvetakis, Appl. Phys. Lett. **83**, 2163 (2003).

[194] C. Xu, C.L. Senaratne, J. Kouvetakis and J. Menendez, Solid-State Electronics **110**, 76 (2015).

[195] P. Aella, C. Cook, J. Tolle, S. Zollner, A.V.G. Chizmeshya, and J. Kouvetakis, Appl. Phys. Lett. **84**, 888 (2004).

[196] P. Moontragoon, R.A. Soref, and Z. Ikonic, J. Appl. Phys. **112**, 073106 (2012).

[197] C.I. Ventura, J.D.Q. Flores, J.D. Fuhr, and R.A. Barrio, Prog. Photovolt. **23**, 112 (2015).

[198] V.R. D'Costa, W. Wang, Q. Zhou, T.K. Chan, T. Osipowicz, E.S. Tok, and Y.C. Yeo, J. Appl. Phys. **116**, 053520 (2014).

[199] V.R. D'Costa, W. Wang, and Y. Yeo, J. Appl. Phys. **120**, 063104 (2016).

[200] M. Medikonda, G.R. Muthinti, R. Vasic, T.N. Adam, A. Reznicek, M. Wormington, G. Malladi, Y. Kim, Y.C. Huang, and A.C. Diebold, J. Vac. Sci. Technol. B **32**, 061805 (2014).

[201] J.H. Fournier-Lupien, S. Mukherjee, S. Wirths, E. Pippel, N. Hayazawa, G. Mussler, J.M. Hartmann, P. Desjardins, D. Buca and O. Moutanabbir, Appl. Phys. Lett. **103**, 263103 (2013).

[202] L.D. Laude, F.H. Pollak, and M. Cardona, Phys. Rev. B **3**, 2623 (1971).

[203] J. Weber and M.I. Alonso, Phys. Rev. B **40**, 5683 (1989).

[204] D.E. Aspnes, Phys. Rev. B **12**, 2297 (1975).

[205] D.E. Aspnes and A.A. Studna, Solid State Commun. **11**, 1375 (1972).

[206] S. Gupta, B. Magyari-Kope, Y. Nishi, and K.C. Saraswat, J. Appl. Phys. **113** (2013).

[207] C.L. Senaratne, J.D. Gallagher, T. Aoki, J. Kouvetakis, and J. Menendez, Chem. Mater. **26**, 6033 (2014).

[208] W. Wang, Q. Zhou, Y. Dong, E.S. Tok, and Y.C. Yeo, Appl. Phys. Lett. **106**, 232106 (2015).

[209] T. Wendav *et al.*, Appl. Phys. Lett. **108**, 242104 (2016).

[210] S. Kim, N. Bhargava, J. Gupta, M. Coppinger, and J. Kolodzey, Opt. Express **22**, 11029 (2014).

[211] J.P. Gupta, N. Bhargava, S. Kim, T. Adam, and J. Kolodzey, Appl. Phys. Lett. **102**, 251117 (2013).

[212] N.V. Den Driesch, D. Stange, S. Wirths, D. Rainko, G. Mussler, and P. Gr, SPIE Photonics West **9752**, 1 (2016).

[213] E. Kasper, Front. Optoelectron. China **3**, 143 (2010).

[214] S. Wirths, D. Buca, and S. Mantl, Prog. Cryst. Growth Charact. Mater. **62**, 1 (2016).

[215] N. Bhargava, J.P. Gupta, T. Adam, and J. Kolodzey, J. Electron. Mater. **43**, 931 (2014).

[216] G. Grzybowski, R.T. Beeler, L. Jiang, D.J. Smith, J. Kouvetakis, and J. Menendez, Appl. Phys. Lett. **101**, 072105 (2012).

[217] S. Gupta, B. Magyari-Köpe, Y. Nishi, and K.C. Saraswat, J. Appl. Phys. **113**, 073707 (2013).

[218] W.J. Yin, X.G. Gong, and S.-H. Wei, Phys. Rev. B **78**, 161203 (2008).

[219] W. Ni, K. Lyutovich, J. Alami, C. Tengstedt, M. Bauer, and E. Kasper, J. Cryst. Growth **228**, 756 (2001).

[220] C. Claeys and E. Simoen, *Germanium-Based Technologies: From Materials to Devices* (Elsevier, Oxford, 2007).

[221] S. Shen, J. Condens. Matter Phys. **228**, 8733 (1994).

[222] D.K. Bowen and B.K. Tanner, *X-Ray Metrology in Semiconductor Manufacturing* (CRC Press, Boca Raton, 2006).

[223] N. Bhargava, *Growth of silicon-germanium-tin alloys and fabrication of magnetic tunnel junction biosensors*, University of Delaware, 2013.

[224] C.J.K. Richardson, L. He, and S. Kanakaraju, J. Vac. Sci. Technol. B **29**, 03C126 (2011).

[225] H. Perez Ladron De Guevara, A.G. Rodriguez, H. Navarro-Contreras, and M.A. Vidal, Appl. Phys. Lett. **83**, 4942 (2003).

[226] S. Zollner, J. Hildreth, and R. Liu, J. Appl. Phys. **88**, 4102 (2000).

[227] O. Gurdal, P. Desjardins, J. Carlsson, N. Taylor, H.H. Radamson, J.E. Sundgren, and J.E. Greene, J. Appl. Phys. **83**, 162 (1998).

[228] S. Gupta, R. Chen, B. Magyari-Kope, H. Lin, Bin Yang, A. Nainani, Y. Nishi, J.S. Harris, and K.C. Saraswat, in 2011 Int. Electron Devices Meet. (IEEE, 2011), pp. 16.6.116.6.4.

[229] H. Lin, R. Chen, Y. Huo, T.I. Kamins, and J.S. Harris, Thin Solid Films **520**, 3927 (2012).

[230] K.A. Bratland, Y.L. Foo, T. Spila, H.-S. Seo, R.T. Haasch, P. Desjardins, and J.E. Greene, J. Appl. Phys. **97**, 044904 (2005).

[231] J. Hart, R. Hazbun, J. Nakos, D. Siegel, C. Funch, J. Kolodzey, and D. Harame, ECS Trans. **64**, 659 (2014).

[232] A.G. Cullis, D.J. Robbins, A.J. Pidduck, and P.W. Smith, MRS Proc. **280**, 383 (1992).

[233] R. Hull, E.A. Stach, R. Tromp, F. Ross, and M. Reuter, Phys. Status Solidi **171**, 133 (1999).

[234] J.E. Ayers, J. Cryst. Growth **135**, 71 (1994).

[235] P.B. Gay, P. Hirsch, ACTA Metall. **1**, 315 (1953).

[236] M. A Moram, C.F. Johnston, M.J. Kappers, and C.J. Humphreys, J. Phys. D-Applied Phys. **42**, 135407 (2009). V.R. DCosta, W. Wang, Q. Zhou, T.K. Chan, T. Osipowicz, E.S. Tok, and Y.-C. Yeo, J. Appl. Phys. **116**, 053520 (2014).

[237] J. Tersoff and F.K. Legoues, Phys. Rev. Lett. **72**, 3570 (1994).

[238] J.W. Matthews and A.E. Blakeslee, J. Cryst. Growth **27**, 118 (1974).

[239] R. People and J.C. Bean, Appl. Phys. Lett. **47**, 322 (1985).

[240] H. Prez Ladrn De Guevara, A.G. Rodriguez, H. Navarro-Contreras, and M.A. Vidal, Appl. Phys. Lett. **83**, 4942 (2003).

[241] P. Moontragoon, Z. Ikoni, and P. Harrison, Semicond. Sci. Technol. **22**, 742 (2007).